STUDY OF FULLY-MIXED HYBRID THERMAL ENERGY STORAGE WITH PHASE CHANGE MATERIALS FOR SOLAR HEATING APPLICATIONS

STUDY OF FULLY-MIXED HYBRID THERMAL ENERGY STORAGE WITH PHASE CHANGE MATERIALS FOR SOLAR HEATING APPLICATIONS

by

Mohamed Yasser Abdelsalam, M.Sc., B.Sc.

A Thesis

Submitted to the School of Graduate Studies

in Partial Fulfillment of the Requirements

for the Degree of Doctor of Philosophy

McMaster University

DOCTOR OF PHILOSOPHY (2017)
(Mechanical Engineering)

McMaster University
Hamilton. Ontario

.

TITLE: Study of Fully-Mixed Hybrid Thermal Energy Storage with Phase Change Materials for Solar Heating Applications

AUTHOR: Mohamed Yasser Abdelsalam, M.Sc.

SUPERVISOR: Dr. James S. Cotton. Professor
Dr. Marilyn F. Lightstone. Professor
Mechanical Engineering Department

NUMBER OF PAGES: xxxvi - 302

To My Wife and Our Little Girl Tia

ABSTRACT

A novel design of hybrid thermal energy storage (HTES) using Phase Change Material (PCM) was evaluated using a mathematical model. Both single and multi-tank (cascaded) storage were explored to span small to large-scale applications (200-1600 litres). The storage element was based on the concept of a fully-mixed modular tank which is charged and discharged indirectly using two immersed coil heat exchangers situated at the bottom and top of the tank. A three-node model was developed to simulate different thermal behaviors during the operation of the storage element. Experiments were conducted on full-scale 200-l single-tank sensible heat storage (SHS) and hybrid thermal energy storage (HTES) to provide validation for the mathematical model. The HTES incorporated rectangular PCM modules submerged in the water tank. Satisfactory agreement was found between the numerical results and the experimental results obtained by Mather (2000) on single and multi-tank SHS. In addition, good agreement was noticed with the experiments performed by the author on single-tank SHS and HTES at McMaster University. The developed model was found to provide high levels of accuracy in simulating different operation conditions of the proposed design of storage element as well as computational efficiency.

A parametric study was undertaken to investigate the potential benefits of the HTES over the SHS, operating under idealistic conditions. The HTES can perform at least two times better than the SHS with the same volume. The PCM volume fraction, melting temperature and properties were found to have critical impact on the storage gains of the

HTES. All the parameters must be adjusted such that: (1) the thermal resistance of the storage element is minimized, and (2) most of the energy exchange with the storage element takes place in the latent heat form.

The performance of the single-tank HTES was evaluated numerically while operating in a solar thermal domestic hot water (DHW) system for a single-family residence. The PCM parameters were selected to maximize the solar fraction during the operation on a typical spring day in Toronto. The use of the HTES can reduce the tank volume by 50% compared to the matched size of the SHS tank. However, the HTES was found to underperform the SHS when the system was operated in different days with different solar irradiation intensities. The effect of different draw patterns was also investigated. The results indicated that thermal storage is needed only when the energy demand is out-of-phase with the energy supply. For the same daily hot water demand, different consumption profiles; ex. dominant morning, dominant evening, dominant night and dispersed consumptions, showed slight impact on the performance of the system.

The concept of multi-tank (cascaded) HTES storage was explored for medium/large scale solar heating applications such as for restaurants, motels, and multi-family residences. The design was based on the series connection of modular tanks through the bottom and top heat exchangers. Each individual tank had a PCM with different melting temperature. The results showed that the cascaded storage system outperformed the single-tank system with the same total volume as a result of the high levels of sequential or tank-to-tank stratification. The use of the cascaded HTES resulted in slight improvement in the solar fraction of the system.

ACKNOWLEDGEMENT

I would like to express the greatest gratitude to my supervisors, Prof. Marilyn Lightstone and Prof. James Cotton for their continuous support and guidance throughout this research project. Without their patience, dedicated supervision and mentoring, this dissertation wouldn't have been possible.

I also wish to show my utmost appreciation to the Smart Net-zero Energy Building Research Network (SNEBRN, NSERC) for funding this project. Through the network annual meetings, I was honored to have known a group of outstanding engineers, researchers and professors from different industrial and academic disciplines.

I would like to thank my colleagues at the Thermal Management Lab (TMRL) team and the technicians at the machine shop for their sincere advice and invaluable assistance.

To my parents and lovely sisters who sacrificed a lot in order for me to live my dream and get the PhD. Degree, thank you for your unconditional love, support and sacrifice. To my late father, You have been always living in my heart. I can never forget your last words to me, "Don't come back now. I'm fine. Finish your studies". May Allah bless your soul in paradise. To my mother, I kiss your hands for all what you have provided me since I was little. Your endless love and prayers are what kept me going.

Last but not least, thank you to my beautiful wife and little daughter "Tia" who brightened my life with tremendous joy and happiness.

STATEMENT OF ORIGINALITY

I hereby certify that all of the work described within this dissertation is the original work of the author. Any published or unpublished ideas and/or techniques from the work of others are fully acknowledged in accordance with the standard referencing practices.

Mohamed Abdelsalam

June, 2017

TABLE OF CONTENTS

LIST OF FIGURES

LIST OF TABLES

NOMENCLATURE

A_c	Cross-sectional area (m^2)
A_{coll}	Solar collector area (m^2)
A_i	Inner surface area of the coil (m^2)
A_o	Outer surface area of the coil (m^2)
c	Specific heat capacity (kJ/kg.K)
c_l	Specific heat capacity of liquid phase of PCM (kJ/kg.K)
c_s	Specific heat capacity of solid phase of PCM (kJ/kg.K)
c_w	Specific heat capacity of water (kJ/kg.K)
d_i	Inner diameter of the coil (m)
d_o	Outer diameter of the coil (m)
E	Energy (kJ)
E_{st}	Stored energy (kJ)
F_R	Solar collector heat removal factor (-)
F'	Solar collector efficiency factor (-)
G_T	Solar incidence radiation (Irradiation) (W/m^2)
H	Height of PCM module (m)
H_f	Latent heat of fusion of PCM (kJ/kg)
h_i	Inner heat transfer coefficient ($W/m^2.K$)
h_o	Outer heat transfer coefficient ($W/m^2.K$)

k	Thermal conductivity (W/m.K)
k_i	Thermal conductivity of the inner fluid (W/m.K)
k_o	Thermal conductivity of the outer fluid (W/m.K)
k_{pipe}	Thermal conductivity of the pipe (W/m.K)
L	Depth of the PCM module (m)
M_{nb}	Mass of fluid in the bottom node of the storage tank (kg)
M_{nt}	Mass of fluid in the top node of the storage tank (kg)
M_{bulk}	Mass of fluid in the middle node (bulk) of the storage tank (kg)
$\dot{m}_b$	Mass flow rate through the bottom coil heat exchanger (kg/s)
$\dot{m}_t$	Mass flow rate through the top coil heat exchanger (kg/s)
N	Number of nodes (-)
NTU	Number of heat transfer units (-)
Nu	Nusselt number = $\frac{hL_c}{k}$ (-)
Pr	Prandtl number = $\frac{\mu c}{k}$ (-)
Pr_i	Prandtl number of the inner fluid (-)
Pr_o	Prandtl number of the outer fluid (-)
Q	Heat transfer rate (W)
$Q_{b\text{-}PCM}$	Heat transfer rate from the middle node to PCM modules (W)
$Q_{coil,b}$	Heat transfer rate from the bottom coil heat exchanger (W)
$Q_{coil,i}$	Heat transfer rate from the i^{th} control volume of the heat exchanger (W)
$Q_{coil,t}$	Heat transfer rate from the top coil heat exchanger (W)
$Q_{cond,b\text{-}nb}$	Diffusion heat transfer rate from the middle node to the bottom node (W)

$Q_{cond,b\text{-}nt}$	Diffusion heat transfer rate from the middle node to the top node (W)
$Q_{Loss,nb}$	Rate of heat loss from bottom node of the storage tank (W)
$Q_{Loss,nt}$	Rate of heat loss from top node of the storage tank (W)
$Q_{Loss,bulk}$	Rate of heat loss from middle node of the storage tank (W)
Ra	Rayleigh number = $\frac{g\beta\Delta T L_c^3}{\nu\alpha}$ (-)
$R_{cond,wall}$	Conduction resistance of the pipe wall (K/W)
Re	Reynolds number = $\frac{\rho v D_h}{\mu}$ (-)
S	Melt front interface position (m)
s	Spacing between PCM modules (m)
Ste	Stefan number = $\frac{c_l \Delta T}{H_f}$ (-)
t	Time (s)
T_{amb}	Ambient temperature (°C)
T_b *or* T_{bulk}	Bulk temperature (°C)
T_c	Coil temperature (°C)
T_i	Initial temperature (°C)
$T_{in,b}$	Inlet temperature to the bottom heat exchanger (°C)
$T_{in,t}$	Inlet temperature to the top heat exchanger (°C)
T_f	Final temperature (°C)
T_m	PCM melting temperature (°C)
T_{mains}	Temperature of mains water (°C)
T_{nb}	Temperature of the bottom node of the storage tank (°C)
T_{nt}	Temperature of the top node of the storage tank (°C)

T_{op}	Operation temperature (°C)
$T_{out,b}$	Outlet temperature to the bottom heat exchanger (°C)
$T_{out,t}$	Outlet temperature to the top heat exchanger (°C)
T_{surr} *or* T_{∞}	Temperature of surrounding (°C)
U	Overall heat transfer coefficient (W/m^2 K)
U_{Loss}	Tank heat loss coefficient to the surrounding (W/m^2.K)
w_{PCM}	Thickness of the PCM module (m)
Δt	Time step (s)
ΔT	Temperature difference (°C, K)
ΔT_{corr}	Corrected temperature difference (°C, K)
Δx	Control volume size (m)

Greek Symbols

α	Thermal diffusivity (m^2/s)
β	Thermal expansion coefficient (K^{-1})
γ	Pump running time multiplier (-)
δ	Thermal penetration thickness (m)
ε	Heat exchanger effectiveness “Appendix A” (-)
ε	Error/uncertainty “Appendix D”
λ	Melt fraction (-)
μ	Dynamic viscosity (Pa.s)
ν	Kinematic viscosity (m^2/s)
ρ	Density (kg/m^3)

τ	Cycle time (s)
φ	PCM volume fraction (-)

Acronyms

CFD	Computational Fluid Dynamics
DHW	Domestic Hot Water
GHG	Green House Gases
HTES	Hybrid Thermal Energy Storage
HTF	Heat Transfer Fluid
HX	Heat Exchanger
LHS	Latent Heat Storage
NCHE	Natural Convection Heat Exchanger
PCM	Phase Change Material
SHS	Sensible Heat Storage
TES	Thermal Energy Storage

CHAPTER ONE

INTRODUCTION

1.1. Background

Energy use in Canada by the residential and commercial/institutional sectors accounted for over 20% of the total energy consumption in 2012 with approximately 2,534 PJ (444 million barrels oil equivalent). Around 67% of the energy consumption in these sectors is attributed to space heating and hot water demands. Approximately, 81% of these energy demands are supplied from fossil fuels and electricity (Energy Fact Book 2015-2016). According to Natural Resources Canada, greenhouse gas (GHG) emissions resulting from these applications accounted for 87 million tonnes of CO_2 equivalent (Energy Use Data Handbook, 2016).

These heating demands can be potentially offsetted by the use of renewable solar thermal energy which is sustainable, abundant and environmentally benign. Currently, a large sector of energy technologies focus on solar energy in order to reduce the consumption of premium fossil fuels and consequently cut down the harmful GHG emissions into the atmosphere. Also, waste heat from commercial and industrial applications in Canada was estimated to be around 1,392 PJ in 2010 (Canadian Energy Systems Analysis Research, http://www.cesarnet.ca/visual-ization/sankey-diagrams-canadas-energy-systems). Waste heat recovery technologies can be integrated with district heating plants in order to cover some of the thermal energy demands and hence improve the utilization of fossil fuels.

The biggest challenge facing the use of solar energy as well as waste heat is their intermittent nature. The availability and magnitude of both sources of thermal energy are time dependent. For example, solar energy is characterized by its diurnal as well as seasonal variability. Also, large amounts of waste heat in most of the industrial applications are only available during the operation time of the industrial facility. On the other hand, the energy demand depends primarily on the energy consumption pattern dictated by the user, which is not always in phase with the energy supply. Consequently, thermal energy storage (TES) is an essential component for bridging the mismatch between the availability of the energy source and the energy demand by the end-user.

Efficient design of TES is critical to the performance and feasibility of the system. The TES element must have the following fundamental characteristics:

1. High energy density per unit volume to reduce the overall space occupied by storage as well as the thermal losses to the surroundings.
2. High storage density per unit mass to reduce the overall weight of the storage component.
3. Appropriate charging and discharging rates depending on the supply and demand profiles.

Figure 1.1 shows a typical configuration of a TES element installed in a solar thermal system. During the times when there is excess energy from the supply (i.e., solar thermal energy), the supply loop (i.e., the solar collector loop, also referred to as the charging loop) is activated to store the excess amount of energy in the storage tank. When the energy demand by the end-user exceeds the amount of energy provided by the supply, the demand loop (also referred to as the discharging loop) is activated to deliver the stored energy to the end-user.

Often these systems require active controls on the supply side in order to avoid extracting energy from the storage tank when the supply is not available. In solar thermal storage systems, the controller compares the temperature difference between the solar collector and the bottom of the storage tank to a setpoint. The pump is then activated only when the setpoint is exceeded. This prevents sending cold fluid into the storage tank during early morning or late afternoon times when the solar irradiation intensity is low.

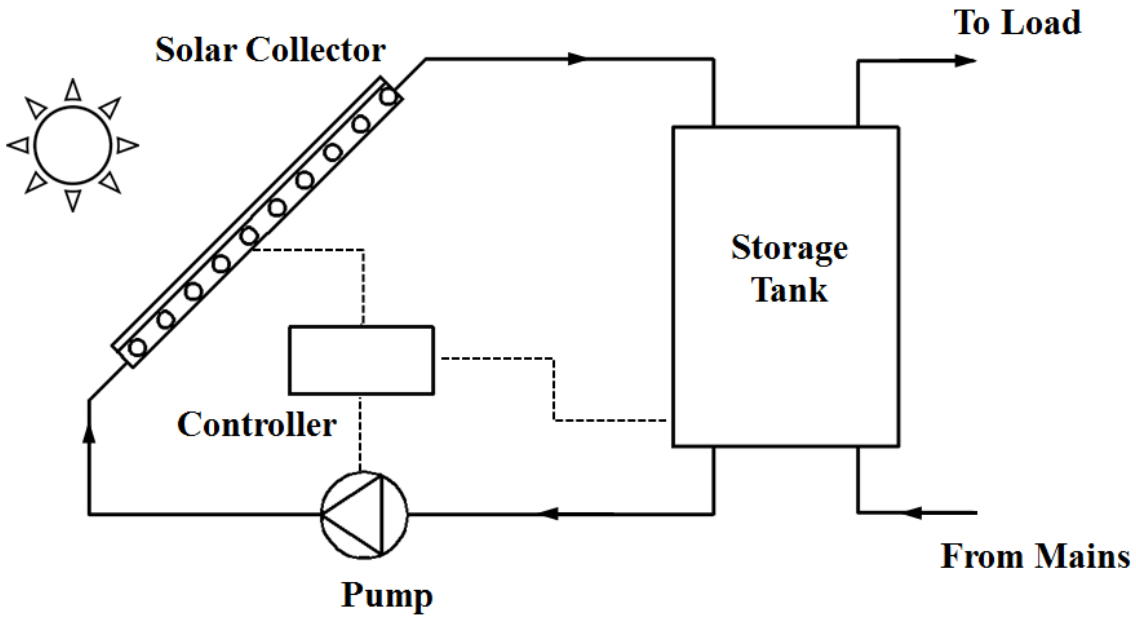

Figure 1.1. Basic components of TES tank integrated in a solar thermal hot water system.

TES designs can be classified according to the type of charging and discharging loops installed in the system:

Direct charging, direct discharging. This design is also referred to as an open system. The fluid circulating through the supply loop is the same as the one circulating in the demand loop; i.e. no intermediate heat exchangers are used. This system has the advantage of high heat transfer characteristics. However, this design does not suit storage systems used in cold climates when the circulating fluid in one or both of the supply and demand loops is prone to

freezing. In addition, these systems require special design of the storage tanks to handle pressurized fluids.

Indirect charging, indirect discharging. This design is also referred to as a closed system. An intermediate heat exchanger separates between the supply side and the storage tank. Another intermediate heat exchanger separates between the storage tank and the demand side. This system has the advantage of isolating the charging and discharging flow loops from the storage content which facilitates the use of antifreeze solution in cold climates. Also, for potable water heating applications, this helps to isolate the stagnant storage content from the potable water and prevents water contamination, such as by Legionnaires disease. Moreover, an indirect system does not require a pressurized storage tank which helps to reduce the cost of the system. This design, however, has larger thermal resistance to heat transfer due to the existence of intermediate heat exchangers. Depending on the application requirements, there are some designs with a combination of direct (indirect) charging and indirect (direct) discharging. There are various designs for the heat exchangers used in the indirect storage systems, as shown in Figure 1.2.

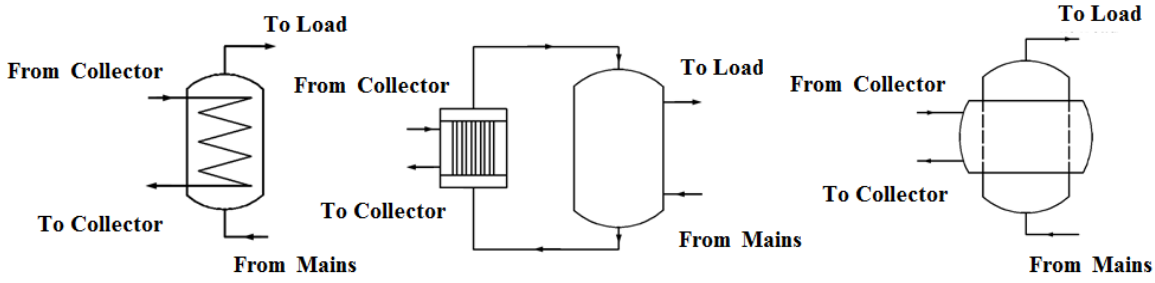

Figure 1.2. Different heat exchanger designs used in TES systems. Left: Immersed coil heat exchanger. Middle: External heat exchanger. Right: Mantle heat exchanger.

The most commonly used designs in North America are the immersed coil heat exchanger and the external heat exchanger. An immersed coil heat exchanger is installed inside the storage tanks and is mainly used to promote mixing and maintain uniform temperature inside the storage tank; i.e. the charging coil is usually installed at the bottom of the tank while the discharging coil is installed at the top of the tank (Hollands 1991, Mather 2000). The immersed coil heat exchanger design typically requires one pump to circulate the heat transfer fluid through the supply loop. The external heat exchanger is installed outside the storage tank and is primarily used to promote thermal stratification inside the storage tank. Thermal stratification refers to the formation of fluid layers with different temperatures inside the storage tank as a result of buoyancy forces. Thermal stratification yields a positive vertical temperature gradient inside the storage tank where the hot fluid layers stay at the top while the cold liquid layers reside at the bottom of the tank. This phenomenon is more favorable to TES systems than fully mixed tank (destratified) since the former yields lower temperatures returning to the supply and higher temperatures delivered to the demand; hence, better overall system performance. Storage tank designs with external heat exchangers typically operate with two pumps; one pumping the storage liquid through the tank and the other circulating the heat transfer liquid through the supply loop. Mantle-type heat exchanger is commonly used in Europe and Australia. It consists of a double-walled storage vessel in which the heat transfer fluid (HTF) is circulated through the jacket surrounding the storage tank. The focus of the current research is on the immersed coil heat exchangers integrated into fully mixed storage tanks.

Many researchers have investigated the performance of natural convection heat exchanger (NCHE) (Cruickshank and Harrison, 2009), shown in Figure 1.3. The side-arm

heat exchanger is installed outside the storage tank and it circulates the storage liquid by virtue of buoyancy driven natural convection flow; i.e. thermosiphon effect. This design of the heat exchanger was proved to be self-regulating and controlling since the buoyancy driven up-flow through the NCHE promotes the displacement of cold liquid at the top of the tank with hotter liquid. Systems utilizing this type of heat exchanger require only one pump to circulate the heat transfer fluid in the supply side and are thus referred to as passive systems. Under certain conditions, passive systems can experience reverse thermosyphoning where hot liquid at the top of the storage tank flows down through the heat exchanger losing heat to the supply loop. In solar thermal storage systems, this might occur during the times of low solar irradiation (early morning or late afternoon).

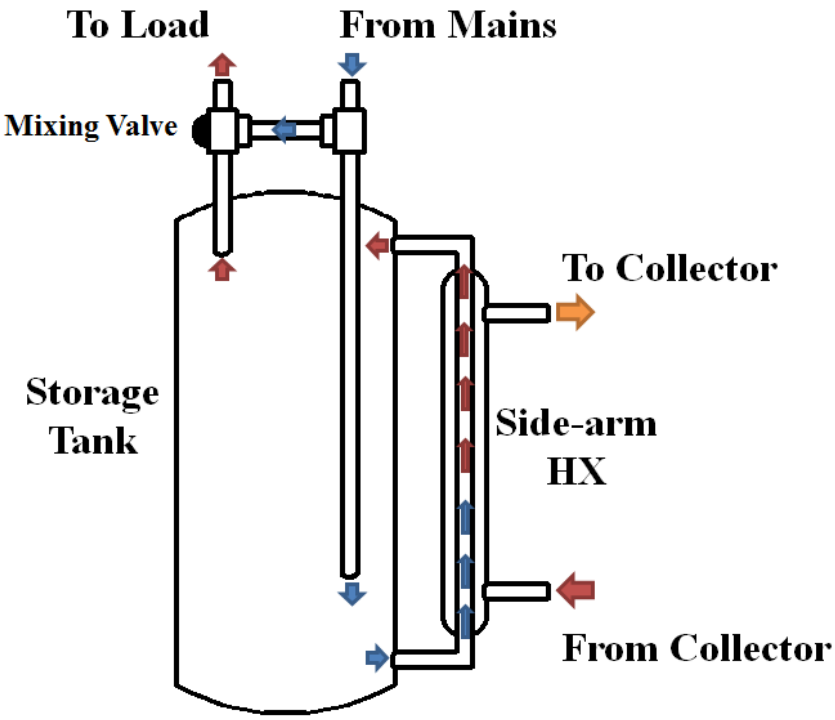

Figure 1.3. Typical design of thermal storage tank with side-arm natural convection heat exchanger (NCHE).

1.2. Thermal Energy Storage

Thermal energy can be stored in various forms: sensible heat, latent heat and reversible thermochemical reactions.

Sensible Heat Storage. Sensible heat storage (SHS) is associated with an increase (during charging) or decrease (during discharging) of the temperature of the thermal storage medium. The amount of energy stored is proportional to the mass; m, specific heat capacity; c, and the change in temperature of the storage medium from the initial temperature (T_i) to the final temperature (T_f), Equation (1.1).

$$E_{st} = m \int_{T_i}^{T_f} c \, dT \tag{1.1}$$

Storage systems with larger energy density (energy stored per unit volume) are characterized by more compact sizes and hence lower cost and thermal losses to the surroundings. As a result, in order to increase the energy storage density of the system, materials with large density and specific heat capacity are more favorable. The most commonly used materials as sensible storage mediums are rock beds and water since they are considerably inexpensive, abundant and have large heat capacities.

Latent Heat Storage. Latent heat storage (LHS) stores energy mainly in the form of latent heat of phase transformation of the storage medium such as: solid-solid, solid-liquid, solid-vapor and liquid-vapor. Solid-vapor and liquid-vapor are rarely used in thermal storage applications since the vapor phase occupies larger volumes and requires complicated designs for pressurized containment. In solid-solid phase transformation, the storage medium stores energy in the form of changing the crystalline structure between two solid phases. Solid-solid transitions are generally associated with small latent heats making them less desirable. A

more attractive technique is latent heat storage by solid-liquid phase transitions since it offers much higher energy storage density when the phase change materials (PCMs) operate around their phase transition temperature (melting temperature). Such materials are characterized by their high latent heat of fusion which allows the storage of large amounts of energy in smaller and lighter systems. For a given PCM with melting temperature; T_m, latent heat of fusion; H_f, and operating from an initial temperature (T_i) until a final temperature (T_f) the energy stored can be calculated by:

$$E_{st} = m[\int_{T_i}^{T_m} c_s \, dT + H_f + \int_{T_m}^{T_f} c_l \, dT] \tag{1.2}$$

where c_s and c_l are the specific heat capacities of the solid and liquid phases, respectively. Paraffin wax has c_s and c_l of approximately 2.1 kJ/kgK, H_f of 189 kJ/kg at T_m of 60°C; 1 kg of this material can store 0.231 MJ when it operates between 50 and 70°C. This is more than 2.8 times the amount of energy that can be stored in 1 kg of water as sensible heat under the same temperature difference.

Thermo-Chemical Storage. Thermo-chemical storage takes place by storing thermal energy through endothermic chemical reactions that can be reversed to recover the stored energy when needed. Generally, chemical reactions offer large energy storage densities due to the high energy levels associated with the formation and destruction of chemical bonds (NATO, 1979). However, these processes are often unstable and impractical when applied for low temperature applications. In addition, safe containment of chemical reactions usually requires costly and complicated measures.

1.2.1. Water-based Sensible Heat Storage

Owing to its large heat capacity, low cost and widespread availability, water is the most commonly used storage medium in SHS systems. Over the past four decades, researchers have investigated various techniques to improve the performance of water storage tanks in order to reduce the overall storage space as well as the cost of the system. A typical household with four individuals would require hot water storage tank of a volume 200 – 300 litres for daily domestic hot water (DHW) needs. Such small-sized storage tanks are readily available in the North American market at reasonable prices. However, medium and large-scale applications such as multi-family residential units, hotels, restaurants, etc. require water storage tanks with larger volumes 500 – 1500 litres. Unfortunately, suitable storage tanks of this size are only produced in limited quantities, resulting in significantly higher costs per unit of storage volume (Cruickshank and Harrison, 2006). Furthermore, bulky-sized tanks are not suitable for retrofit applications since they are difficult to handle through doorways. As such, they are often constructed on site and maintained at low pressure to avoid the risk of leakage.

1.2.2. PCM-based Latent Heat Storage

Since the mid-70s, solid-liquid PCMs (will be referred hereafter as PCMs) have captured the attention of many researchers as excellent candidates for thermal energy storage applications (Lane 1980, Abhat 1983). PCMs are commonly known for their relatively high latent heat of fusion during phase transformation, which allows for more compact designs of the TES system. This feature is of particular importance where building spaces are at premium, as in commercial buildings, offices, and/or where space and access are limited such

as during retrofitting in residential houses. Moreover, melting/solidification processes of the PCMs often take place at fixed temperature, referred to here as the melting temperature (T_m). This feature has several potential advantages to TES system performance: (1) imposes passive control on the temperature of the system, (2) reduces the maximum operating temperature of the system, which will lead to reduction of thermal losses, (3) enhances the collected energy efficiency in some applications such as in solar thermal storage since the system with PCMs can send liquid with lower temperature to the solar collector yielding larger collector efficiency.

This dissertation is focusing on the low temperature applications with $T_{op} < 100°C$ such as domestic hot water and space heating, solar cooling, greenhouse heating, etc. PCMs with melting temperatures within this range are grouped into the two categories of organic and inorganic compounds and their eutectics, as illustrated in Figure 1.4.

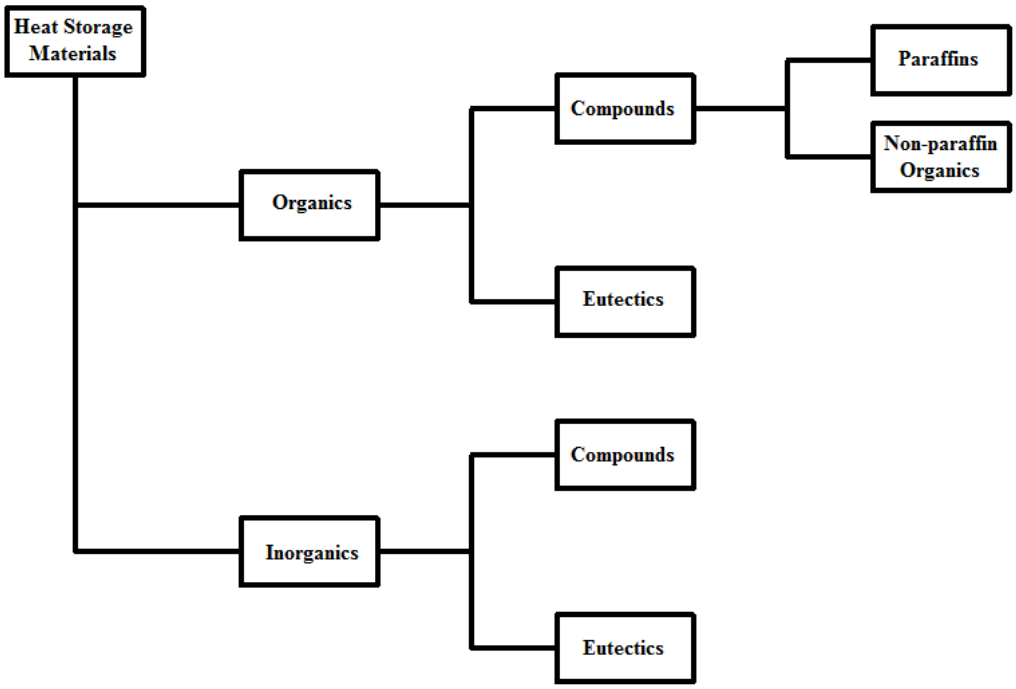

Figure 1.4. Classification of PCMs

Organic compounds are classified into paraffins, non-paraffins and their eutectics, whereas inorganic compounds include hydrated salts and their eutectics. Organic materials have many desirable properties compared to inorganic materials. Some of these advantages are: congruent melting/solidification, rare supercooling problems and compatibility with various containment materials (Abhat, 1983). However, the main disadvantages of these materials are their relatively high cost and low thermal conductivities. Inorganic materials are characterized by better thermal properties, e.g. one order of magnitude higher thermal conductivity than organics, lower cost and widespread availability in market. However, most of the inorganic compounds suffer from aqueous segregation during successive heating/cooling cycles, supercooling, as well as general tendency to chemically react with typical containment materials.

The use of PCMs in TES systems was intensively investigated in the literature targeting a broad span of aspects including measuring the thermophysical properties, kinetic stability under cycling conditions, compatibility with containment materials, heat transfer performance in different heat exchanger configurations and under various operating conditions. Several comprehensive review papers were found in literature that compile the research done on PCM-based TES systems (Hasnain 1997, Zalba *et al.* 2003, Farid *et al.* 2004, Sharma *et al.* 2009, Nkwetta and Haghighat 2013) as well as the potential enhancement techniques for their performance (Jegadheeswaran and Pohekar 2009, Agyenim *et al.* 2010).

1.3. Multi-tank Thermal Energy Storage

Multi-tank TES systems have been studied by researchers as a promising alternative for bulky storage tanks for medium and large-scale applications such as: restaurants, motels,

multi-family residences, etc. (Bejan 1982, Taylor and Krane 1991, Arata and de Winter 1991, Sekulic and Krane 1992a,b, Mather *et al.* 2002, Cruickshank and Harrison 2011). These systems offer many advantages: (1) they are modular in design and can be mass-produced at reasonable prices, (2) they are much easier to handle through doorways for retrofitting, (3) they can be interconnected in different configurations; series or parallel, and (4) some designs can be stacked vertically to reduce the storage space.

1.3.1. Multi-tank Sensible Heat Storage using Water

Bejan (1982) illustrated that serially connected sensible storage tanks promoted "sequential stratification", which led to considerable reduction of entropy generation and improved the overall performance of the system. That is, each tank was found to maintain a temperature level higher than that of the following tank, which helped to maximize the energy extraction from the supply loop as well as the energy grade delivered to the demand side. In addition, Dickenson *et al.* (2013) and Cruickshank and Harrison (2009) demonstrated that both series and parallel configurations of three-tank water storage could achieve high levels of thermal stratification depending on the supply and demand profiles. Figure 1.5 illustrates the multi-tank water storage system using series configuration for charging and discharging proposed by Cruickshank and Harrison (2011).

Mather (2000) also studied the performance of eight 200-litre water tanks connected in series via immersed coil heat exchangers installed at the bottom of the tanks for charging and another installed at the top of the tanks for discharging when integrated with a solar DHW system. The solar fraction, which is the fraction of the thermal energy delivered to the load from the solar collector, of the multi-tank system was found to be comparable with that obtained from a perfectly stratified 1600-litre single tank.

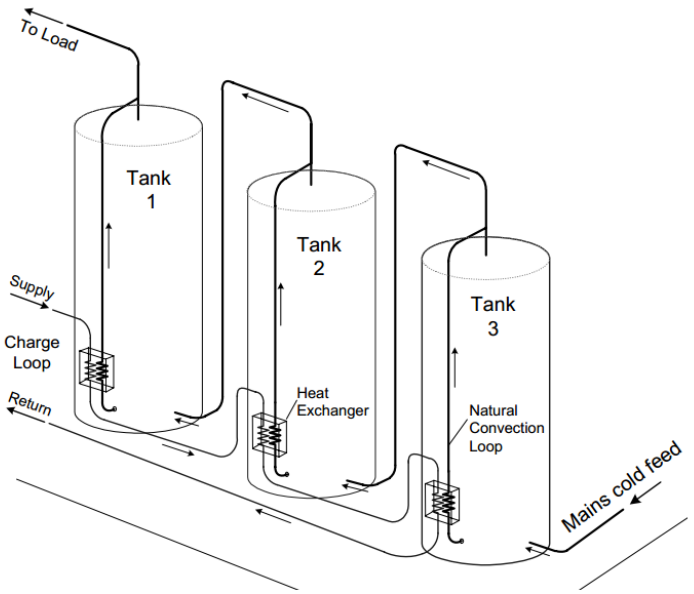

Figure 1.5. Multi-tank water storage system: series configuration for charging and discharging proposed by Cruickshank and Harrison (2011).

1.3.2. Cascaded Latent Heat Storage using PCMs

PCMs have recently found their place as thermal energy storage materials in vast range of applications from Coffee Joulies™ (Patent US D665280 S1, 2012) in hot-drink mugs to astronaut suits (Trevino and Orndoff, 2000).

Although PCMs are commonly known for their high energy storage density and temperature modulation abilities, their major drawback is their low thermal conductivity. This introduces some challenges to the use of PCMs in TES systems since they will increase the thermal resistance and hence decrease the overall efficiency of the system. This motivated a large stream of research studies on the enhancement of the performance of PCMs in TES systems (Agyenim *et al.*, 2010). A group of studies investigated different techniques to increase the effective thermal conductivity of the PCMs by introducing metal matrices (Hoogendoorn and Bart 1992, Trelles and Dufly 2003) or high conductivity metal particles

(Mettawee and Assassa, 2007). Another group explored different designs of heat exchangers integrated with PCMs in order to reduce the thermal resistance of the PCM using micro-encapsulation (Hawlader *et al.* 2003, Griffiths and Eames 2007), finned heat exchangers (Chow *et al.* 1996, Velraj *et al.* 1997) or heat pipes (Shabgard *et al.* 2010).

The weak performance of the PCM can be offsetted by increasing the temperature difference between the PCM and the heat transfer fluid during the charging and discharging processes. This inspired the concept of using cascaded or multi-stage PCMs with different thermophysical properties in TES systems (Farid and Kanzawa, 1989). Faster charging and discharging rates were observed in storage systems where the melting temperatures of the cascaded PCMs decreased (increased) in the direction of flow of the charging (discharging) heat transfer fluid. However, only a handful of studies were found in the literature about the implementation of the cascaded-PCM storage in different applications; high temperature applications such as solar power concentrators (Michels and Pitz-Paal 2007, Seeniraj and Narasimhan 2008, Shabgard *et al.* 2012), waste heat recovery from diesel engines (Chinnapandiana *et al.*, 2011) and low temperature applications (Watanabe *et al.* 1993, Gong and Mujumder 1996, Tian and Zhao 2013).

1.4. Motivation and Research Proposal

The current study was inspired by the work of Mather (2000) on modular multi-tank SHS system for medium to large-scale solar domestic hot water application (total storage volume of 1600 litres). Figure 1.6 illustrates a schematic of the multi-tank storage system. The design proposed by the authors was meant to solve the problems posed by installing large storage tanks for domestic water heating application. The volume of each individual tank was 200 litres where immersed coil heat exchangers inside each tank for charging and

discharging were installed. These heat exchangers resulted in well mixed fluid inside each tank during the charging and discharging periods by promoting natural convection currents. However, sequential or tank-to-tank stratification was maintained between the tanks.

The system designed in this study also benefitted from the thermal-diode effect; shown in Figure 1.7. This effect was shown to direct the heat transfer to the appropriate tank where the bulk temperature is less than the charging flow temperature ($T_b < T_c$). This occurs because heat transfer from the coils is a result of natural convection flow currents which are damped when $T_b > T_c$. This phenomenon was proved to offer many advantages: (1) Tank-to-tank stratification is enhanced which reduces the carryover losses between successive tanks especially at the times when the supply is sending cold fluid to the storage component, (2) The energy is stored in the tank with right temperature level, (3) The effectiveness of heat exchange with the storage component is improved which leads to higher overall system efficiency since colder liquid returns to the supply and hotter liquid is delivered to the load (Mather *et al.*, 2002).

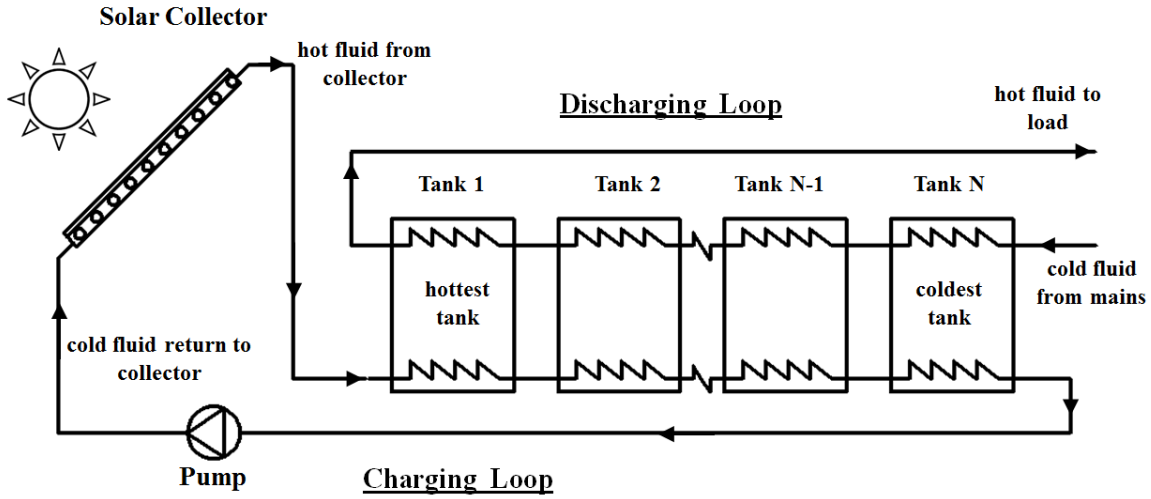

Figure 1.6. Schematic layout of the multi-tank SHS integrated in a solar hot water system. (Adapted from Mather *et al.*, 2002).

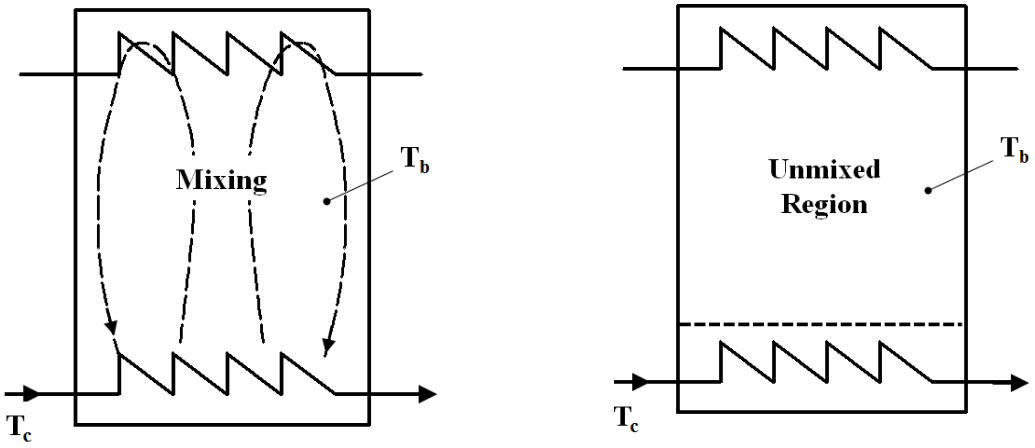

Figure 1.7. Illustration of thermal diode effect in a single SHS tank. Left: When $T_b < T_c$, the tank is fully mixed due to the natural convection currents. Right: When $T_b > T_c$, thermal diode effect acts to stratify the tank (Adapted from Mather, 2000).

A novel design of a multi-tank hybrid TES (HTES) system, consisting of a series of modular tanks filled with water and PCM modules, was proposed as shown in Figure 1.8.

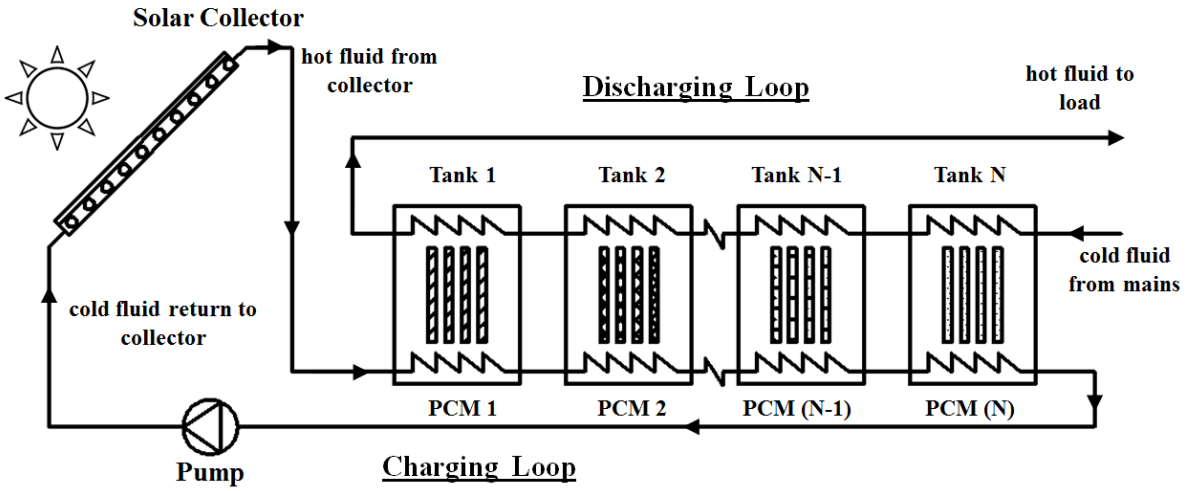

Figure 1.8. Proposed solar thermal hybrid TES system comprising N serially-connected tanks filled with water and PCM modules with different melting temperatures.

This design is expected to benefit from the advantages of the modular multi-tank design in addition to the promising energy storage capabilities of the PCM. Furthermore,

using PCMs with different melting temperatures in the series of tanks is expected to enhance the sequential stratification especially when the bulk temperature of each tank is controlled around the melting temperature of its corresponding PCM. This will lead to lower return temperature to the solar collector and higher delivered temperature to the load, hence higher overall system efficiency. However, the operation of thermal storage systems, the HTES in particular, is transient, highly non-linear and sensitive to various design and operation conditions. Selection of the PCMs with appropriate melting temperatures, thermo-physical properties, design configuration, and dimensions of the PCM modules inside the tanks are expected to have critical effects on both the dynamic and steady-state performance of the storage system.

As such, this dissertation addresses the design, operation and evaluation of a single-tank HTES with PCM modules suitable for solar thermal domestic hot water applications. In addition, the concept of multi-tank HTES system is explored for large-scale DHW demands and the potential benefits of the PCM in enhancing the performance of the system are highlighted.

1.5. Objectives of the Research Project

The objectives of this research project are:

1. Introduce a novel design of a fully-mixed single-tank HTES with rectangular PCM modules.
2. Develop a simplistic mathematical model that simulates the performance as well as the different thermal behaviors of the single-tank HTES accurately under a variety of operation conditions.

3. Use different analytical solutions and benchmark problems to verify the individual components of the mathematical model.
4. Design, instrument, build and calibrate a full-scale experimental facility for the single-tank HTES to validate the results of the mathematical model.
5. Perform a parametric analysis on the performance of the single-tank HTES system under idealized operation conditions to investigate the effect of key design and selection parameters of the PCM modules.
6. Extend the validated model to simulate the performance of the multi-tank HTES and compare the results to those of the multi-tank SHS provided in the literature (Mather 2000).
7. Conduct numerical simulations on single- and multi-tank HTES operating in solar thermal DHW systems. Realistic weather data (solar irradiation and ambient temperature) and DHW draw patterns should be used to provide understanding of the true benefits of the HTES over the conventional SHS.
8. Investigate the influence of changing the operation conditions such as different seasons and different DHW consumption patterns, on the performance of the HTES system compared to the SHS system.

1.6. Contribution of Research

The main contributions of this research are summarized as follows:

1. Introducing a novel design of thermal energy storage system suitable for solar thermal DHW applications.

2. Designing, building and instrumenting a full-scale testing apparatus in the TMRL Laboratory at McMaster University for single-tank SHS and HTES with PCM modules. This experimental facility can be used for various prospective future investigations.
3. Developing, verifying and validating a computationally inexpensive modeling tool, capable of accurately simulating the performance of the proposed design of single- and multi-tank storage systems.
4. Determining the key design and operation parameters that influence the performance of the proposed HTES system.
5. Identifying the key properties limitations during the selection of PCM that are suitable for certain operation conditions. This motivates research and advancement in the Material Science area to synthesize PCMs with resilient properties that can span wide range of operation conditions efficiently.
6. Illustrating the effect of different operation conditions such as the weather data and the demand profiles on the performance of the HTES system compared to the SHS system.
7. Highlighting the potential benefits of the multi-tank HTES with tuned PCM melting temperatures in medium to large-scale solar thermal DHW applications.
8. Introducing a research proposal to undertake an extensive optimization study on the properties tuning of the PCMs in individual tanks of the multi-tank HTES system.

1.7. Organization of Research and Thesis Document

The research work presented in this dissertation consists primarily of three parts:

A. Developing a mathematical model to simulate the performance of the proposed design of single and multi-tank HTES system. The main focus was on the solar

thermal DHW application since it contributes potentially to the offsetting of the electricity/fossil fuel consumption in one of the largest sectors in the energy market. Also, another model was developed to evaluate the performance of a SHS system with the same design and operation parameters for comparison.

B. Validating the mathematical model using experimental tests on both systems; the SHS and the HTES. A full-scale single-tank thermal storage experimental apparatus was designed, constructed, calibrated and commissioned. The experimental results were used to validate the mathematical models.

C. Performing numerical simulations on the storage elements when integrated in a solar thermal DHW system to illustrate the potential benefits of the HTES over the conventional SHS. Small-scale systems suitable for single-family residence were investigated. Also, the concept of the multi-tank storage for medium/large scale systems was studied.

The written dissertation is arranged into the following chapters:

Chapter One presents a general overview about the solar thermal systems and various thermal energy storage concepts. It also highlights the motivation behind this research work.

Chapter Two provides a comprehensive literature review of the previous research work conducted in the field of thermal energy storage using sensible and latent storage mediums. Special consideration was given to various thermal storage designs in solar thermal DHW application.

Chapter Three presents the mathematical model developed to simulate the performance of the single and multi-tank SHS and HTES systems.

Chapter Four describes the full-scale thermal storage experimental apparatus designed and constructed for testing. The experimental test matrix and testing procedures were outlined.

Chapter Five demonstrates the verification and validation procedures for the mathematical models. Verification/validation was discussed on both the component level and the system level.

Chapter Six discusses the results of the numerical simulations conducted on the single and multi-tank SHS and HTES systems. The potential benefits of the proposed HTES system were discussed.

Chapter Seven presents the conclusions drawn from the research work and provides recommendations for future areas of study.

CHAPTER TWO

LITERATURE REVIEW

2.1. Introduction

As illustrated in the previous chapter, thermal stratification phenomenon is crucial to the performance of thermal storage systems; especially liquid-based thermal storage. By virtue of the buoyancy effects, the hot liquid layers tend to reside at the top of the tank while the cold layers sink towards the bottom. The level of thermal stratification inside a storage tank is measured qualitatively by the extent to which the hot liquid layers are separated from the cold layers. As such, all mechanisms that act to induce or promote mixing inside the storage tank are often referred to as destratification mechanisms. Thermal stratification is desirable in thermal storage systems since it ensures delivering hotter fluids to the demand side and colder fluids to the supply side. The former yields reduced needs for auxiliary heating and the latter leads to increased effectiveness of the heat exchange process on the supply side. As such, thermal storage designs with high levels of thermal stratification lead to significant improvement of the overall efficiency of the system. Many studies have been focusing on various designs of thermal storage tanks that promote thermal stratification especially in solar thermal storage applications.

During the early 1980s, the concept of using multi-tank or cascaded storage systems was first introduced in the literature to replace bulky systems conventionally used in medium to large-scale applications (Bejan, 1982). Multi-tank storage has been the subject of many

research studies exploring different designs and configurations in order to enhance the effective stratification and hence, the overall performance of the system.

2.2. Single-tank Thermal Energy Storage

A comprehensive review on thermal stratification and its benefits in single-tank storage systems was presented by Han *et al.* (2008). Some studies investigated the effect of different key design and operation parameters on thermal stratification in water storage tanks (Lavan and Thompson 1977, Sharp and Loehrke 1979, Buckles and Klein 1980, Hollands and Lightstone 1989, Zurigat *et al.* 1990, Cataford and Harrison 1990, Ghajar and Zurigat 1991, Kleinbach *et al.* 1993, Andersen and Furbo 1999). Some of these factors included the level of thermal insulation, the methods of charging and discharging; ie. direct or indirect, the inlet and outlet configurations as well as the supply and demand profiles.

The integration of innovative techniques that improves the level of thermal stratification inside the storage tanks such as using baffles (Shah and Furbo, 2003, Altuntop *et al.* 2005), diffusers (Ghaddar 1994, Chung *et al.* 2008) and floating inlets (van Koppen and Thomas, 1978) has also been studied. Others explored the effect of adding PCMs at certain locations inside the storage tank to enhance thermal stratification and prolong the availability of hot water for the load (Mehling *et al.* 2002, Cabeza *et al.* 2006, Ibáñez *et al.* 2006, Talmatsky and Kribus 2008, Kousksou *et al.* 2011). The results of these studies are discussed in detail below.

2.2.1. Water-based Single-tank Storage

Hollands and Lightstone (1989) demonstrated that 37% increase in the delivered energy in forced-flow solar systems can be achieved using a “micro-flow” stratified tank

compared to a fully mixed storage tank of the same volume. The increase in the efficiency of the system was attributed mainly to: (1) the fact that low flow rate of direct charging led to minimal amount of mixing and hence maintained water at higher temperature at the top of the tank to be delivered to the load, and (2) thermal stratification allowed cold liquid to return to the solar collector which increases its efficiency due mainly to significant reduction in thermal losses to the surrounding (Duffie and Beckman, 2013). Similar results were found by Ghaddar (1994) in both forced-flow and thermosiphon modes of a solar thermal storage system. However, low flow rate did not show significant effect on thermal stratification during summer when the collector plate temperature is the highest. This resulted in larger thermal losses from the collector.

There are four main mechanisms for destratification in storage tanks: (1) inlet jet mixing, (2) vertical heat conduction, (3) heat losses through the walls of the tank, and (4) plume entrainment. Inlet jet mixing takes place when the inlet jet has sufficient momentum to mix the contents of the storage tank. Vertical heat conduction in the storage fluid and through the tank walls induces mixing and causes destratification. As such, it is recommended to use tanks with thin and low thermal conductivity walls in order to suppress the natural convection currents developed at the walls which act to mix the fluid inside the tank (Hess and Miller, 1982). In addition, non-uniform thermal losses through the tank walls, due to non-uniform insulation or surface area, induce natural convection currents inside that storage tank and cause destratification. Plume entrainment was found to be a key mechanism for destratification (Hollands and Lightstone, 1989). Plume entrainment occurs when fluid enters the storage tank at a temperature that induces inverse temperature gradients inside the tank.

Many researchers investigated different destratification mechanisms and explored novel techniques to minimize their effect on thermal storage systems.

Lavan and Thompson (1977) developed an experimental correlation that showed that the level of stratification inside a water tank during direct discharging increased as the Reynolds number (based on the inlet pipe diameter) decreased, the aspect ratio of the tank increased and the Grashof number (based on the tank diameter and the temperature difference between the initial temperature of the tank and the inlet temperature) increased. In addition, 7% degradation of stratification was noticed when the steel tank was used instead of plexiglass tank. This was attributed to heat conduction through the walls since steel has two orders of magnitude higher thermal conductivity than plexiglass.

Shah and Furbo (2003) used CFD simulation to investigate the effect of different inlet designs on the energy quality during the discharging process. They concluded that a simple inlet pipe design is more destructive to the energy quality compared to baffle plate designs. The flat plate baffle inlet provided the highest degree of stratification as shown Figure 2.1.

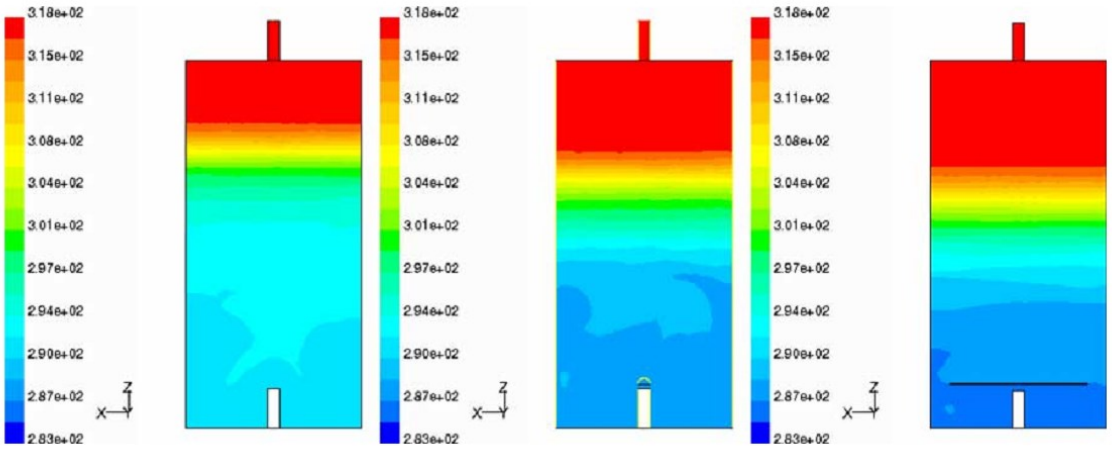

Figure 2.1. CFD simulation results showing the temperature distribution in the tank centre plane after 5 min of 10 lpm inlet flow followed by 30 s with no flow. Left: Pipe inlet. Centre: Hemispherical baffle. Right: Flat baffle. (Shah and Furbo 2003).

Altuntop *et al.* (2005) studied the effect of using 12 different designs of obstacles inside a solar thermal storage tank on the degree of stratification. Using ANSYS Fluent 6.1.22 CFD simulations, it was shown that placing obstacles inside the storage tank resulted in better stratification than the case with no obstacle. Also, obstacles with a gap in the center promoted higher degrees of stratification than other designs.

In order to reduce the effect of inlet jet mixing, diffusers can be used at the inlet of the storage tank to reduce the inlet velocity of the jet. Ghaddar (1994) compared the experimental results from solar thermal charging of a water tank using conventional straight pipe inlet to a multi-hole ring diffuser with perforated plate. The ring diffuser design was meant to produce slow uniform flow from the top of the tank. For thermosiphon operation mode, the ring diffuser inlet was found to improve the thermal stratification in the tank and increased the overall system efficiency by 10% over the straight pipe design and by about 25% over the well-mixed tank. For forced circulation operation mode, the overall system efficiency increased by 20% over the straight pipe design and by about 35% over the well-mixed tank. Chung *et al.* (2008) demonstrated that the design of the inlet and outlet diffusers has significant effect of the thermocline thickness development with discharging time.

van Koppen and Thomas (1978) introduced the novel idea of floating inlet from the solar collector to the storage tank as a means of improving the thermal stratification inside the tank, as illustrated in Figure 2.2. A flexible hose was used to move vertically by virtue of buoyancy forces to direct the flow to the position inside the tank with the same temperature level.

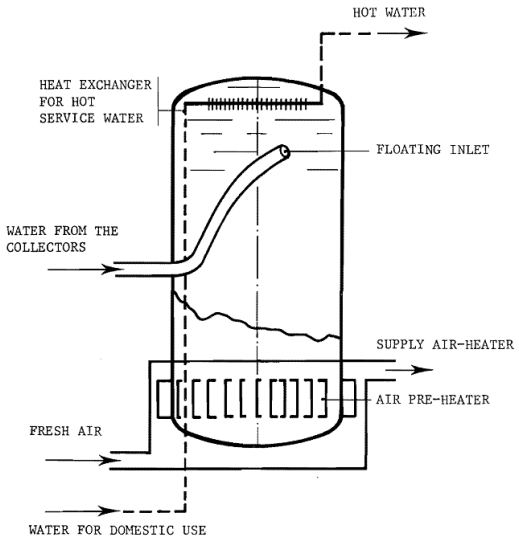

Figure 2.2. Water storage tank with a floating inlet proposed by van Koppen and Thomas (1978).

The performance of thermal storage systems is sensitive to the magnitude and distribution of the daily hot water draw profiles. Buckles and Klein (1980) showed that for recurring draw patterns in a solar thermal system, the early morning draws yielded the lowest solar fractions while the mid-afternoon draws resulted in the highest solar fractions. In addition, the effect of day-to-day variations of the draw profiles; namely non-recurring draw patterns, was shown to reduce the solar fraction significantly compared to the recurring draw patterns. A theoretical study was carried out by Knudsen (2002) who investigated the effect of using different domestic hot water profiles with different imposed mixing rates in solar storage tank. The study demonstrated that a mixing rate of 40% at the bottom of the storage tank reduced the net annual utilized solar energy by 10-16%. Also, a perfectly stratified storage tank, operating under realistic draw profiles proposed by Jordan and Vajen (2001) showed lower performance than that operating under theoretical early morning or late after-noon draw profiles.

Furbo *et al.* (2005) performed theoretical and experimental investigation on the benefits of applying active control on the operation of the auxiliary heating element in the solar storage system in order to reduce the unnecessary use of electric energy. Although the study had shown the potential of increasing the thermal performance of the system by 5-35%, a priori knowledge of the consumption draw profile is necessary.

Using different daily DHW draw-off profiles on a water tank initially fully mixed at 80°C, Spur *et al.* (2006) illustrated that the performance of the storage tank is greatly influenced by the number of draw-offs per day, the times at which long draw-offs take place during the day and the flow rates of such long draw-offs. Several short draw-offs were found to provide more energy to the load than single long draw-off.

2.2.2. Hybrid Single-Tank Storage

Many researchers had focused their studies on PCM modules integrated in water-tank storage systems, referred to here as Hybrid Thermal Energy Storage (HTES) systems. Such systems are deemed to harness the advantages of both systems; the water as a SHS medium is abundant, cheap and has large sensible heat capacity, whereas the PCM as a LHS medium has large latent heat capacity and steady operation temperature during phase transformation. The concept of adding PCM modules in the water tanks introduces many critical parameters to the design and operation of the storage system. These parameters include: the volume fraction of the PCM (or the packing ratio), the properties of the PCM; especially the melting temperature, the configuration of the modules (ex. Rectangular, cylindrical, spherical, etc.), and the placement of the modules inside the storage tank. All these parameters have been the subject of many studies since they play important roles in the performance of the thermal storage system.

Mehling *et al.* (2002) presented the effect of placing PCM at the top section of a thermally stratified tank. This concept proved to provide significantly higher gains in storage capacity in addition to substantial delays in the cool down time of the top layer of the tank. It was shown that two times reduction of the cool down time of the discharged water can be achieved given careful optimization of the PCM design parameters such as the melting temperature range and the latent heat of fusion. Experiments done by Al-Hinti *et al.* (2010) illustrated that the existence of PCM in water tanks helped maintain the temperature inside the tank around the melting temperature of the PCM. Cabeza *et al.* (2006) explored the effect of changing the volume fraction of the PCM employed at the top of the water tank on the performance during different discharging processes. The experimental results demonstrated that the PCM helped maintain the top layers of the tank at high temperature, around the melting temperature of the PCM, for longer times. Increasing the number of PCM modules yielded larger amounts of water available at high temperature for the load. In addition, including more PCM modules in the storage tank allowed for faster temperature recovery after complete discharge of the tank thanks to the large latent heat capacity of the PCM.

de Gracia *et al.* (2011) numerically investigated the influence of the PCM cylindrical module design on the performance of a HTES system during different draw-off scenarios. The effect of the duration of the draw-off and the time spacing between each draw-off had been studied. It was shown that the systems with PCM had higher hot water discharge capacity, and their demand coverage increased from 40% to 55% depending of the design of the PCM modules. The systems with large number of small tubes could provide hot water for longer time during the first draw-off but limited time in the other draw-offs. In these systems part of the heat stored by the PCM was released to the water during this first discharge

because of the high area of heat transfer between the PCM tubes and the water. On the other hand, systems with fewer tubes of larger diameter stored the heat in the PCM for posterior demands.

Nallusamy *et al.* (2007) investigated experimentally the thermal behavior of a packed bed TES system that consisted of spherical PCM capsules (paraffin with melting temperature; T_m = 60 °C) surrounded by SHS medium (water). The SHS medium also acted as the HTF in this system. Their results showed that employing PCM in the TES system leads to better control of the HTF flow temperature owing to the constant melting temperature of the PCM which in turn yielded favorable heat transfer rates during the change in phase. However, the first layer of the spherical capsules receiving the HTF flow showed faster melting rate than the last layer further downstream. This led to more energy stored in the liquid PCM in the form of sensible energy which is at least one order of magnitude less than the latent heat of fusion of the same PCM at the same temperature operation range of the experiments. Reddy *et al.* (2012) reported the effect of the charging mass flow rates on the charging rates of a HTES system with different PCMs encapsulated in spherical containers. A 3-fold increase of the mass flow rate was found to decrease the melting time by around 23%. This was attributed to the effect of the charging mass flow rate on the heat transfer coefficient between the heat transfer fluid (HTF) and the PCM. In addition, the results showed that the spherical PCM containers with the smaller diameter demonstrated higher melting rates owing to the reduction of the thermal resistance of the PCM in addition to the increase of the surface area-to-volume ratio.

Al-Hinti *et al.* (2010) carried out a one-day experiment on a HTES tank charged by a solar collector for 5.5 hours followed by a complete discharge of the tank. The PCM was

found to first, reduce the temperature drop of the storage tank significantly and second, assist in the quick temperature recovery of the system to be ready for later discharges. TRNSYS simulations were conducted by Morrison and Abdel-khalik (1978) to study the performance of solar space-heating system using air-based and water based storage with and without PCM. The effect of heat exchange number of transfer units (NTU), the storage medium volume (or mass), the solar collector area and the type of PCM used were investigated. The solar fraction, defined as the fraction of energy supplied by the solar collector to the load, was found to increase with the increase of the storage mass or volume per unit area of the solar collector until it plateaued. As such, volume can be reduced by 75% (using $Na_2SO_4.10H_2O$) and 50% (using Paraffin wax) of the volume needed by the rock-bed in air-based system, illustrated in Figure 2.3a. The former has lower melting temperature and higher latent heat of fusion, as such; it is believed that it led to lowering the inlet temperature to the collector and hence increasing the collector efficiency. In liquid-based system, the water tank slightly outperformed the system with paraffin wax. Figure 2.3b shows that the system with the hydrated salt PCM could provide the same solar fraction as the water tank in half the volume.

Similar results were found by Ibanez *et al.* (2006) who modified a simulation module in TRNSYS to simulate the performance of HTES system with cylindrical PCM modules. After experimentally validating their numerical results, simulations were performed to investigate the effect of PCM volume fraction and melting temperature on the solar fraction of the solar DHW system for a family house in Lleida, Spain, shown in Figure 2.4. As the volume fraction of the PCM increased the solar fraction increased until it plateaued. Also, 9-18% increase in the solar fraction was obtained from HTES with PCM melting temperature

of 45 and 55 °C, respectively compared to SHS system with water only. The solar collector efficiency, however, was found to be insensitive to the volume fraction and the melting temperature of the PCM.

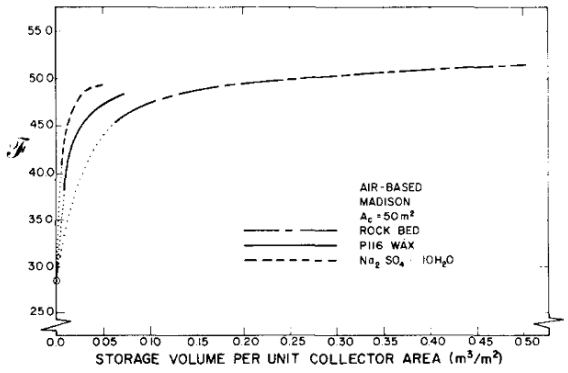

Figure 2.3a. Comparison between the solar fraction ($\mathscr{F}$) of air-based systems with sensible and latent heat storage. (Morrison and Abdel-khalik, 1978).

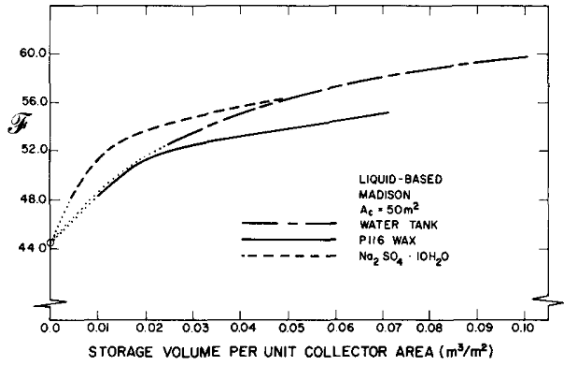

Figure 2.3b. Comparison between the solar fraction ($\mathscr{F}$) of liquid-based systems with sensible and latent heat storage. (Morrison and Abdel-khalik, 1978).

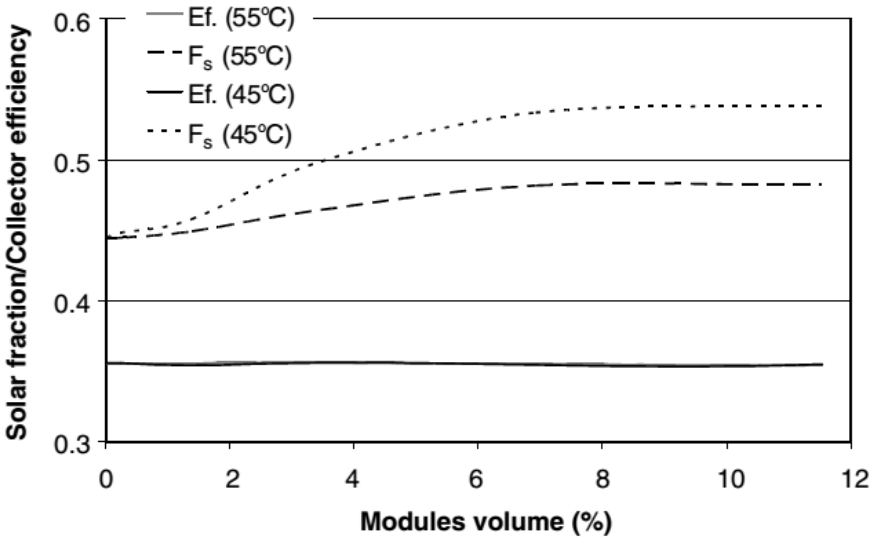

Figure 2.4. The effect of PCM melting temperature and volume percentage of the HTES tank on the solar fraction and the efficiency of solar collector. (Ibanez *et al.*, 2006).

Talmatsky and Kribus (2008) investigated numerically the performance of a single tank solar water heating system with and without PCM over the course of a year. Their study showed that although including PCM in the tank decreases the required storage volume, it does not increase the solar fraction to the end-user or the collector efficiency compared to the system without PCM. This was attributed to the fact that the storage gain during daytime was offset by the greater heat losses during nighttime due to the higher tank temperatures maintained by the PCM. Kousksou *et al.* (2011) reproduced the results obtained by Talmatsky and Kribus (2008) and then studied the sensitivity of the system behavior to the melting temperature of the PCM. They pointed out that in one of the systems studied by Talmatsky and Kribus, the PCM melting temperature was too high, and therefore both water and PCM were storing sensible heat for almost all the time. By reducing the PCM melting temperature and keeping every other property of the system unchanged, they were able to reduce the annual auxiliary electrical energy requirements of the system (by using PCM in the tank) from 7% to 14%. This improvement emphasized the high sensitivity of the storage system performance to the PCM melting temperature.

Bony and Citherlet (2007) integrated a numerical model to an existing TRNSYS module for stratified storage tanks to study the effect of using PCM with different configurations (rectangular plates, cylindrical and spherical modules) on the performance of the thermal storage system for DHW applications. They compared their numerical results to experimental measurements conducted on a square water tank in which PCM modules were submerged. Overall agreement was claimed by the authors through the comparison of the temperature profiles at different locations inside the PCM module. The heat transfer coefficient between the PCM surface and the sensible storage medium (water) was assumed

based on natural convection correlations over different geometric configurations (Bergman *et al.* 2011, Cengel *et al.* 1998). Extending the numerical model to simulate annual performance of their storage system under typical solar profiles and DHW draw patterns (Bony and Citherlet, 2007-a), the system with PCM showed higher frequency of the operation of the backup burner compared to the system without PCM. This was attributed to the inherent high thermal resistance of the PCM due to its low thermal conductivity as well as the geometry of the module.

An experimentally validated numerical model was developed by Haillot *et al.* (2013) using FORTRAN 90 to simulate the transient performance of a novel HTES design as a replacement for the use of PCM in the storage tank or the collector. Figure 2.5 demonstrates a schematic layout of the proposed design of the storage system.

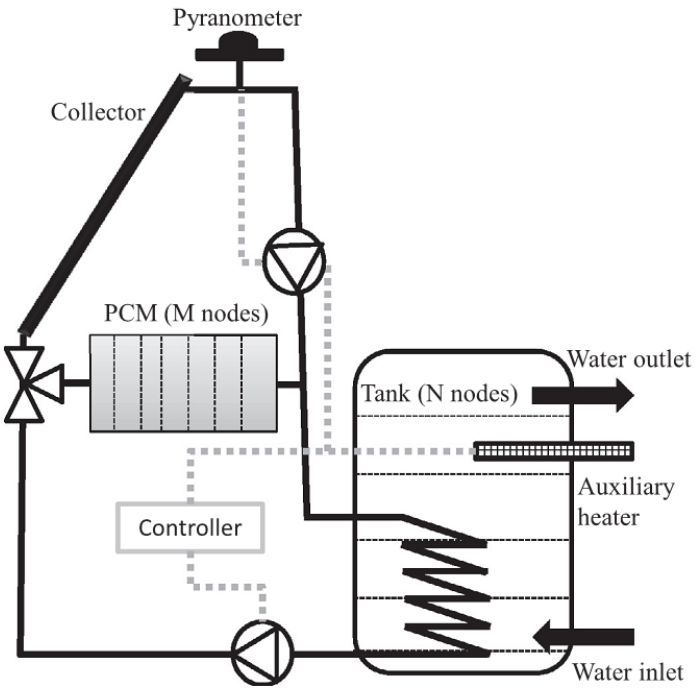

Figure 2.5. Layout of the solar DHW-PCM system proposed by Haillot *et al.* (2013).

A parametric study was conducted to investigate the effect of different parameters on the solar fraction of the system during a summer and a winter month used for DHW application. The parameters were: the storage tank volume, the PCM volume and the melting temperature. The results were found to agree with other research work found in literature, shown in Figure 2.6-2.7.

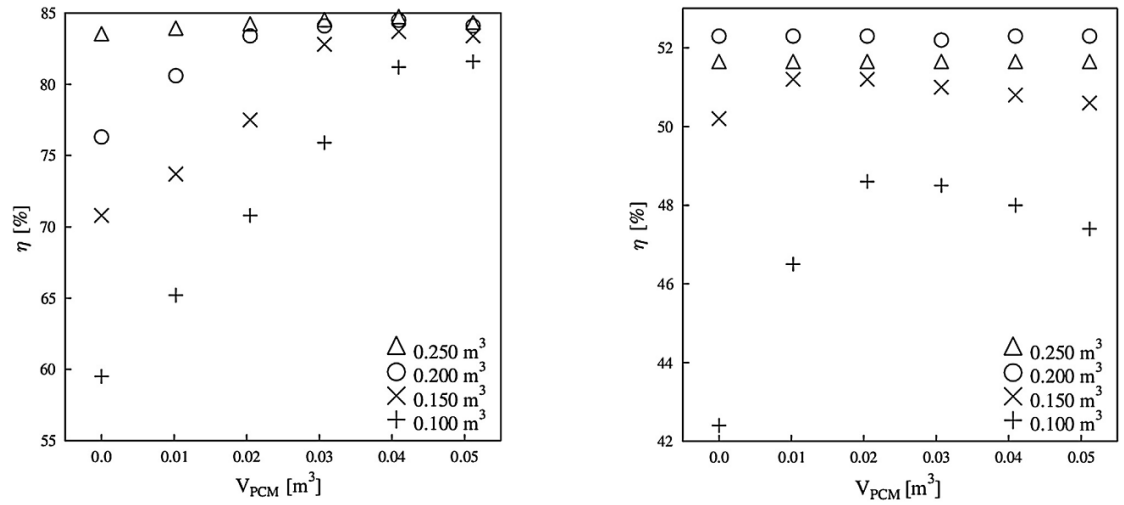

Figure 2.6. The effect of the tank volume [m^3] and the PCM volume [m^3] on the solar fraction, η [%]. Left: Summer month. Right: Winter month. (Haillot *et al.*, 2013).

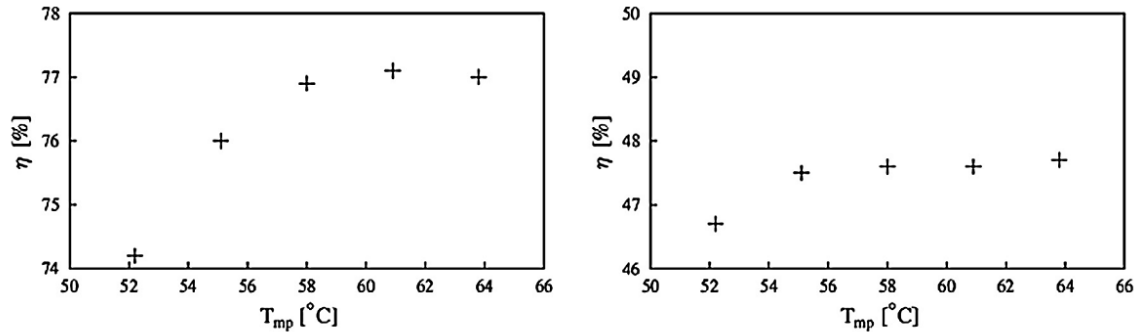

Figure 2.7. The effect of the the PCM melting temperature [°C] on the solar fraction, η [%]. Left: Summer month. Right: Winter month. (Haillot *et al.*, 2013).

An optimization study was then conducted using genetic algorithm to maximize the solar fraction; i.e. minimize the electric power consumption by the auxiliary heater. The optimization showed that summer season would have a different optimum from the winter season. For that reason, the authors recommended that the annual performance of the system should be considered.

2.3. Multi-tank Thermal Energy Storage

The concept of multi-tank sensible storage system was first introduced by Bejan (1982) in an effort to minimize the entropy generation during the charging and discharging processes. Having the storage system divided into a series of tanks reduces the temperature difference associated with the heat transfer between the storage tank and the charging/discharging heat exchangers. This leads to a reduction of the exergy destruction; i.e. preserving the quality of energy in the storage tanks. Taylor and Krane (1991) conducted an analytical study and agreed that it was possible to maintain the thermodynamic quality of energy in distributed storage element with reasonable sizes.

Farid and Kanzawa (1989) were the first to develop a mathematical model to simulate the performance of air-based storage system with cascaded PCMs having different melting temperatures. Arranging PCMs with decreasing (increasing) melting temperatures in the air flow direction during charging (discharging) showed higher heat transfer rates than in the system with single PCM melting temperature. This was attributed to the PCM effect on increasing the potential temperature difference between the charging or discharging streams with the PCMs, yielding higher charging and discharging rates. These numerical results were validated later using experimental work carried out by Farid *et al.* (1990).

These studies motivated many researchers to explore the benefits of multi-tank or cascaded storage systems in various applications. Some studies focused on the SHS systems, while others followed the track of latent-heat cascaded systems.

2.3.1. Water-based Multi-tank Storage

Arata and de Winter (1991) provided a comparison between the performance of a single mixed tank and a multi-tank storage with two and three tanks in solar water heating system. The study was carried out under fully-mixed tank conditions, no heat losses, constant demand and solar input profiles. It was concluded that the multi-tank system outperformed the single fully-mixed tank due to tank-to-tank stratification.

Mather *et al.* (2002) studied the application of a serially connected 8-tank SHS system to store solar thermal energy for domestic hot water supply. The charging and discharging immersed coil heat exchangers inside each tank were designed to maintain well mixed fluid inside each tank during the charging and discharging periods by promoting driving natural convection currents. However, effective stratification was maintained between the tanks. The system designed in this study also benefitted from the thermal-diode effect; i.e. the charging flow only stores energy in tanks with bulk temperature below the charging flow temperature. This phenomenon proved to enhance the performance of the storage system and the solar collector as well. In his MSc. Thesis, Mather (2000) performed a numerical comparative study between eleven different designs of SHS installed in a solar DHW system. The numerical results showed that the solar fraction of the eight 200-L tank system was comparable to that of a perfectly stratified 1600-L tank system. This highlights the ability of the multi-tank system to attain high levels of tank-to-tank stratification. Similar results were found by Cruickshank and Harrison (2004).

Ragoonanan *et al.* (2006) demonstrated the benefit of dividing an indirect thermal storage vessel into two storage compartments with the heat exchanger placed in series within the compartments for discharge of the thermal storage tank as illustrated in Figure 2.8. It was concluded that high temperatures could be maintained in the second compartment nearest to the heat exchanger outlet for longer times compared to the undivided storage. As such, hot water could always be delivered to the load for most of the discharge process. In addition, using appropriately sized heat exchanger and storage capacity, the divided storage was found to deliver between 5-11% more energy to the load than the undivided storage.

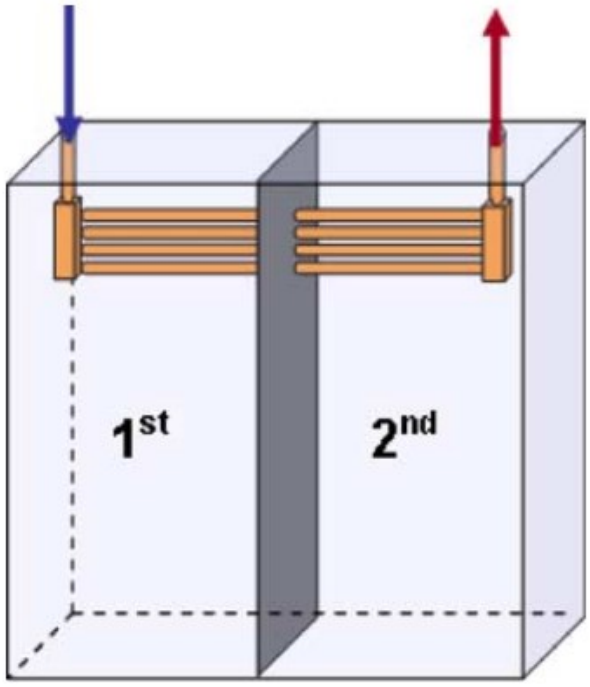

Figure 2.8. Indirect discharging through divided storage with two compartments. (Ragoonanan *et al.*, 2006).

Cruickshank and Harrison (2011) also investigated the effect of using three 270-L tank SHS system using water on the sequential stratification inside the storage tanks configured in series and in parallel as shown in Figures 2.9a and 2.9b, respectively.

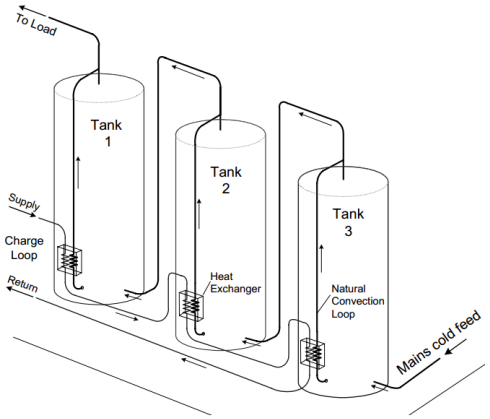

Figure 2.9a. Multi-tank water storage system: series configuration for charging and discharging. (Cruickshank and Harrison, 2011)

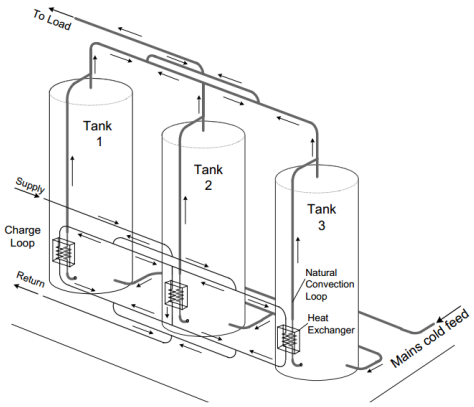

Figure 2.9b. Multi-tank water storage system: parallel configuration for charging and discharging. (Cruickshank and Harrison, 2011)

In their study they charged the tanks using thermo-syphon heat exchangers. They found that the lower charging flow rate enhances the sequential stratification in the series configuration of the storage tanks. That is, the storage system was observed to direct the input energy to the tank with the closest temperature distribution. However, higher charging flow rates in the series configuration resulted in water leaving the first tank without losing much energy and entering the second tank with almost the same temperature as before. This caused similar temperature distributions between the tanks in series and parallel configurations. Also, they reported that significant amounts of mixing inside the tanks as well as temperature drop were noticed in the series configuration during the times when the supply temperature was low. This was mainly attributed to the reverse thermosyphoning caused by discharge or carry-over of heat from a high temperature storage to a lower temperature storage.

Dickinson *et al.* (2012) investigated the thermal behavior of the three 270-L tank system described above with different configurations experimentally and computationally, when subjected to standard draw profiles. They concluded that indirect series charging and direct parallel discharging were the best configuration in terms of improved sequential stratification along the tanks as well as the energy grade delivered to the load.

2.3.2. Latent-Heat Cascaded Storage

Watanabe *et al*. (1992) showed that by using PCMs with different melting points the charging and discharging rates of a latent heat storage system could be significantly improved, which led to higher exergy efficiency. Their numerical model demonstrated that the efficiency of the system was highly dependent on the melting point distribution of the PCMs. According to their study, the optimum melting point difference of the PCMs could be achieved when the difference between the water temperature and the melting point of PCMs was almost constant along the fluid flow direction in the system.

Gong and Mujumdar (1996) developed a 1-D finite element phase change heat conduction model for alternating melting-freezing of a slab consisting of several different immiscible PCMs subjected to cyclical boundary conditions. They investigated the effects of different arrangements of the PCMs with different melting points and thermophysical properties and the effects of different boundary conditions on the charge-discharge rates of thermal energy when energy was charged from one side of a composite slab and discharged from the other. The enhancement of the cumulative energy charged/discharged in each melting or freezing period was higher using 3 PCMs than 2 PCMs in a slab compared to single PCM. In the case of 3 PCMs, an enhancement of 22% could be obtained. Similar study was carried out by Shaikh and Lafdi (2006), but using 2-D control volume numerical

simulations for a composite PCM slabs. They found out that for the same set of thermophysical properties, the total energy charged by the melting of the composite slab arrangements could be significantly enhanced compared to that of a single PCM slab by using composite PCMs with different melting temperatures.

Cui *et al.* (2003) compared the performance of a single-PCM LHS system with a three-PCM LHS system employed in a heat receiver for NASA 2-kW solar dynamic power system shown in Figure 2.10. The three-PCM system was found to promote higher charging/discharging rates as well as more uniform outlet HTF temperature.

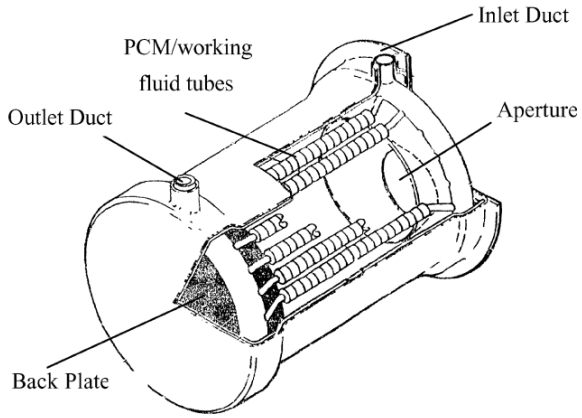

Figure 2.10. Cascaded LHS system integrated in a heat receiver for space solar power unit. (Cui *et al.*, 2003).

Michels and Pitz-Paal (2007) carried out an experimental study on the cascaded latent heat storage system in which three different PCMs were used. The experiments were conducted to investigate the effect of employing LHS system using PCMs with different melting temperatures arranged in series for parabolic trough solar power plants. High temperature oil was used as the heat transfer fluid with charging temperature of 390 °C and discharging temperature at 285 °C. The authors also developed a numerical model to extend their study to five PCM storage system cascaded in series, as illustrated in Figure 2.11. They

concluded that cascaded LHS systems with multiple PCMs provide high storage potentials compared to systems with non-cascaded PCM provided that the PCM thermal conductivity was increased by 4 times. This illustrated the fact that the poor thermal conductivity of PCMs is a detriment to the performance of the storage system. Also, the authors found out that the selection of the melting temperatures of the PCMs and the size and configuration of the PCM with respect to the heat transfer fluid (HTF) components are critical to the successful utilization of the storage capacity of the PCMs.

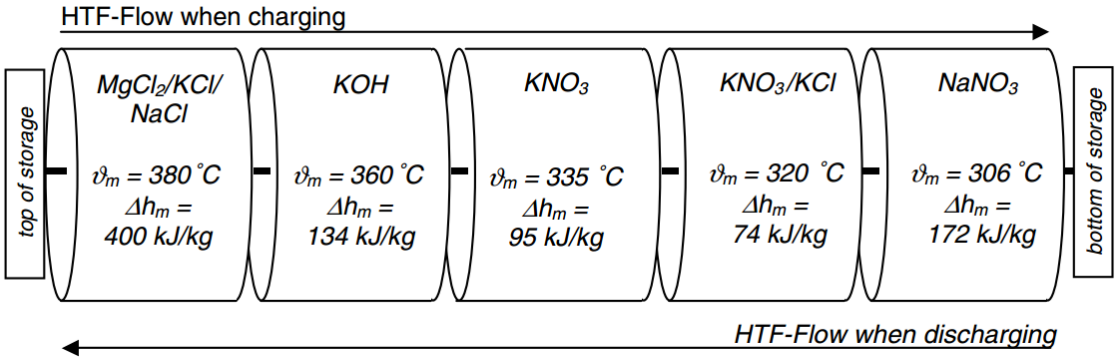

Figure 2.11. Cascaded LHS system with five PCMs (hydrated salts) for parabolic trough solar power plants. (Mitchels and Pitz-Paal, 2007).

For the same class of application; high temperature solar thermal electric generation, Shabgard *et al.* (2012) approached the problem of high thermal resistance of the PCMs by developing a thermal network model for a 3-PCM cascaded LHS system with gravity assisted heat pipes between the HTF flow and the PCMs. They concluded that the heat pipes showed significant acceleration of the charging and discharging rates. Besides, the cascaded LHS with different PCM melting temperatures helps to maintain constant temperature difference between the HTF and the PCM. As a result, the cascaded LHS system was found to provide more uniform melting in the PCMs compared to the non-cascaded system, the feature that led to more effective utilization of the PCM storage capacity. In addition, when

the authors conducted a 2nd law analysis they found out that the cascaded system recovered 10% more exergy compared to non-cascaded LHS system.

Chinnapandiana *et al.* (2011) designed and fabricated a heat recovery system consisting of a finned shell and tube heat exchanger and a TES tank with paraffin as PCM storage material for waste heat recovery from diesel engine exhaust. Castor oil was used as tube side fluid to extract heat from exhaust gas. The thermal performance of the heat recovery heat exchanger and the storage system was studied for a charging process of PCM in the thermal storage tank for various engine load conditions. In addition, the advantage of a cascaded latent energy storage system over the single storage tank system was highlighted. It was concluded that the integration of the heat recovery heat exchanger with the engine led to percentage of the energy saved varying from 10 to 15 % in the case of the single storage tank as the load increased from 25 % to full load. However, 11 to 20 % energy savings was observed in the case of the cascaded storage system as the load increased from 25 % to full load.

Tian and Zhao (2013) designed a LHS system with 2 coaxial channels where the heat transfer fluid flowed in the outer channel while the PCM was placed inside the inner channel. Water was used as heat transfer fluid. They presented and compared three different systems; single-stage LHS, cascaded LHS and metal foam-enhanced cascaded LHS. They observed that the cascaded system enhanced heat exchange rate by up to 30% compared to single-stage system. While the metal foam-enhanced cascaded system enhanced heat exchange rate by 2–7 times compared to the ordinary cascaded system, depending on the properties of metal-foam samples (porosity, pore density and thermal conductivity). Seeniraj and Narasimhan (2008) investigated numerically the performance enhancement of LHS unit employing

multiple PCMs and fins. The multiple PCM model resulted in appreciable energy storage in the form of latent heat as compared to a single PCM model.

2.4. Comments on Previous Literature

Since the early 1970s, thermal energy storage (TES) has been the subject of intensive research work since the efficient design of TES potentially promotes for better utilization of energy. An abundance of research studies was found in literature on thermal energy storage systems spanning wide range of applications including solar thermal/power and waste heat recovery. Researchers investigated various TES designs for the purpose of increasing the storage efficiency. However, most of these studies were conducted under specific operation conditions that limited the applicability of their results in realistic applications. These conditions are listed as follows:

1. Many researchers focused their studies on TES on the component level. As such, the coupling effect between the storage element and the system dynamics were ignored. For instance, in realistic applications such as solar thermal DHW system, the dynamic performance of the storage element directly impacts the efficiency of the solar collector which in turn affects the operation of the storage element.
2. Many studies investigated the performance of the TES system under idealistic operation conditions such as: fixed charging temperature, fixed draw volume, etc. These studies fail to anticipate the annual performance of TES systems in realistic applications where the supply and demand profiles are typically time variant.
3. Very few investigations considered the effect of the sizing of the storage element on the performance of the system.

The current dissertation proposes a novel design of TES using modular water tanks with PCM modules, shown in Figure 1.8. The performance of this design in solar DHW system was extensively investigated for both small-scale (i.e., single-tank storage) as well as medium/large scale (i.e., multi-tank storage) applications. In the current study, the above-mentioned limitations, noticed in previous studies, were addressed as follows:

1. The performance of the proposed design (HTES) was investigated when integrated into a solar DHW system.
2. Realistic operation conditions were applied to the system to explore the effect of the variability in the climate conditions and the DHW demand patterns on the diurnal performance of the system.
3. Extensive parametric analysis was carried out on the HTES to provide understanding of the potential benefits of the PCMs. The critical effect of the storage sizing on the performance of the system was illustrated.

CHAPTER THREE

MATHEMATICAL MODELING

3.1. Introduction

This chapter presents the mathematical models developed to simulate the performance of the proposed design of single and multi-tank SHS and HTES elements. The mathematical models were developed primarily in two stages: (1) developing the mathematical model for each component of the single-tank storage element; i.e. the coil heat exchangers and the storage medium, and (2) integrating the mathematical models of all the components into one comprehensive system model that is able to capture the dynamic coupling between the individual components of a single-tank storage. For the multi-tank storage, the single-tank storage model was repeated for each tank and then coupled together through the flow rates and temperatures at the inlets and outlets of the coil heat exchangers.

The proposed design of the multi-tank HTES system is similar to the design proposed by Mather (2000). A detailed layout of the proposed multi-tank HTES connected to a solar thermal system is shown in Figure 3.1. A number of modular tanks are serially connected via immersed coil heat exchangers installed at the bottom of the tanks for charging and another installed at the top for discharging. PCM modules with different thermophysical properties are submerged in each tank.

The performance of such systems is very complicated since it is transient, non-linear and it depends on a long list of coupled variables. Moreover, building a full-scale

experimental facility that is capable of testing the transient behavior of these systems under realistic supply and demand scenarios would be extremely costly.

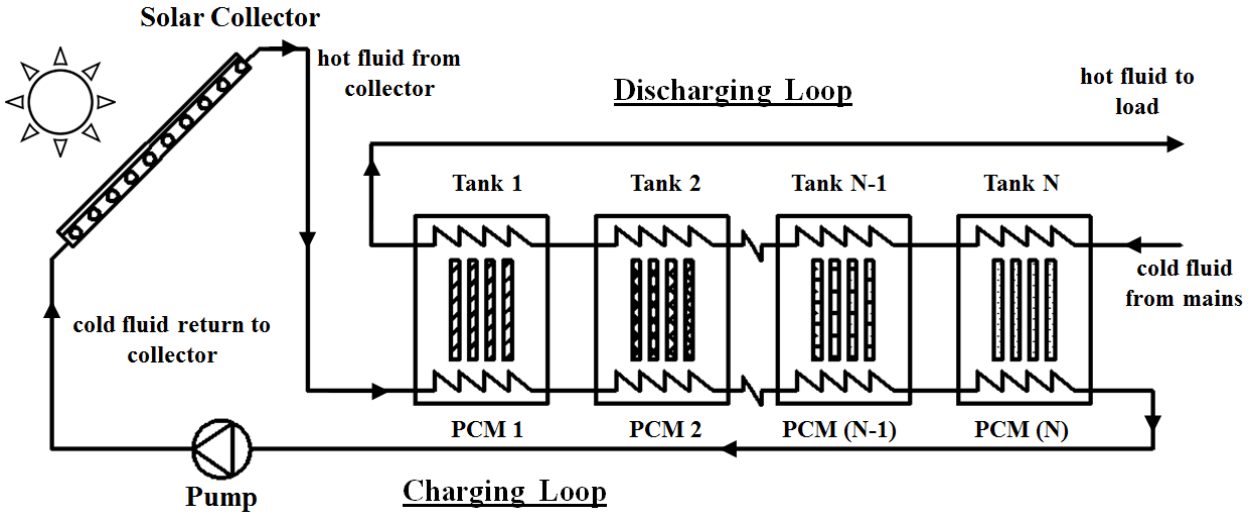

Figure 3.1. Layout of the proposed design of multi-tank HTES connected to solar thermal system.

Mathematical modeling offers the advantage of simulating the performance of complicated nonlinear systems accurately without the need for expensive and time-intensive experiments. As such, the mathematical model needs to be accurate enough to capture all the physical behaviors of the simulated system and simple enough to be computationally efficient. Experimental validation is still required to provide confidence in the simulation results, yet the experimental setup can be designed to validate the model with minimum expenses. Chapter Four illustrates the detailed design and construction of the experimental facility used for the validation of the mathematical model.

This chapter starts by discussing the thermal behavior of the proposed system. Then, the mathematical model developed to simulate its transient performance under different supply and demand profiles is presented. The procedures of modeling and solving the energy balance equations for different components of the system are demonstrated. In addition, the implementation of the model algorithms is discussed.

3.2. Thermal Behavior of Single-tank HTES System

In order to better understand the performance of the multi-tank HTES system, the thermal behavior of the single-tank HTES system is first explored. Also, the thermal behavior of the single and multi-tank SHS system (with water only), extensively studied by Mather (2000), is presented for comparison. Figures 3.2a-b depict the basic components of the single-tank storage with water only and with water and PCM modules, respectively.

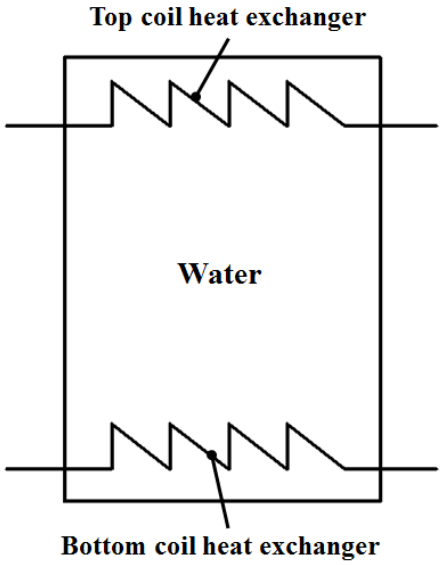

Figure 3.2a. Basic components of a single-tank sensible heat storage (SHS).

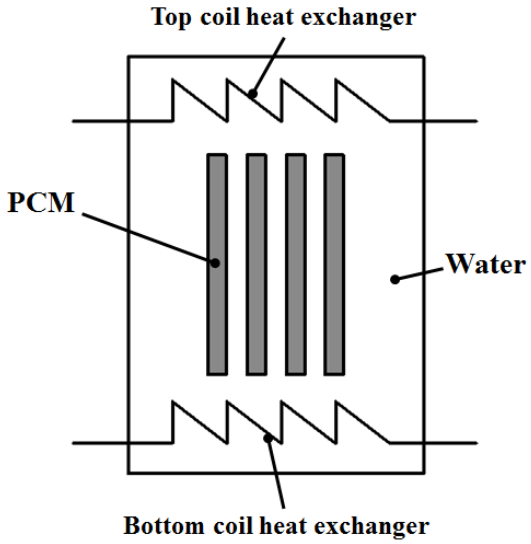

Figure 3.2b. Basic components of a single-tank hybrid thermal energy storage (HTES).

Heat transfer takes place into or from the tanks in both systems through the immersed coil heat exchangers. In addition, heat transfer occurs through the walls of the tanks due to thermal losses to the surrounding. Since there is no forced fluid flow through the storage tanks, there are only two mechanisms that control the heat transfer; conduction and natural convection. Conduction always exists whenever there is temperature gradient inside the tank. Natural convection heat transfer takes place due to buoyancy effects associated with density gradients inside the tank. That is, hot liquid layers have lower density and tend to seek higher

levels inside the tank, while cold liquid layers have higher density and tend to sink towards the bottom of the tank. The natural convection flow patterns inside the tank are directly influenced by the geometry of the tank, the design and location of the immersed coil heat exchangers, the thermal properties of the storage liquid and the temperature differences inside the tank.

Despite the complexity of the flow patterns associated with natural convection heat transfer inside the storage tank, the design of the heat exchangers in the proposed system will tend to maintain a simple one-dimensional temperature profile. To better illustrate this statement, consider the behavior of a single water tank with a suspended coil heat exchanger shown in Figure 3.3a. Assume that the water inside the tank is initially maintained at uniform temperature. If the heat transfer fluid (HTF) enters the coil heat exchanger at a temperature higher than the initial temperature inside the tank, the water layer adjacent to the heat exchanger will heat up and produce buoyancy forces. These forces will mix the water inside the tank. Newton (1995) performed 2-D simulations, using FLUENT software, to study mixing in solar thermal storage tanks with immersed coil heat exchangers. The results showed that the heat transferred from the heat exchanger acted to produce natural convection currents which promoted mixing of the liquid surrounding and above the coil. The region below the coil was found to be only heated by conduction. As such, a vertically stratified tank, shown in Figure 3.3b, would result from this configuration, with warm liquid surrounding and above the heat exchanger, and liquid below the heat exchanger at near the initial temperature of the tank.

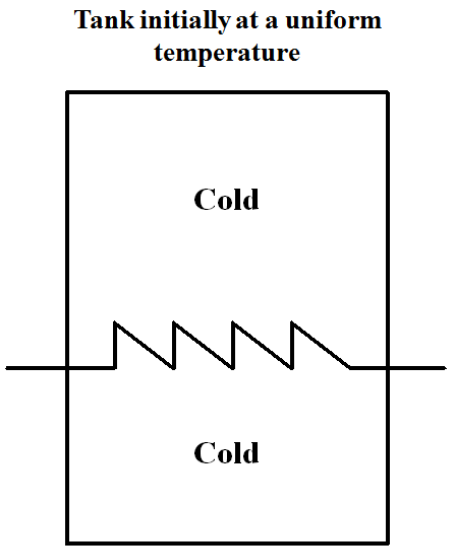

Figure 3.3a. Water tank maintained at a uniform initial temperature.

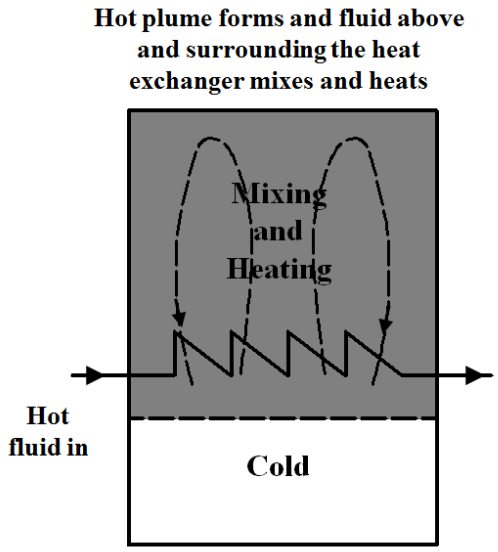

Figure 3.3b. Water tank after admitting hot fluid to the heat exchanger inlet leading to mixing of the region surrounding and above the heat exchanger.

Newton (1995) also explored the behavior of a tank which is initially stratified as shown in Figure 3.4a. The natural convection currents developed by the coil heat exchanger will act to heat and mix the regions surrounding and above the heat exchanger while preserving the thermal identity of the bottom cold and the top warm regions, Figure 3.4b. The middle region would mix with the top warm region only when the temperature of the middle region reaches that of the top region, Figure 3.4c. Similar behaviors are expected when the temperature of the HTF entering the coil heat exchanger is lower than that inside the tank. Downward convection currents will occur to mix the region surrounding and below the coil heat exchanger, while the liquid above it will remain relatively unaffected. Mixing will take place with the colder bottom region only when the temperature of the middle region decreases to the same temperature of the bottom region.

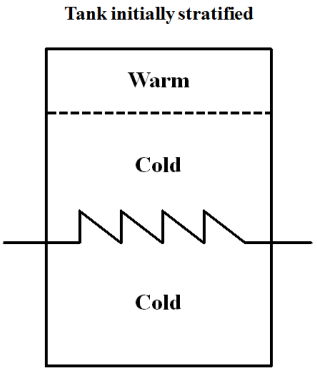

Figure 3.4a. Water tank maintained at a stratified condition; warm region sitting on top the cold region

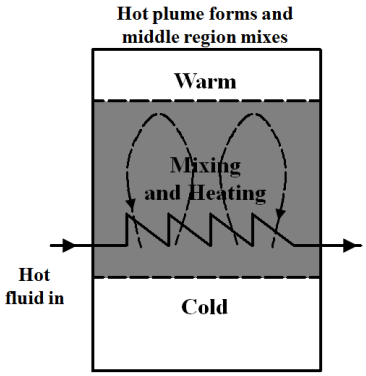

Figure 3.4b. Water tank after admitting hot fluid to the heat exchanger inlet leading to mixing of the region surrounding and above the heat exchanger.

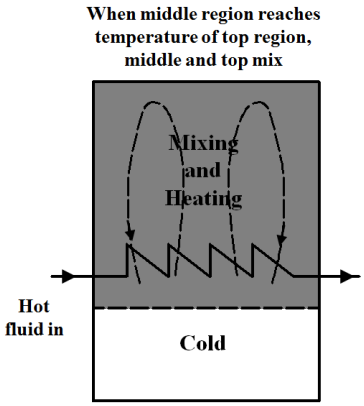

Figure 3.4c. Mixing between the middle region and the top region takes place when the temperature of the middle region exceeds that of the top region.

The design proposed in this study is motivated by the results obtained from Newton's CFD simulations. The charging coil heat exchanger is installed very close to the bottom of the tank in order to minimize the region where cold liquid stagnates under the heat exchanger. Similarly, the discharging coil heat exchanger is installed very close to the top of the tank. Therefore, the thermal behavior of the proposed system depends primarily on the temperature difference between the HTF entering the heat exchangers and the bulk temperature distribution inside the storage tank. Figure 3.5 illustrates the reaction of the storage tank to different inlet fluid temperatures entering the bottom coil heat exchanger. When the temperature entering the heat exchanger is higher than the bulk temperature of the tank, natural convection currents will act to mix the contents of the tank. When the temperature entering the heat exchanger is lower than the bulk temperature of the tank, natural convection currents will act to stratify the tank; i.e. a stable colder liquid layer will form surrounding the heat exchanger at the bottom of the tank, while the rest of the tank remains relatively unaffected. The latter behavior was referred to in Mather's thesis (2000) as

the thermal diode effect, since it is similar in effect to the electrical diode. The proposed design promotes the transfer of heat in the "right direction"; from the charging coil at the bottom of the tank into the discharging coil at the top of the tank. Heat transfer in the opposite direction is essentially suppressed by virtue of the thermal diode effect. In the multi-tank system, this allows for the energy to be transferred to the correct tank in order to promote tank-to-tank stratification. Similar yet opposite behavior is expected to occur when the top heat exchanger is operating.

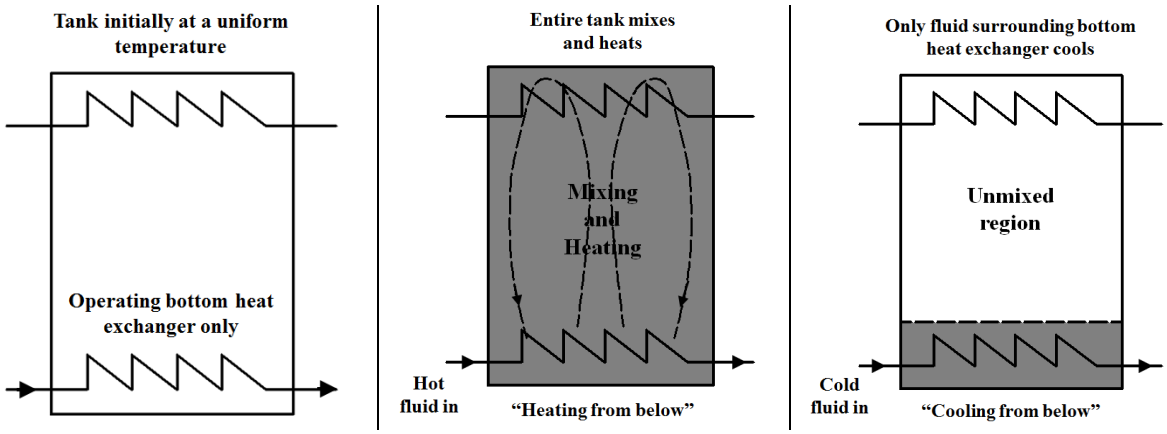

Figure 3.5. Left: Water tank maintained at a uniform temperature. Center: Mixing due to the admission of hot fluid at the inlet to the bottom heat exchanger. Right: Thermal diode due to the admission of cold fluid at the inlet to the bottom heat exchanger.

It is worth noting that the efficiency of the thermal dioding is not as high as the electrical dioding, since the heat is still allowed to transfer in the "incorrect direction"; i.e. from the top coil heat exchanger and/or into the bottom coil heat exchanger. However, the amount of energy that can be transferred is limited by the size of the liquid region surrounding the heat exchanger. In addition, depending on the thermal conductivity of the storage medium, heat transfer by conduction will act to increase the amount of energy transferred in the "incorrect direction".

Introducing PCM modules in the middle region of the tank between the top and bottom regions of the coil heat exchangers will act to enhance the mixing inside the tank. Sarafraz (2013) conducted 2-D CFD simulations using ANSYS CFX to study the effect of introducing rectangular PCM modules in a rectangular water tank charged using an isothermal coil heat exchanger installed at the bottom of the tank. The simulations showed that the existence of the PCM modules enhanced the natural convection flow currents inside the storage tank and hence led to better mixing. The temperature difference established between the water and the PCM modules during the charging process augmented the circulation currents inside the tank as illustrated by the velocity vector plot shown in Figure 3.6. Figure 3.7 demonstrates the effect of the circulation current on the uniform temperature distribution inside the HTES tank with rectangular PCM modules. The relative placement of the PCM modules with respect to the coil heat exchanger was found to have a critical influence on the strength of the mixing currents. Higher levels of mixing were observed in the cases where the upward flowing currents from the hot coil were not opposed by the downward flowing currents from the cold PCM modules.

Consider the case when the HTES tank, initially maintained at a uniform temperature, is charged from the bottom coil heat exchanger with the inlet temperature of the HTF higher than the temperature of the tank as seen in Figure 3.8a. Heat is transferred from the coil to the water surrounding it as shown in Figure 3.8b. Natural convection currents will occur to mix the contents of the tank and heat the water uniformly. Hydrodynamic and thermal boundary layers between the water and the surface of the PCM modules develop along the height of the modules. Once the temperature of the water starts increasing above the temperature of the PCM, heat transfers from the water into the PCM modules.

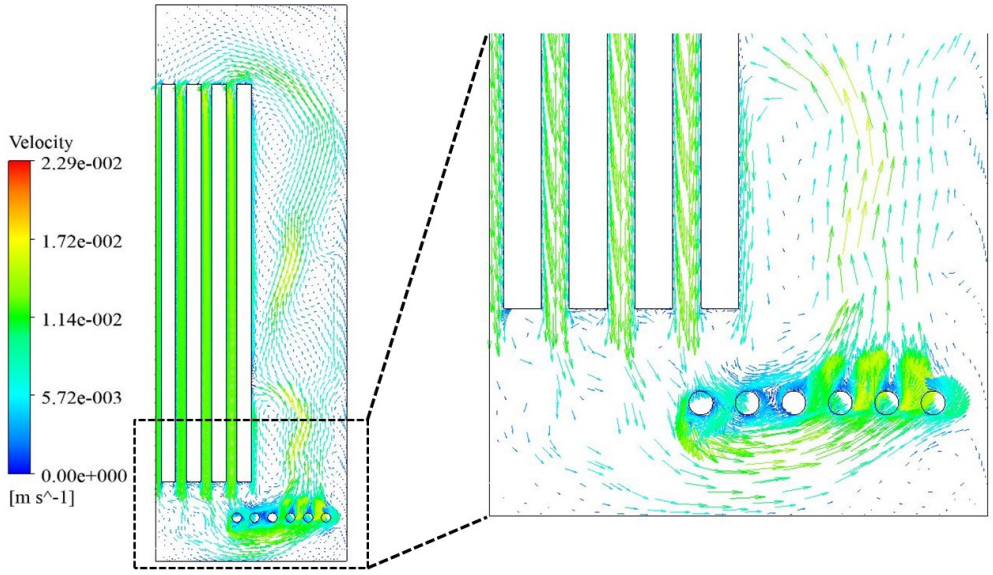

Figure 3.6. Natural convection flow currents inside HTES due to upflow buoyancy currents from the hot coil heat exchanger and the downflow buoyancy currents from the cold PCM modules. (Sarafraz, 2013).

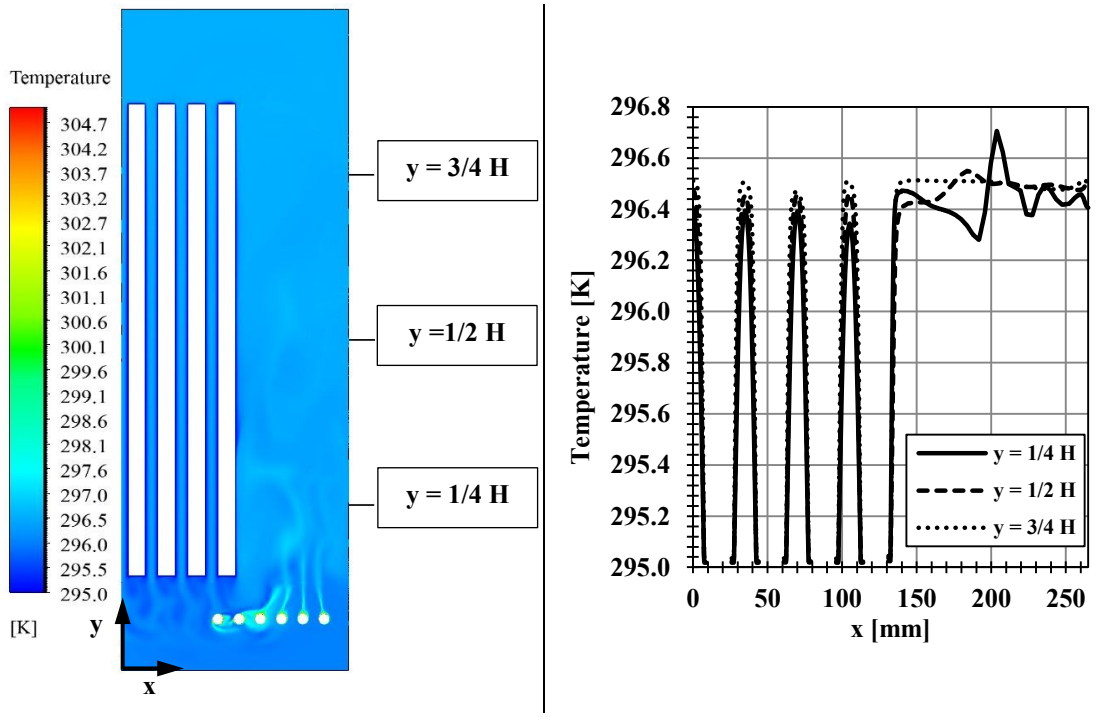

Figure 3.7. Temperature distribution along the width of the HTES tank with PCM at different tank heights. Left: Temperature contours. Right: Spacial distribution of temperature in the HTES tank. (Sarafraz, 2013).

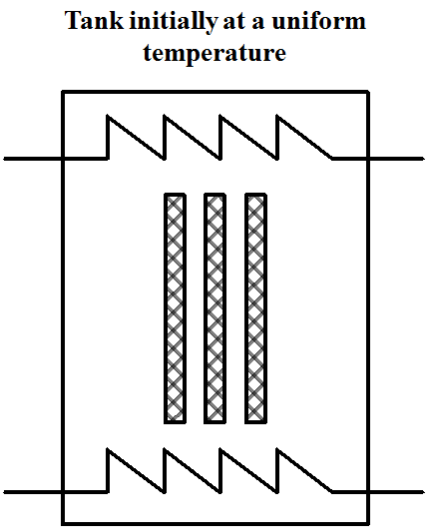

Figure 3.8a. HTES tank maintained at a uniform initial temperature.

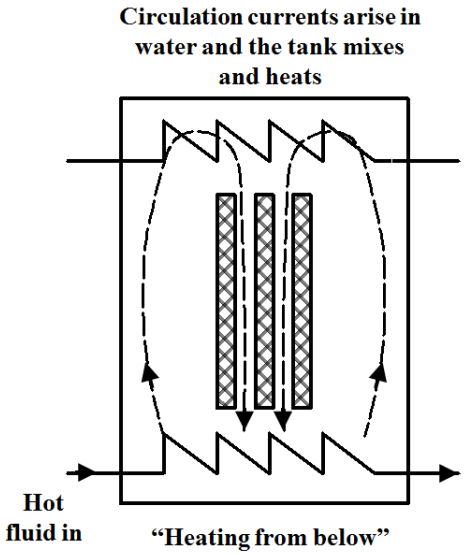

Figure 3.8b. HTES tank after admitting hot fluid to the bottom heat exchanger inlet leading to mixing currents.

During the cases when thermal dioding is in effect, the regions surrounding the coil heat exchangers will be affected, while the middle region where the PCM modules are located will remain relatively unaffected. According to the temperature difference between the water in the middle region and the PCM modules, natural circulation currents will arise to attain thermal equilibrium.

3.3. Mathematical Model of Single-tank HTES

The thermal behavior of the proposed design of the storage tank with and without the PCM modules was observed, based on CFD simulations (Newton, 1995 and Sarafraz, 2013) as well as the experimental results by Mather (2000), to essentially divide the storage tank into three regions. These regions are defined as the regions surrounding the bottom and top coil, respectively and the middle region between the coils. Each region is characterized by being fully mixed with a uniform temperature distinct from the other two regions. This

observation motivated the developed mathematical model to discretize the storage tank into three fully-mixed control volumes.

3.3.1. Tank Model

Consider first the case of a single tank with water only as the thermal storage medium as shown in Figure 3.9a. The symbols T_{nb}, T_{nt} and T_{bulk} will represent the temperatures of the bottom coil heat exchanger node, the top coil heat exchanger node and the middle (bulk) node, respectively. The temperature of each node is representative of the uniform temperature of the corresponding control volume. The heat transfer mechanisms in the coil heat exchanger nodes are due to natural convection from the coils, thermal diffusion to/from the adjacent node and thermal losses through the walls of the tank, Figure 3.9b. The energy equations for both coil heat exchanger thermal nodes become:

$$M_{nb}c_w\frac{dT_{nb}}{dt} = Q_{coil,b} + Q_{cond,bulk-nb} - Q_{loss,nb} \tag{3.1}$$

$$M_{nt}c_w\frac{dT_{nt}}{dt} = Q_{coil,t} + Q_{cond,bulk-nt} - Q_{loss,nt} \tag{3.2}$$

The heat transfer mechanisms in the bulk node are attributed to thermal diffusion to/from adjacent node(s) and thermal losses through the walls of the tank. The energy balance on the bulk node yields:

$$M_{bulk}c_w\frac{dT_{bulk}}{dt} = -Q_{cond,bulk-nb} - Q_{cond,bulk-nt} - Q_{bulk-PCM} - Q_{loss,bulk} \tag{3.3}$$

The variables $Q_{coil,b}$ and $Q_{coil,t}$ in Equations (3.1) and (3.2) denote the heat transfer rates from the bottom and top coil heat exchangers, respectively. The variables $Q_{cond,bulk-nb}$ and

$Q_{cond,bulk-nt}$ in Equations (3.1), (3.2) and (3.3) represent the heat transfer by diffusion from the bulk node into the bottom coil node and the top coil node, respectively. The heat transfer from the water in the bulk region into the PCM modules is represented by $Q_{bulk-PCM}$.The thermal losses from the three nodes through the walls of the tank are designated by $Q_{loss,nb}$, $Q_{loss,nt}$ and $Q_{loss,bulk}$.

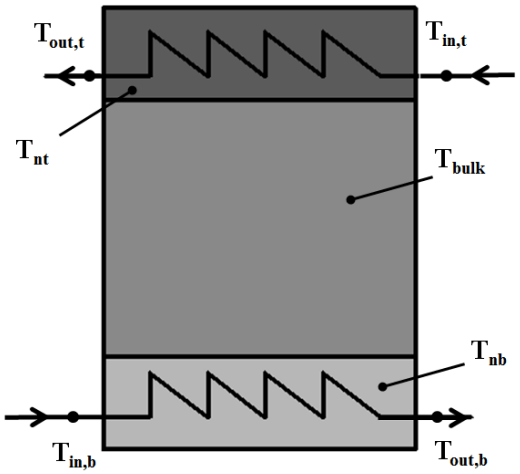

Figure 3.9a. Illustration of the temperatures of the SHS tank nodes and coil heat exchangers.

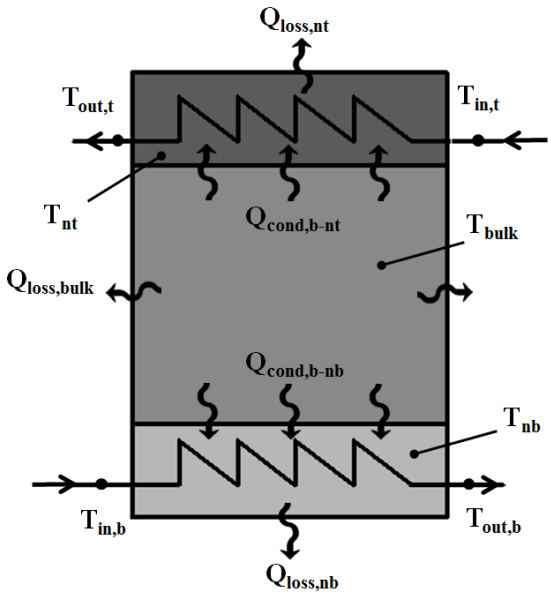

Figure 3.9b. Illustration of the heat transfer mechanisms through the boundaries of the SHS tank nodes.

Thermal mixing is always applied in the cases where negative vertical temperature gradient exists. That is, the model mixes any two adjacent nodes where the bottom node is hotter than the top node. The mixing takes place by applying mass weighted average of the temperatures of both nodes: node1 and node2 [Eq. (3.4)]. Figures 3.10a and 3.10b illustrate the thermal mixing of two nodes.

$$T_{mix} = \frac{M_{node1}T_{node1} + M_{node2}T_{node2}}{M_{node1} + M_{node2}} \tag{3.4}$$

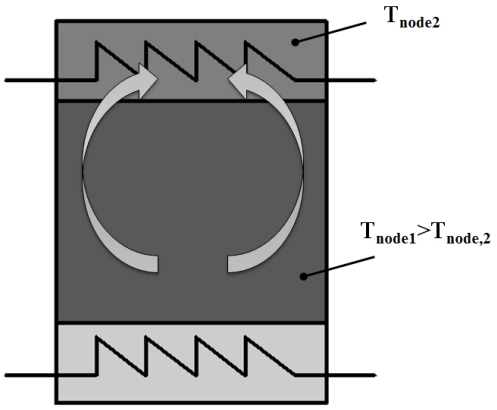

Figure 3.10a. Thermal mixing takes place when there is negative temperature gradient between two adjacent nodes.

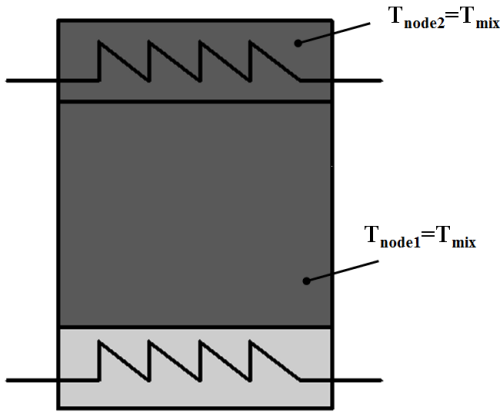

Figure 3.10b. Both nodes mix to a uniform temperature T_{mix}.

3.3.2. Heat Exchanger Model

The coil heat exchanger is modelled as a straight pipe immersed in an infinite isothermal medium. The pipe is discretized using a 1-D grid in the axial direction. The effect of coiling is assumed negligible on the heat transfer and the heat exchanger is treated as a straight pipe. Figure 3.11 depicts the 1-D discretization of the coil heat exchanger.

The energy balance equation on node (i) can be formulated as:

$$M_i c \frac{dT_i}{dt} = \dot{m}c(T_{i-1} - T_i) - Q_{coil,i} \tag{3.5}$$

The energy balance represented by Equation (3.5) has the following assumptions:

1. Each thermal node has a uniform temperature in the radial direction.
2. The axial conduction heat transfer is negligible compared to the convective heat transfer.

3. The convective heat transfer between the nodes is calculated by applying full upwinding of the temperature of the upstream node.

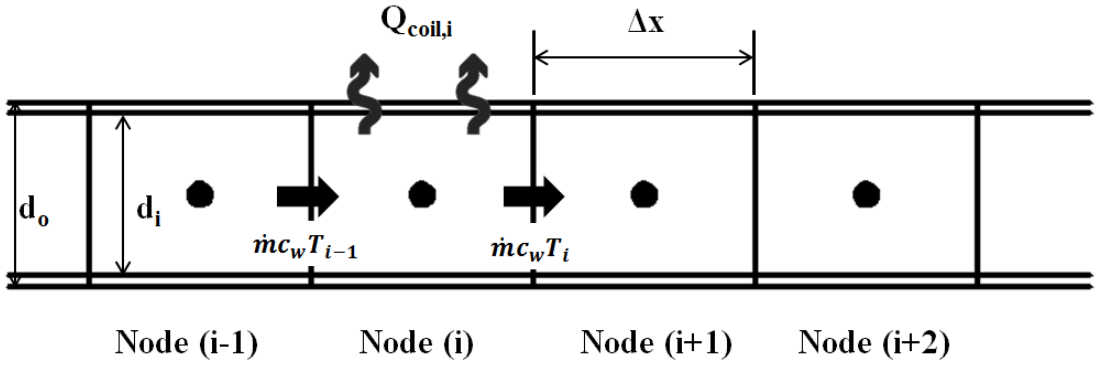

Figure 3.11. 1-D discretization of the coil heat exchanger.

The heat transfer rate through the walls of the heat exchanger; $Q_{coil,i}$, can be represented by the following equation:

$$Q_{coil,i} = UA(T_i - T_\infty) = UA\Delta T \tag{3.6}$$

The variable T_∞ is the temperature of the thermal node surrounding the heat exchanger, while *UA* is the overall thermal conductance through the boundaries of the node. The overall thermal conductance can be calculated from the resistance circuit shown in Figure 3.12 using the following equation:

$$UA = [\frac{1}{h_i A_i} + R_{cond,wall} + \frac{1}{h_o A_o}]^{-1} \tag{3.7}$$

The variables h_i and h_o are the heat transfer coefficients on the inner and outer sides of the pipe, while A_i and A_o are the inner and outer surface areas of the node. Note that the thermal mass of the pipe was neglected. The conductive resistance of the pipe thickness is denoted $R_{cond,wall}$.

$$A_i = \pi d_i \Delta x, \text{ and } A_o = \pi d_o \Delta x \tag{3.8}$$

$$R_{cond,wall} = \frac{\ln(\frac{d_o}{d_i})}{2\pi k_{pipe} \Delta x} \tag{3.9}$$

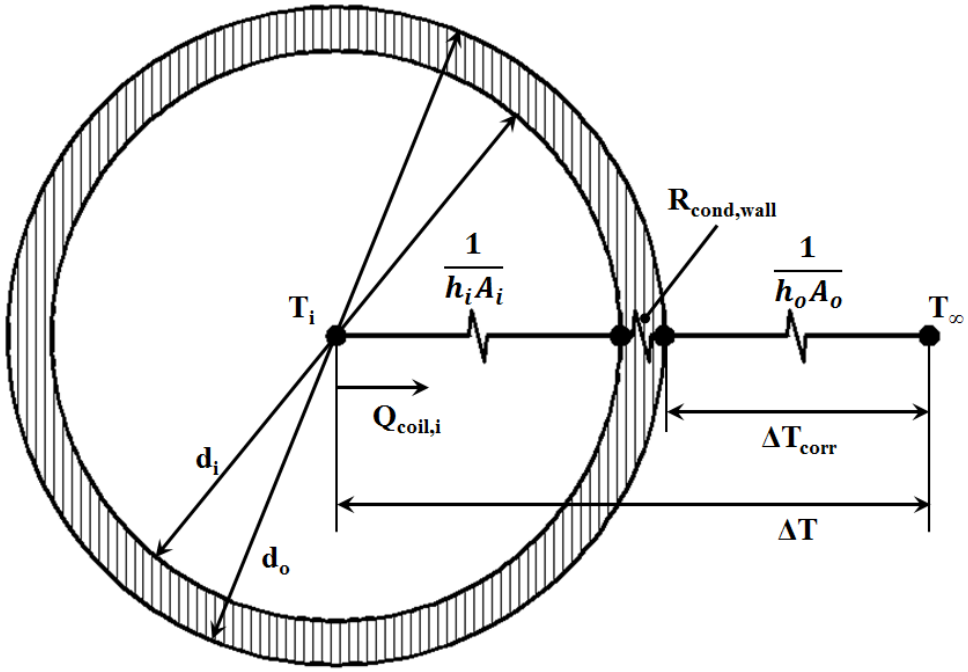

Figure 3.12. Cross section view of the coil illustrating the thermal resistance diagram.

The internal heat transfer is modelled as forced convection and the external heat transfer is modelled as natural convection. The inner convection heat transfer coefficient (h_i) is calculated based on the correlations for forced convection in a smooth pipe as recommended in Incropera and DeWitt (2014):

$$h_i = \frac{Nu_i k_i}{d_i} \tag{3.10}$$

The inner Nusselt number is a function of Reynolds number (Re_i) and Prandtl number (Pr_i). The Reynolds number is calculated by:

$$Re_i = \frac{4\dot{m}}{\pi d_i \mu} \tag{3.11}$$

The Prandtl number is calculated by:

$$Pr_i = (\frac{\mu c}{k})_i \tag{3.12}$$

For fully developed laminar flow ($Re_i \leq 3000$ and $Pr_i \geq 0.6$), the inner Nusselt number is taken as the value for an isothermal circular pipe:

$$Nu_i = 3.66 \tag{3.13}$$

For turbulent flow ($3000 < Re_i < 5\times10^6$ and $0.5 < Pr_i < 2000$), the inner Nusselt number is calculated using Gnielinski (1976) correlation:

$$Nu_i = \frac{(f/8)(Re_i - 1000)Pr_i}{1 + 12.7(f/8)^{1/2}(Pr_i^{2/3} - 1)} \tag{3.14}$$

where,

$$f = (0.79 \ln Re_i - 1.64)^{-2} \tag{3.15}$$

The outer heat transfer coefficient (h_o) is calculated by the natural convection correlations proposed by Raithby and Hollands (1998) for long horizontal cylinders in an infinite isothermal medium. The outer heat transfer coefficient is calculated based on the outer Nusselt number (Nu_o):

$$h_o = \frac{Nu_o k_o}{d_o} \tag{3.16}$$

The outer Nusselt number (Nu_o) is calculated by:

$$Nu_o = [Nu_l^m + Nu_t^m]^{1/m}, where\ m \cong 10 \tag{3.17}$$

The value Nu_l is calculated by:

$$Nu_l = \frac{2F}{\ln(1 + 2F/Nu^T)} \tag{3.18}$$

where,

$$F = 1 - \frac{0.13}{(Nu^T)^{0.16}} \tag{3.19}$$

$$Nu^T = 0.772\bar{C_l}Ra_o^{0.25} \tag{3.20}$$

$$\bar{C_l} = \frac{0.671}{[1 + (0.492/Pr_o)^{9/16}]^{4/9}} \tag{3.21}$$

The value Nu_t is calculated by:

$$Nu_t = \bar{C_t}Ra_o^{1/3} \tag{3.22}$$

where $\bar{C_t} \cong 0.1$ for isothermal circular cylinder over a wide range of Prandtl numbers. The outer Prandtl number is calculated by:

$$Pr_o = (\frac{\mu c}{k})_o \tag{3.23}$$

The outer Rayleigh number (Ra_o) is calculated by:

$$Ra_o = \frac{g\beta d_o^3}{\upsilon\alpha}\Delta T_{corr} \tag{3.24}$$

The value of ΔT_{corr} represents the temperature difference between the outer surface of the pipe and the surrounding fluid. It is calculated by:

$$\Delta T_{corr} = \Delta T - Q_{coil,i}\left(\frac{1}{h_i A_i} + R_{cond,wall}\right) \tag{3.25}$$

The thermophysical properties of the water were updated in the model based on the film temperature between the water and the surface of the heat exchanger coil.

3.3.3. Model for Thermal Diffusion between Tank Nodes

Thermal diffusion takes place between any two thermal nodes inside the tank when there is a temperature difference between them. Conduction heat transfer rate between the adjacent nodes; $Q_{cond,bulk\text{-}nc}$ and $Q_{cond,bulk\text{-}nd}$, can be approximated by:

$$Q_{cond,bulk-nb} = kA_{c,nb}\frac{T_{bulk} - T_{nb}}{\delta_{bulk-nb}} \tag{3.26}$$

$$Q_{cond,bulk-nt} = kA_{c,nt}\frac{T_{bulk} - T_{nt}}{\delta_{bulk-nt}} \tag{3.27}$$

The values of $A_{c,nb}$ and $A_{c,nt}$ are the cross-section areas of the charging and discharging heat exchanger nodes. The thermal diffusion length scales; $\delta_{bulk-nb}$ and $\delta_{bulk-nt}$, are calculated based on the analytical solution to the thermal diffusion through a semi-infinite solid with an isothermal boundary condition, Bergman *et al*. (2011).

$$\delta = \sqrt{\pi \alpha t} \tag{3.28}$$

The above equation simply represents the growth of the thermocline thickness between the tank nodes with time (t). The applicability of this thermal diffusion model has the following limitations:

1. The temperature values of the nodes should always be spatially uniform.
2. The temporal variation of the bulk temperature during the diffusion process should be small.
3. For the applications considered by this study, the time integral of the heat transfer by diffusion should be considerably smaller than that of the heat transfer by convection.

3.3.4. Model for Thermal Losses through Tank Walls

The rate of heat loss from each node to the surrounding through the tank walls can be calculated by:

$$Q_{loss,node} = (UA)_{node}(T_{node} - T_{surr}) \tag{3.29}$$

The value of $(UA)_{node}$ is the thermal conductance through the node boundaries to the storage surrounding which is assumed infinite at T_{surr}.

3.3.5. Model for Heat Transfer into PCM Modules

In the HTES tanks, the PCM modules are introduced in the middle region of the tank; i.e. within the bulk control volume. As such, the heat transfer between the water in the middle region and the PCM modules needs to be considered in the energy balance of the bulk control volume, as shown in Equation (3.3). Natural convection is the mechanism of heat transfer from the water in the bulk node to the surface of the PCM modules, whereas the heat transfer into the PCM modules is primarily governed by conduction. During the melting

process of the PCM, natural convection circulation can occur in the melt region when the aspect ratio, that is the ratio of the height to the thickness of the PCM module is $H/L<Ra^{1/4}$ (Jany and Bejan, 1988). Figure 3.13a demonstrates the different components of the HTES tank and the temperatures of the thermal nodes and the heat exchangers inside the tank. Figure 3.13b illustrates the heat flows through the boundaries of the tank nodes.

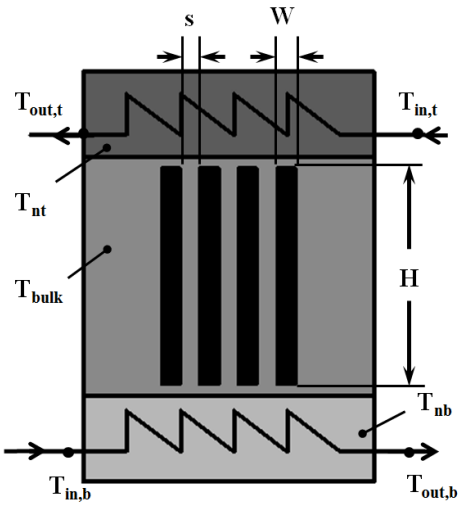

Figure 3.13a. Illustration of the temperatures of the HTES tank nodes and coil heat exchangers.

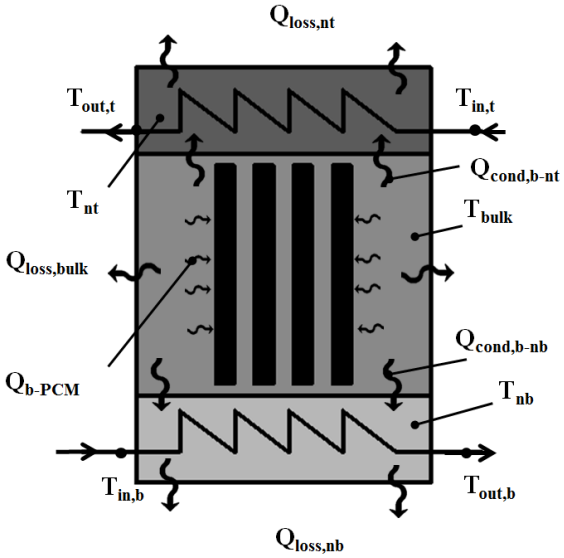

Figure 3.13b. Illustration of the heat transfer mechanisms through the boundaries of the HTES tank nodes.

Natural convection heat transfer from the water to the surface of the PCM module. The heat transfer rate from the water to the surface of the PCM modules is calculated by:

$$Q_{bulk-PCM} = \frac{A_{PCM}(T_{bulk} - T_{PCM,o})}{\frac{1}{h_{b-PCM}} + \frac{t_{cont}}{k_{cont}}} \tag{3.30}$$

The conductive thermal resistance due to the thickness of the PCM container is represented in Equation (3.30) as a function of the thickness (t_{cont}) and the thermal conductivity (k_{cont}) of the container.

This equation has the following assumptions:

1. The temperature of the water jacket surrounding the PCM modules is uniform, based on the results from the CFD simulations by Sarafraz (2013).
2. All the PCM modules have identical design and performance; i.e. all of the PCM modules will have the same surface temperature ($T_{PCM,o}$) at all times.

The heat transfer coefficient ($h_{bulk\text{-}PCM}$) is calculated according to the Nusselt number correlation proposed by Raithby and Hollands (1975) for natural convection of isothermal flat plates submerged in an infinite isothermal medium.

$$h_{bulk-PCM} = \frac{Nu_{bulk-PCM}\, k}{s} \tag{3.31}$$

The value of k is the thermal conductivity of water in the bulk node and the characteristic length of the equation (s) is taken to be the spacing between the PCM modules.

$$Nu_{bulk-PCM} = [(Nu_{fd})^{m} + (0.608 Ra^{*0.25})^{m}]^{1/m},\ \ m = -1.9 \tag{3.32}$$

$$Nu_{fd} = \frac{Ra^{*}}{24} \tag{3.33}$$

The modified Rayleigh number (Ra^{*}) is defined by:

$$Ra^{*} = \frac{g\beta(T_{bulk} - T_{PCM,o})s^{3}}{\upsilon\alpha}\frac{s}{H} \tag{3.34}$$

The thermophysical properties of the water were updated in the model based on the film temperature between the water and the surface of the PCM modules.

Heat transfer into the PCM modules. The current study focuses on the study of rectangular PCM modules in square tanks. Rectangular design of PCM modules has many advantages compared to other designs such as cylindrical and spherical:

1. Easy to manufacture and readily available in the market.
2. For the same volume of the PCM used in the storage tank, the number of modules required is smaller and hence much cheaper and easier to install and maintain.
3. For the same thickness of the containment material, a smaller tank volume is occupied by the containment material. This leads to lower cost and better performance since the majority of the volume allotted for the PCM modules will be occupied by the PCM itself.

Slender modules as shown in Figure 3.14 are chosen for this study in order to minimize the thermal resistance inside the PCM modules. A one-dimensional heat transfer model inside the PCM modules is applied. As such, the heat transfer is assumed to be dominant in the direction normal to the surfaces of the rectangular container of the PCM and that variations in the vertical direction are neglected.

First, consider the 1-D heat conduction through the PCM module symmetric about the center-plane with a melting temperature T_m submerged in a fully-mixed fluid with a time varying temperature $T_\infty(t)$.

Initially, the following is assumed;

$$T_i(x) < T_m \; and \; T_\infty(t) > T_m$$

The variable $T_i(x)$ represents the spatial distribution of the initial temperature inside the PCM. The melting will first take place at the surface of the PCM module (x=0) at certain time ($t=t_m>0$).

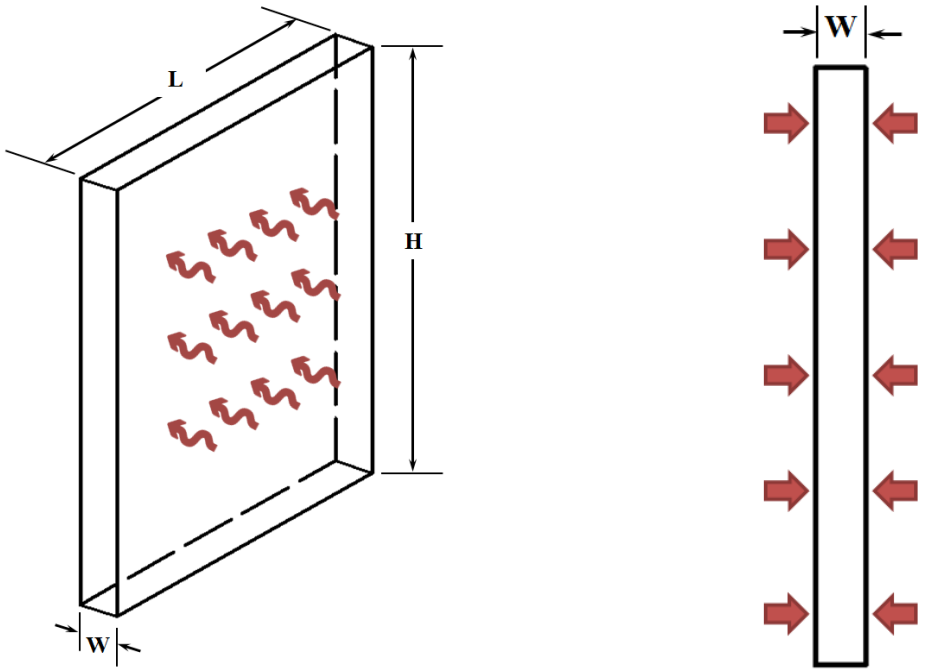

Figure 3.14. Illustration of the dimensions and the heat flow through the rectangular PCM module.

The governing heat transfer equations during different time periods are as follows:

$$\rho c_s \frac{\partial T(x,t)}{\partial t} = k_s \frac{\partial^2 T(x,t)}{\partial x^2}, \quad for\ 0 < x < \frac{W}{2}, 0 < t < t_m\ and$$

$$for\ S(t) < x < \frac{W}{2}, t > t_m \tag{3.35}$$

$$\rho c_l \frac{\partial T(x,t)}{\partial t} = k_l \frac{\partial^2 T(x,t)}{\partial x^2}, \quad for\ 0 < x < S(t), t > t_m \tag{3.36}$$

$$-k_s \frac{\partial T(0,t)}{\partial x} = h_{b-PCM}[T_\infty(t) - T(0,t)], \quad for\ t < t_m \tag{3.37}$$

$$-k_l \frac{\partial T(0,t)}{\partial x} = h_{b-PCM}[T_\infty(t) - T(0,t)], \quad for\ t > t_m \tag{3.38}$$

$$\frac{\partial T(W/2,t)}{\partial x} = 0, \qquad for\ t > 0\ (due\ to\ symmetry) \tag{3.39}$$

$$T(x,0) = T_i(x), \qquad S(t_m) = 0 \tag{3.40}$$

$$T(S(t),0) = T_m, \qquad t > t_m \tag{3.41}$$

$$-k_l \frac{\partial T(S(t),t)}{\partial x} + k_s \frac{\partial T(S(t),t)}{\partial x} = \rho H_f \frac{dS(t)}{dt}, \qquad t > t_m \tag{3.42}$$

where, S(t) represents the melt front location at a given time, t, measured from the surface of the PCM module.

In order to solve these equations simultaneously while marching forward in time, the problem should be split into two distinct problems: a pure heat conduction problem when there is no phase transformation and Stefan problem when phase transformation takes place. The Stefan problem is more difficult to solve due to the geometric nonlinearity; i.e. energy balance equation has to be satisfied at the melt front interface at all times and the location of the interface x=S(t) has to be calculated concurrently.

Front tracking approaches have been developed in order to explicitly track the melt front interface in Stefan problems. One approach uses adaptive time steps in order to align the melt front interface with the grid interfaces (Douglas and Gallie, 1955). The isotherm migration technique (Crank, 1981) fixes the time step while varying the grid spacing to accommodate the progression of the melt front inrerface. All front tracking techniques were found to perform well in simple problems. However, they cannot deal with complications arising in real appliactions such as extreme thermal cycling and multiple melt fronts. As

such, these techniques are unviable as simulation tools for modeling realistic phase change processes.

The enthalpy method, referred to as a volume tracking method, is the only viable method since it bypasses the explicit tracking of the melt front interface. In this approach the jump condition at the interface, Equation (3.42), is automatically satisfied as a natural boundary condition to the problem. This method has many advantages such as being versatile, convenient, adaptable, easily programmable for 1, 2 and 3-dimensional phase-change problems. However, the major drawback of the enthalpy method is that it cannot deal with instabilities associated with the phase transformation processes such as supercooling.

The enthalpy method in 1-D domain. The solution to the enthalpy method is based on the fact that the energy conservation law, expressed in terms of enthalpy and temperature, along with the equation of state contain all the physical information needed to determine the evolution of the phases. Using the control volume approach, the integral of the energy equation for a control volume V over a time step Δt is written as:

$$\int_t^{t+\Delta t} \frac{\partial}{\partial t}\left(\int_V E\, dV\right) dt = \int_t^{t+\Delta t} \int_A -\vec{q}.\vec{n}\, dA\, dt \tag{3.43}$$

where, E=ρe is the enthalpy per unit volume and $-\vec{q}.\vec{n}$ is the net heat flux into the control volume through its boundaries A, where $\vec{n}$ is the unit vector normal to A.

The idea is to discretize the solution domain into finite number of control volumes V_j, and apply the energy conservation equation; Equation (3.43), on each control volume, Figure 3.15.

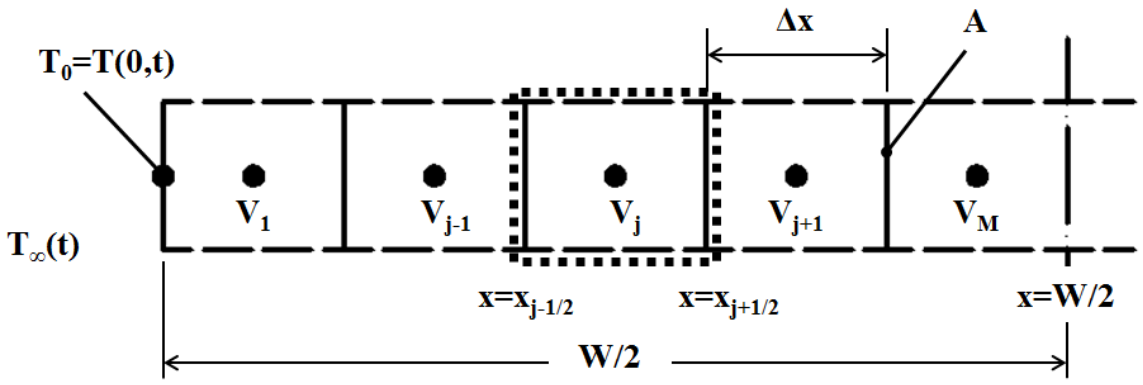

Figure 3.15. 1-D discretization of the PCM. Only half of the domain is shown due to symmetry about the centre-plane of the PCM module.

The equation of state is responsible for identifying the state of the control volume (solid phase, liquid phase or melt interface) based on the value of the enthalpy of the control volume; $E_j \leq 0$ means that V_j is solid, $E_j \geq \rho H_f$ means that V_j is liquid, and $0 \leq E_j \leq \rho H_f$ means that V_j is partly solid and partly liquid (contains a melt front interface). The fraction of the latter control volume that is occupied with liquid can be calculated by:

$$The\ melt\ fraction;\quad \lambda_j = \frac{E_j}{\rho H_f} \tag{3.44}$$

Contrary to the front tracking methods, the enthalpy method utilizes a volume-tracking technique for the melt front interface location by calculating the enthalpy of each control volume in the domain.

In the current study, the PCM 1-D domain extends in the range $0<x<W/2$ as shown in Figure 3.15. the material is initially in the solid phase:

$$T(x,0) = T_i(x) \leq T_m, \qquad 0 \leq x \leq W/2 \tag{3.45}$$

The face x=0 is heated convectively by a fluid at temperature $T_\infty(t) \geq T_m$:

$$q(0,t) = h_{b-PCM}[T_\infty(t) - T(0,t)], \qquad t > 0 \tag{3.46}$$

The face x=W/2 coincides with the symmetry plane:

$$q(W/2,t) = 0, \qquad t > 0 \tag{3.47}$$

The energy integral (Equation 3.43) applied to the control volume $V_j = A \times \Delta x_j$ becomes:

$$\int_{t_n}^{t_{n+1}} \frac{\partial}{\partial t}\left(A \int_{x_{j-1/2}}^{x_{j+1/2}} E(x,t)\, dx \right) dt = -\int_{t_n}^{t_{n+1}} A \int_{x_{j-1/2}}^{x_{j+1/2}} \frac{\partial q(x,t)}{\partial x}\, dx\, dt \tag{3.48}$$

The enthalpy E(x,t) can be represented by the following equation:

$$E(x,t) = \begin{cases} \int_{T_m}^{T(x,t)} \rho c_s dT\,, & T(x,t) \le T_m \ \ (solid\ phase) \\ \int_{T_m}^{T(x,t)} \rho c_l dT + \rho H_f, & T(x,t) \ge T_m \ \ (liquid\ phase) \end{cases} \tag{3.49}$$

The phases are described by:

$$E(x,t) \le 0 \Longrightarrow solid\ phase\ at\ (x,t)$$

$$0 < E(x,t) < \rho H_f \Longrightarrow melt\ front\ interface\ at\ (x,t)$$

$$E(x,t) \ge \rho H_f \Longrightarrow liquid\ phase\ at\ (x,t)$$

For simplicity, c_s and c_l are assumed constants. Therefore, the enthalpy equations reduce to:

$$E(x,t) = \begin{cases} \rho c_s[T(x,t) - T_m], & T(x,t) \le T_m \ \ (solid\ phase) \\ \rho c_l[T(x,t) - T_m] + \rho H_f, & T(x,t) \ge T_m \ \ (liquid\ phase) \end{cases} \tag{3.50}$$

Solving for the temperature, T(x,t):

$$T(x,t) = \begin{cases} T_m + \dfrac{E(x,t)}{\rho c_s}, & for\ E(x,t) \le 0\ \ (solid\ phase) \\ T_m, & for\ 0 < E(x,t) < \rho H_f\ (melt\ front\ interface) \\ T_m + \dfrac{E(x,t) - \rho H_f}{\rho c_l}, & for\ E(x,t) \ge \rho H_f\ \ (liquid\ phase) \end{cases} \tag{3.51}$$

The discretization of the heat fluxes and the boundary conditions yields:

$$T_j^0 = T_i(x), \qquad j = 1, \dots, M \tag{3.52}$$

$$q_{1/2}^{n+\theta} = -\frac{T_1^{n+\theta} - T_\infty^{n+\theta}}{\dfrac{1}{h_{b-PCM}} + R_{1/2}}, \qquad R_{1/2} = \frac{1/2\ \Delta x}{k_1} \tag{3.53}$$

$$q_{M+1/2}^{n+\theta} = 0 \tag{3.54}$$

$$E_j^{n+1} = E_j^n + \frac{\Delta t_n}{\Delta x_j}\left[q_{j-1/2}^{n+\theta} - q_{j+1/2}^{n+\theta}\right], \qquad j = 1, \dots, M \tag{3.55}$$

where,

$$q_{j-1/2}^{n+\theta} = -\frac{T_j^{n+\theta} - T_{j-1}^{n+\theta}}{R_{j-1/2}}, \qquad R_{j-1/2} = \frac{1/2\Delta x_{j-1}}{k_{j-1}} + \frac{1/2\Delta x_j}{k_j}, \qquad j = 2, \dots, M \tag{3.56}$$

$$T_j^n = \begin{cases} T_m + \dfrac{E_j^n}{\rho c_s}, & for\ E_j^n \le 0\ \ (solid\ phase) \\ T_m, & for\ 0 < E_j^n < \rho H_f\ (melt\ front\ interface) \\ T_m + \dfrac{E_j^n - \rho H_f}{\rho c_l}, & for\ E_j^n \ge \rho H_f\ \ (liquid\ phase) \end{cases} \tag{3.57}$$

The melt fraction of the control volume V_j can be defined as:

$$\lambda_j^n = \begin{cases} 0, & for\ E_j^n \le 0\ \ (solid\ phase) \\ \dfrac{E_j^n}{\rho H_f}, & for\ 0 < E_j^n < \rho H_f\ (melt\ front\ interface) \\ 1, & for\ E_j^n \ge \rho H_f\ \ (liquid\ phase) \end{cases} \tag{3.58}$$

The liquid volume in the control volume that has the melt front interface is $\lambda_j^n \Delta x_j A$ and the solid volume is $(1-\lambda_j^n)\Delta x_j A$.

The effective conductivity of the interface control volume is calculated using the harmonic average of the solid and liquid phase thermal conductivities:

$$k_j^n = [\frac{\lambda_j^n}{k_l} + \frac{1-\lambda_j^n}{k_s}]^{-1}, \qquad j = 1, \dots, M \tag{3.59}$$

A fully implicit scheme ($\theta = 1$) is chosen to solve the system of the algebraic equations resulting from the discretization. Introducing a new term:

$$u = T - T_m \tag{3.60}$$

The heat flux $q_{j-1/2}^{n+1}$ can be rewritten as:

$$q_{j-1/2}^{n+1} = \frac{u_{j-1}^{n+1} - u_j^{n+1}}{R_{j-1/2}^{n+1}}, \qquad j = 1, \dots, M \tag{3.61}$$

Therefore,

$$E_j^{n+1} = E_j^n + \frac{\Delta t_n}{\Delta x_j}\left[\frac{1}{R_{j+1/2}^{n+1}} u_{j+1}^{n+1} - (\frac{1}{R_{j+1/2}^{n+1}} + \frac{1}{R_{j+1/2}^{n+1}}) u_j^{n+1} + \frac{1}{R_{j-1/2}^{n+1}} u_{j-1}^{n+1}\right], \qquad j = 1, \dots, M \tag{3.62}$$

The thermal resistances of the boundary nodes j=1 and j=M are adjusted accordingly:

$$u_0 = T_\infty - T_m, \qquad R_{1/2} = \frac{1}{h_{b-PCM}} + \frac{1/2\Delta x_1}{k_1} \tag{3.63}$$

$$u_{M+1} = u_M, \qquad R_{M+1/2} = \frac{1/2\Delta x_M}{k_M} \tag{3.64}$$

The remaining thermal resistances take the standard form:

$$R_{j-1/2} = \frac{1/2\Delta x_{j-1}}{k_{j-1}} + \frac{1/2\Delta x_j}{k_j}, \qquad j = 2, \ldots., M \tag{3.65}$$

$$R_{j+1/2} = \frac{1/2\Delta x_{j+1}}{k_{j+1}} + \frac{1/2\Delta x_j}{k_j}, \qquad j = 1, \ldots., M-1 \tag{3.66}$$

The enthalpy and the normalized temperature u are related by:

$$E(x,t) = \begin{cases} \rho c_s u(x,t), & u(x,t) \le 0 \ \ (solid\ phase) \\ \\ \rho c_l u(x,t) + \rho H_f, & u(x,t) \ge 0 \ \ (liquid\ phase) \end{cases} \tag{3.67}$$

$$u(x,t) = \begin{cases} \dfrac{E(x,t)}{\rho c_s}, & for\ E(x,t) \le 0 \ \ (solid\ phase) \\ 0, \qquad for\ 0 < E(x,t) < \rho H_f\ (melt\ front\ interface) \\ \dfrac{E(x,t) - \rho H_f}{\rho c_l}, & for\ E(x,t) \ge \rho H_f \ \ (liquid\ phase) \end{cases} \tag{3.68}$$

At each time step (Δt_n), the set of algebraic equations, represented by Equation (3.62) at j=1,…,M, are solved iteratively using Gauss-Seidel method. The j-th equation is solved for the j-th unknowns (E_j^{n+1} *and* u_j^{n+1}) using the latest values available for all other variables.

Equation (3.62) can be rewritten for a given time step (Δt_n) as:

$$E_j^{(p+1)} + \frac{\Delta t_n}{\Delta x_j}\left[\frac{1}{R_{j+1/2}^{(p)}} + \frac{1}{R_{j-1/2}^{(p)}}\right] u_j^{(p+1)} = E_j^n + \frac{\Delta t_n}{\Delta x_j}\left[\frac{1}{R_{j+1/2}^{(p)}} u_{j+1}^{(p)} + \frac{1}{R_{j-1/2}^{(p)}} u_{j-1}^{(p+1)}\right] \tag{3.69}$$

The iterations should proceed from p=1, 2, 3,…. until convergence is achieved.

In order to resolve the inherent nonlinearity in Equation (3.69), the equation can be rewritten as:

$$E_j^{(p+1)} + C_j^{(p)} u_j^{(p+1)} = z_j^{(p)}, \qquad j = 1, \dots, M \tag{3.70}$$

where, $C_j^{(p)}$ and $z_j^{(p)}$ are known quantities:

$$C_j^{(p)} = \frac{\Delta t_n}{\Delta x_j}\left[\frac{1}{R_{j+1/2}^{(p)}} + \frac{1}{R_{j-1/2}^{(p)}}\right] \tag{3.71}$$

$$z_j^{(p)} = E_j^n + \frac{\Delta t_n}{\Delta x_j}\left[\frac{1}{R_{j+1/2}^{(p)}} u_{j+1}^{(p)} + \frac{1}{R_{j-1/2}^{(p)}} u_{j-1}^{(p+1)}\right] \tag{3.72}$$

As a result, the solution becomes:

$$u_j^{(p+1)} = \begin{cases} \dfrac{z_j^{(p)}}{\rho c_s + C_j^{(p)}}, & for\ z_j^{(p)} \le 0\ \ (solid\ phase) \\ 0, \qquad for\ 0 < z_j^{(p)} < \rho H_f\ (melt\ front\ interface) \\ \dfrac{z_j^{(p)} - \rho H_f}{\rho c_l + C_j^{(p)}}, & for\ z_j^{(p)} \ge \rho H_f\ \ (liquid\ phase) \end{cases} \tag{3.73}$$

For each iteration, p=1, 2, 3,… the values of $C_j^{(p)}$ and $z_j^{(p)}$ are computed in order to calculate $u_j^{(p+1)}$ for all control volumes j=1, 2,….,M. This process is repeated for the next iteration p until convergence criterion is satisfied:

$$max_{1\le j\le M}\left|u_j^{(p+1)} - u_j^{(p)}\right| < Tolerance \tag{3.74}$$

The initial iteration can assume the old time step values:

$$u_j^{(1)} = u_j^n = T_j^n - T_m \tag{3.75}$$

The boundary value remains fixed during the iteration;

$$u_0^{(n+1)} = T_\infty^{n+1} - T_m \tag{3.76}$$

Upon convergence, the new temperatures are obtained $u_j^{(n+1)} = u_j^{(p+1)}$ from the latest iteration for all j=1,….,M. Then, the new temperatures and enthalpies can be calculated:

$$T_j^{n+1} = u_j^{n+1} + T_m \tag{3.77}$$

$$E_j^{n+1} = z_j - C_j u_j^{n+1} \tag{3.78}$$

The melt fraction values at the new time step can then be calculated using:

$$\lambda_j^{n+1} = \begin{cases} 0, & for\ E_j^{n+1} \le 0\ \ (solid\ phase) \\ \dfrac{E_j^{n+1}}{\rho H_f}, & for\ 0 < E_j^n < \rho H_f\ (melt\ front\ interface) \\ 1, & for\ E_j^n \ge \rho H_f\ \ (liquid\ phase) \end{cases} \tag{3.79}$$

Figure 3.16 shows the flow chart that depicts the solution procedure of the temperature and melt fraction profiles inside the PCM module.

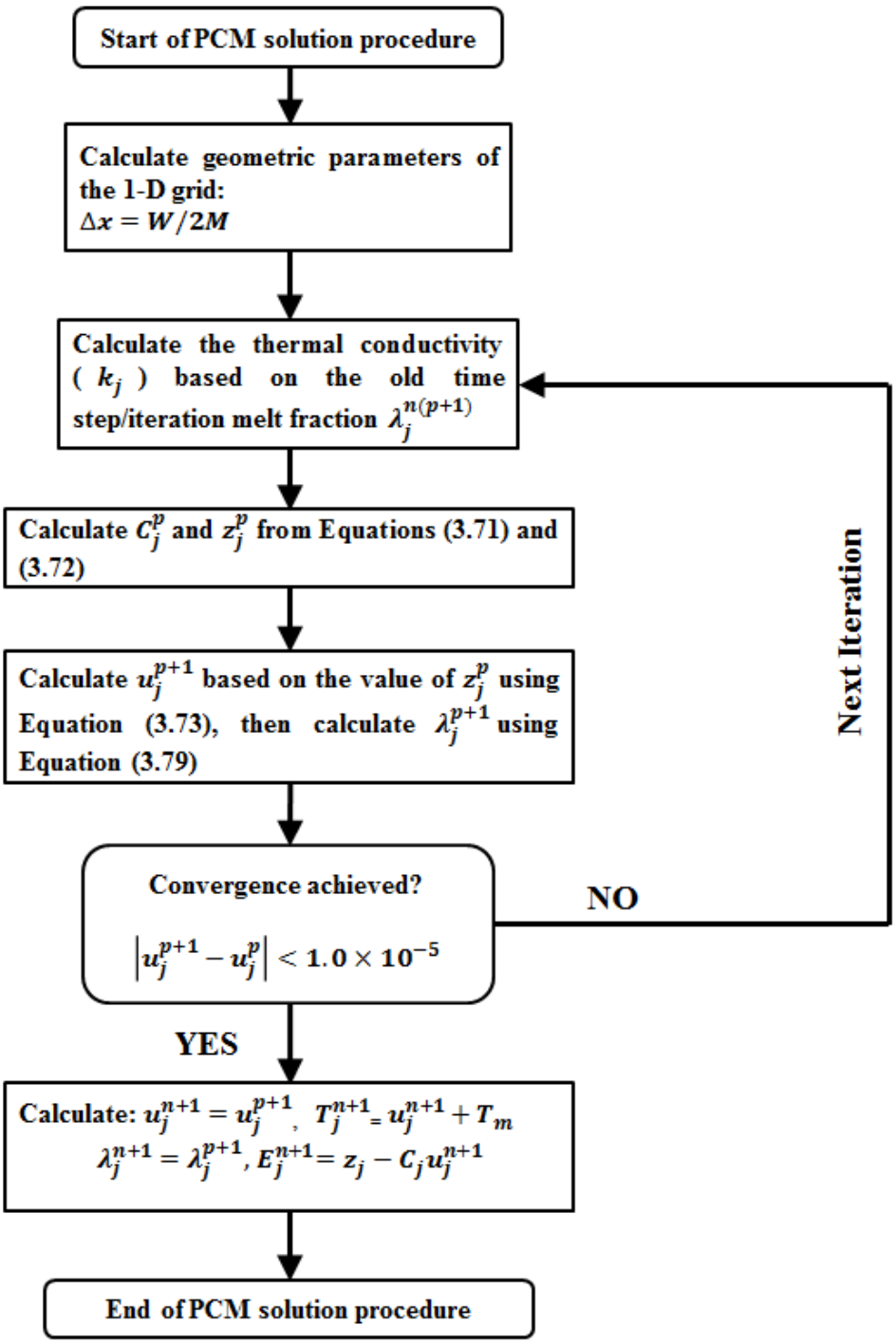

Figure 3.16. Flow chart that depicts the solution procedure of the heat transfer model into the PCM modules.

3.4. Thermal Behavior of Multi-tank HTES

Consider the three-tank HTES system shown in Figure 3.17. Each tank contains PCM modules with different geometric and thermophysical parameters submerged in water. As illustrated in the thermal behavior of the single-tank storage, the proposed design acts to store energy during the charging process from the bottom coil heat exchanger, in the tank with the right energy level. The thermal diode effect helps to bypass the tanks with temperature higher than the inlet HTF which minimizes the exergy destruction due to tank-to-tank mixing.

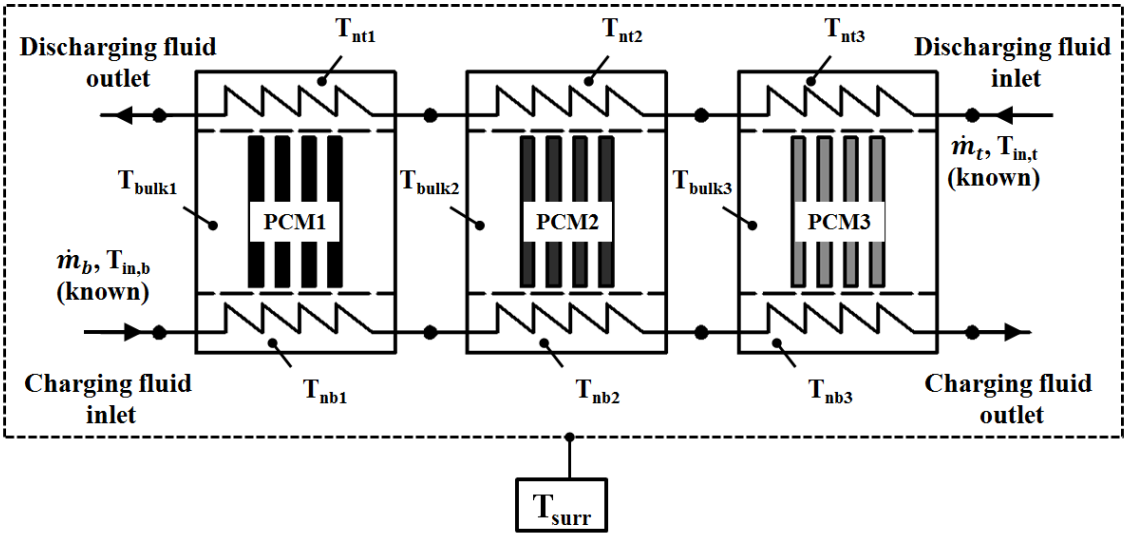

Figure 3.17. Basic components of a three-tank HTES system.

As such, sequential stratification is established among the series of tanks where the first tank becomes the hottest and the last tank becomes the coldest. It is clear that the best configuration for the discharging coil heat exchanger is in the counter direction of the charging coil heat exchanger. The discharging HTF flows from the coldest tank towards the hottest tank. This results into maximum energy extraction from the storage during the periods when the energy demand exceeds the energy supply.

3.5. Mathematical Modeling of Multi-tank HTES

The thermal behavior of the proposed design of the multi-tank storage with and without the PCM can be simulated by coupling the performances of the individual tanks. As shown in Figure 3.17, the inputs to the multi-tank system are the mass flow rate entering the top and bottom heat exchangers ($\dot{m}_b$ and $\dot{m}_t$), the inlet temperatures of the HTFs entering the top and bottom heat exchangers ($T_{in,b}$ and $T_{in,b}$) and the temperature of the system's surrounding (T_{surr}). the key parameters of the system include the number of tanks, the dimensions of each tank, the heat transfer coefficient for the thermal losses, the position and geometric parameters of the coil heat exchangers (such as length, internal and external diameters, etc.).

To simplify the implementation of the model, a number of assumptions were applied:

1. All the thermal properties of the storage medium are assumed constants and independent of the temperature. The properties are chosen by the user at an appropriate average temperature based on the application.
2. Thermal expansion and contraction of the storage medium are assumed negligible.

3.5.1. Solution Procedure

At the beginning of each time step, only the two temperatures at the inlets to the top and bottom heat exchangers are known. The remaining temperatures at the inlets to the intermediate tanks are not known. All the temperatures are needed to calculate the heat transfer rates from the heat exchangers in each tank to solve the energy balance equations. In order to accelerate the solution of the multi-tank model, time lagging method is applied where the old time step temperatures of the nodes of each tank are assumed to prevail over

the current time step. This alleviates the solution of the heat exchanger model inside each tank to calculate the heat transfer rates and the outlet temperatures needed for the next time step. Equation (3.5) can be solved using the implicit time scheme:

$$T_i^{n+1} = T_i^n + \frac{\Delta t_n}{M_i c}[\dot{m}C(T_{i-1}^{n+1} - T_i^{n+1}) - (UA)_i^{n+1}(T_i^{n+1} - T_\infty^n)], \qquad i = 1, \dots, N \tag{3.80}$$

The temperature at the inlet to the heat exchanger is known ($T_0^{n+1} = T_{in}^{n+1}$) and the value of T_∞^n represents the old time step value of the thermal node in the tank that contains the heat exchanger. Gauss-Seidel iterative method is used to solve the system of algebraic equations until convergence. The convergence criteria are set to:

$$max_{1\le i\le N}\left|\frac{T_i^{(p+1)} - T_i^{(p)}}{T_i^{(p)}}\right| < 1.0 \times 10^{-3}, and$$
$$max_{1\le i\le N}\left|\frac{Q_i^{(p+1)} - Q_i^{(p)}}{Q_i^{(p)}}\right| < 1.0 \times 10^{-3} \tag{3.81}$$

The solution of the heat exchanger model yields the outlet temperature (T_N^{n+1}) and the heat transfer rate from the heat exchanger:

$$Q_{coil}^{n+1} = \sum_{i=1}^{N}(UA)_i^{n+1}(T_i^{n+1} - T_\infty^n) \tag{3.82}$$

Figure 3.18 shows the flow chart that depicts the solution procedure of the heat exchanger equations.

The coupling between the series of tanks is applied by equating the outlet temperature of each tank to the inlet of the following tank. As such, the heat exchanger model can be solved in all of the tanks simultaneously.

The heat transfer rates calculated to or from the heat exchangers are then used in the energy balance equations of the heat exchanger nodes in the tanks to update their temperatures. These equations are solved explicitly in time.

$$T_{nb}^{n+1} = T_{nb}^{n} + \frac{\Delta t_n}{M_{nb} c_w} [Q_{coil,b}^{n} + Q_{diff,bulk-nb}^{n} - Q_{loss,nb}^{n}] \tag{3.83}$$

$$T_{nt}^{n+1} = T_{nt}^{n} + \frac{\Delta t_n}{M_{nt} c_w} [Q_{coil,t}^{n} + Q_{diff,bulk-nt}^{n} - Q_{loss,nt}^{n}] \tag{3.84}$$

$$T_{bulk}^{n+1} = T_{bulk}^{n} + \frac{\Delta t_n}{M_{bulk} c_w} [-Q_{diff,bulk-nb}^{n} - Q_{diff,bulk-nt}^{n} - Q_{bulk-PCM}^{n} - Q_{loss,bulk}^{n}] \tag{3.85}$$

The heat transfer by diffusion between adjacent nodes ($Q_{diff,bulk-nb}^{n}$ and $Q_{diff,bulk-nt}^{n}$) and the heat losses from the tanks to the surrounding ($Q_{loss,nb}^{n}$, $Q_{loss,nt}^{n}$ and $Q_{loss,bulk}^{n}$) are substituted for using the old time step values. The mixing algorithm is then activated to allow for mixing between the nodes with negative vertical temperature gradient.

In order to simulate the performance of the multi-tank SHS system with no PCM, the same procedure is followed with the omission of the heat transfer rate from the bulk node into the PCM modules ($Q_{bulk-PCM}$). Figure 3.19 illustrates the flow diagram depicting the solution procedure for the multi-tank HTES model.

3.6. Implementation of the Model

The mathematical models of the multi-tank SHS and HTES systems were programmed in FORTRAN 95. In Chapter Five, extensive verification and validation of the mathematical model components were undertaken. The component models were verified against benchmark analytical solutions in order to ensure the ability of the model to capture the physical behavior of the different components of the storage tank. In addition, the integrated model was validated against the experimental results obtained from the lab tests conducted on the single-tank SHS and HTES. Chapter Six presents the numerical simulations of the performance of the single and multi-tank storage in realistic operation of solar DHW systems. The specific details of the implementation of the models are discussed in those chapters.

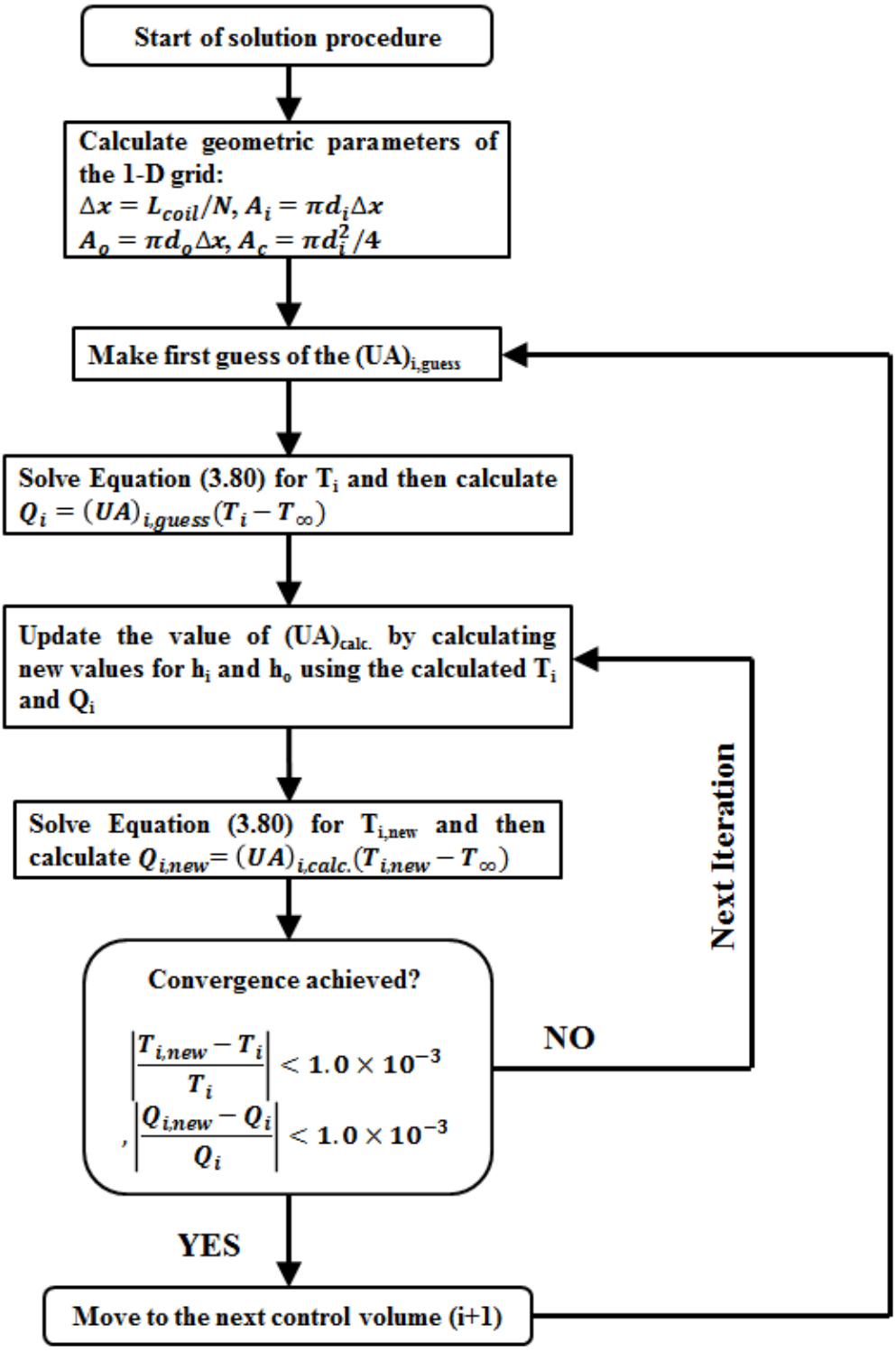

Figure 3.18. Flow chart that depicts the solution procedure of the heat exchanger equations.

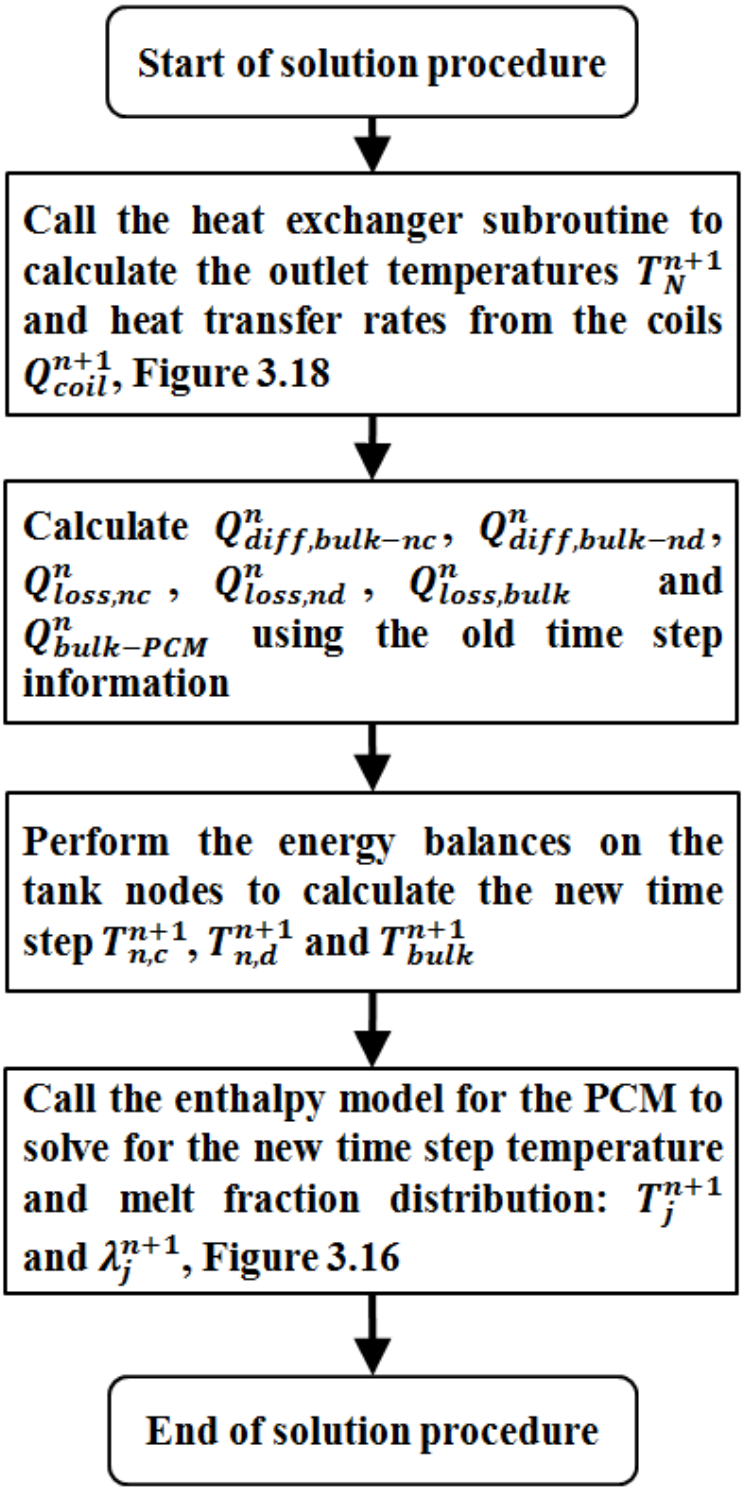

Figure 3.19. Flow chart that depicts the solution procedure of the mathematical model.

CHAPTER FOUR

EXPERIMENTAL FACILITY AND TEST MATRIX

4.1. Introduction

An experimental test facility was designed and constructed in order to provide experimental data for validation of the mathematical modelling. As described in the previous chapter, the performance of the multi-tank storage system can be simulated by coupling individual tanks together through the bottom and top heat exchangers. As such, the validation of the mathematical model can be carried out by conducting experiments on a single storage tank. The test matrix was designed such that different operation scenarios are examined. These scenarios included fixed/variable inlet temperatures to the top and bottom heat exchangers as well as sequential/simultaneous charging and discharging processes. Also, the experiments focused on testing the interesting thermal behaviors expected from the proposed design of the storage tank with and without the PCMs. The mathematical model can be considered validated if it can capture the important physical phenomena that take place inside the storage tank such as thermal mixing and thermal dioding.

A series of twelve experiments were designed to (1) demonstrate the thermal behavior of the proposed design of the single-tank SHS and HTES systems, and (2) provide data for validation of the mathematical model of the single and multi-tank SHS and HTES systems. Both simplistic and realistic operating conditions were considered. The experimental facility consisted primarily of four main components: (1) a heat source that acts as the energy supply,

(2) a heat sink that acts as the energy demand, (3) the storage element, and (4) the measurement instrumentation and the data acquisition system. The heat source is a 30-kW_e (approximately 90 kW_{th}) gas turbine equipped with a gas-to-water heat recovery unit. The heat sink is a 5-kW deionized water chiller. The storage element is a 200-L square tank equipped with two immersed coil heat exchangers. A racking system was designed to support rectangular PCM modules inside the tank for HTES testing.

Experimental testing required temperature and flow rate measurements in order to monitor the heat flows and analyze the energy balance through the storage tank. A data acquisition (DAQ) system was installed and programmed to collect the temperature and the flow rate measurements. Calibrations of the measurement instruments were performed and uncertainty analysis was done to illustrate the error propagation to the derived variables. Appendix D presents the details of the calibration procedure and the uncertainty analysis.

Worth mentioning is the fact that the operation of the gas turbine was difficult to automate and required continuous presence of the researcher during the whole time of testing. This imposed some limitations on the length and complexity of the test procedure that could be performed.

This chapter describes the equipment and the testing procedure that were used to carry out the experiments on the single-tank SHS and HTES. Also, the experimental test matrix designed to illustrate the thermal behavior of the storage component is presented. The results from the experiments are presented along with the model predictions in Chapter Five.

4.2. Experimental Testing Facility

The general layout of the test facility is shown in Figures 4.1-4.3. The testing facility can be divided into three main components: (1) the heat source which is used to provide the

storage tank with the hot fluid, (2) the heat sink which is responsible for providing the storage tank with cold fluid, (3) the storage component which consists of the storage tank, the top and bottom coil heat exchangers and the PCM modules, and (4) the measurement instrumentation and the DAQ system for data collection.

4.2.1. Heat Source

The heat source consists of a Capstone MicroTurbine (Model C30 - https://www.capston-e-turbine.com/products/c30). It is a natural-gas operated gas turbine that can produce up to 30-kW_e. The turbine is equipped with a control system that allows varying the output electrical power between 0 and 30 kW_e via a LabVIEW interface program. At its rated power, the gas turbine operates with an efficiency of 25±2%. This would result in thermal energy available in the exhaust of the turbine of 90 kW_{th} ±8%. The exhaust gas temperature can reach up to 275°C depending on the inlet air temperature, the back pressure on the turbine and the quality of fuel combustion. The exhaust system of the gas turbine is equipped with a gas-to-liquid heat recovery unit to allow for waste heat recovery research work. An exhaust heat recovery silencer radial (HRSR series from Cain Industries "Model Serial Number: 5771" - http://www.cainind.com-/cain_cat_cogenera-tion.php) is used as a cross-flow heat exchanger between the exhaust gas in the shell and a coolant flowing through a bundle of finned tubes, "Cain HX" in Figures 4.1-4.3. The design of the heat exchanger is equipped with a by-pass valve that is meant to control the amount of exhaust gas flowing through the heat recovery unit between 0-100 percent. A Honeywell micro-processor based stand-alone controller (Model: UDC2500 - https://www-.honeywellprocess.com/library-/marketing/tech-specs/51-52-03-36.pdf) is integrated with the heat exchanger to monitor and control the inlet temperature of the coolant side of the heat exchanger. The controller was

auto-tuned to maintain the set-point temperature within ±0.5°C. The maximum temperature at the inlet was set to 80°C to avoid boiling inside the finned tubes of the heat exchanger.

The liquid side of the heat exchanger was filled with water from the chilled water supply lines managed by the facility services at McMaster University. A sample of the water was subjected to a blowdown test at the MRCMS at McMaster University and was found to consist of 99.6% water and 0.4% rust inhibitors. The water loop was kept pressurized at 55 psi and an expansion tank was used to mitigate the thermal expansion inside the loop. A vertical multi-stage centrifugal pump (Goulds e-SV series - http://goulds.com/centrifugal-pumps-boosters/multi-stage-pumps/esv-series/#product-tab-overview) is installed at the inlet of the heat exchanger to circulate the water through the whole loop. A plate heat exchanger is integrated between the water loop of the heat exchanger and a branch from the chilled water supply line. The chilled water line provides continuous supply of chilled water at approximately 5°C. A globe valve "GV-3" is used to control the flow rate of the chilled water through the plate heat exchanger. The plate heat exchanger acts as a heat sink for the hot water from the heat exchanger in order to assist in regulating the set-point temperature. The storage tank is connected in series with the supply line of hot water exiting the heat exchanger and upstream of the plate heat exchanger. A by-pass ball-type valve "BV-3" is installed between the side branches to the storage tank in order to control the flow rate of the hot water from the heat exchanger loop into the immersed coil heat exchanger inside the tank.

4.2.2. Heat Sink

A water chiller (Kodiak Recirculating Chillers, Lytron Inc., Model: RC045 - http://ww-w.lytron.com/Cooling-Systems/Standard/Recirculating-Chillers/Kodiak) is used as

the source of cold fluid to the storage tank. The chiller has a cooling capacity of 5.9 kW and it can control the temperature of the coolant in the range of 5-35°C with a temperature stability of ±0.1°C. Deionized water was used inside the chiller as the working fluid. The flow rate of the deionized water from the chiller is controlled with a two 1/2-inch globe valves. One valve is used as a primary flow regulator "GV-4" and the other is a bypass valve (not shown in the figures) that acts to provide fine tuning on the flow rate.

4.2.3. Storage Tank

Storage tank. The thermal storage tank was fabricated from 11-gage 304-stainless steel sheets. Four 21×34-inch sheets were welded together to form the side walls of the tank. A 21×21-inch sheet was welded to form the bottom of the tank. The final dimensions of the tank are 0.527×0.533×0.860 m. Four 3/4-inch stainless steel angles were welded to the rim of the tank and then four 1/4-inch holes were drilled and tapped for the lid-alignment bolts. Another 22.5×22.5-inch sheet was used as a lid. Two handles were attached to the lid and four 1/4-inch holes were drilled for alignment with the tank. When filled with 200 L of water, the height of the water column inside the tank is 0.72 m. A 1-inch hole is drilled at the bottom of the tank and a stainless steel ball valve is installed for tank draining. Figure 4.4 illustrates a schematic of the storage tank filled with water only. The basic components and dimensions of the tank are shown in the figure. Figure 4.5 presents the storage tank design including the PCM modules and support rack.

Two types of insulation were used to reduce the thermal losses from the tank to the surroundings. The sides were wrapped in a flexible, 102 mm (4 inch) thick, RSI 2.55, fiberglass insulation with aluminum foil facing. The top and bottom surfaces of the tank were insulated with 51 mm (2 inch) thick, RSI 1.8, styrofoam sheets.

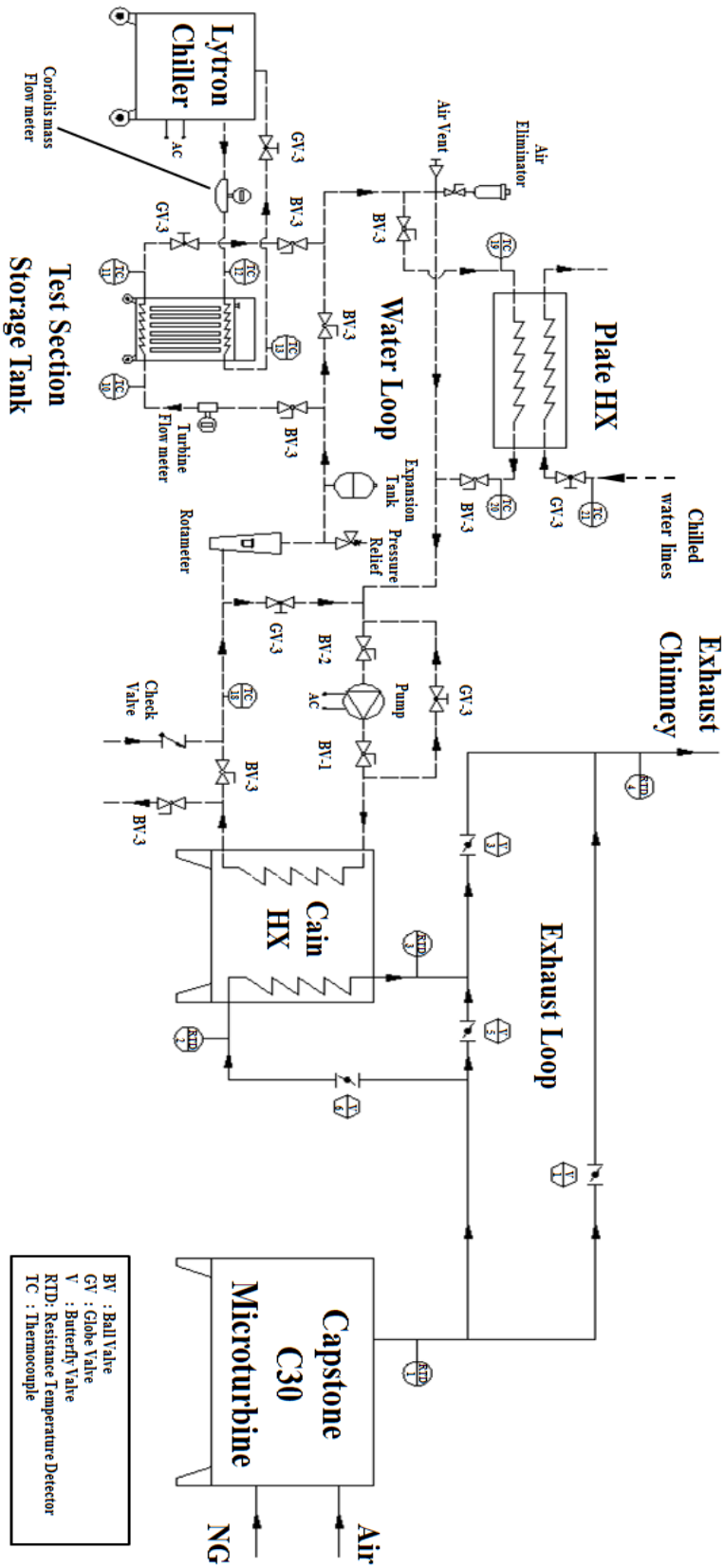

Figure 4.1. Layout of the experimental test facility.

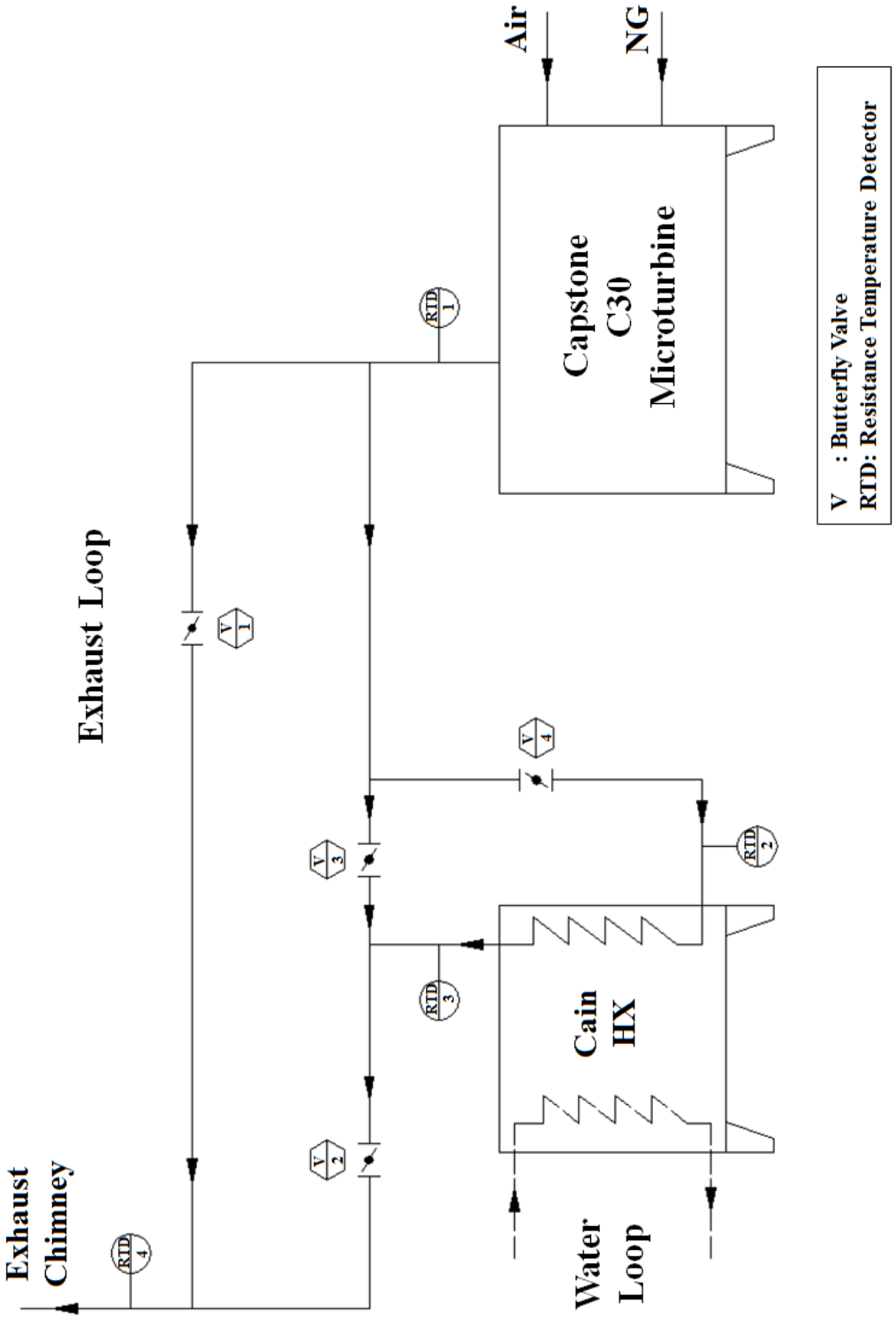

Figure 4.2. Layout of the exhaust loop in the experimental test facility.

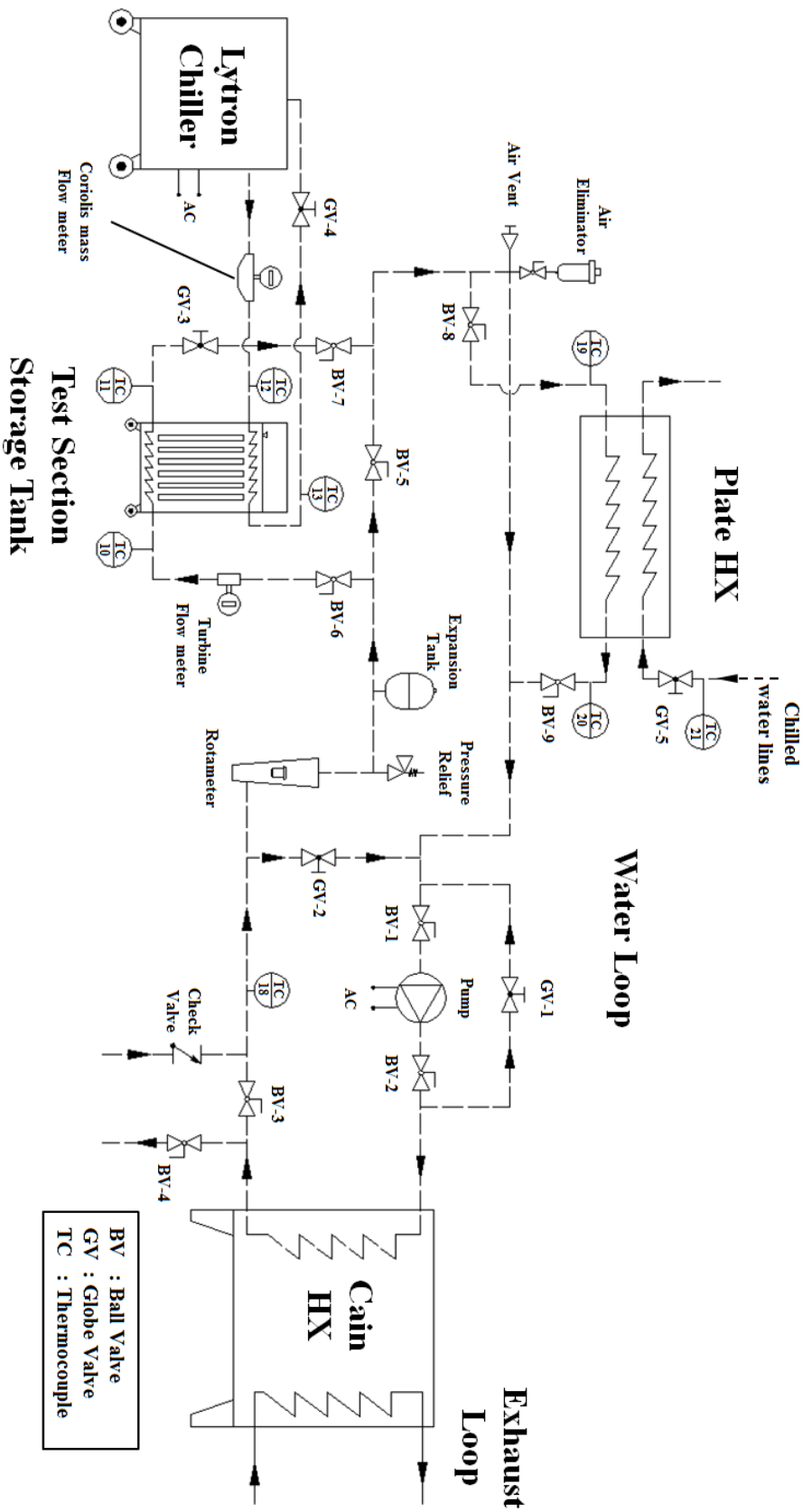

Figure 4.3. Layout of the water loop in the experimental test facility.

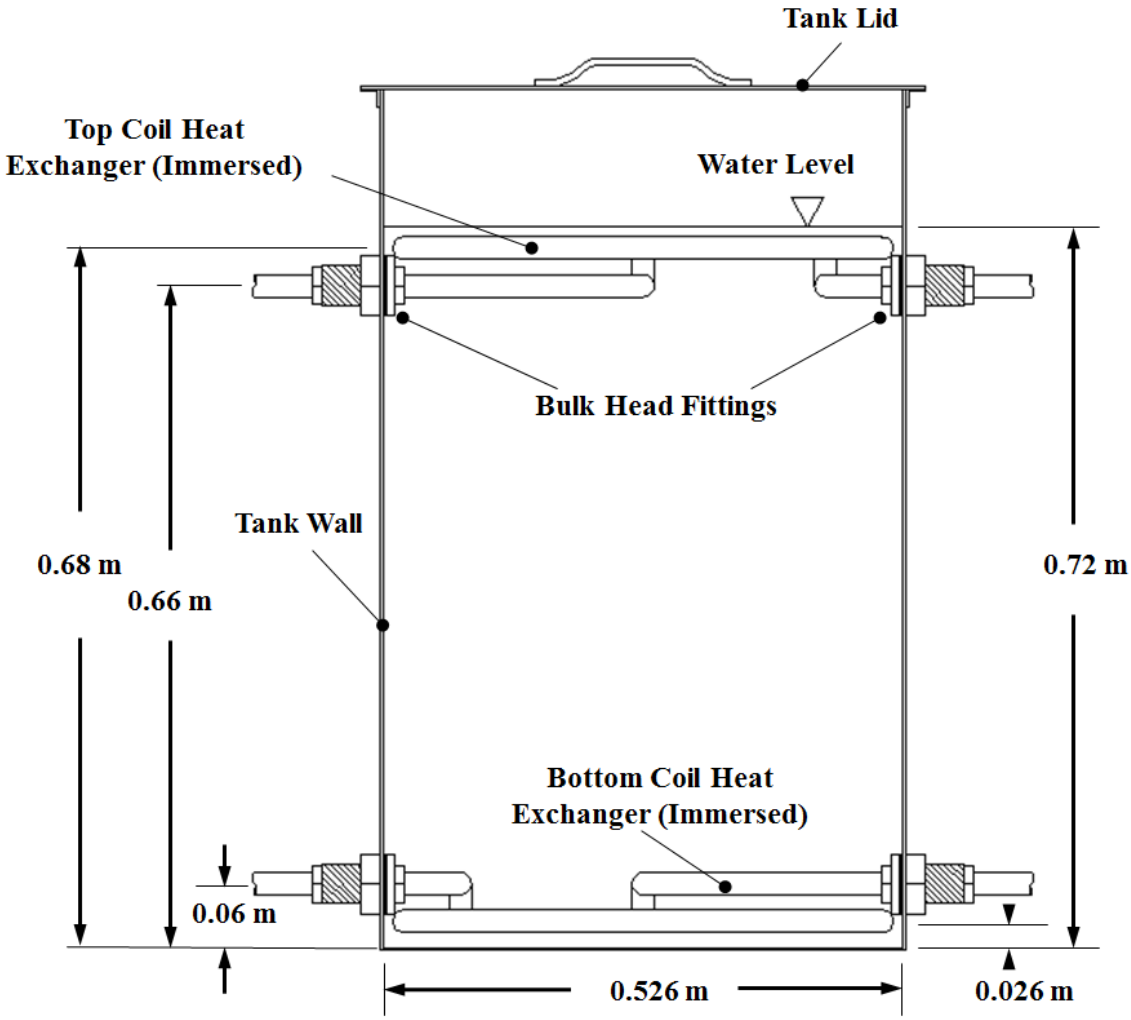

Figure 4.4. Layout of the storage tank with water only illustrating the basic dimensions of the tank and the immersed coil heat exchangers.

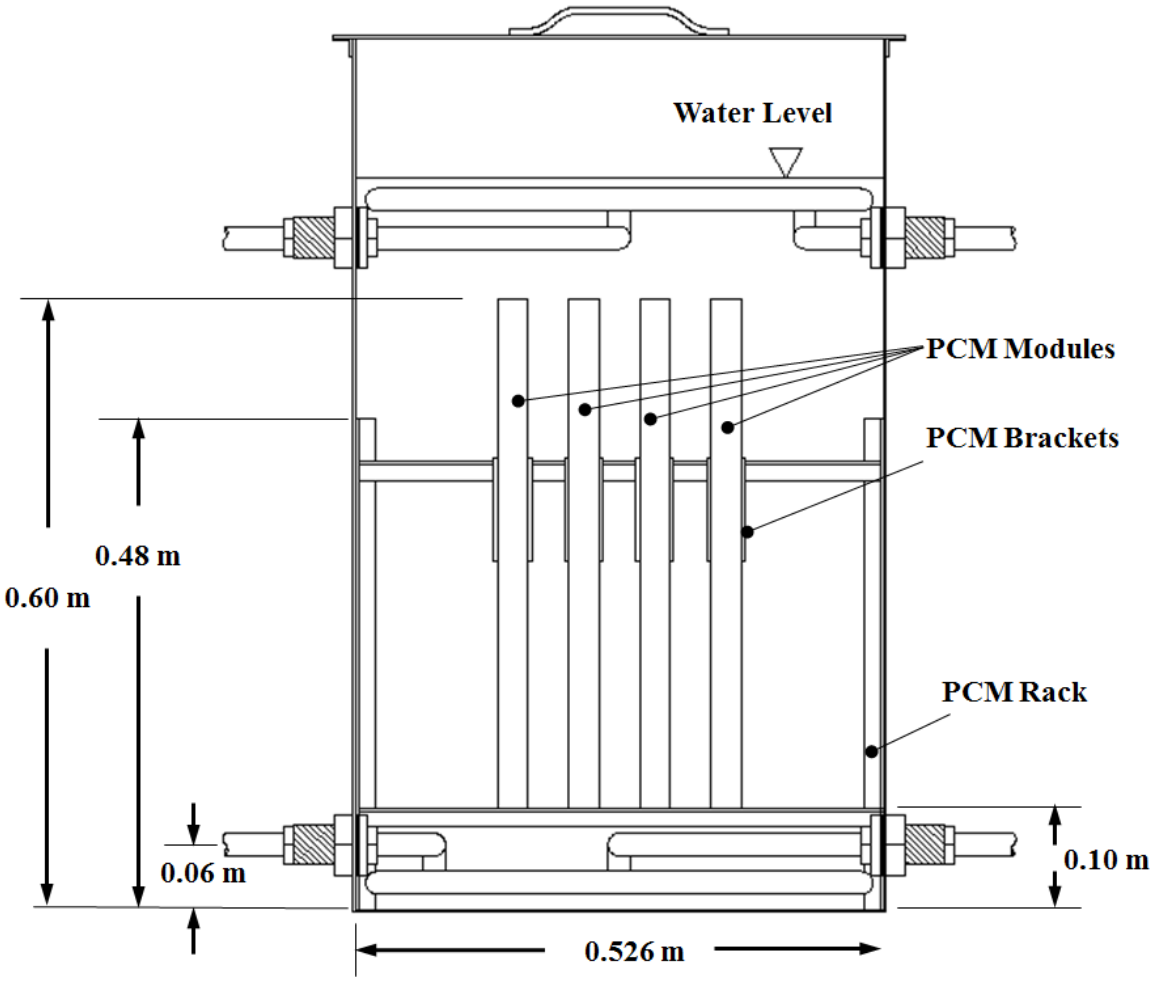

Figure 4.5. Layout of the storage tank with water and PCM modules illustrating the PCM support rack.

Immersed Coil Heat Exchangers. Two identical immersed coil heat exchangers were installed inside the storage tank, one near the bottom and the other near the top. Each heat exchanger was constructed by soldering copper pipes, with inner diameter of 19.5 mm (3/4 inch) and outer diameter of 22.2 mm (7/8 inch), to form a square spiral coil. The total length of each coil was 7.5 m and it consisted of five and a half turns with a center-to-center spacing between each turn of approximately 32 mm. Six 15-mm thick acrylic spacers were used to maintain the bottom heat exchanger 26 mm from the bottom of the tank. The top heat

exchanger was installed 0.68 m from the bottom of the tank. It was levelled horizontally and supported by linen strings. Figure 4.6 shows the design of the square-spiral coil.

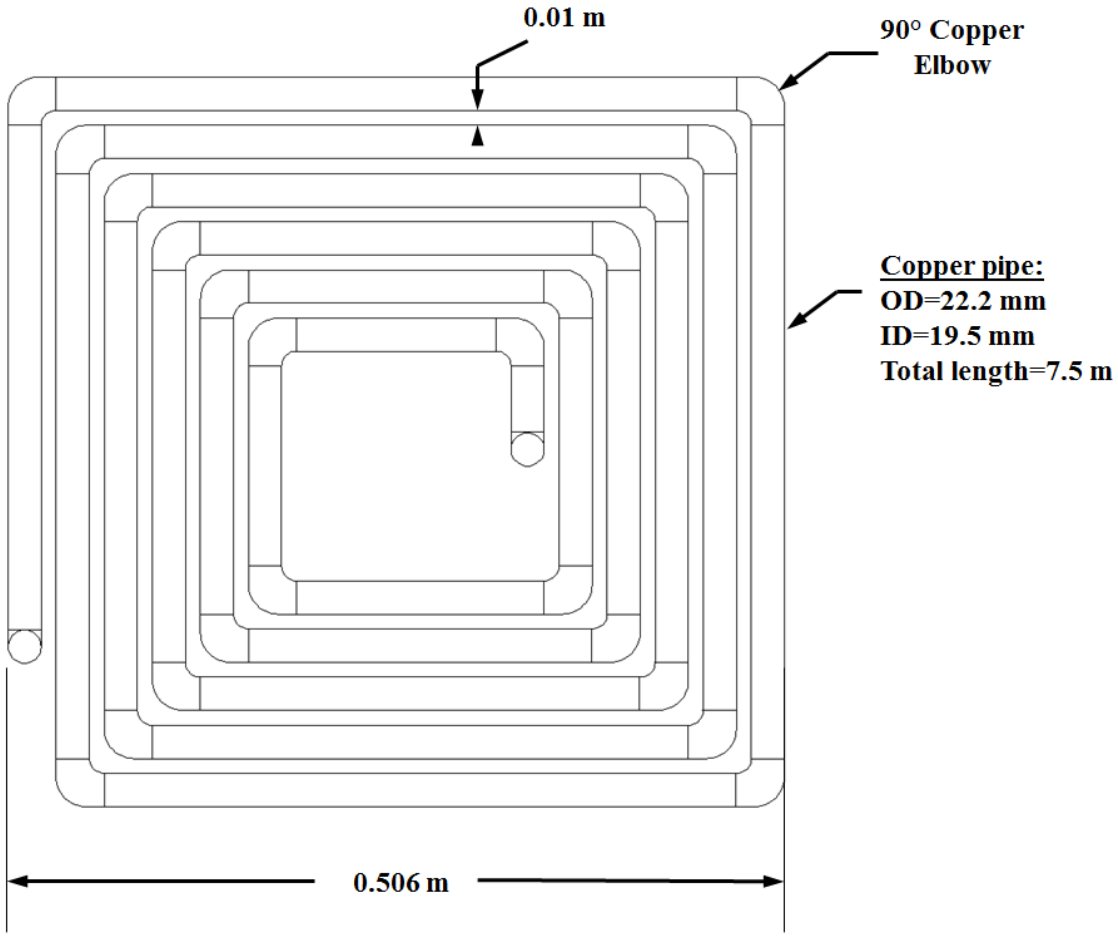

Figure 4.6. Schematic of the design of the square-spiral coil illustrating basic dimensions.

Four holes were drilled in the tank walls to fit four 1-inch bulk head fittings. Fittings were used to connect the coil heat exchangers inside the tank with the piping system outside. The hot water coming from the heat recovery heat exchanger was transferred primarily through a high temperature 1/2-inch hose to 1/2-inch Y strainer (Mesh 100). The strainer was plumbed upstream of a turbine flow meter which was connected to the inlet of the bottom heat exchanger. The exit of the bottom heat exchanger is connected to a 3/4-inch globe valve

for flow regulation. High temperature hose connects the valve back to the heat recovery heat exchanger loop. The cold water coming from the chiller to the top coil heat exchanger inside the tank was transferred primarily through a PVC hose. A Coriolis mass flow meter was installed upstream of the inlet to the top heat exchanger. The return from the coil heat exchanger to the chiller flowed through a PVC hose. Foam pipe wrap (RSI 0.9-0.97) was used to thermally insulate the pipe work in the vicinity of the storage tank.

PCM Modules. A stainless steel rack was designed and constructed to support the PCM modules inside the storage tank during the hybrid storage experiments. The PCM module consisted of two rectangular high density polyethylene (HDPE) containers originally manufactured for ice packs (https://czjisi.en.alibaba.com/product/605713-57593-803686568/Cold_chain_equipment_gel_box_cooler.html). Each container was manufactured by blow molding into a rectangular shape with dimensions of 0.515×0.205×0.03 m. Schematics of the containers are shown in Figure 4.7. The wall thickness of the container was approximately 3 mm. The container had one opening for filling and draining, approximately 30 mm in diameter. A polyethylene plug was used to close the module. A single PCM module was created by attaching two containers together as shown in Figure 4.8. Four brackets made of 1/16-inch thick aluminum sheets were used to join and support the two containers. Aluminum angles were riveted to the side brackets, with a 1/4-inch slot machined on the horizontal leg of the angle to allow for a guide 1/4-inch bolt and nut to fasten the module to the rack through the rail. Figure 4.9 shows the assembly of the PCM modules on the support rack.

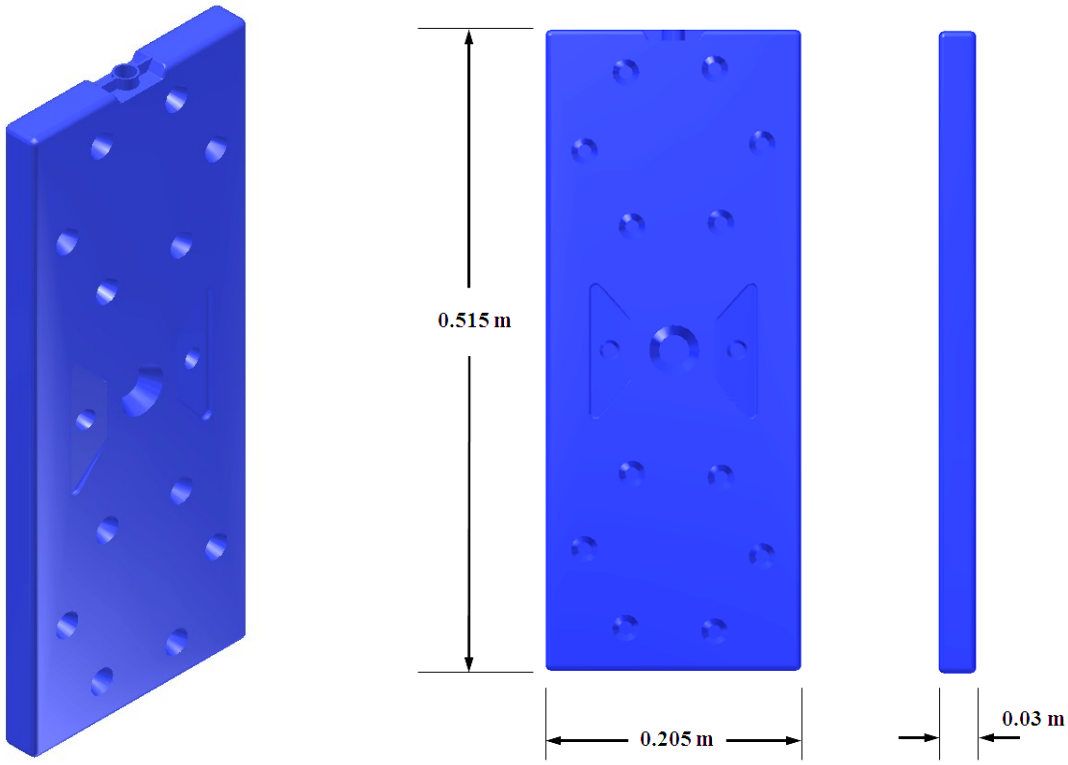

Figure 4.7. Schematic of the PCM container demonstrating basic dimensions.

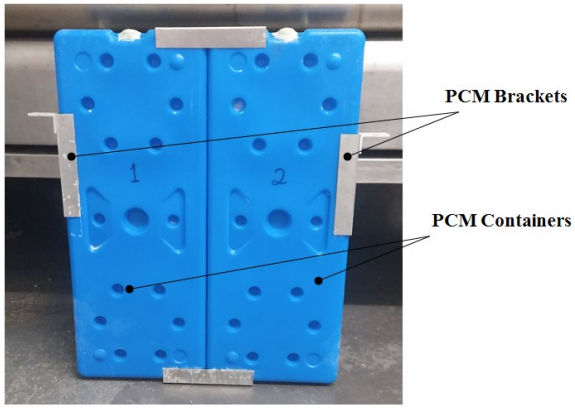

Figure 4.8. Layout of the PCM module consisting of two containers held together by the aluminum brackets.

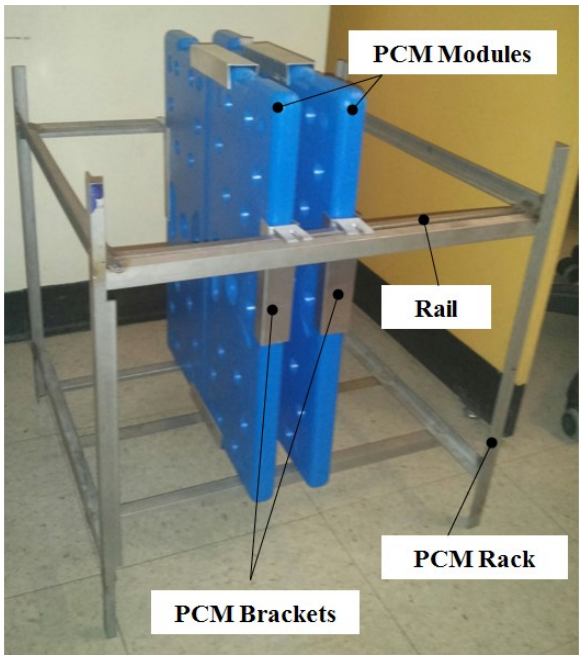

Figure 4.9. Assembly of the PCM modules on the support rack. The side brackets are fastened to the rail to adjust the PCM module spacing.

Twenty containers were chosen for the experimental tests. According to the manufacturer, the volume of each container was 2600 ml. Simple tests were carried out on each container to measure the internal and the total volumes of the container. First, all the containers were weighed empty using a scale with accuracy of ±1 g. The average mass of the empty containers was found to be 497 g with a standard deviation of ±3 g. Second, the containers were filled with tap water and then weighed. The temperature of the water inside the containers was recorded right before the weighing to estimate the water density. The average mass of the modules filled with water was found to be 2889 g with a standard deviation of ±5 g. Third, the average internal volume of the containers was calculated to be 2396 ml with a standard deviation of ±7 ml. Assuming the density of the HDPE is approximately 970 kg/m^3, the total volume was then calculated to be 2908 ml with a standard deviation of ±5 ml.

Phase Change Material (PCM). Dodecanoic acid (a.k.a. Lauric acid) was used as the latent energy storage medium during the experiments and was supplied by Sigma Aldrich Canada (http://www.sigmaaldrich.com/catalog/product/aldrich/w261408?lang=en&region=-CA). Lauric acid lies under the family of organic fatty acids which are characterized by considerably high latent heat of fusion (~180 kJ/kg) and narrow temperature range of phase transformation (~42-44 °C). The thermophysical properties of the Lauric acid were extracted primarily from Yaws' handbook of thermodynamic and physical properties of chemical compounds (Yaws and Gabbula, 2003). Table 4.1 illustrates the temperature correlations provided for various thermophysical properties of the Dodecanoic (Lauric) acid.

Table 4.1. Thermophysical properties of the Dodecanoic (Lauric) acid.

Property (symbol)	**Value or temperature correlation (temperature in Kelvin) (Yaws, 2003)**	**Unit**
Melting temperature (T_m)	41-44	°C
Heat of fusion (H_f)	181.2	kJ/kg
Liquid density (ρ_l)	$284.2 * 0.266^{-(1-T/734)^{0.293}}$	kg/m^3
Liquid specific heat capacity (c_l)	$253.598 + 11.272 * T - 0.0248 * T^2 + 2.186 \times 10^{-5} * T^3$	J/kg.K
Liquid thermal conductivity (k_l)	$0.163 + 1.922 \times 10^{-5} * T - 2.107 \times 10^{-7} * T^2$	W/m.K
Liquid viscosity (μ_l)	$\frac{10^{(-8.602+1871.3T^{-1}+0.0152*T-1.2\times10^{-5}*T^2)}}{1000}$	Pa.s
Liquid expansion coefficient (β_l)	$5.299 \times 10^{-4} * (1 - T/734)^{-0.707}$	K^{-1}
Solid specific heat capacity (c_s)	$1.011 \times 10^3 - 5.612 * T + 0.0321 * T^2$	J/kg.K

Note that Yaws' handbook did not provide data on the density and thermal conductivity of the Lauric acid in the solid state. Lutton (1967) reported that the density of Lauric acid in solid state at 25°C is 1007 kg/m^3 (Lutton, 1967). In the same reference the latent heat of fusion was reported in the range 177.4-178 kJ/kg. The thermal conductivity of the Lauric acid in the solid state was stated as 0.44 W/m.K (Mezaki *et al*., 2000).

Table 4.2 demonstrates the range of all the available thermophysical properties of the Lauric acid in the temperature range from 20 – 60°C, corresponding to the temperature range within which the experiments were carried out. The last column presents the percent deviation of the property value between the two temperatures.

Table 4.2. Variability of thermophysical properties of the Dodecanoic (Lauric) acid.

Property	**Value at T = 20°C**	**Value at T = 60°C**	**% deviation from value at 60°C**
Density (ρ)	1007* (kg/m^3)	862.9 (kg/m^3)	+16.7%
Specific heat capacity (c)	2.13 (kJ/kg.K)	2.06 (kJ/kg.K)	+3.4%
Thermal conductivity (k)	0.44* (W/m.K)	0.15 (W/m.K)	+193.3%
Liquid dynamic viscosity (μ)	----	$0.81\text{-}0.56\times10^{-2}$ (Pa.s)**	----
Liquid Expansion coefficient (β)	----	$0.79\text{-}0.81\times10^{-3}$ (K^{-1})**	----

* These values were reported for the solid phase without reference to a specific temperature.
** The values are presented for liquid phase in the temperature range: 44 (melting temperature) – 60°C.

The Lauric acid was provided by the supplier in the form of solid flakes packaged in plastic buckets. The following procedure was undertaken to fill twenty HDPE containers with the Lauric acid:

1. Sixteen 1000-ml Pyrex glass beakers were filled with solid flakes of the Lauric acid as received from the supplier.
2. The filled beakers were placed in a temperature-controlled oven and kept at 70°C for a minimum of 10 hours.
3. The empty HDPE containers were submerged in a constant-temperature water bath maintained at approximately 55°C.
4. Each beaker, filled with liquid Lauric acid at 70°C, was weighed before and after pouring the liquid into the HDPE containers.
5. Each container was filled until the top, then was closed by a plug and left to cool down in the ambient air.
6. The time spent to fill each container never exceeded 10 minutes.

7. After cooling down, each container was weighed with accuracy of ±1 g.

The average mass of the PCM in the containers was calculated from the difference of the weight of the beakers before and after pouring into the container and was found to be 2091 g with a standard deviation of ±14 g. Similar result was found from the difference between the weight of the PCM container before and after filling with Lauric acid. The average mass of the PCM in the containers was found to be 2096 g with a standard deviation of ±12 g.

Water. Tap water was used in the experiments as the sensible heat storage medium. The properties of water in the temperature operation range were evaluated using NBS/NRC steam tables (Haar, 1984). These tables were also used to evaluate the thermophysical properties of the water used as the heat transfer fluid through the top and bottom coil heat exchangers. Table 4.3 shows the thermophysical properties of water in the temperature range 20 – 60°C. The last column presents the percent deviation from the property value at 60°C.

Table 4.3. Thermophysical properties of water.

Property	**Value at T = 20°C**	**Value at T = 60°C**	**% deviation from value at 60°C**
Density (ρ)	998.2 (kg/m^3)	983.2 (kg/m^3)	+1.5%
Specific heat capacity (c)	4.183 (kJ/kg.K)	4.183 (kJ/kg.K)	+0.0%
Thermal conductivity (k)	0.586 (W/m.K)	0.641 (W/m.K)	-8.6%
Dynamic viscosity (μ)	1.0×10^{-3} (Pa.s)	0.467×10^{-3} (Pa.s)	+114.1%
Thermal Expansion coefficient (β)	0.209×10^{-3} (K^{-1})	0.522×10^{-3} (K^{-1})	-60.0%

4.2.4. Measurement Instrumentation and Data Acquisition (DAQ) System

DAQ System. The data acquisition hardware consisted of a Windows 7 personal computer, and a National Instrument 8-slot USB chassis (NI cDAQ-9178 - http://sine.ni.com/nips/cds/view-/p/lang/en/nid/207534) that held five different cards. Three cards were used for recording thermocouple measurements; two 16-channel, thermocouple input cards (NI 9213 - http://sine-.ni.com/nips/cds/view/p/lang/en/nid-/208788), and another 4-channel, thermocouple input card (NI 9211 - http://sine.ni.com/nips/cds-/view/p/lang/en/nid/208787). One card (4-channel, PT100 RTD Analog Input, NI 9217 - http://sine.ni.com/nips/cds/view/p/lang/en-/nid/208804) was dedicated for temperature measurements by RTDs that were installed to monitor the temperatures at different locations on the turbine exhaust system "RTD 1-4". The last card was a 4-channel Universal (current/voltage) Analog Input (NI 9219 - http://sine.ni.com/nips/cds/view-/p/lang/en/nid/208789) that was used to record the measurement signals from both the turbine flow meter and the Coriolis mass flow meters. The chassis communicated with the computer through a USB cable. A LabVIEW program was developed to facilitate the recording and conversion of the data collected by the DAQ system. The program output was then saved in data files and stored on the computer hard disk.

Flow Rate Measurements. Two flow meters were installed to measure the flow rates through the bottom and top immersed coil heat exchangers. A 1/2-inch turbine flow meter (Omega, FTB101 - http://www.omega.ca/pptst_eng/FTB100.html) was installed upstream of the inlet of the bottom coil heat exchanger. It provided a linear flow measurement in the range of 1.32 – 13.2 lpm with a nominal K-factor of 13000 pulses/gal. It was recommended by the manufacturer that a straight 1/2-inch pipe, 10-D in length was installed upstream of

the flow meter and another pipe, 5-D in length was installed right after the flow meter. Also, to reduce the potential risk of fouling and damage of the turbine meter, a 100-mesh Y-strainer with a maximum particle size of 0.0055 inch. A signal conditioner (Omega, FLSC-61 - http://www.omega.ca/pptst_eng-/FLSC60.html) was mounted on the turbine flow meter to scale the frequency measurement to 12 Volts-DC output signal that could be recorded by the DAQ system.

A 1/2-inch Coriolis mass flow meter (Endress+Hauser, Proline Promass 80E - http://www.-endress.com/en/Field-instruments-overview/Flow-measurement-producto-verview-/Product-Coriolis-flowmeter-Proline-Promass-80E) was installed upstream of the inlet of the top coil heat exchanger. It can measure the flow rate of liquids in the range of 0-6500 kg/h (~110 lpm for water). The output of the mass flow meter is scaled over 4-20 mA with a resolution of ±0.5 µA. Based on the data provided by the manufacturer, the base accuracy of the mass/volume flow rate measurement is ±0.2% of the reading. The Proline Promass 80E meter also provided density and temperature measurements with accuracy of ±0.02 g/cm^3 and ±0.5±0.005.T°C, respectively. This mass flow meter was used as the flow rate calibrator for the turbine flow meter installed on the bottom coil heat exchanger.

Temperature Measurements. All temperature measurements in the storage tank were performed by T-type thermocouples, using either 1/16-inch (Omega - TMQSS-062U) or 1/32-inch (Omega - TMQSS-032U) ungrounded thermocouples. Nine 6-inch long thermocouples (TMQSS-062U) were inserted through the side walls of the tank using compression fittings (SWAGELOK, B-100-2BT). The tip of each thermocouple was adjusted at 10 mm from the inner walls of the tank. Another nine thermocouples (TMQSS-032U) with different lengths were attached to a thermocouple rack that was supported to the tank lid

down the centre-line of the tank. The thermocouple rack was manufactured from a 1/4-inch stainless steel square rod with nine 1/16-inch holes. Nine ceramic sleeves (1/32 inch inner diameter, and 1/16 inch outer diameter) were glued to the rack holes to support the thermocouples. Four 6-inch long thermocouples (TMQSS-062U) were installed very close to the inlets and outlets of the top and bottom heat exchangers. The thermocouples were inserted through compression fittings along the axes of the pipes, pointing in the opposite direction of the flow. Four 6-inch long thermocouples (TMQSS-062U) were taped to the four external faces of the side-wall insulation to monitor the ambient temperature. The thermocouples were adjusted such that the tip was extending 127 mm (5 inch) from the centre-point of each face. Figure 4.10 illustrates the approximate layout of the thermocouples within the tank and the identification numbers of the thermocouples. Table 4.4 lists the vertical positions of the thermocouples.

Table 4.4. The locations of the thermocouples inside the square tank (measured from the bottom of the tank).

Thermocouple	**Vertical location [mm]**
TC-1	31.8
TC-2	63.5
TC-3, 3a, 3b	127.0
TC-4	241.3
TC-5, 5a, 5b	355.6
TC-6	469.9
TC-7, 7a, 7b	584.2
TC-8	660.4
TC-9	685.8

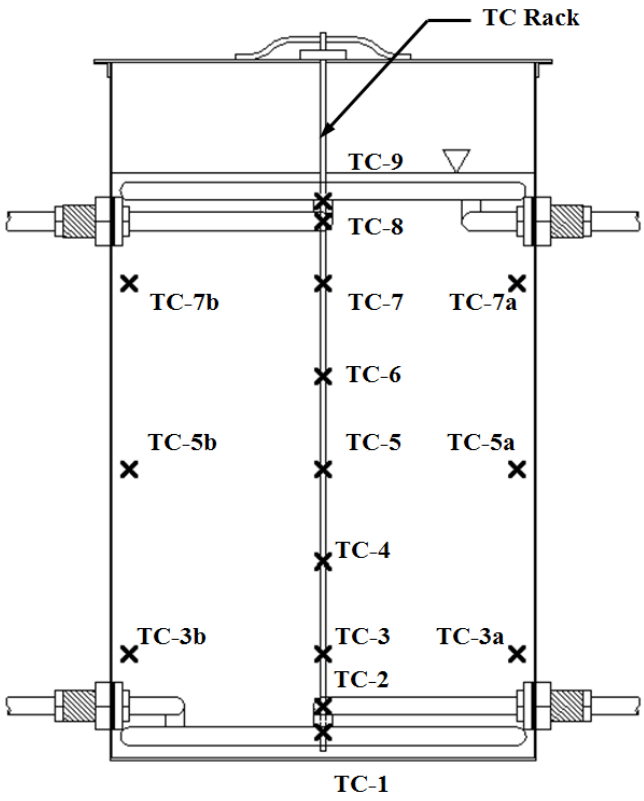

Figure 4.10. Layout of the storage tank showing the thermocouple rack and the locations of the thermocouples mounted inside the tank.

4.3. Procedures

4.3.1. Testing and Calibration

Before the experimental testing, the equipment was thoroughly tested and calibrated. Detailed error analysis and uncertainty propagation is presented in Appendix D.

Flow Meters. The accuracy of the Coriolis mass flow meter was taken as provided by the manufacturer; i.e. ±0.2% of the reading. It was used to calibrate the turbine flow meter. Both flow meters were connected in series to the Lytron chiller. The flow rate was adjusted from 0 to 6 lpm with a step of 0.5 lpm. In each test, the flow rate was left to reach a steady

state, and then the readings from both flow meters were recorded by the DAQ for 60 s. The results were then correlated and the accuracy of the turbine flow meter was estimated to be ±0.072 lpm based on 95% confidence interval.

Thermocouples. All 26 thermocouples used in the test section were calibrated in a constant temperature bath using a platinum resistance thermometer (RTD), accurate to ±0.01°C. The accuracy of the thermocouples was estimated to be ±0.81°C based on 95% confidence interval.

4.3.2. Experimental Procedure

The experiment procedures are divided into two categories: a series of five experiments conducted on the storage tank with water only as the storage medium (SHS), and a series of seven experiments conducted on the storage tank with water and PCM modules (HTES).

Sensible Heat Storage (SHS). The first set of experiments was designed to progressively provide validation data for the various aspects of the mathematical model for the SHS system. The first experiment examines the thermal losses from the storage tank to the surroundings. The second experiment characterizes the performance of the immersed coil heat exchanger. The third and fourth experiments examine the different thermal behaviors inside the tank during mixing and thermal diode processes. The fifth experiment explores the thermal performance of the SHS tank under sequential charging and discharging processes. Temperature measurements in all the tests were collected every 1 second from the thermocouples inside the tank as well as at the inlet and outlet from the bottom and/or top coils. Note that results from all the experiments are presented in Chapter Five.

Experiment B1: The purpose of the test was to evaluate the value of the thermal loss conductance through the tank walls and the thermal insulation layers to the surroundings, UA_{loss}. This test started with increasing the initial temperature of the tank to 60°C and allowing it to cool down over a period of seven days. Temperature measurements were recorded every 20 seconds. The ambient temperature was also recorded at the same rate from the four thermocouples fixed around the tank.

Experiment B2: The second test was designed to characterize the performance of the bottom immersed coil heat exchanger when the heat transfer from the coil promotes mixing inside the storage tank. This experiment provides data that is used to assess the validity of the heat transfer correlations governing the performance of the coil heat exchanger. The water inside the tank starts uniformly at a temperature of 20°C. Water enters the bottom coil heat exchanger at a mass flow rate of 0.05 kg/s with a fixed temperature of 54°C (causing the tank to mix). The input sequence is shown in Table 4.5.

Table 4.5. Input sequence for Experiment B2

Bottom Coil HX		
Time interval	**Mass flow rate [kg/s]**	**Inlet temperature [°C]**
0-5.5 h	0.05	54

Experiment B3: This experiment examines the performance of the storage tank when the heat transfer from the bottom coil heat exchanger acts to mix the tank for a period of time followed by another period where the thermal diode becomes in effect. This test provides data for validation of the mathematical model of the heat exchanger. It also provides data that is used for development of the tank mixing model since the data can be used to help

determine the height of the bottom thermal node in the model. The water inside the tank is initially at a uniform temperature of 27°C. Water enters the bottom coil heat exchanger at a mass flow rate of 0.05 kg/s with a fixed temperature of approximately 60°C (causing the tank to mix) for 3.5 hours. The inlet temperature was then adjusted to 40°C (causing the tank to stratify) for 3 hours. The input sequence is shown in Table 4.6. Between the two stages of the experiment the flow valve was closed for 30 minutes until the inlet temperature reaches the setpoint.

Table 4.6. Input sequence for Experiment B3.

Bottom Coil HX		
Time interval	**Mass flow rate [kg/s]**	**Inlet temperature [°C]**
0-3.5 h	0.05	60
The flow valve was closed for 0.5 hour to reach the setpoint		
4-7 h	0.05	40

Experiment B4: This test illustrates the performance of the storage tank during three stages of operation: (1) when the heat transfer from the bottom coil heat exchanger acts to stratify the tank for a period of time, (2) then mixing takes place during the second stage, and (3) last, thermal dioding is induced at the third stage. The results from this test were used to validate the mathematical model of the heat exchanger as well as the mixing model of the tank. The water inside the tank started uniformly at 50°C. Water enters the bottom coil heat exchanger at a mass flow rate of 0.05 kg/s with a fixed temperature of approximately 29°C (will cause the tank to stratify) for 3 hours. The inlet temperature was then adjusted to 59°C (will cause the tank to mix) for 2.5 hours. Between the first two stages of the experiment the flow valve was closed for 30 minutes until the inlet temperature reaches the setpoint. At the

end of the second stage the inlet temperature was adjusted to 30°C for 1.5 hours without stopping the flow through the coil. The input sequence is shown in Table 4.7.

Table 4.7. Input sequence for Experiment B4.

Bottom Coil HX		
Time interval	**Mass flow rate [kg/s]**	**Inlet temperature [°C]**
0-3 h	0.05	29
The flow valve was closed for 0.5 hour to reach the setpoint		
3.5-6 h	0.05	59
6-7.5 h	0.05	30

Experiment B5: This test illustrates the performance of the storage tank during sequential charging and discharging process. The input sequence is shown in Table 4.8.

Table 4.8. Input sequence for Experiment B5.

Bottom Coil HX			**Top Coil HX**	
Time interval	**Mass flow rate [kg/s]**	**Inlet temperature [°C]**	**Mass flow rate [kg/s]**	**Inlet temperature [°C]**
0-3 h	0.05	58.5	0	---
3-6 h	0	---	0.05	25

Both the bottom and top coil heat exchangers are operating sequentially. The bottom coil charges the tank during the first stage of the experiment while the top coil is idled, then the top coil discharges the tank during the second stage while the bottom coil is idled. The water inside the tank started uniformly at 21.5°C. Water enters the bottom coil heat exchanger at a mass flow rate of 0.05 kg/s with a fixed temperature of approximately 58.5°C (will cause the tank to mix for charging) for 3 hours. The flow valve to the bottom coil is then closed and the

flow valve for the top coil is opened to a flow rate of 0.05 kg/s. The inlet temperature to the top coil heat exchanger was set to 25°C (will cause the tank to mix for discharging) for 3 hours.

Hybrid Thermal Energy Storage (HTES). The second set of experiments was designed to progressively provide validation data for the various aspects of the mathematical model for the HTES system containing phase change materials. The experiments are divided into three subgroups. The first subgroup examines the performance of the HTES tank when operating with different number of PCM modules (4, 6 and 8 modules). The tests in this subgroup were conducted by operating the bottom coil heat exchanger in the mixing mode. The second subgroup explores the effect of the spacing between the PCM modules (10, 20, 30 and 40 mm). In these tests, the number of modules was kept fixed to 6 modules. Both subgroups help evaluate the validity of the heat transfer models between the water and the PCM modules as well as inside the modules. The third subgroup illustrates the performance of the HTES tank when both coils are operating (sequential vs. simultaneous). Before running the experiment, the tank was filled with tap water until a height of 0.72 m and left with the submerged PCM modules over night to reach a uniform temperature. Temperature measurements were collected every 1 second from the thermocouples inside the tank as well as at the inlet and outlet from the bottom and/or top coils. The ambient temperature was also recorded at the same rate from the four thermocouples fixed around the tank.

Experiment C1: The water inside the tank starts uniformly at a temperature of 23°C. Water enters the bottom coil heat exchanger at a mass flow rate of 0.05 kg/s with a fixed temperature of 59°C (will cause the tank to mix). Four PCM modules were submerged in the water with a spacing of 20 mm. The input sequence is shown in Table 4.9.

Table 4.9. Input sequence for Experiment C1.

	Bottom Coil HX			
Time interval	**Mass flow rate [kg/s]**	**Inlet temperature [°C]**	**# of PCM modules**	**Spacing between modules [mm]**
0-6 h	0.05	59	4	20

Experiment C2: The water inside the tank starts uniformly at a temperature of 25°C. Water enters the bottom coil heat exchanger at a mass flow rate of 0.05 kg/s with a fixed temperature of 59°C (will cause the tank to mix). Six PCM modules were submerged in the water with a spacing of 20 mm. The input sequence is shown in Table 4.10.

Table 4.10. Input sequence for Experiment C2.

	Bottom Coil HX			
Time interval	**Mass flow rate [kg/s]**	**Inlet temperature [°C]**	**# of PCM modules**	**Spacing between modules [mm]**
0-6 h	0.05	59	6	20

Experiment C3: The input sequence is shown in Table 4.11.

Table 4.11. Input sequence for Experiment C3.

	Bottom Coil HX			
Time interval	**Mass flow rate [kg/s]**	**Inlet temperature [°C]**	**# of PCM modules**	**Spacing between modules [mm]**
0-6 h	0.05	59	8	20

The water inside the tank starts uniformly at a temperature of 29°C. Water enters the bottom coil heat exchanger at a mass flow rate of 0.05 kg/s with a fixed temperature of 59°C (will cause the tank to mix). Eight PCM modules were submerged in the water with a spacing of 20 mm.

Experiment C4: The water inside the tank starts uniformly at a temperature of 22°C. Water enters the bottom coil heat exchanger at a mass flow rate of 0.05 kg/s with a fixed temperature of 59°C (will cause the tank to mix). Six PCM modules were submerged in the water with a spacing of 10 mm. The input sequence is shown in Table 4.12.

Table 4.12. Input sequence for Experiment C4.

	Bottom Coil HX			
Time interval	**Mass flow rate [kg/s]**	**Inlet temperature [°C]**	**# of PCM modules**	**Spacing between modules [mm]**
0-6 h	0.05	59	6	10

Experiment C5: The water inside the tank starts uniformly at a temperature of 24°C. Water enters the bottom coil heat exchanger at a mass flow rate of 0.05 kg/s with a fixed temperature of 59°C (will cause the tank to mix). Six PCM modules were submerged in the water with a spacing of 30 mm. The input sequence is shown in Table 4.13.

Table 4.13. Input sequence for Experiment C5.

	Bottom Coil HX			
Time interval	**Mass flow rate [kg/s]**	**Inlet temperature [°C]**	**# of PCM modules**	**Spacing between modules [mm]**
0-6 h	0.05	59	6	30

Experiment C6: This test illustrates the performance of the HTES tank during sequential charging and discharging process. The water inside the tank starts uniformly at a temperature of 22°C. Water enters the bottom coil heat exchanger at a mass flow rate of 0.05 kg/s with a fixed temperature of 59°C (will cause the tank to mix - charging) for 3.25 hours. The flow rate through the bottom coil is then stopped. Water enters the top coil heat exchanger at a flow rate of 0.05 kg/s with a fixed temperature of 26°C (will cause the tank to mix - discharging) for 3 hours. Six PCM modules were submerged in the water with a spacing of 40 mm. The input sequence is shown in Table 4.14.

Table 4.14. Input sequence for Experiment C6.

	Bottom Coil HX		**Top Coil HX**	
Time interval	**Mass flow rate [kg/s]**	**Inlet temperature [°C]**	**Mass flow rate [kg/s]**	**Inlet temperature [°C]**
0-3.25 h	0.05	59	0	---
3.25-6.25 h	0	---	0.05	26

Experiment C7: This experiment examines the performance of the HTES tank during simultaneous charging and discharging process. The water inside the tank starts uniformly at a temperature of 22°C. Water enters the bottom coil heat exchanger at a mass flow rate of 0.05 kg/s with a fixed temperature of 59°C (will cause the tank to mix - charging) for 6 hours. The flow rate through the bottom coil is then stopped. After 2.5 hours of the test, water enters the top coil heat exchanger at a flow rate of 0.05 kg/s with a fixed temperature of 25°C (will cause the tank to mix - discharging) for 2 hours, followed by 2.5 hours with an inlet temperature of 20°C (will cause the tank to mix - discharging). Six PCM modules were submerged in the water with a spacing of 40 mm. The input sequence is shown in Table 4.15.

Table 4.15. Input sequence for Experiment C7.

	Bottom Coil HX		**Top Coil HX**	
Time interval	**Mass flow rate [kg/s]**	**Inlet temperature [°C]**	**Mass flow rate [kg/s]**	**Inlet temperature [°C]**
0-2.5 h	0.05	59	0	---
2.5-6 h	0.05	59	0.05	25
6-7 h	0	---	0.05	20

CHAPTER FIVE

MATHEMATICAL MODEL VALIDATION

5.1. Introduction

This chapter describes the methodology and procedures followed to validate the mathematical model presented in Chapter Three. The mathematical model of the multi-tank storage system was based on the mathematical models of individual tanks coupled together through the top and bottom coil heat exchangers. The performance of each individual tank was simulated by coupling of the mathematical models of the different components inside the storage tank. These components include the coil heat exchanger, the PCM modules in the HTES tank and the water as the sensible storage medium.

This chapter commences with verification of the critical components of the storage tank, the coil heat exchanger model and the PCM model. The verification was carried out by isolating the component models and testing them in theoretical or benchmark cases. Sensitivity analysis was also performed to investigate the effect of the variation of the thermophysical properties with temperature. This helped in the quantification of the accuracy of assuming constant properties in the numerical simulations.

The complete model of the single and multi-storage system was then compiled and validated against the experimental results presented by Mather (2000) in his Master's thesis for SHS system with water as the storage medium. The experimental results deduced from six different tests performed by Mather were extracted and digitized for comparison.

Finally, the results obtained from the experiments, described in the previous chapter, were used to validate the mathematical model of the storage tank with PCMs. As mentioned in Chapter Four, the experimental test matrix was designed in order to ensure that the mathematical model was accurately simulating the heat transfer phenomena of the storage system for realistic conditions. The model considers the heat transfer to/from the coil heat exchangers, heat transfer between adjacent thermal nodes inside the tank, thermal losses to the surrounding, heat transfer into/from the PCM modules, thermal mixing due to buoyancy driven currents and thermal dioding due to stable positive temperature gradients.

5.2. Component Verification

The mathematical models of the coil heat exchanger and the PCM modules were verified against analytical or benchmark solutions. First, the coil heat exchanger model was isolated and tested by considering the heat exchanger submerged in an infinite medium with constant temperature T_{∞}. A systematic approach was applied to explore the impact of the transient term in the heat exchanger model, the heat exchanger effectiveness and the thermophysical properties.

Second, the PCM model was verified against the Stefan and Neumann problems for phase change heat transfer. The Stefan problem applies to 1-D cases where the wall temperature is constant and the initial temperature of the entire domain coincides with the melting temperature of the PCM. The Neumann problem assumes that the initial temperature of the solution domain is not equal to the melting temperature of the PCM. Both problems have closed-form analytical solutions for the transient temperature and melt front profiles during conduction-dominated melting/solidification inside rectangular PCM modules. The results of the verification cases are presented in Appendix A.

The mathematical model of the heat exchanger was verified against the case where a coil heat exchanger is submerged in an infinite isothermal medium with a temperature T_∞=20°C. The mass flow rate through the coil is 0.05 kg/s and the inlet temperature is maintained constant at 60°C. The effect of the mesh size and the time step were investigated. In addition, the influence of the thermophysical properties of the fluid was explored. The results illustrated that the sensitivity of the results to the mesh size and the time step diminishes for $N_{coil}\geq100$ and $\Delta t\leq4$ s, where the variations of outlet temperature and the heat transfer rate from the coil heat exchanger were found to be unnoticeable. In addition, the results were found to be sensitive to the thermophysical properties of the external fluid. As such, temperature dependent properties should be used in the numerical simulations.

Mesh and time step sensitivity analyses were then undertaken for the verification of the PCM model. The results were shown to be insensitive to the time step for $\Delta t\leq10$ s. However, the effect of the cell size was found to diminish significantly for $\Delta x\leq1$ mm. In addition, the model results were seen to have excellent agreement with the analytical solutions for the cases when the Stefan number is less than 2.5.

5.3. System Validation

5.3.1. Single and Multi-tank SHS

Seven experiments were selected from the work done by Mather (2000) on single and multi-tank SHS with water as the storage medium. These experiments were simulated using the current model in order to validate the ability of the model to capture the physical behavior of the storage tank without PCM.

Mather's experiments were carried out on a cylindrical tank, 0.58 m in diameter. Two coil heat exchangers, made of copper tubing, were installed inside the tank. The bottom heat exchanger was located 60 mm and the top heat exchanger was located 720 mm away from the bottom of the tank. Each coil had an inner diameter of 11.43 mm, an outer diameter of 12.7 mm and a total length of 5.98 m. The height of the water inside the tank was 762 mm. The sides of the tank were wrapped in a flexible, 89 mm thick, RSI 2.1, fiberglass insulation with aluminum foil facing. The top and bottom were insulated with 51 mm, RSI 1.4, styrofoam sheets. The properties of the water flowing through the coil heat exchangers were assumed constant as presented in Table 5.1. The properties listed in the table were found to show slight sensitivity to the temperature variation along the heat exchangers.

Table 5.1. Thermophysical properties of water.

Property	Density, ρ [kg/m^3]	Specific heat capacity, c [J/kg.K]	Thermal conductivity, k [W/m.K]
Value	993.0	4180.0	0.63

The first experiment conducted by Mather was to evaluate the thermal losses from the storage tank to the surrounding. The tank was filled with water at 46.5°C, and then was left to cool down spontaneously over four days. The average ambient temperature was reported to be 20.4°C. Figure 5.1 illustrates the temporal profile of the average temperature inside the tank over the time of the test. The experimental results were analyzed using the following equation

$$Mc\frac{dT_{av}}{dt} = (UA)_{loss}(T_{av} - T_{amb}) \tag{5.1}$$

The value of $(UA)_{loss}$ was found to fit the correlation

$$(UA)_{loss} = c_1(T_{av} - T_{amb})^n \tag{5.2}$$

The value of c_1 was found to be 0.78 and n was 0.23.

This correlation was adopted in the current model to simulate the thermal losses from the storage tank. The model was then executed with a time step of 1 s and the numerical results were compared with the experimental results in Figure 5.1. Agreement was found within the experimental uncertainty, reported as ±0.4°C for the temperature measurements.

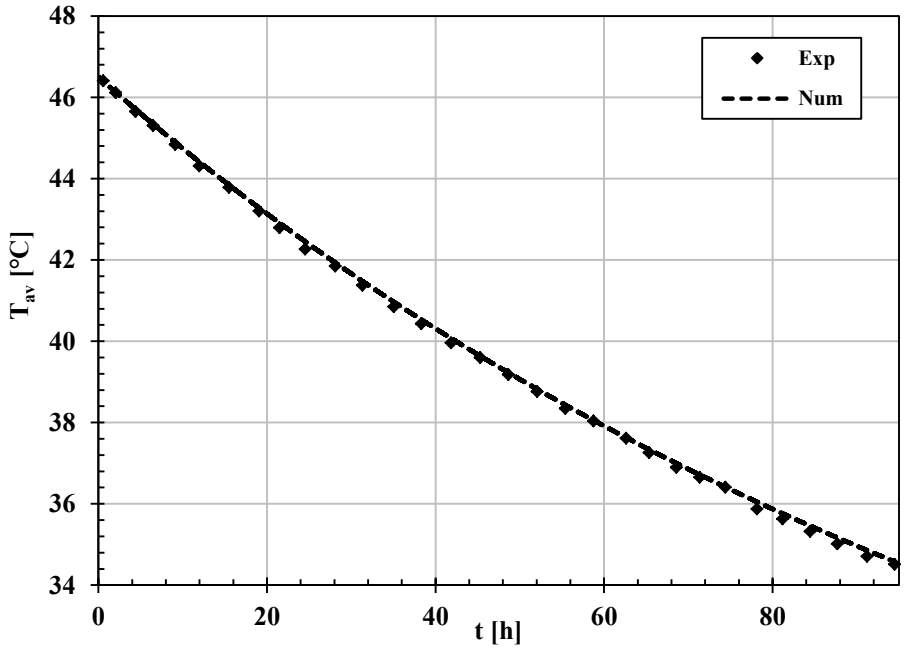

Figure 5.1. The volume-weighted average temperature of the water in SHS tank during the thermal loss characterization test. The experimental results were extracted from Mather (2000).

A. Experiment A1

Mather's experiment commenced with water flowing through the bottom coil heat exchanger of a single water tank at a flow rate of 0.05 kg/s. The inlet temperature was 60°C for 3 hours, followed by 30°C for 2 hours. The initial temperature of water inside the tank was 18.5°C. Figure 5.2a illustrates a schematic of the water tank divided into 21 control volumes depicting the locations of the thermocouples used for temperature monitoring inside the tank (Mather, 2000).

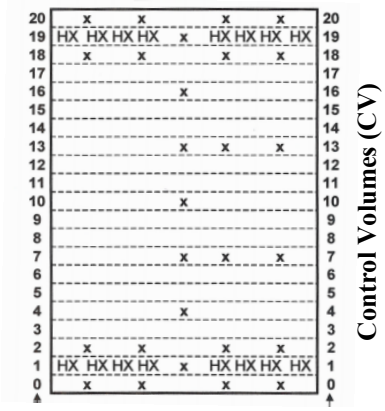

Figure 5.2a. Schematic of the water tank divided into 21 control volumes. The 'x' depicts the locations of thermocouples and the 'HX' depicts the locations of the bottom and top heat exchangers. (Mather, 2000).

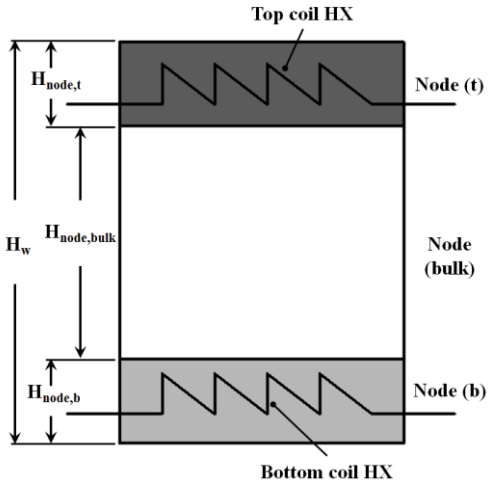

Figure 5.2b. Schematic of the water tank divided into 3 thermal nodes for the proposed numerical model. Bottom node: Node (b), bulk node: Node (bulk) and top node: Node (t).

Figure 5.3a shows the temperatures measured at the outlet of the coil heat exchanger as well as the temperature measured at the heat exchanger control volume (CV1 in Figure 5.2a). The proposed numerical model requires the identification of the heights of thermal nodes inside the tank ($H_{node,b}$, $H_{node,bulk}$ and $H_{node,t}$), illustrated in Figure 5.2b. Good agreement was obtained between the experimental and numerical results when the height of the bottom node ($H_{node,b}$) was set to the height of the coil heat exchanger. Figure 5.3b

demonstrates the heat transfer rate from the coil heat exchanger (Q_{HX}) calculated from the measured outlet temperature using:

$$Q_{HX} = \dot{m}c(T_{in} - T_{out}) \tag{5.3}$$

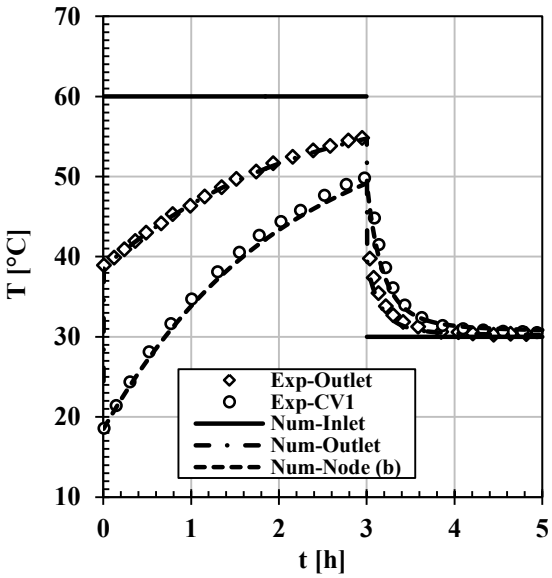

Figure 5.3a. Temporal profiles of the inlet and outlet temperatures of the bottom coil HX and the temperature of CV1 in Figure 5.2a. The dashed line shows the numerical profile for Node (b) in Figure 5.2b. The experimental results were extracted from Mather (2000).

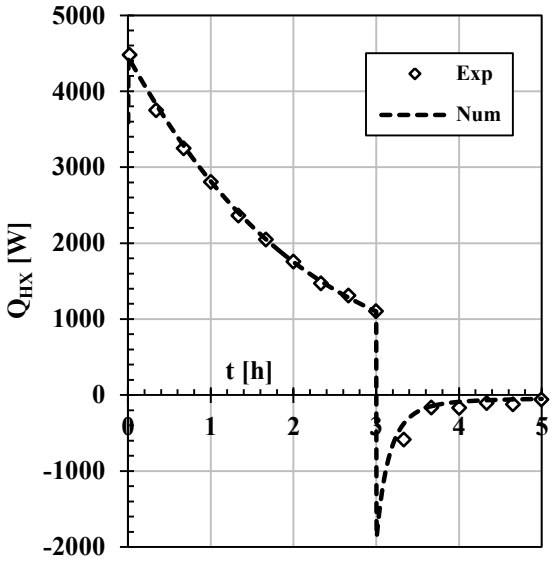

Figure 5.3b. Temporal profile of the heat transfer rate (Q_{HX}) of the bottom coil HX. The experimental results were extracted from Mather (2000).

B. Experiment A2

A similar experiment was carried out using the top coil heat exchanger only. The mass flow rate was fixed at 0.05 kg/s, while the inlet temperature was set to 30°C for 3 hours followed by 60°C for 2 hours. The initial temperature of the water inside the tank was 60°C. The height of the top node was set in the numerical model to 60 mm. Figures 5.4a and 5.4b show comparison between the experimental and numerical results.

Both Experiments A1 and A2 demonstrate the capability of the numerical model to simulate the thermal behavior of the water storage tank accurately during different operation

scenarios. In both experiments, it is seen that during the first three hours of the experiments the tank was fully mixed due to the action of buoyancy currents from the coils. During the following two hours the tank was in thermal diode mode where the heat transfer was restricted to the thermal control volume surrounding the heat exchanger only. This was also evident from the heat transfer rate values where the heat transfer rate is comparatively lower during thermal dioding.

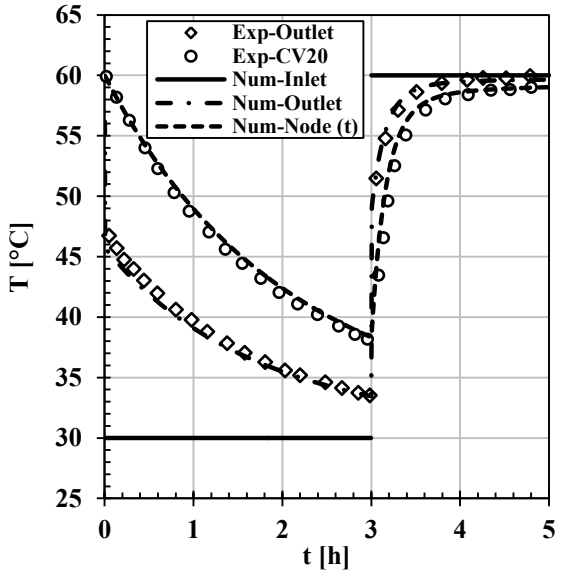

Figure 5.4a. Temporal profiles of the inlet and outlet temperatures of the top coil HX and the temperature of CV20 in Figure 5.2a. The dashed line shows the numerical profile for Node (t) in Figure 5.2b. The experimental results were extracted from Mather (2000).

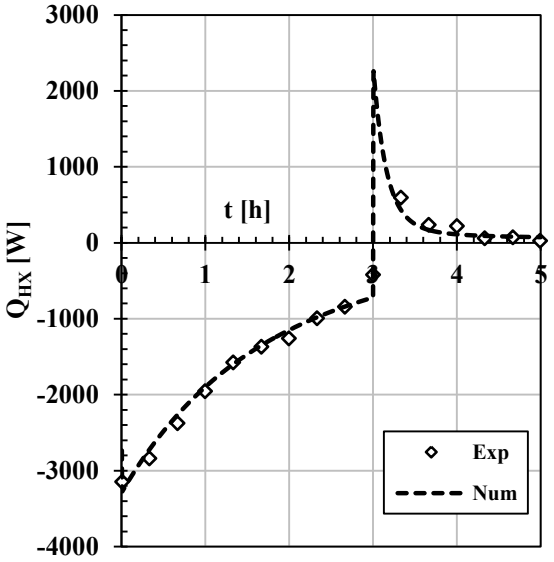

Figure 5.4b. Temporal profile of the heat transfer rate (Q_{HX}) of the top coil HX. The experimental results were extracted from Mather (2000).

Experiments (A3-A7) were conducted by Mather (2000) to show different operations of the single and multi-tank SHS. Comparison between the experimental results and the numerical simulations are provided in Appendix B.

In general, satisfactory agreement was also observed between the experimental and numerical results with a maximum deviation of ±0.75°C for the temperature and ±5% for the heat transfer rate. As such, the numerical model was proved to be capable of accurately

simulating the transient behavior of single and multi-tank storage system with water as the sensible storage medium.

5.3.2. Experiments on Single-tank HTES with PCM

In this section, the experiments described in Chapter Four were used to provide further validation for the proposed numerical model in particular for the HTES with PCM. Five experiments (B1-B5) were carried out to investigate the transient performance of a single-tank storage system without PCM. Whereas seven experiments (C1-C7) were meant to illustrate the performance of the HTES with PCM under different operation conditions. Detailed description of the experiments and the test procedures are presented in Chapter Four.

A. Experiment B1

The first experiment was designed to characterize the thermal losses from the storage tank. The tank was filled with 199.2 l of water. The height of the water inside the tank was 0.72 m. A 3.5-kW immersed electric heater was used to heat the water inside the tank to a temperature of 60°C. The tank was left to cool down spontaneously for seven days. The tank was discretized into 9 control volumes in the vertical direction corresponding to the 9 different locations of the thermocouples inside the tank. Figure 5.5 shows a schematic of the tank, illustrating the vertical locations of the thermocouples and the discretization control volumes. Table 5.2 presents the values of the heights of the nine control volumes.

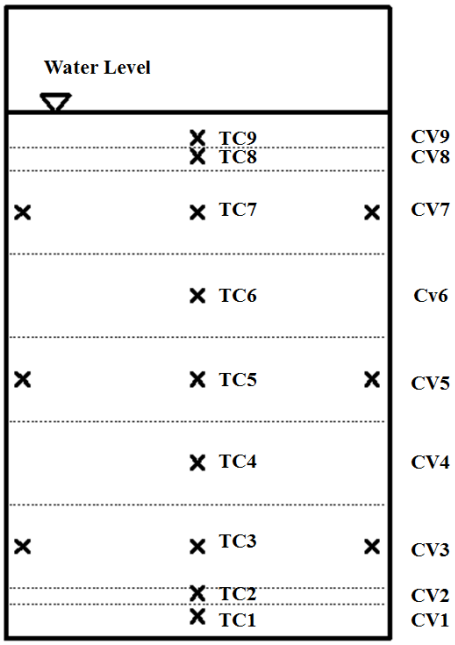

Figure 5.5. Schematic of the square tank discretized vertically into nine control volumes (CVs), each CV encompassing one or more thermocouples for temperature measurement. CVs 3, 5 and 7 have three thermocouples at different locations.

Table 5.2. The heights of thermal control volumes inside the square tank.

Control Volume	Height [mm]
1	47.6
2	22.2
3	114.3
4	114.3
5	114.3
6	114.3
7	114.3
8	31.8
9	46.9

Figure 5.6 demonstrates the temperature measurements of all the thermocouples installed inside the tank. The dotted line depicts the volume-weighted average temperature

inside the tank (T_{av}). Note that the temperatures at the CVs 3, 5 and 7 were the average temperature measured by three different thermocouples located at the same horizontal plane but in different positions. The thermal losses were evaluated based on the following equation:

$$Mc\frac{dT_{av}}{dt} = Q_{loss} \tag{5.4}$$

The value of M is the mass of the water inside the tank during the thermal loss characterization test. The value of Q_{loss} was calculated using:

$$Q_{loss} = (UA)_{loss}(T_{av} - T_{amb}) \tag{5.5}$$

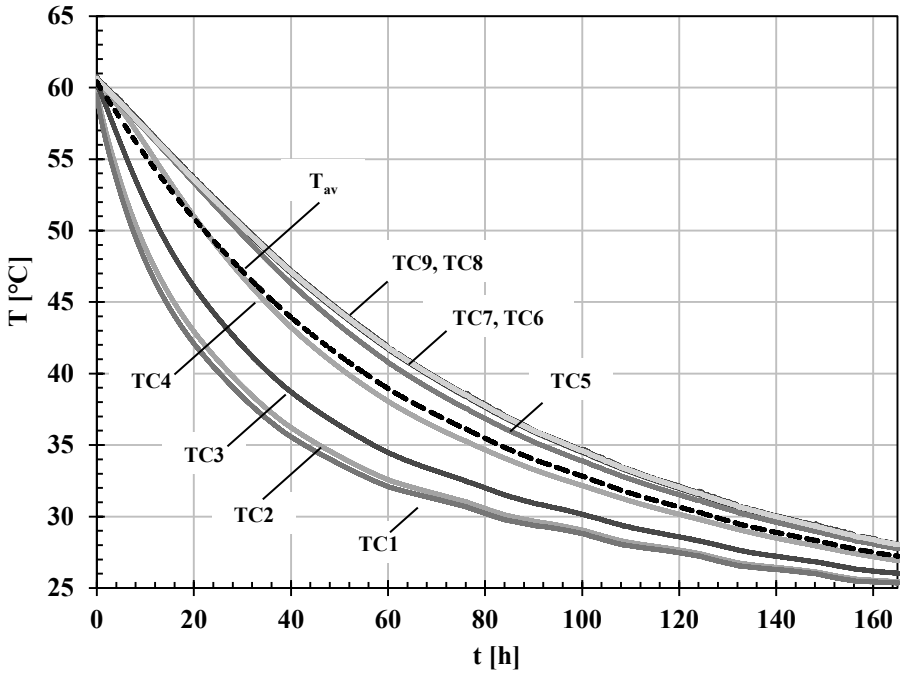

Figure 5.6. Temporal profiles of temperature measurements from the nine CVs during the thermal loss test. The temperature at CVs 3, 5 and 7 were taken as the average of the three thermocouples placed in the given CV. The dashed line represents the volume-weighted average of the temperature measurements in the nine CVs.

The ambient temperature (T_{amb}) was taken as the arithmetic average of the temperature measurements obtained from four thermocouples located at different positons

around the tank (T_{a1}, T_{a2}, T_{a3} and T_{a4}). Figure 5.7 illustrates the temperature measurements from the four thermocouples located around the storage tank to monitor the ambient temperature history during the experiment.

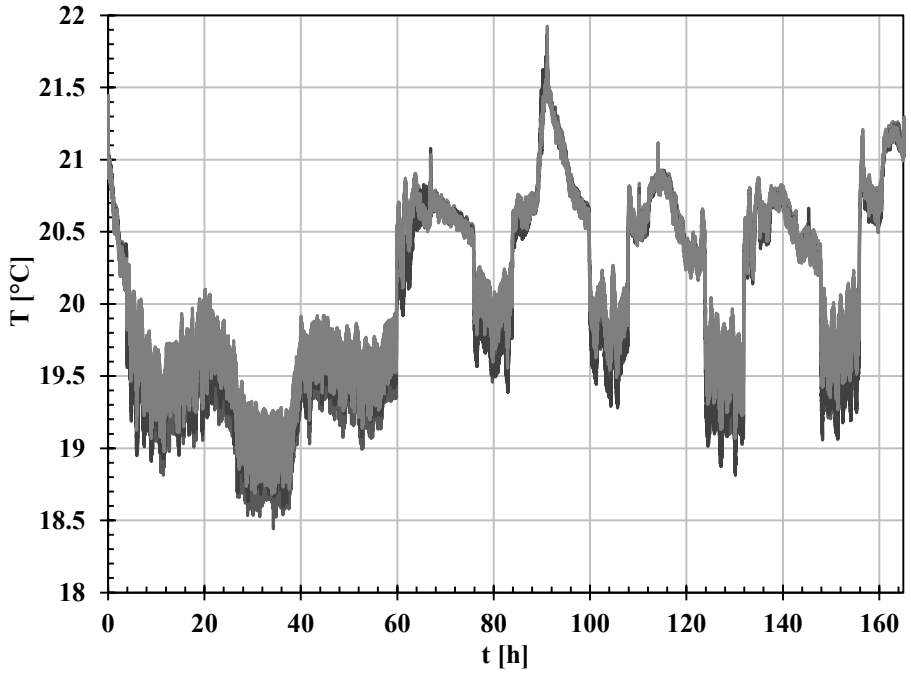

Figure 5.7. Temporal profiles of ambient temperature measurements from the four thermocouples (T_{a1}, T_{a2}, T_{a3} and T_{a4}) during the thermal loss test.

It is seen that over the seven days of the experiment the average ambient temperature was around 20°C with a variation of ±1.2°C.

The volume of the water inside the tank was estimated to be 199.1 L and the mass was calculated to be 198.7 kg. The value of $(UA)_{loss}$ was calculated from Equation (5.2) and plotted against (T_{av}-T_{amb}) in Figure 5.8. A correlation was deduced for the $(UA)_{loss}$:

$$(UA)_{loss} = 1.20\ (T_{av} - T_{amb})^{0.26} \tag{5.6}$$

It is seen that the values of the constant and the exponent of the equation are similar to those deduced from Mather's experiments in Equation (5.2). As a result, the thermal loss rate can be calculated using:

$$Q_{loss} = 1.20\ (T_{av} - T_{amb})^{1.26} \tag{5.7}$$

The correlation for the thermal loss rate (Q_{loss}) was incorporated into the numerical model and the experiment was simulated to compare the numerical with the experimental results. Figure 5.9 shows excellent agreement between the experimentally measured average temperature of the tank and the numerical prediction with maximum deviation of less than ±0.5°C.

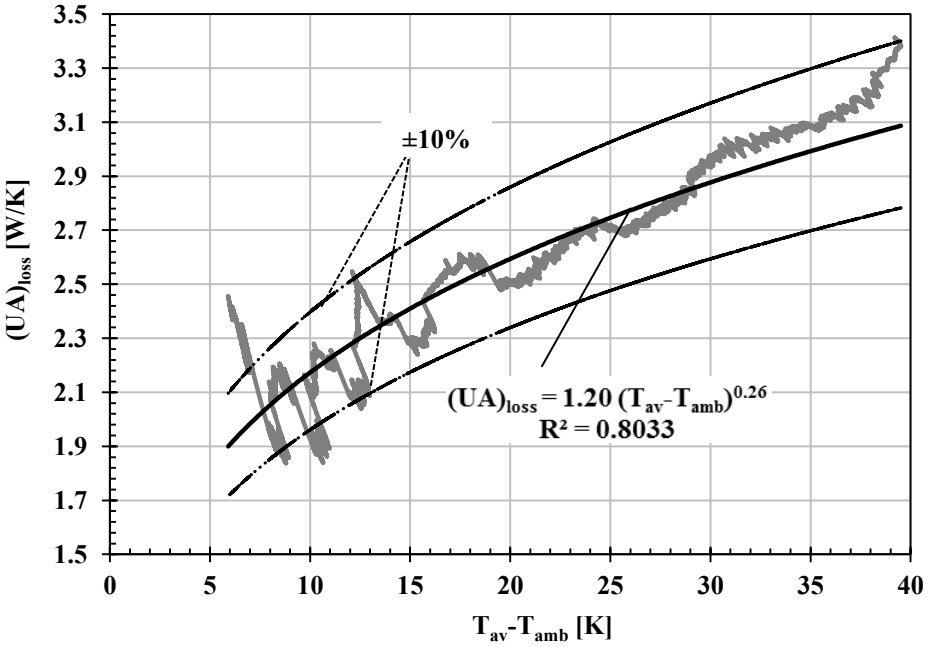

Figure 5.8. Thermal loss conductance $(UA)_{loss}$ versus the temperature difference between the average temperature in the tank and the ambient temperature (T_{av}-T_{amb}). The dashed line represents deviation from the correlation by ±10%.

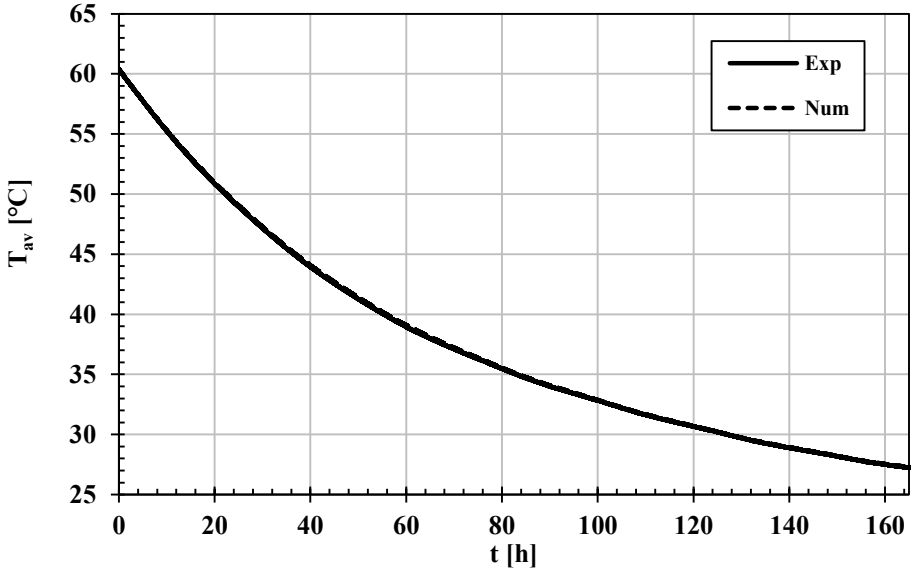

Figure 5.9. Temporal profiles of average tank temperature during the thermal loss test.

B. Experiment B2

In this experiment, the tank was filled with water to a height of 0.72 m at a temperature of approximately 20°C. The bottom coil heat exchanger was operated with a flow rate of 0.05 kg/s and a fixed inlet temperature of 54°C. The experiment was carried out over 5.5 hours during which the temperature inside the tank, as well as the ambient temperature, were monitored and recorded with results shown in Figure 5.10. Note that the temperatures measured at nine different vertical locations in the tank coincided. This mixing inside the tank arises from the natural convection currents originating from the bottom coil heat exchanger. The experiment was simulated using the numerical model and the results were shown in Figures 5.11-5.13.

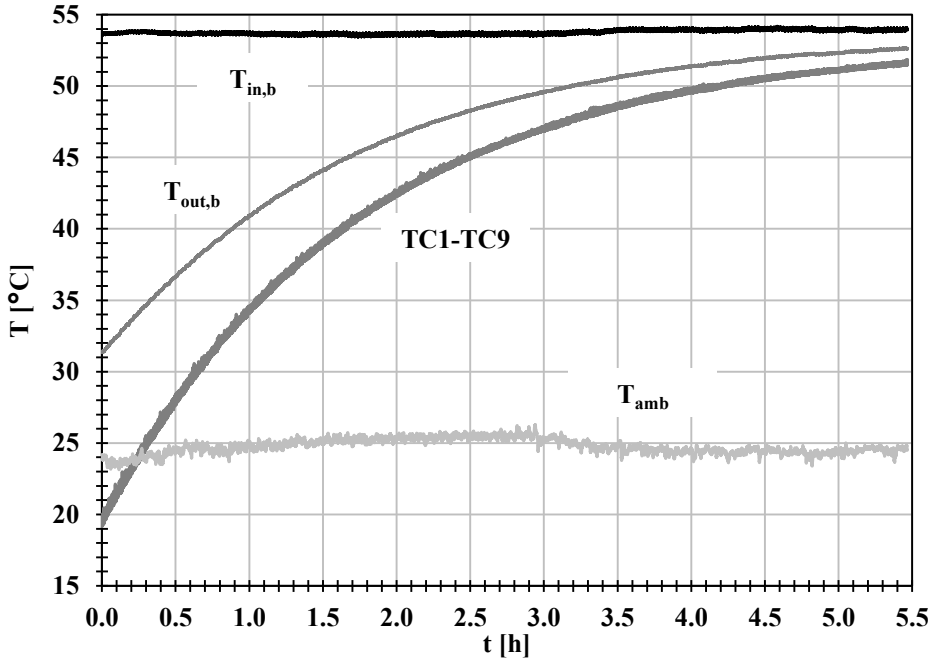

Figure 5.10. Temporal profiles of the inlet and outlet temperatures of the bottom coil HX, the temperature measurements of CVs (1-9) and the ambient temperature from Experiment B2.

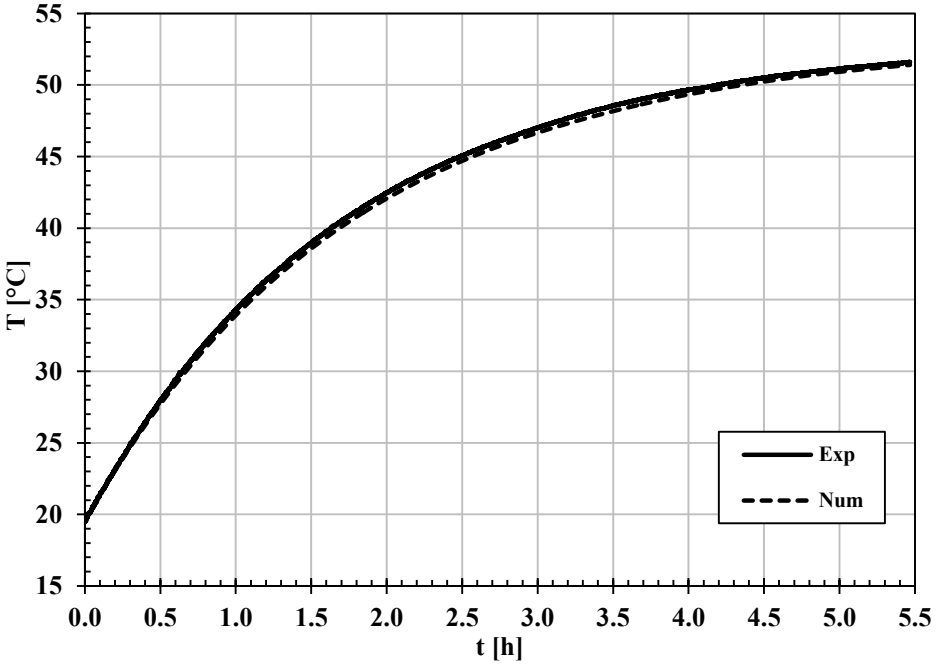

Figure 5.11. Temporal profile of the bulk temperature of the tank; Experimental: the volume-weighted average of the nine CVs, Numerical: the average of the three nodes. Experiment B2.

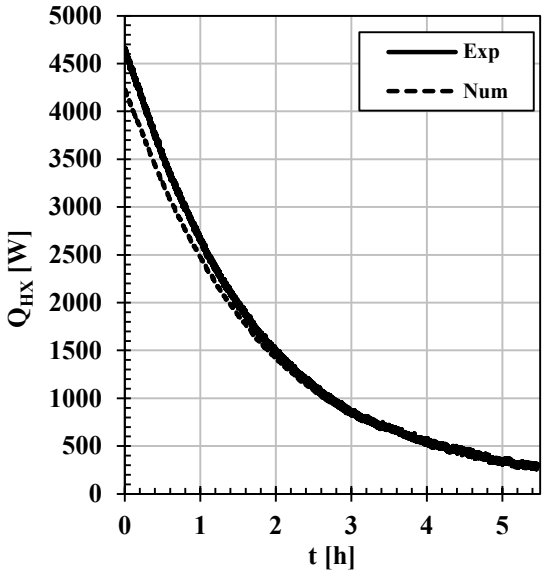

Figure 5.12. Temporal profile of the heat transfer rate (Q_{HX}) of the bottom coil HX. Experiment B2.

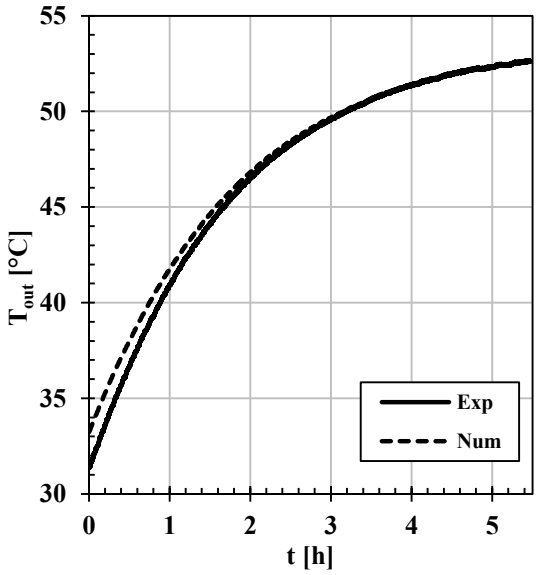

Figure 5.13. Temporal profile of the outlet temperature (T_{out}) of the coil HX. Experiment B2.

Good agreement, less than ±0.5°C, was observed in the average temperature inside the tank, as shown in Figure 5.11. However, Figures 5.12 and 5.13 show deviation in the heat transfer rate and the outlet temperature of the coil heat exchanger. The numerical model seemed to underestimate the heat transfer rate from the coil heat exchanger. The under-prediction of the heat transfer from the coil is likely due to the use of heat transfer correlations developed for straight pipes rather than coils. The spiral design of the coil has an enhancement effect on the heat transfer rate. It was reported that the internal forced convection heat transfer in spiral coil is approximately 50% higher than in a straight pipe (Naphon and Suwagrai, 2007). Also, Cianfrini *et al.* (2007) proved numerically that the external natural convection heat transfer from parallel circular cylinders is 20% higher than that from a single cylinder. This pertains to the cases when Rayleigh number in the order of 10^5 and spacing-to-diameter ratio between cylinders of 0.4. The numerical results were found to agree well with the experimental results when an enhancement factor of 1.13 is multiplied by the overall thermal conductance of the coil heat exchanger. This enhancement factor is

seen to be in closer agreement with the reported values for the natural convection heat transfer from parallel cylinders (Cianfrini *et al.* 2007). This is because the natural convection on the external surface of the coil heat exchanger is the limiting mechanism of the heat transfer. As such, the enhancement factor was applied in the model for all the following validation cases.

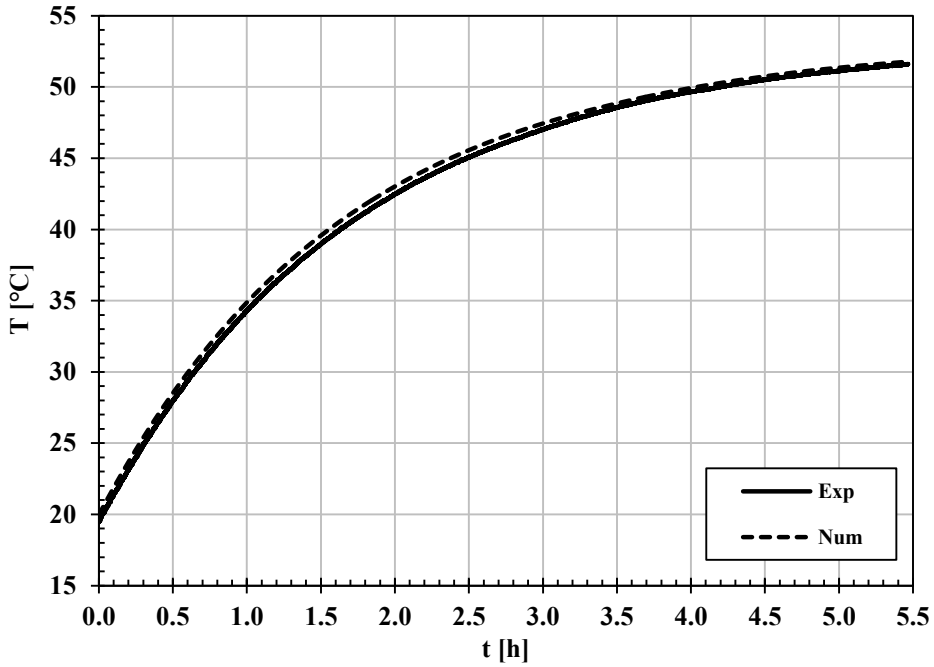

Figure 5.14. Temporal profile of the bulk temperature of the tank; Experimental: the volume-weighted average of the nine CVs, Numerical: the average of the three nodes. Experiment B2. An enhancement factor of 1.13 is multiplied by the overall thermal conductance of the coil heat exchanger.

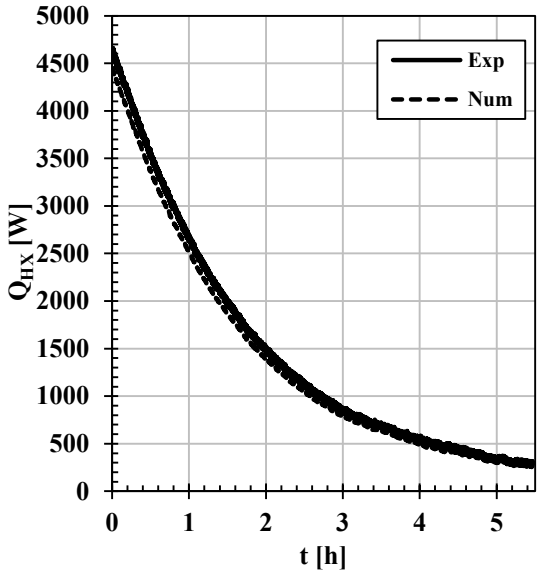

Figure 5.15. Temporal profile of the heat transfer rate (Q_{HX}) of the bottom coil HX. Experiment B2. An enhancement factor of 1.13 is multiplied by the overall thermal conductance of the coil heat exchanger.

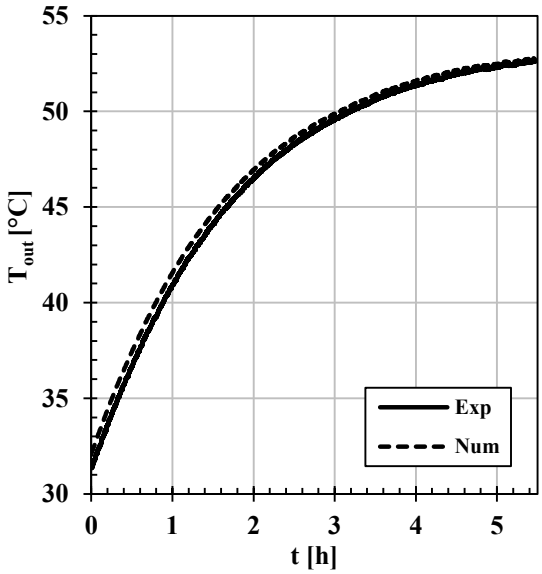

Figure 5.16. Temporal profile of the of the outlet temperature (T_{out}) of the coil HX. Experiment B2. An enhancement factor of 1.13 is multiplied by the overall thermal conductance of the coil heat exchanger.

C. Experiment B3

This experiment demonstrated the performance of the SHS tank during thermal dioding conditions. Table 5.3 provides the test procedures for Experiment B3.

Table 5.3. Input sequence for Experiment B3.

Bottom Coil HX		**Top Coil HX**	
Time interval	**Inlet temp.**	**Time interval**	**Inlet temp.**
0-3.5 h	Flow, 60°C	0-3.5 h	No flow
The flow valve was closed for 0.5 hour to reach the setpoint			
4-7 h	Flow, 40°C	4-7 h	No flow

The experiment started with water inside the tank at 27°C. The mass flow rate through the coil was maintained at around 0.05 kg/s. The temperature profiles measured at the inlet and outlet of the bottom heat exchanger, the surroundings and the nine different vertical locations inside the tank are shown in Figure 5.17. During the first period of the experiment when the inlet temperature was 60°C (higher than the bulk temperature of the tank), all the thermocouples inside the tank were typically measuring the same temperature. When the inlet temperature dropped to 40°C (lower than the bulk temperature inside the tank), natural convection heat transfer from the coil diminished, resulting in the thermal diode effect. The temperature of the fluid in the vicinity of the coil (indicated by TC1 and TC2) dropped in response to the low temperatures of the coil. The temperature at 95 mm above the coil (TC3) started to drop after about 30 minutes as a result of heat conduction to the coil region. The fluid above that region stayed at a spatially uniform hot temperature.

Figures 5.18a and 5.18b show the temperature measurements from three different thermocouples situated at the same vertical location of TC3 and TC7, respectively. The figures justify the assumption of one-dimensional thermal behavior of the proposed storage tank.

The numerical model was executed to simulate the transient performance of the tank during the experiment. The height of the bottom node was set in the model to obtain matched results between the experiment and the numerical simulation. The height was found to be approximately 58 mm from the bottom of the tank. It is worth noting that the horizontal level at which the inlet and outlet of the bottom coil heat exchanger was 63.5 mm (~2.5 in), whereas the level of the centre-plane of the coil itself was 26 mm (~1 in). As such, it is

expected that the thermal region surrounding the coil, that is the thermal diode region, should lie between these two levels.

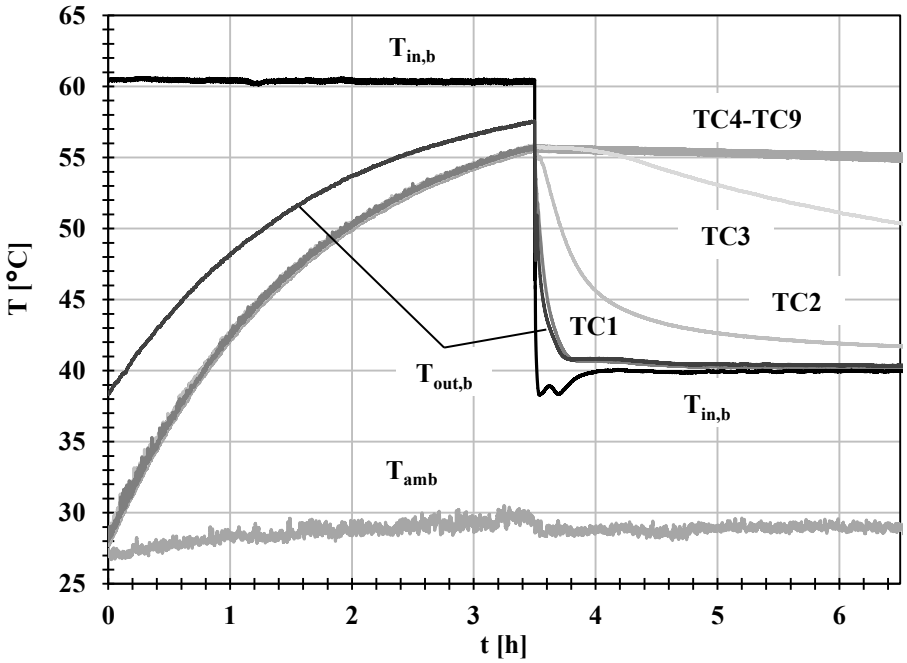

Figure 5.17. Temporal profiles of the inlet and outlet temperatures of the bottom coil HX, the temperature measurements of CVs (1-9) and the ambient temperature from Experiment B3.

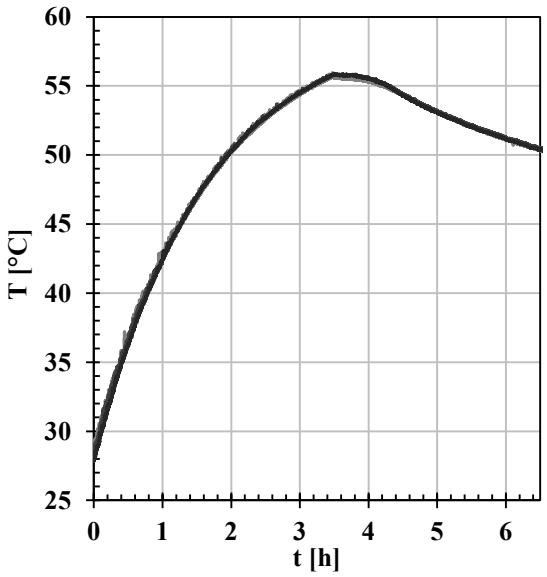

Figure 5.18a. Temporal profiles of the temperature measurements of three different thermocouples in CV3. Experiment B3.

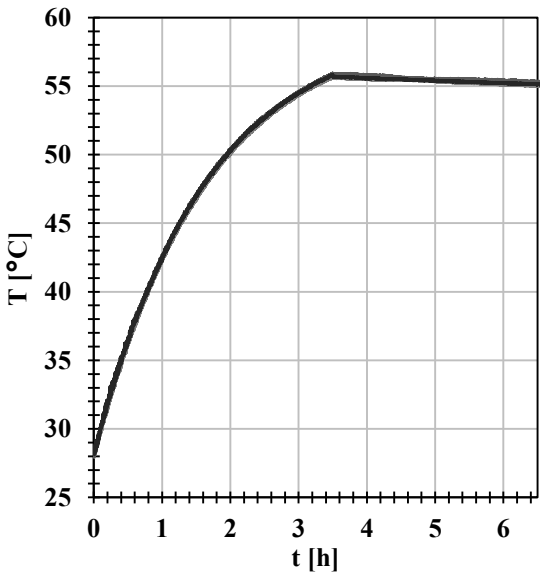

Figure 5.18b. Temporal profiles of the temperature measurements of three different thermocouples in CV7. Experiment B3.

Figure 5.19 shows agreement within ±0.5°C between the experimental and numerical temperature profiles for outlet of the heat exchanger as well as the bulk temperature of the tank (the average temperature between the middle and top nodes). Similar agreement was also noticed between the bottom node temperature calculated by the numerical model and the temperature measured by thermocouple (TC1), as seen in Figure 5.20. The predicted heat transfer rate from the coil heat exchanger is seen to lie within ±5% except during the thermal dioding, the deviation from experiments is shown in Figure 5.21 to be around ±30% due to the low heat transfer rate. These deviations were found to comply with the experimental uncertainties, described in Appendix D.

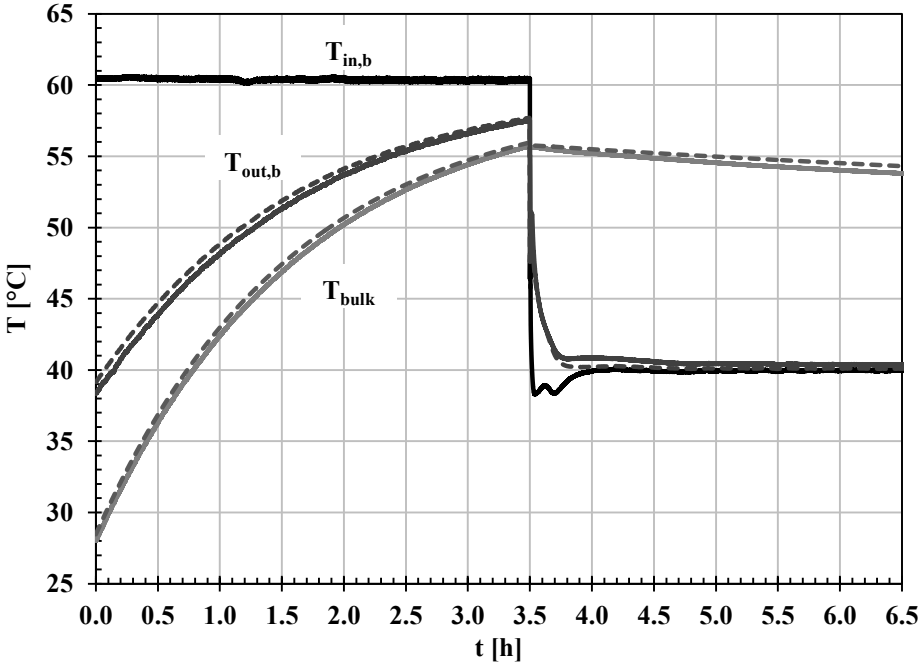

Figure 5.19. Temporal profiles of the inlet and outlet temperatures of the bottom coil HX, the bulk temperature of the tank; Experimental: the volume weighted average temperature of CVs 2-9, Numerical: the average temperature of the middle and the top nodes. Experiment B3. Solid lines: Experimental, dashed lines: Numerical.

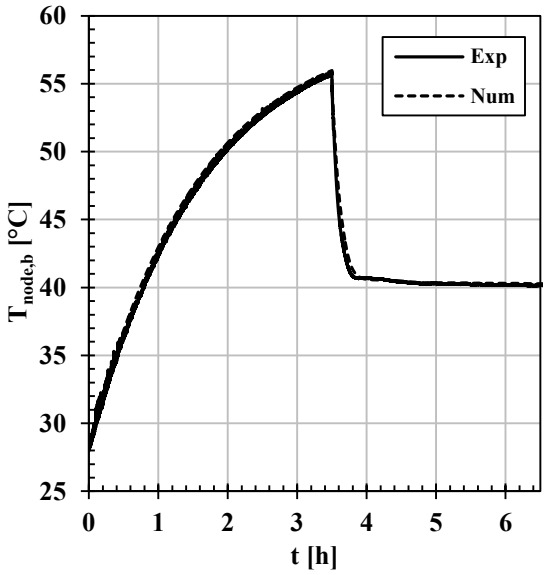

Figure 5.20. Temporal profiles of the temperature of the bottom CV; Experimental: CV1 (TC1), Numerical: Node (b). Experiment B3. Solid lines: Experimental, dashed lines: Numerical.

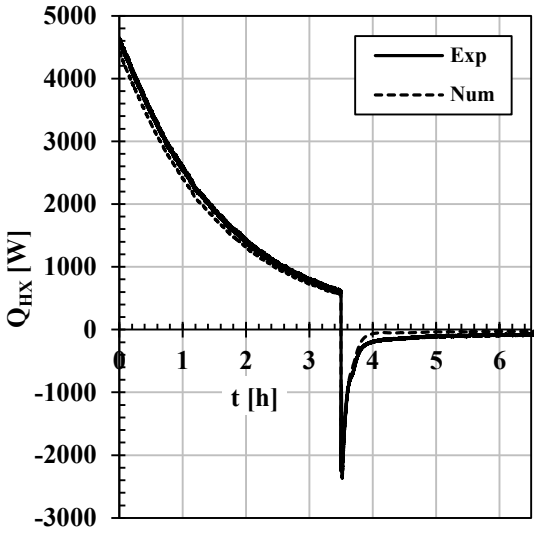

Figure 5.21. Temporal profiles of the heat transfer rate (Q_{HX}) of the bottom coil HX. Experiment B3. Solid lines: Experimental, dashed lines: Numerical.

D. Experiment B4

The thermal behavior of the SHS tank during transition between different operation modes (thermal dioding followed by mixing then thermal dioding again) was investigated in Experiment B4. The initial temperature of the water inside the tank was maintained at 50°C and the flow rate through the bottom heat exchanger was set to 0.05 kg/s. Table 5.4 presents the test procedures for Experiment B4.

Figure 5.22 shows the temperature profiles for the bulk of the tank (the average temperature between the middle and top nodes), the inlet and outlet of the bottom coil heat exchanger. As seen in Figures 5.22-5.24, satisfactory agreement, within ±0.75°C for the temperature and ±10% for the heat transfer rate, was observed between the experimental and numerical results.

Table 5.4. Input sequence for Experiment B4.

Bottom Coil HX		**Top Coil HX**	
Time interval	**Inlet temp.**	**Time interval**	**Inlet temp.**
0-3 h	Flow, 29°C	0-3 h	No flow
The flow valve was closed for 0.5 hour to reach the setpoint			
3.5-6 h	Flow, 59°C	3.5-6 h	No flow
6-7.5 h	Flow, 30°C	6-7.5 h	No flow

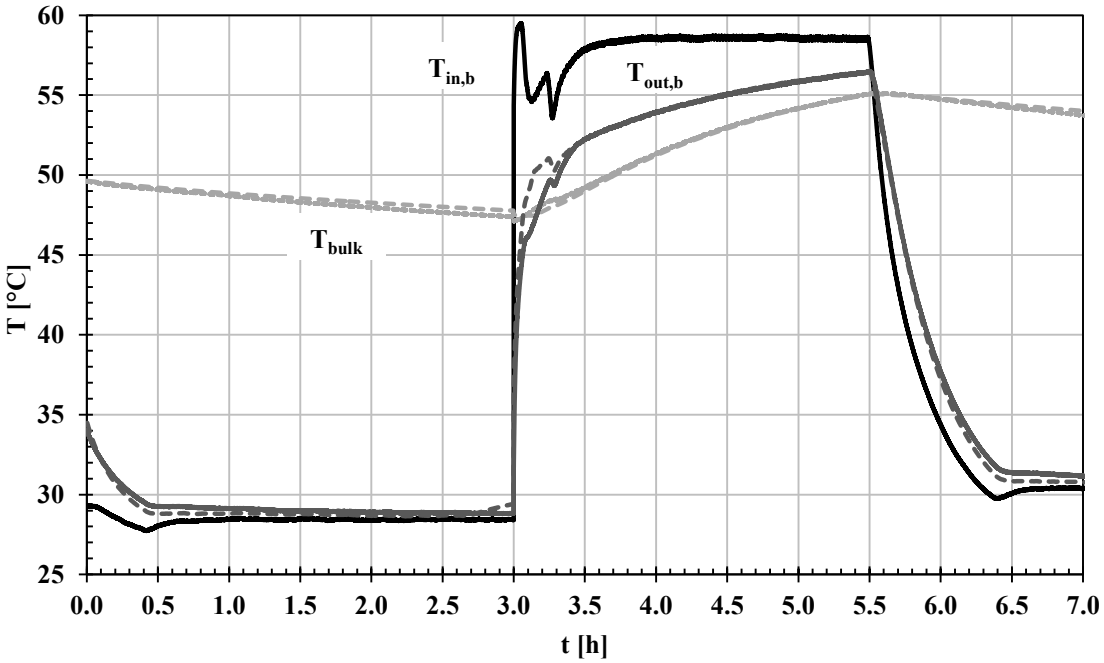

Figure 5.22. Temporal profiles of the inlet and outlet temperatures of the bottom coil HX, the bulk temperature of the tank; Experimental: the volume weighted average temperature of CVs 2-9, Numerical: the average temperature of the middle and the top nodes. Experiment B4. Solid lines: Experimental, dashed lines: Numerical.

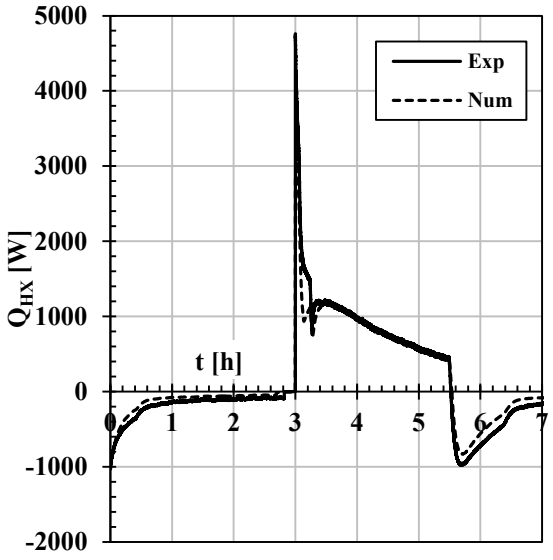

Figure 5.23. Temporal profiles of the heat transfer rate (Q_{HX}) of the bottom coil HX. Experiment B4. Solid lines: Experimental, dashed lines: Numerical.

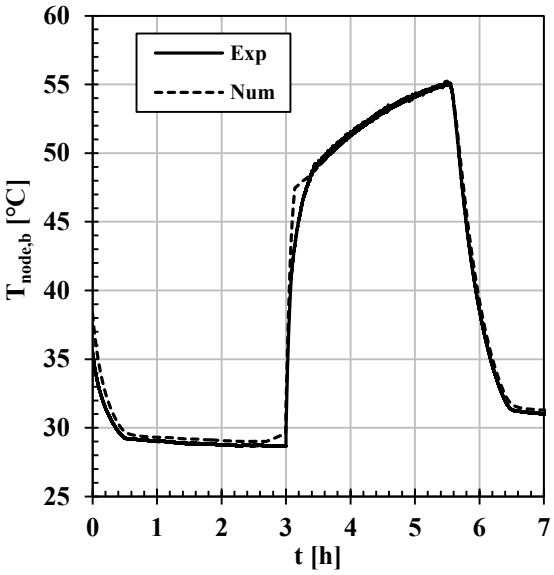

Figure 5.24. Temporal profiles of the temperature of the bottom CV; Experimental: CV1 (TC1), Numerical: Node (b). Experiment B4. Solid lines: Experimental, dashed lines: Numerical.

E. Experiment B5

Experiment B5 explored the thermal behavior of the single-tank SHS under sequential charging and discharging. Table 5.5 presents the test procedures for Experiment B5.

Table 5.5. Input sequence for Experiment B5.

Bottom Coil HX			**Top Coil HX**	
Time interval	**Mass flow rate [kg/s]**	**Inlet temperature [°C]**	**Mass flow rate [kg/s]**	**Inlet temperature [°C]**
0-3 h	0.05	58.5	0	---
3-6 h	0	---	0.05	25

The initial temperature of the water inside the tank was around 21.5°C. Figure 5.25 shows the temperature measurements in the coils and the tank. The overlap of the

measurements of TC1-TC9 indicates that the tank is fully mixed. This is a result of the strong natural convection circulations arising from the heat transfer at the coils. Agreement was also found between the experimental and numerical results, as shown in Figures 5.26 and 5.27.

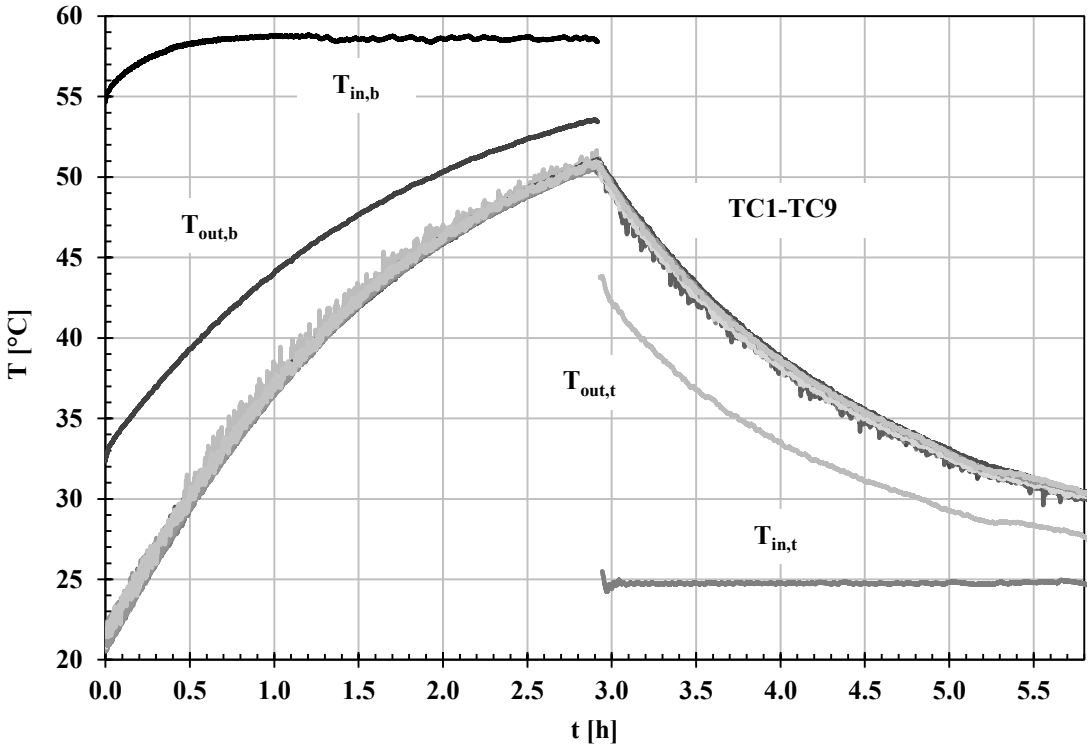

Figure 5.25. Temporal profiles of the inlet and outlet temperatures of the bottom and top coil HXs, the temperature measurements of CVs (1-9) and the ambient temperature from Experiment B5.

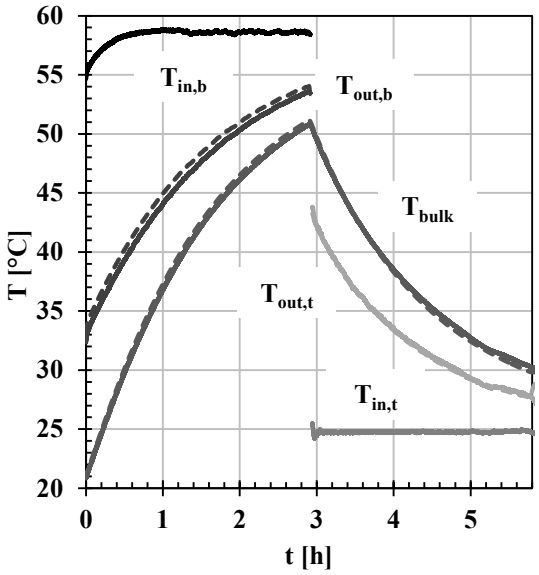

Figure 5.26. Temporal profiles of the inlet and outlet temperatures of the bottom and top coil HXs, the bulk temperature of the tank; Experimental: the volume-weighted average temperature of CVs 1-9, Numerical: the average temperature of all three nodes. Experiment B5. Solid lines: Experimental, dashed lines: Numerical.

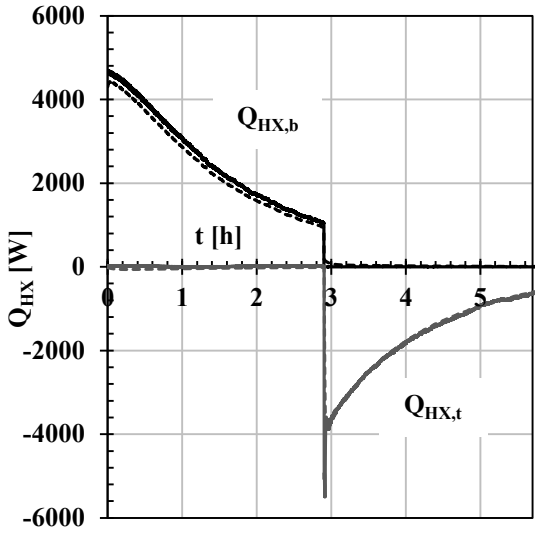

Figure 5.27. Temporal profiles of the heat transfer rate (Q_{HX}) of the bottom and top coil HXs. Experiment B5. Solid lines: Experimental, dashed lines: Numerical.

F. Experiments (C1-C7) – Single-tank HTES with PCM

In Experiments (C1-C7) PCM modules were installed inside the water tank to investigate the performance of the HTES system. These experiments were carried out, primarily, to validate the ability of the numerical model to simulate the thermal behavior of storage system with PCM modules. Table 5.6 presents the detailed specifications of Experiments (C1-C7).

Figure 5.28 illustrates the temperature profiles measured during Experiment C1 for the inlet and outlet of the bottom heat exchanger as well as for the twenty thermocouples installed inside the tank. It is shown that the existence of four PCM modules inside the tank did not interfere with the thermal mixing due to the convection currents from the coil. It is

evident that the water inside the tank was maintained at uniform temperature during the whole time of the experiment.

Table 5.6. Specifications of the sequence followed for Experiments C1-C7.

Exp.	Bottom Coil HX		Top Coil HX		# of PCM modules	Spacing between modules [mm]
	Time interval	Inlet temp.	Time interval	Inlet temp.		
C1	0-6 h	Flow, 59 °C	0-6 h	No flow	4	20
C2	0-6 h	Flow, 59 °C	0-6 h	No flow	6	20
C3	0-6 h	Flow, 59 °C	0-6 h	No flow	8	20
C4	0-6 h	Flow, 59 °C	0-6 h	No flow	6	10
C5	0-6 h	Flow, 59 °C	0-6 h	No flow	6	30
C6	0-3.25 h	Flow, 59 °C	0-3.25 h	No Flow	6	40
	3.25-6.25 h	No flow	3.25-6.25 h	Flow, 26 °C		
C7	0-2.5 h	Flow, 59 °C	0-2.5 h	No Flow	6	40
	2.5-6 h	Flow, 59 °C	2.5-4.5 h	Flow, 25 °C		
	6-7 h	No flow	4.5-7 h	Flow, 20 °C		

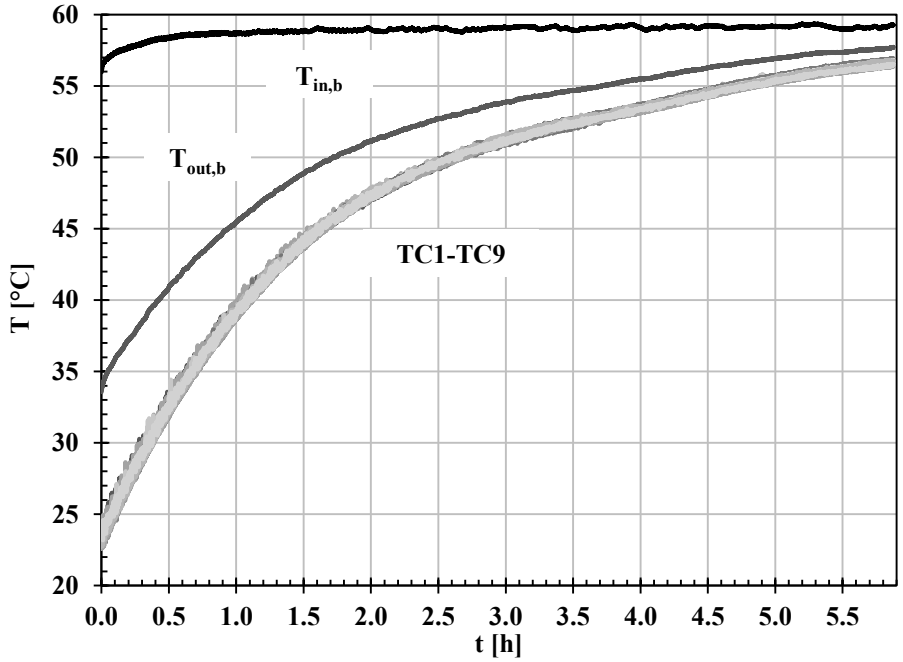

Figure 5.28. Temporal profiles of the inlet and outlet temperatures of the bottom coil HX, the temperature measurements of CVs (1-9) and the ambient temperature from Experiment C1.

The PCM parameters in the numerical model were set as shown in Table 5.7.

Table 5.7. Thermophysical properties of the PCM (Lauric acid).

Property	**Density, ρ [kg/m^3]**	**Specific heat capacity, c_s=c_l [J/kg.K]**	**Melting temperature, T_m [°C]**	**Latent heat of fusion, H_f [kJ/kg]**	**Thermal conductivity, k_s=k_l [W/m.K]**
Value	870	2150	41	182	0.17

The results of the numerical model simulation were compared to the experimental results in Figures 5.29 and 5.30. Similar figures are shown for Experiments C2-C7, Figures 5.31-5.48.

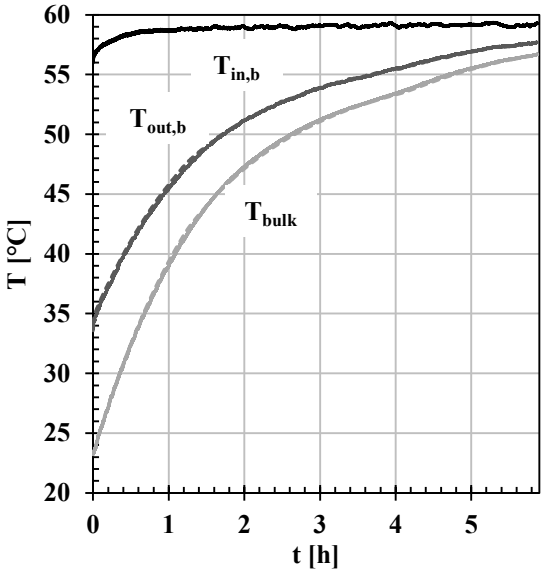

Figure 5.29. Temporal profiles of the inlet and outlet temperatures of the bottom coil HX, the bulk temperature of the tank; Experimental: the average temperature of CVs 1-9, Numerical: the average temperature of all three nodes. Experiment C1. Solid lines: Experimental, dashed lines: Numerical.

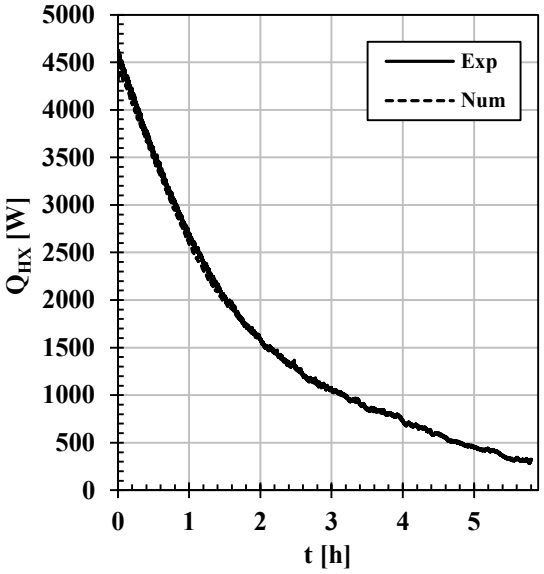

Figure 5.30. Temporal profiles of the heat transfer rate (Q_{HX}) of the bottom coil HX. Experiment C1. Solid lines: Experimental, dashed lines: Numerical.

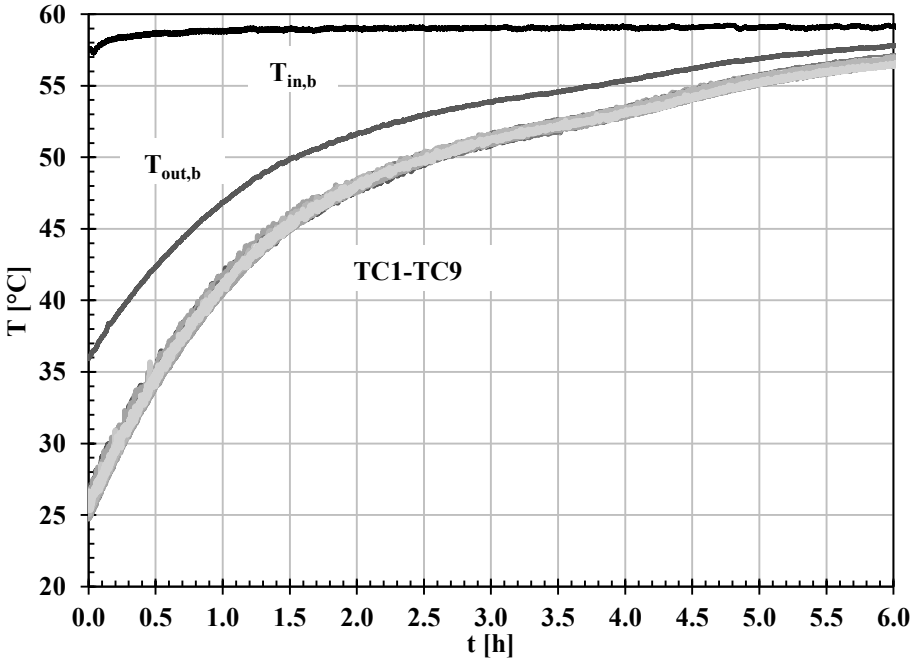

Figure 5.31. Temporal profiles of the inlet and outlet temperatures of the bottom coil HX and the temperature measurements of CVs (1-9) from Experiment C2.

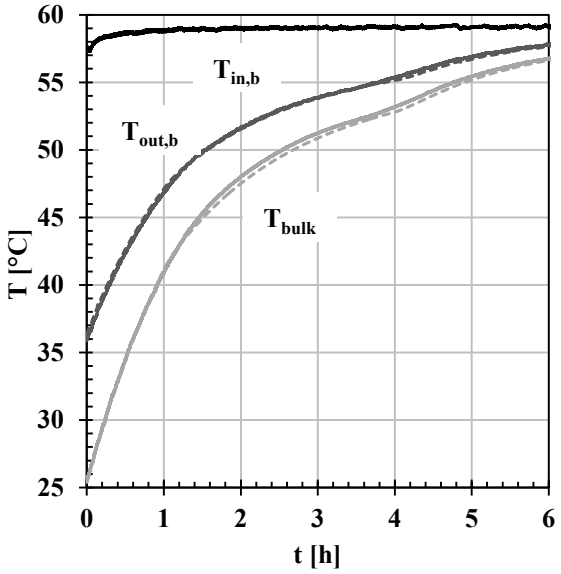

Figure 5.32. Temporal profiles of the inlet and outlet temperatures of the bottom coil HX, the bulk temperature of the tank; Experimental: the average temperature of CVs 1-9, Numerical: the average temperature of all three nodes. Experiment C2. Solid lines: Experimental, dashed lines: Numerical.

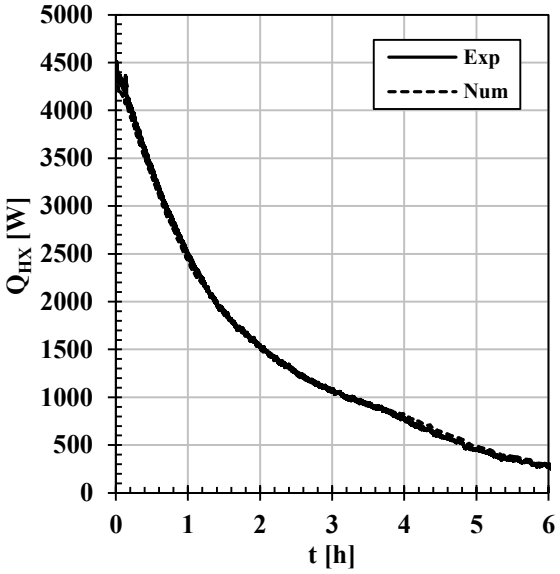

Figure 5.33. Temporal profiles of the heat transfer rate (Q_{HX}) of the bottom coil HX. Experiment C2. Solid lines: Experimental, dashed lines: Numerical.

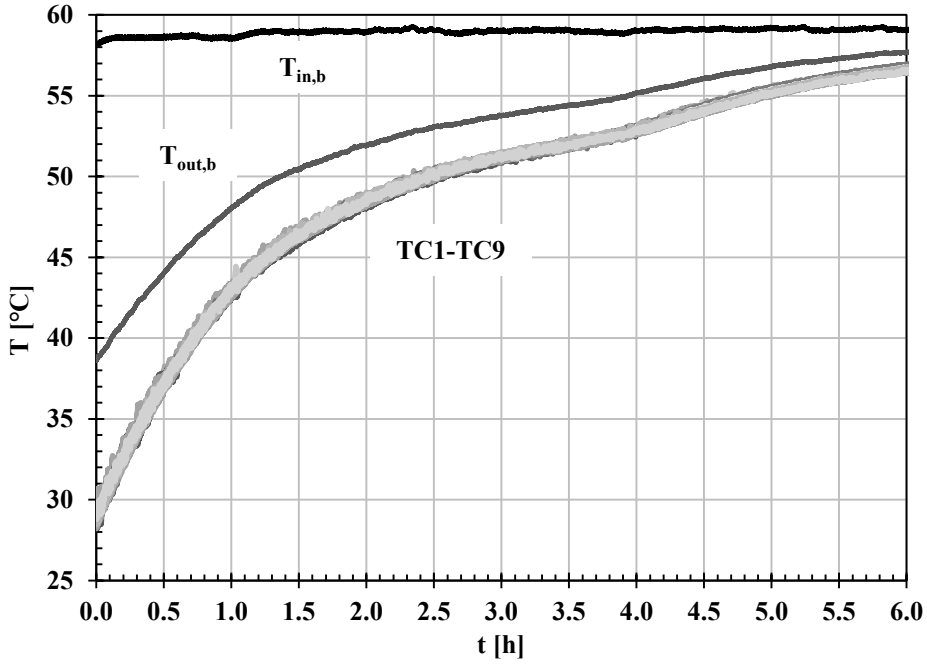

Figure 5.34. Temporal profiles of the inlet and outlet temperatures of the bottom coil HX and the temperature measurements of CVs (1-9) from Experiment C3.

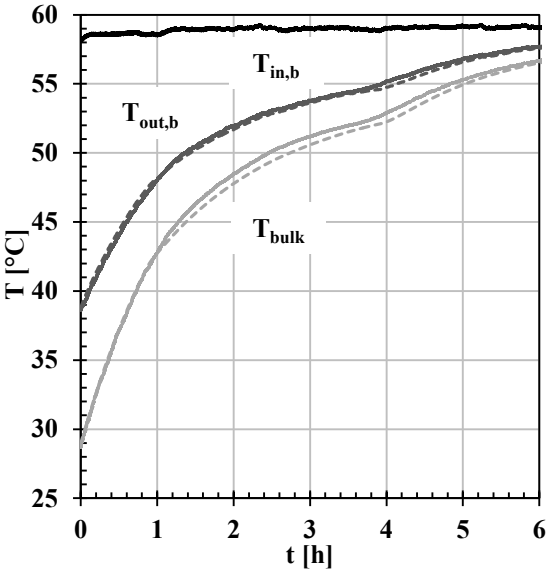

Figure 5.35. Temporal profiles of the inlet and outlet temperatures of the bottom coil HX, the bulk temperature of the tank; Experimental: the average temperature of CVs 1-9, Numerical: the average temperature of all three nodes. Experiment C3. Solid lines: Experimental, dashed lines: Numerical.

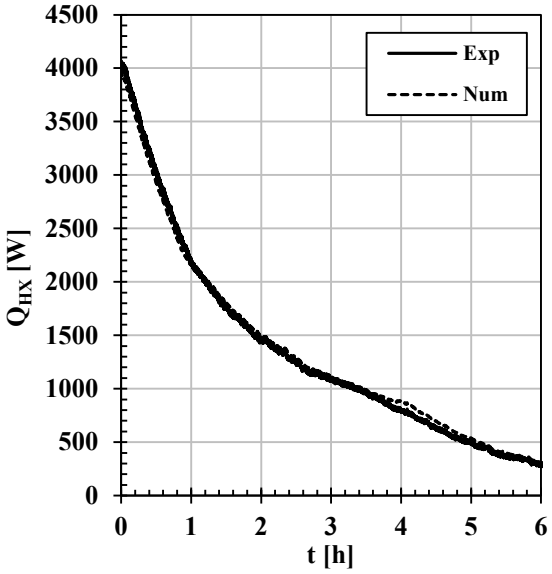

Figure 5.36. Temporal profiles of the heat transfer rate (Q_{HX}) of the bottom coil HX. Experiment C3. Solid lines: Experimental, dashed lines: Numerical.

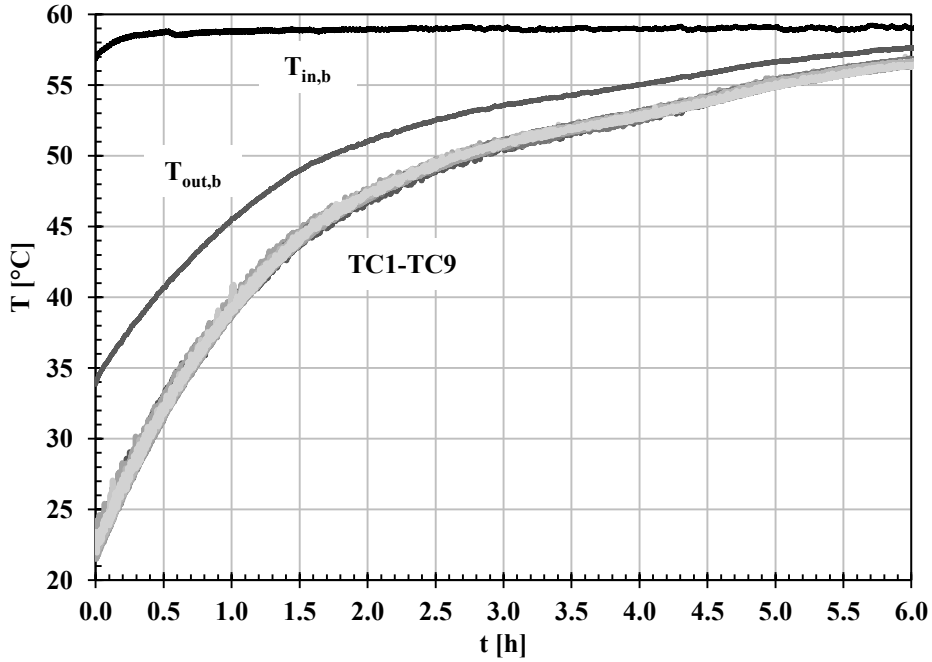

Figure 5.37. Temporal profiles of the inlet and outlet temperatures of the bottom coil HX and the temperature measurements of CVs (1-9) from Experiment C4.

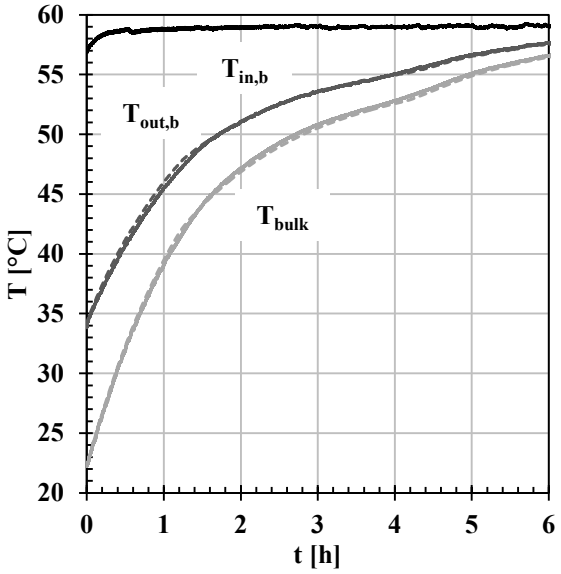

Figure 5.38. Temporal profiles of the inlet and outlet temperatures of the bottom coil HX, the bulk temperature of the tank; Experimental: the average temperature of CVs 1-9, Numerical: the average temperature of all three nodes. Experiment C4. Solid lines: Experimental, dashed lines: Numerical.

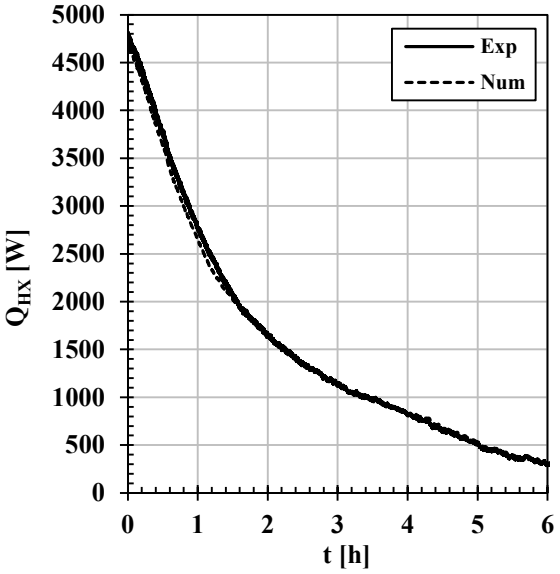

Figure 5.39. Temporal profiles of the heat transfer rate (Q_{HX}) of the bottom coil HX. Experiment C4. Solid lines: Experimental, dashed lines: Numerical.

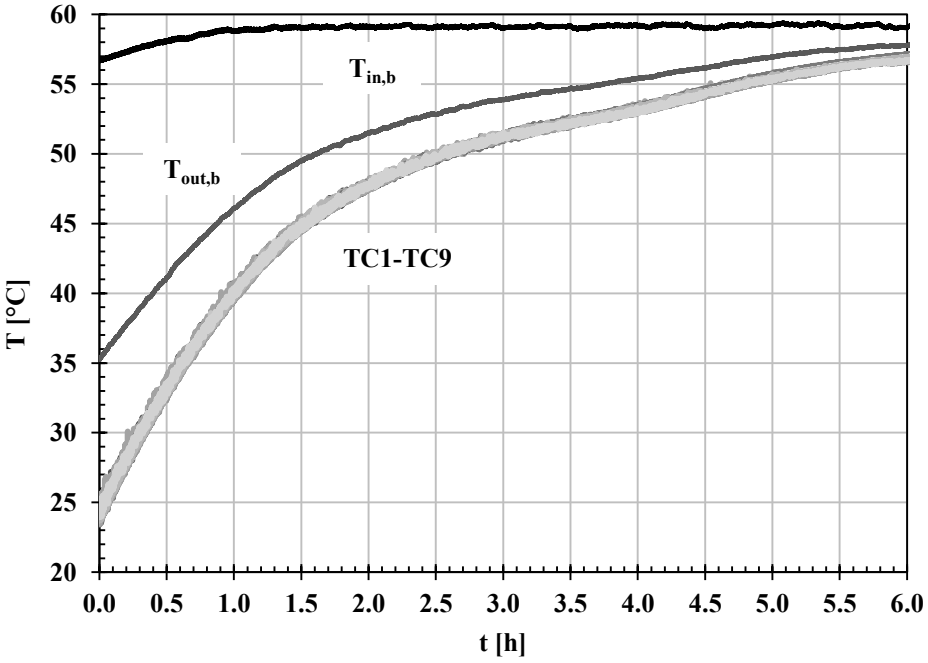

Figure 5.40. Temporal profiles of the inlet and outlet temperatures of the bottom coil HX and the temperature measurements of CVs (1-9) from Experiment C5.

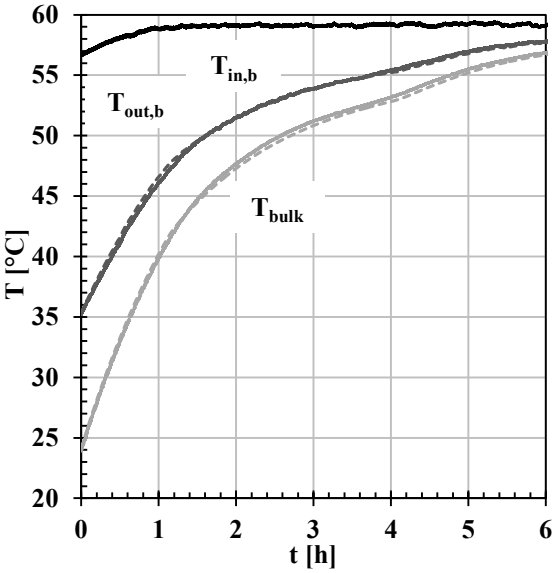

Figure 5.41. Temporal profiles of the inlet and outlet temperatures of the bottom coil HX, the bulk temperature of the tank; Experimental: the average temperature of CVs 1-9, Numerical: the average temperature of all three nodes. Experiment C5. Solid lines: Experimental, dashed lines: Numerical.

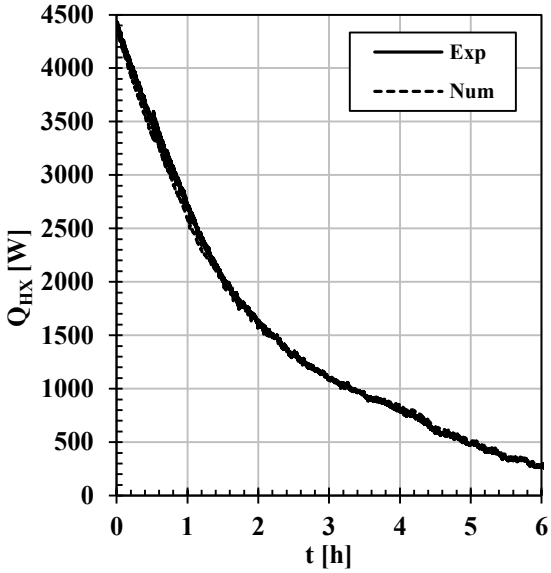

Figure 5.42. Temporal profiles of the heat transfer rate (Q_{HX}) of the bottom coil HX. Experiment C5. Solid lines: Experimental, dashed lines: Numerical.

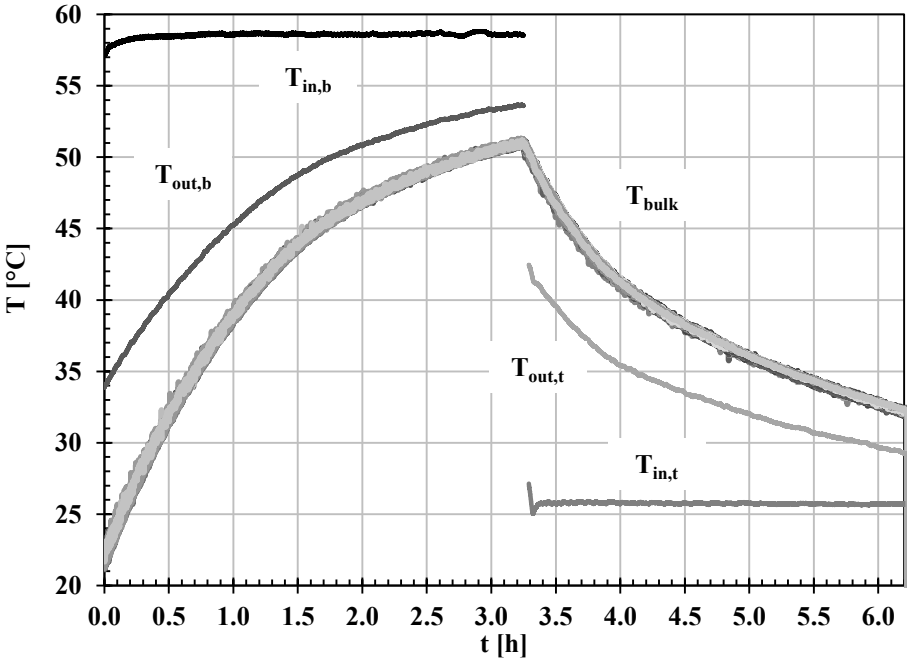

Figure 5.43. Temporal profiles of the inlet and outlet temperatures of the bottom coil HX and the temperature measurements of CVs (1-9) from Experiment C6.

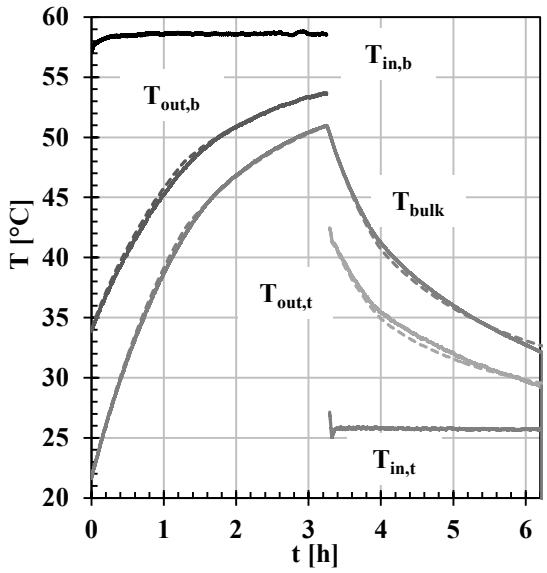

Figure 5.44. Temporal profiles of the inlet and outlet temperatures of the bottom and top coil HXs, the bulk temperature of the tank; Experimental: the average temperature of CVs 1-9, Numerical: the temperature of the middle node. Experiment C6. Solid lines: Experimental, dashed lines: Numerical.

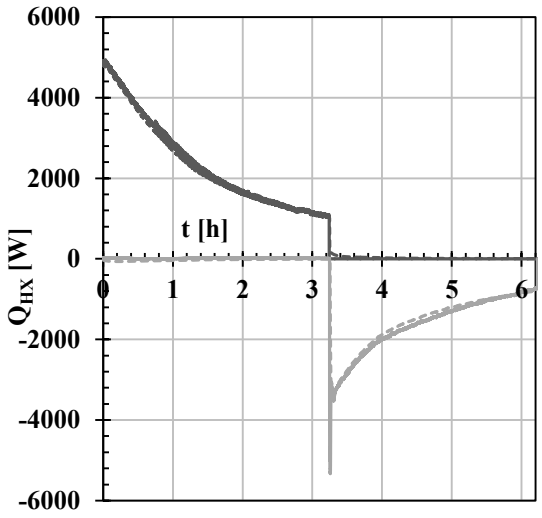

Figure 5.45. Temporal profiles of the heat transfer rate (Q_{HX}) of the bottom and top coil HXs. Experiment C6. Solid lines: Experimental, dashed lines: Numerical.

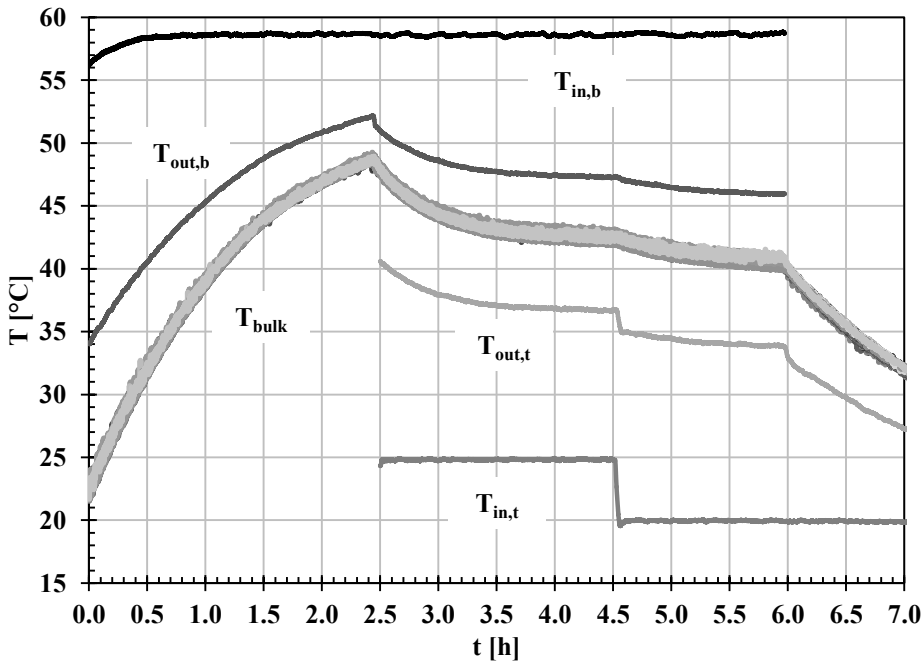

Figure 5.46. Temporal profiles of the inlet and outlet temperatures of the bottom coil HX and the temperature measurements of CVs (1-9) from Experiment C7.

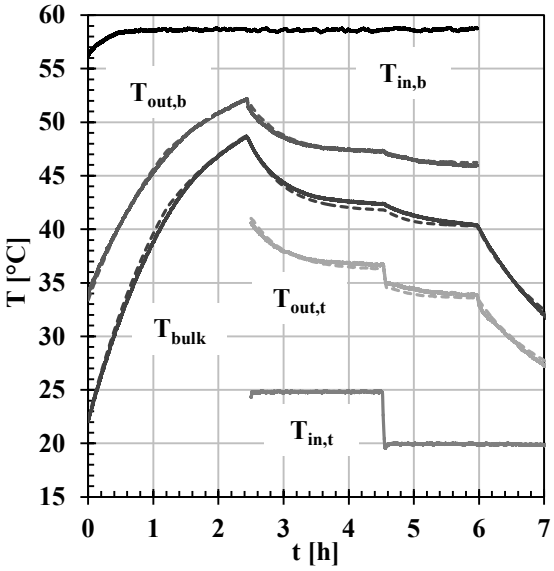

Figure 5.47. Temporal profiles of the inlet and outlet temperatures of the bottom and top coil HXs, the bulk temperature of the tank; Experimental: the average temperature of CVs 1-9, Numerical: the temperature of the middle node. Experiment C7. Solid lines: Experimental, dashed lines: Numerical.

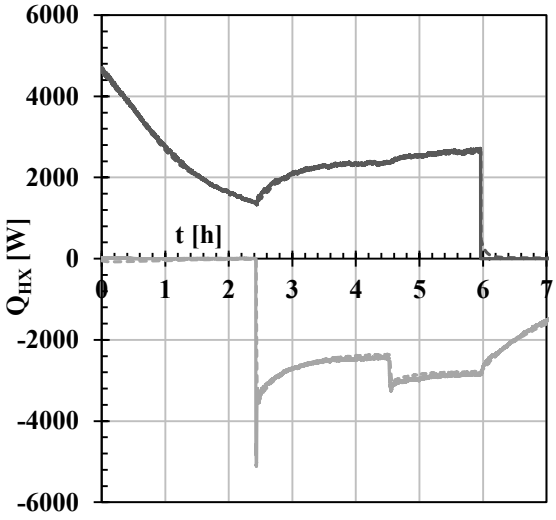

Figure 5.48. Temporal profiles of the heat transfer rate (Q_{HX}) of the bottom and top coil HXs. Experiment C7. Solid lines: Experimental, dashed lines: Numerical.

5.4. Summary

The mathematical models of the individual components of the storage tank were verified against analytical and/or benchmark solutions, presented in Appendix A. The verification cases showed that the mathematical models developed for the individual components simulate the physical behaviors accurately. The integrated model of the SHS tank was validated against experimental results presented by Mather (2000) for single and multi-tank storages. Then, the experimental study described in Chapter Four for single-tank SHS and HTES were used to ensure the validity of the mathematical model.

It can be concluded that the mathematical model was capable of accurately capturing all the physical behaviors inside the storage tank with and without PCMs. As such, the next chapter will present numerical simulations for single and multi-tank HTES systems to

explore their transient performance in realistic applications. Comparison with similar systems with water only as the storage medium will also be provided to illustrate the potential benefits of the proposed model.

CHAPTER SIX

NUMERICAL SIMULATIONS – RESULTS AND DISCUSSION

6.1. Introduction

This chapter uses the mathematical model presented in Chapter Three of this thesis to explore the performance of the multi-tank thermal storage system for a range of operating conditions. As presented in Chapter Five, the model has been systematically validated to ensure that it is able to capture the important thermophysical phenomena. Moreover, the computational efficiency of the model allows for a wide range of systems-based simulations to be performed.

The goal of this analysis is thus to develop a clear assessment of the benefits of the hybrid thermal energy storage (HTES) in comparison with a sensible heat storage (SHS) in the context of a solar domestic hot water system. A systematic assessment is performed. It begins with a single tank operating under controlled inlet temperatures at both the top and bottom coils. An extensive parametric analysis is presented to highlight the effect of the key design parameters. The analysis is then extended to a single-tank solar thermal system. The impact of different types of household domestic hot water load is explored in this context. Finally, the systems analysis is applied to a multi-family residential unit in which multi-tank modular thermal storage is required.

6.2. Single-tank Thermal Energy Storage: SHS versus HTES

In this section, the effect of introducing PCM modules on the performance of the HTES tank is explored and compared to that for a SHS tank. Numerical simulations were carried out for both systems, shown in Figures 6.1a and 6.1b, during charging through the bottom coil heat exchanger with a fixed mass flow rate ($\dot{m}_b$) and inlet temperature ($T_{in,b}$).

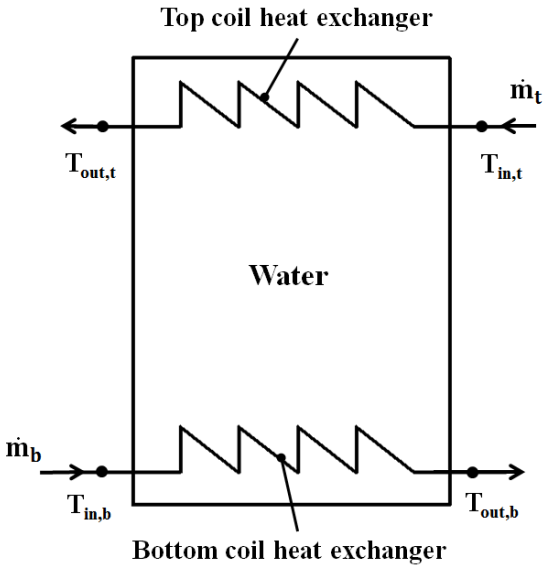

Figure 6.1a. Schematic for the SHS element.

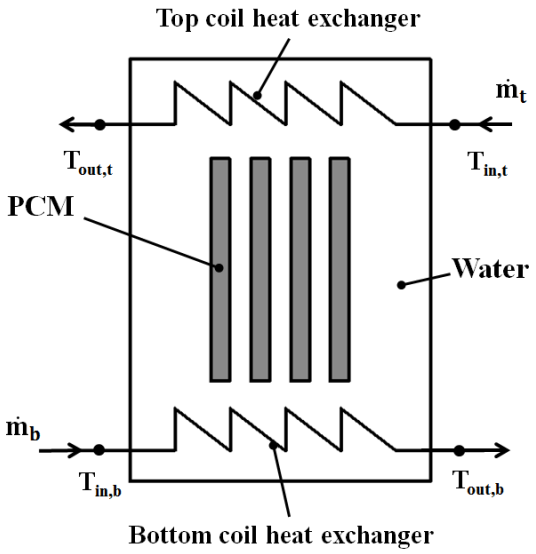

Figure 6.1b. Schematic for the HTES element with rectangular PCM modules.

The top coil heat exchanger was idled. Both tanks have a square cross-section of 0.53 m x 0.53 m and 0.72 m in height yielding a nominal tank volume of 200 L. The tanks were assumed to be perfectly adiabatic. The top and bottom heat exchangers were square spiral copper coils of length 7.5 m. Each coil had an inner diameter of 0.019 m (3/4 in) and an outer diameter of 0.022 m (7/8 in). Thirteen rectangular PCM modules were used in the HTES tank; 0.5 m in height, 0.51 m in length and 0.03 m in thickness. The modules were arranged inside the tank with a spacing of 10 mm between adjacent modules. The volume of the PCM

inside the tank was approximately 99 l (~50% of the tank volume). The thermophysical properties for water and Lauric acid are provided in Tables 6.1 and 6.2, respectively.

Table 6.1. Thermophysical properties of water.

Property	**Value**
Density (ρ_w)	998 (kg/m^3)
Specific heat capacity (c_w)	4.183 (kJ/kg.K)
Thermal conductivity (k)	0.63 (W/m.K)
Dynamic viscosity (μ)	0.75×10^{-3} (Pa.s)
Thermal Expansion coefficient (β)	0.35×10^{-3} (K^{-1})

Table 6.2. Thermophysical properties of Lauric acid.

Property	**Value**
Density (ρ_{PCM})	870 (kg/m^3)
Specific heat capacity (c_{PCM})	2.15 (kJ/kg.K)
Melting temperature (T_m)	45 (°C)
Latent heat of fusion (H_f)	182 (kJ/kg)
Liquid thermal conductivity (k_l)	0.15 (W/m.K)
Solid thermal conductivity (k_l)	0.15 (W/m.K)

A simulation was performed in which water at 60°C flows through the bottom coil at a flow rate of 0.05 kg/s for a period of 8 hours. Both systems are initially at 20°C. The predicted fluid temperatures for both tanks and the PCM melt fraction are shown in Figure 6.2. The water temperature for the SHS tank follows the expected exponential behavior. With PCM present, however, three distinct transient behaviors are observed. At early times the water temperature initially increases at a faster rate as a result of the low specific heat

capacity of the PCM. Once the temperature of the HTES tank reaches the melting temperature of the PCM (after around 1.4 hours), the water temperature profile flattens until the PCM is fully molten at about 6.8 hours. Beyond 6.8 hours, energy storage is through sensible heating of the PCM. Kinks in the temperature profile appear at both the start and end of melting as a result of the change in the heat transfer phenomena. In comparison to the SHS system, it is seen that the presence of PCM in the tank acts to modulate the water temperature by reducing the rate of increase of water temperature during the melting period.

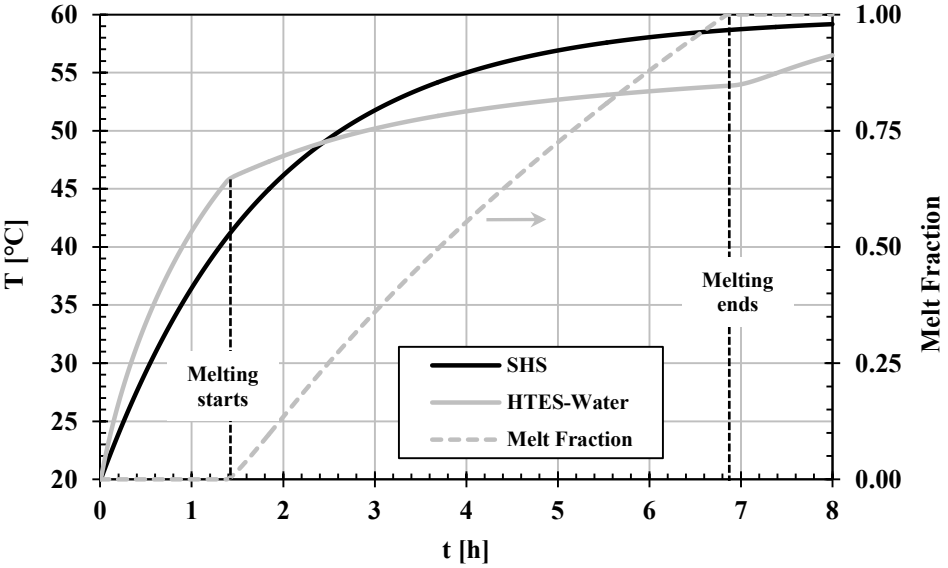

Figure 6.2. The temporal profiles of the water temperature in the SHS and HTES tanks and the melt fraction of the PCM in the HTES tank during charging from the bottom coil heat exchanger. Left axis: Temperature [°C]. Right axis: Melt Fraction.

The coil heat transfer rate is shown in Figure 6.3. The SHS heat transfer follows an exponential behavior with the heat transfer decreasing as the water temperature increases. In contrast, the modulation feature of the PCM in the HTES tank is seen to maintain higher potential temperature difference between the heat exchanger and the water inside the tank. This leads to higher heat transfer rate from the coil heat exchanger during the period in which the PCM is melting. It is also seen that during the time period when the PCM is storing

energy in the form of sensible heat (i.e., before the dashed line in Figure 6.3), the charging rate of the HTES is lower than that of the SHS. This is due to the low specific heat capacity of the PCM. This observation explains the reason why storage systems utilizing PCMs show better performance than SHS systems when the time scales of the charging and/or discharging are large (de Gracia *et al.* 2011).

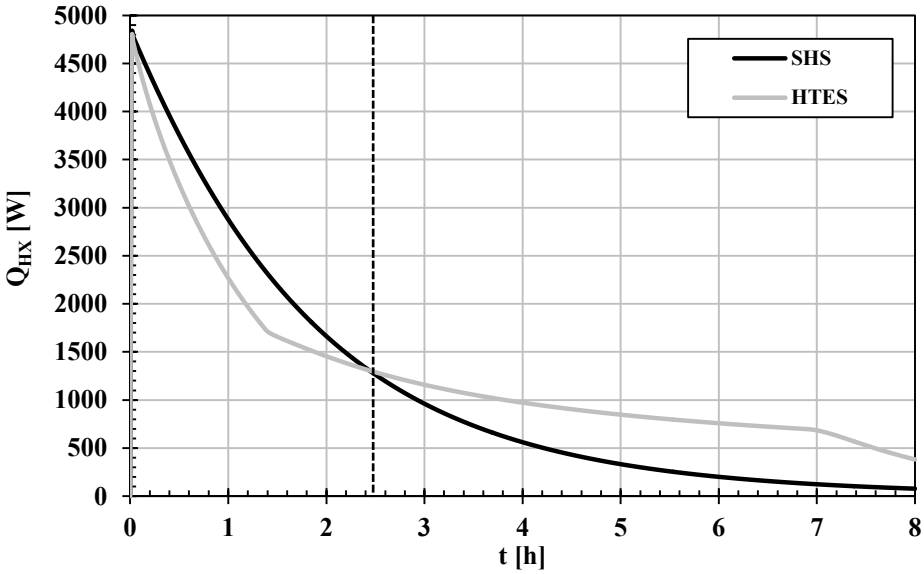

Figure 6.3. The temporal profiles of the bottom coil heat transfer rate in the SHS and HTES tanks during charging.

The corresponding energy stored in each tank is shown in Figure 6.4. The presence of the PCM results in a moderate increase in the energy storage capacity of the tank by the end of the 8 hour charging period. This moderate gain is a result of the relatively large temperature range that the tank is exposed to since the tank is initially at 20^{o}C and the coil temperature is 60^{o}C. As such, the HTES system is penalized by the poor sensible storage property of the PCM. The storage gain of the HTES over the SHS tanks is also plotted in Figure 6.4. The storage gain is defined as the percentage of excess energy stored in the HTES tank compared to that stored in the SHS tank:

$$Storage\ Gain\ [\%] = (\frac{E_{stored,HTES}}{E_{stored,SHS}} - 1) \times 100 \quad (6.1)$$

The dashed line in the figure (at t=5.2 h) illustrates the breakeven point of the HTES; the time after which the storage gain has a positive value. Before this time the energy stored in the SHS tank is larger than that stored in the HTES tank owing primarily to the low heat capacity of the PCM compared to water. However, it is seen that by the end of the charging process the HTES tank stored approximately 16% more energy than the SHS tank.

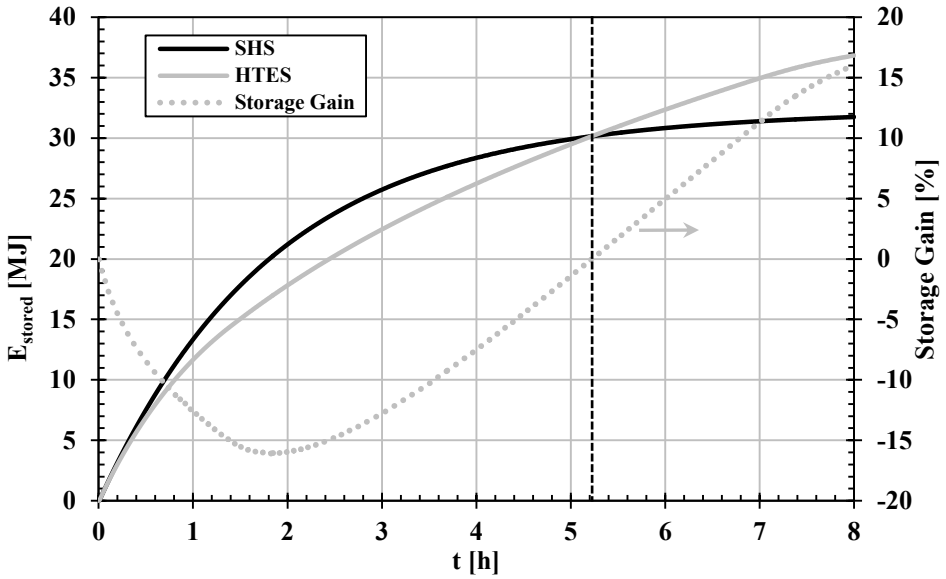

Figure 6.4. The temporal profiles of the total energy stored in the SHS and HTES tanks and the storage gain during charging from the bottom coil heat exchanger. Left axis: Energy stored [MJ]. Right axis: Storage Gain [%].

Another feature that is worth mentioning in the HTES element is the effect of the PCM on the outlet temperature from the bottom coil heat exchanger. Figure 6.5 shows the temporal profiles of the outlet temperature from the coil heat exchanger for both tanks. The heat transfer fluid exits the coil initially at 20°C and after the transit time of the coil (approximately 45 s), the outlet temperature increases to 37°C. It is shown that the outlet temperature from the coil in the HTES tank is influenced by the existence of PCM. The

outlet temperature in the HTES tank is observed to be lower than that from the coil of the SHS tank for almost 70% of the charging time. Such feature is advantageous to the performance of the storage element when integrated in a solar hot water system. For instance, when the HTES tank is installed into a solar collector loop, the return temperature to the solar collector will be lower than that from a similar SHS tank. This will act to reduce the thermal losses from the collector and hence, increase the efficiency of the collector. This highlights the potential gains in the collected energy that can be achieved by integrating the proposed storage tank in solar thermal systems. Similar results can be obtained if the storage element is integrated in a waste heat recovery system. The passive control of the HTES tank on the temperature of the fluid returning to the energy supply can be utilized to enhance the effectiveness of the heat exchange between the supply and the heat transfer fluid.

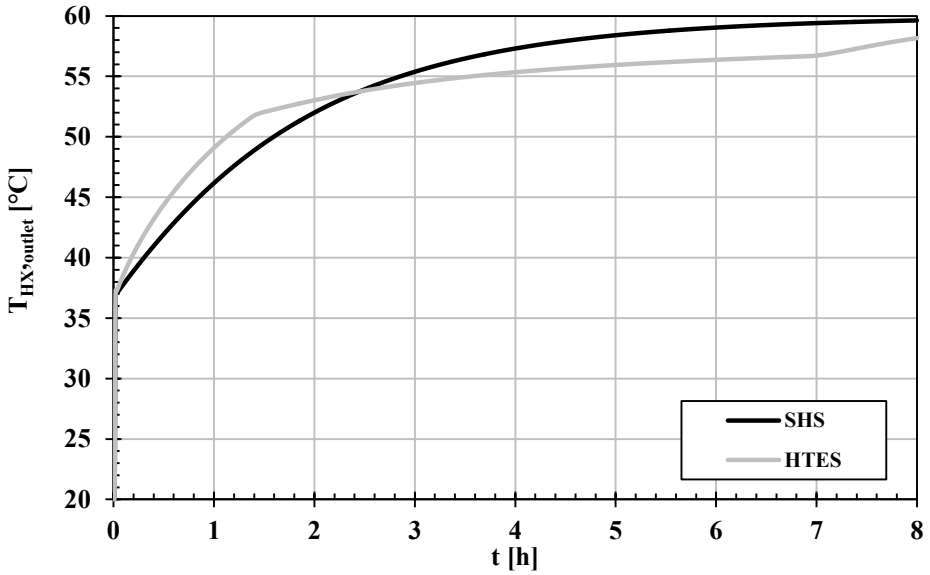

Figure 6.5. Bottom coil outlet temperature transient for the SHS and HTES tanks.

The previously shown results provide basic understanding of the key differences between the conventional SHS and the proposed HTES with PCMs. In addition, it sheds the

light on the potential benefits of the PCMs when integrated in the storage tank. These benefits can be summarized as follows:

1. The existence of PCM modulates the operation temperature of the HTES water while the PCM undergoes phase transformation.
2. The temperature modulation feature helps to improve the heat transfer rate between the heat exchanger and the storage medium, yielding higher storage gains.
3. The temperature modulation feature also extends to reducing the outlet temperature from the charging coil heat exchanger (i.e., the return temperature to the supply). This should result into improvement in the effectiveness of the heat exchange between the heat transfer fluid and the supply.

While PCMs have a high energy storage capacity when undergoing phase change, those materials are penalized by low specific heat in comparison to water. The theoretical storage gain for the hybrid system is shown below.

$$Storage\ Gain\ [\%] = [\varphi \frac{\rho_{PCM}}{\rho_w} \frac{H_f}{c_w \Delta T_{SHS}} + (1-\varphi) \frac{\Delta T_{HTES}}{\Delta T_{SHS}} + \varphi \frac{\rho_{PCM} c_{PCM}}{\rho_w c_w} \frac{\Delta T_{HTES}}{\Delta T_{SHS}} - 1] \times 100 \quad (6.2)$$

The value of φ represents the fraction of the tank volume occupied by the PCM. The values of ΔT_{HTES} and ΔT_{SHS} are the maximum changes in temperature of the HTES and the SHS tanks, respectively. It can be concluded from the above equation that the benefits from the proposed HTES can be hypothetically maximized by

1. Decreasing the temperature swing on the SHS tank (ΔT_{SHS}). This may be impractical since the temperature swing of the storage element is a consequence of the boundary

conditions as well as the design parameters of the system such as the tank size, the heat exchanger effectiveness, etc. However, this highlights that applications with a reduced operating temperature range can benefit from PCM based thermal storage.

2. Increasing the volume fraction of the PCM. This will lead to more energy stored in the form of latent heat provided that there is enough energy supply. This will result into enhanced temperature modulation since less energy is stored in the sensible form.
3. Selecting PCM with larger density (ρ_{PCM}), specific heat capacity (c_{PCM}) and latent heat of fusion (H_f).

In practice, implementing these techniques to enhance the storage gain of the HTES is not straightforward. For instance, increasing the latent heat of fusion (H_f) is expected to increase the amount of energy stored in the latent form. However, it will decrease the sensible energy due to lower temperature change of the tank (ΔT_{HTES}). This demonstrates the need for optimization of the various key parameters of the HTES element in order to better understand the true realizable benefits over the conventional SHS element. In addition, the above equation does not account for the coupling effect or the feedback mechanism between the storage element and the energy supply. Any change in any of the design parameters of the storage element will influence the performance of the energy supply which will reflect back on the efficiency of the storage element.

The performance of the storage element is expected to be influenced by various boundary conditions and design parameters;

1. **Boundary Conditions**. These involve all the parameters imposed on the storage element from the external system where it is installed. These include the inlet flow

rates and temperatures to the bottom and top coil heat exchangers and the operation time intervals for both coils.

2. **Design Parameters**. These involve the parameters chosen by the designer for the different components of the storage element. These include the size of the tank, the locations and dimensions of the coil heat exchangers, the number of PCM modules, the dimensions of the PCM module and the thermophysical properties of the PCMs.

6.2.1. Sequential Charging/Discharging Operation: Parametric Analysis

In order to provide a comprehensive picture of the effect of the key parameters of the HTES element on the storage performance, simulations were carried out to investigate the dynamic behavior of the HTES versus the SHS tanks during sequential operation of the bottom and top heat exchangers. In these simulations, the boundary conditions were fixed such that the mass flow rates through the heat exchangers were $\dot{m}_b = \dot{m}_t = 0.05$ kg/s and the inlet temperatures to the bottom and top coils were $T_{in,b}$=60°C and $T_{in,t}$=30°C, respectively. Also, the sequential operation was adjusted as illustrated in Figure 6.6; the bottom coil operated solely for 8 hours followed by 8 hours when the top coil operated solely.

The same tank and PCM geometries were used as in the previous study. In order to remove the influence of initial conditions, the charge/discharge cycle was repeated until a periodic steady state was reached. The sequential operation of the storage element represents a simplified case of the operation in realistic systems when the supply and demand are out of phase. However, the inlet temperatures to the heat exchangers are fixed in order to reduce the complexity associated with the coupling effects with the supply and demand loops.

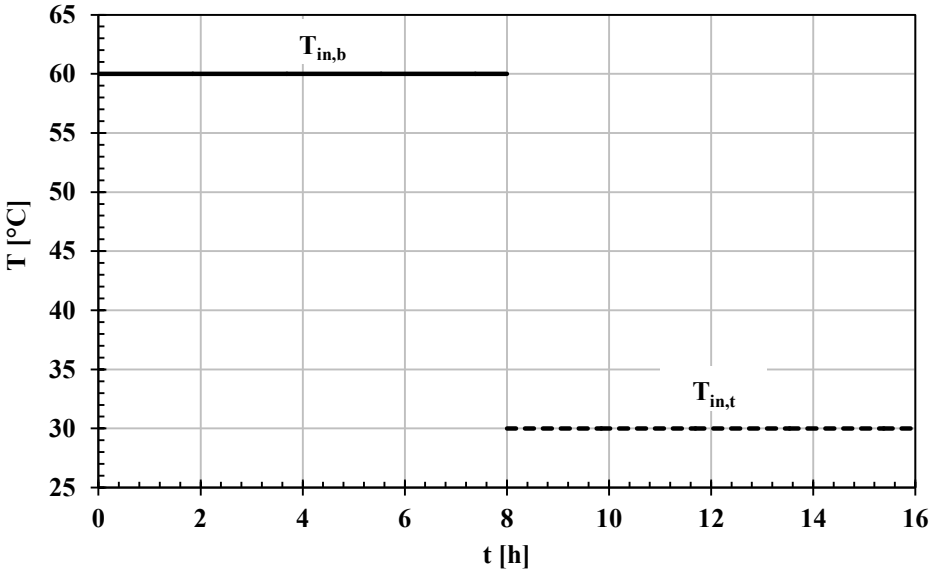

Figure 6.6. The temporal profiles of the inlet temperature to the bottom and top heat exchangers during the sequential charging/discharging operation. Solid line: the inlet temperature to the bottom coil. Dashed line: the inlet temperature to the top coil.

Applying the energy equation to the storage element, the energy stored can be calculated at any time (assuming that the energy is equal to zero initially):

$$\int_0^t Q_{HX,b}\, dt + \int_0^t Q_{HX,t} = E_{stored}(t) \tag{6.3}$$

During steady state operation, the energy equation yields:

$$\int_0^\tau Q_{HX,b}\, dt + \int_0^\tau Q_{HX,t} = 0 \tag{6.4}$$

The value of τ represents the cycle time. This indicates that the energy stored during the charging process should equate to the energy recovered during the discharging process given that the tank is perfectly insulated. As such, the convergence criterion for the steady state simulations was chosen to be:

$$\frac{E_{stored}(\tau) - E_{stored}(0)}{E_{stored}(0)} \leq 0.1\% \tag{6.5}$$

Figure 6.7 shows the predicted temperature transients and melt fraction for the SHS and the HTES tanks operating under steady state sequential charging/discharging cycle.

Looking at the temporal profiles of the stored/recovered energy in the SHS and the HTES tanks in Figure 6.8, it is seen that the HTES tank can handle approximately 27.5% more energy than the SHS tank. It can be concluded that the operation scenario has a critical influence on the storage gain realized from the HTES element.

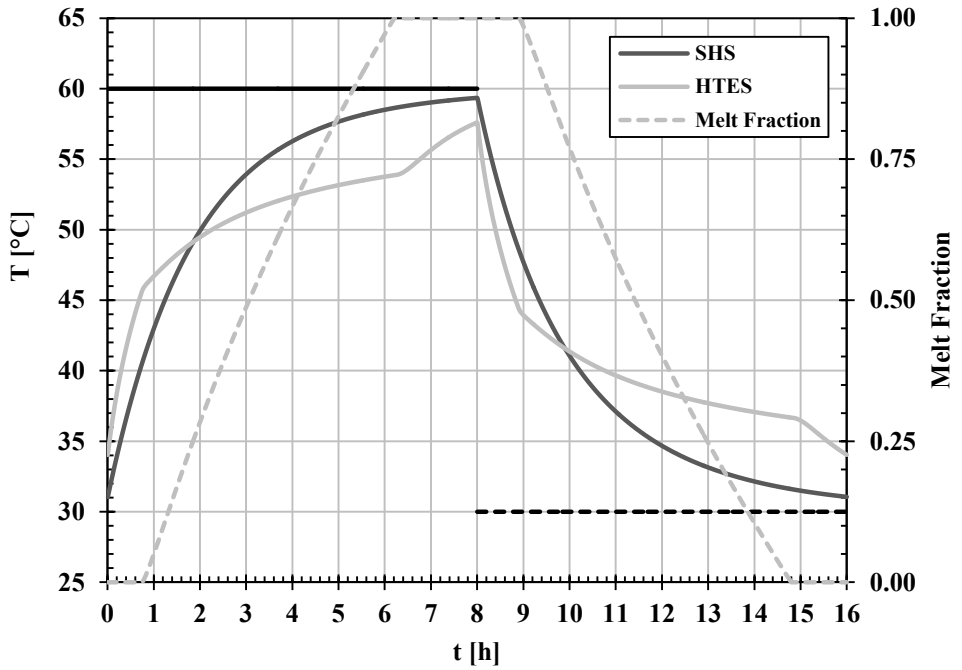

Figure 6.7. The temporal profiles of the water temperature in the SHS and HTES tanks and the melt fraction of the PCM in the HTES tank during the sequential charging/discharging steady state (cyclic) operation. Left axis: Temperature [°C]. Right axis: Melt Fraction.

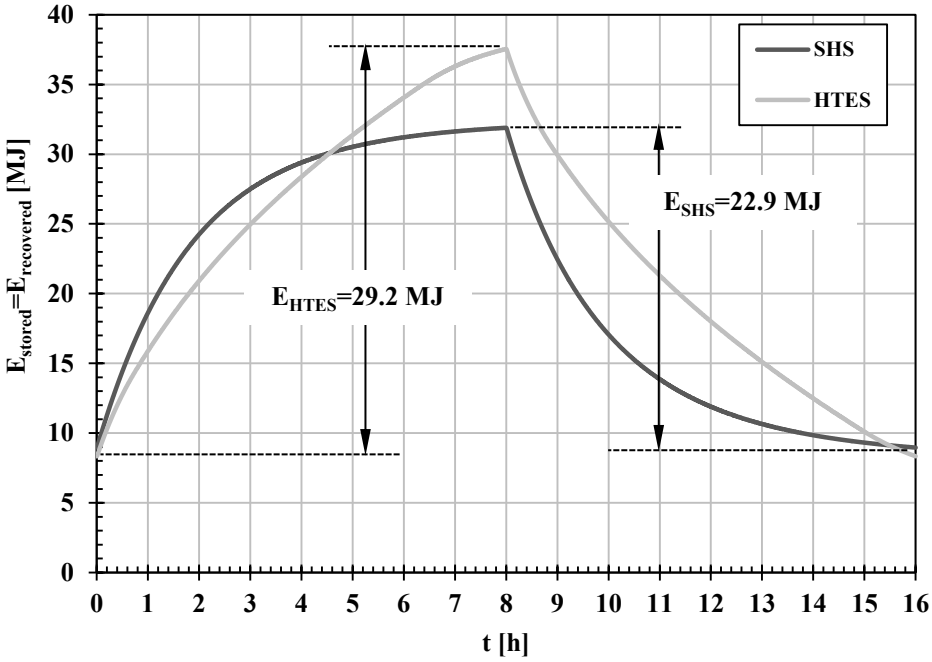

Figure 6.8. The temporal profiles of the total energy stored/recovered in the SHS and HTES tanks during the sequential charging/discharging steady state (cyclic) operation.

In the next section, a parametric analysis was undertaken to investigate the effect of key design parameters on the dynamic performance of the SHS and HTES elements during steady state sequential charging and discharging. This analysis is meant to illustrate the fundamental differences between both storage elements in applications where the energy supply and demand are out of phase. Although this operation scenario does not resemble the operation of thermal storage elements in actual applications, yet they will provide a closer representation of the realistic behavior.

A set of numerical simulations were performed to investigate the isolated influence of the key design parameters of the HTES element on the storage gain. During these simulations, the boundary conditions were fixed such that the mass flow rates through the heat exchangers were $\dot{m}_b = \dot{m}_t$=0.05 kg/s and the inlet temperatures to the bottom and top

coils were $T_{in,b}$=60°C and $T_{in,t}$=30°C, respectively. Also, the sequential operation was adjusted as illustrated in Figure 6.6.

A base case was chosen to pivot the parametric analysis. The same tank, coil, and PCM module geometry as used previously was considered. The number of the PCM modules used in the base case was reduced to eight which yielded a PCM volume fraction of about 30%. A module spacing of 10 mm was maintained. The thermophysical properties of water and PCMs were assumed as shown in Tables 6.1 and 6.2. The parametric analysis was undertaken such that each parameter was varied individually while maintaining all other parameters at their base case values. The key design parameters and their studied values are presented in Table 6.3.

Table 6.3. Key design parameters for the HTES

Design parameter (symbol)	**Values**	**Unit**
PCM volume fraction (φ)	0.1, **0.3***, 0.4, 0.5	---
PCM melting/solidification temperature (T_m)	30, 40, **45**, 50, 60	°C
Density of PCM (ρ_{PCM})	700, 800, **870**, 1000	kg/m^3
Specific heat capacity of PCM (c_{PCM})	1.0, **2.15**, 3.0, 4.18	kJ/kg.K
Latent heat of fusion of PCM (H_f)	100, **182**, 250, 300	kJ/kg
Thermal conductivity of PCM (k_{PCM})	0.1, **0.17**, 1.0, ∞	W/m.K
PCM module thickness (w_{PCM})	10, 20, **30**, 40, 60	mm
Length of coil heat exchangers (L_{coil})	**7.5**, 37.5, 75, 375	m

* The base case parameters.

A. Effect of PCM Volume Fraction (φ)

The effect of the PCM volume fraction was explored by running four numerical simulations with different number of PCM modules placed inside the HTES tank. For the

chosen dimensions of the PCM module, the maximum volume fraction of PCM that can be placed inside the tank while maintaining 10 mm spacing between modules is approximately 0.5 (13 modules). Table 6.4 presents the geometrical constants pertaining to the chosen volume fractions.

Table 6.4. Geometrical constants corresponding to the PCM volume fraction.

	PCM Volume Fraction (φ)			
	φ=0.1	**φ=0.3**	**φ=0.4**	**φ=0.5**
Number of modules	3	8	10	13
Total volume [L]	22.8	60.8	76.1	98.9
Actual volume fraction (V_{tank}=200 L)	0.11	0.30	0.38	0.49
Total surface area of PCM module [m^2]	1.52	4.06	5.07	6.59

Figure 6.9 illustrates the effect of the PCM volume fraction on the temporal profiles of the water temperature inside the HTES tank. The profile for the water temperature inside the SHS tank operating is also shown for comparison.

During charging (the first 8 hours), as the PCM volume fraction increases, the specific heat capacity of the HTES decreases; leading to a faster rise in the temperature of the tank and earlier initiation of melting. During melting, the water temperature is observed to flatten more towards the melting temperature of the PCM creating a greater temperature modulation effect. This is attributed to the linear increase in the total surface area of the PCM modules with the increase of volume. This results into a reduction in the thermal resistance between the water and the PCM modules and consequently, the temperature of the water approaches the surface temperature of the PCM module. When the melting ends the

temperature profiles are observed to kink due to the superheating of the liquid PCM. Again the rate of the water temperature increase is higher in the case with larger PCM volume fraction due to the lower equivalent specific heat capacity.

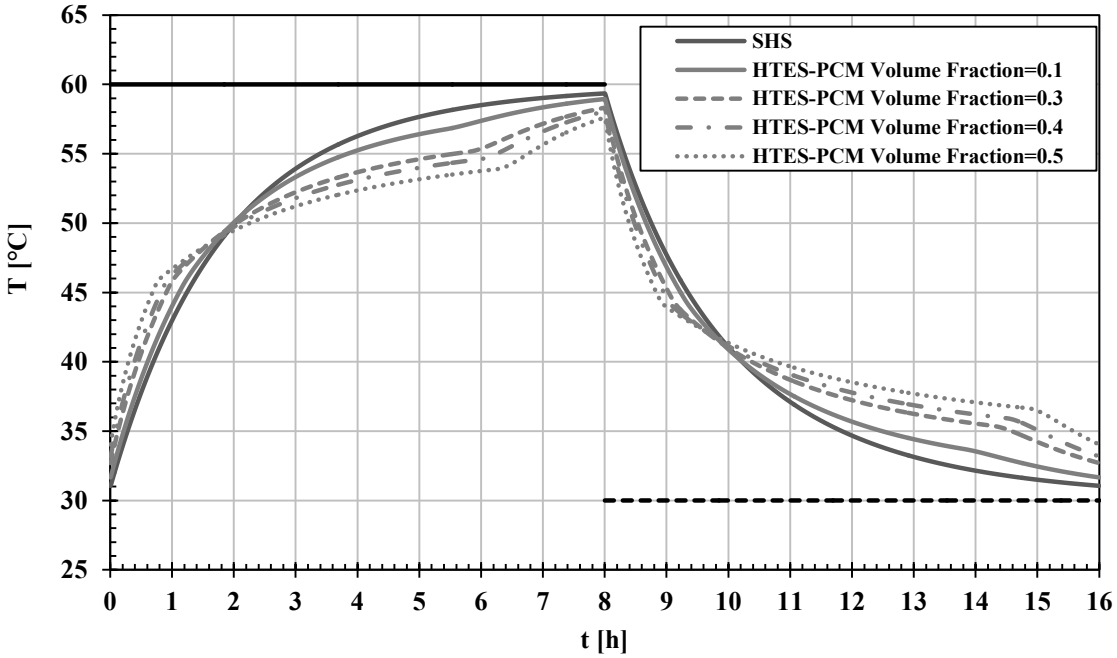

Figure 6.9. The temporal profiles of the water temperature in the SHS and HTES tanks with different PCM volume fractions during the sequential charging/discharging steady state (cyclic) operation.

Figure 6.10 illustrates the time progress of the melt fraction of the PCM in the HTES tank with different PCM volume fractions. It is shown that the tank with larger PCM volume fraction starts melting earlier due to the fast rate of temperature increase of the water. However, the melting takes place at slower rate due to the larger volume of the PCM that needs to be melted. It is seen that the performance of the system during the discharging period (the second 8 hours) is similar to that during the charging period but in the opposite direction.

Figure 6.11 shows the total energy deposited and extracted from the tank during a periodic cycle as a function of PCM volume fraction. The total energy is decomposed into its

three components: sensible energy in water, sensible energy in PCM and latent energy in PCM. The SHS tank is represented in this figure by the value of PCM volume fraction equal to zero. Figure 6.12 presents the storage gain, Equation (6.1), versus the volume fraction of the PCM. It is seen that higher storage gain can be achieved by increasing the PCM volume fraction inside the HTES tank.

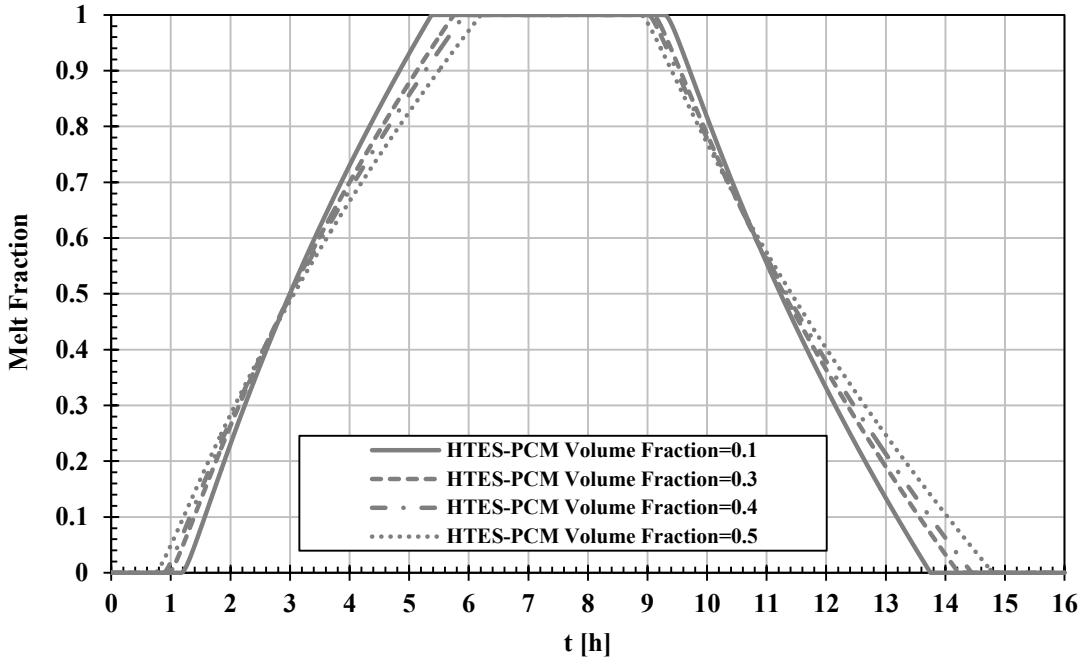

Figure 6.10. The temporal profiles of the PCM melt fraction in the HTES tank with different PCM volume fractions during the sequential charging/discharging steady state (cyclic) operation.

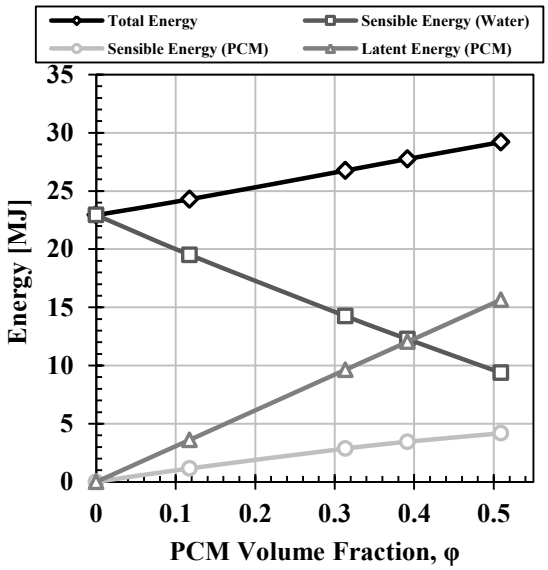

Figure 6.11. Energy accounting [MJ] for the HTES tank versus the PCM volume fraction. The SHS tank is represented by the data point at which φ=0.

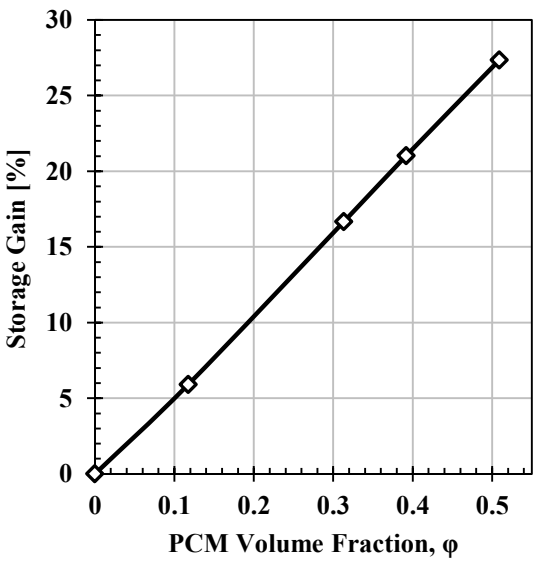

Figure 6.12. Storage gain [%] for the HTES tank versus the PCM volume fraction. The SHS tank is represented by the data point at which φ=0.

B. Effect of PCM Melting Temperature (T_m)

The effect of the PCM melting temperature is investigated by conducting numerical simulations for the HTES tank with five different PCM melting temperatures. The values were chosen to simulate the extreme cases ($T_m=T_{in,b}=60°C$ and $T_m=T_{in,t}=30°C$) as well as the average temperature of the charging and discharging inlet temperatures ($T_m=45°C$). Also, two other melting temperatures ($T_m=40°C$ and $T_m=50°C$) were tested to better illustrate the trends.

Figure 6.13 shows the water temperature profiles in the SHS and HTES tanks. It is expected that the HTES tank with PCM melting at 60°C and 30°C will not experience any phase change. It is seen that the temperature profiles for these two cases coincide. In addition, they are similar to that of the SHS tank except that the rate of temperature increase and decrease during the charging and discharging is faster. This behavior is a result of the PCM storing energy in the form of sensible heat only. For the case when the PCM melting

temperature is 40°C, the PCM melts completely during charging but undergoes partial solidification during discharging. The opposite is observed for the case where the melting temperature is 50°C. The PCM undergoes partial melting during charging followed by complete solidification during discharging. The last case, where the melting temperature is at the average value of the inlet temperatures to the bottom and top heat exchangers (45°C), shows symmetric performance during the charging and discharging.

Figure 6.14 shows that the PCM in the case with melting temperature of 45°C contributed completely in the phase change process. This indicates that the latent heat of the PCM is fully utilized in the process of energy exchange between charging and discharging periods. In the cases where the melting temperature is 40°C and 50°C, the PCM contributed only partially to the phase change process. This means that a fraction of the PCM inside the HTES tank performed only as a sensible energy storage medium. In the extreme cases, all the PCM inside the tank acted as sensible energy storage medium. In the case with the melting temperature of 60°C, the PCM never melts and remains for the whole operation in the solid phase. Whereas in the case with melting temperature of 30°C, the PCM never solidifies and remains for the whole operation in the liquid phase.

Figures 6.15 and 6.16 illustrate the existence of an optimum PCM melting temperature with which the energy stored/recovered during the sequential operation is at maximum. This optimum is shown to coincide with the average temperature of operation of the storage element. If the melting temperature is selected away from the optimum value, the potential temperature difference between the heat exchangers and water deviates from the maximum leading to reduction of the total energy stored/recovered. In addition, partial

melting and/or solidification are more likely to occur in cases where the melting temperature is off the optimum.

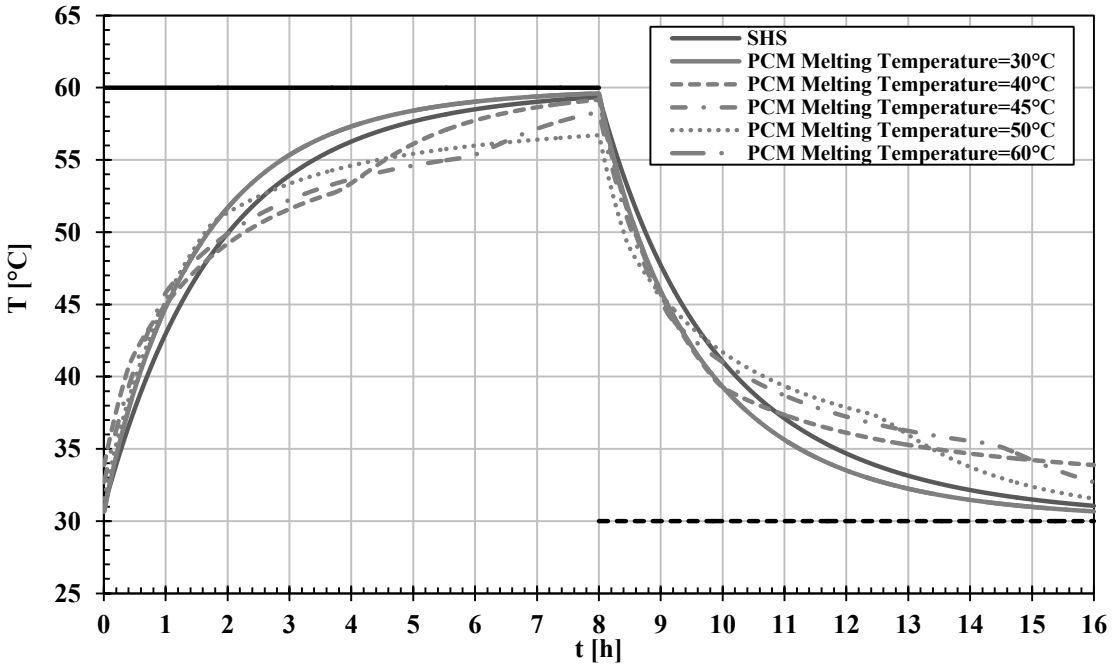

Figure 6.13. The temporal profiles of the water temperature in the SHS and HTES tanks with different PCM melting temperatures during the sequential charging/discharging steady state (cyclic) operation.

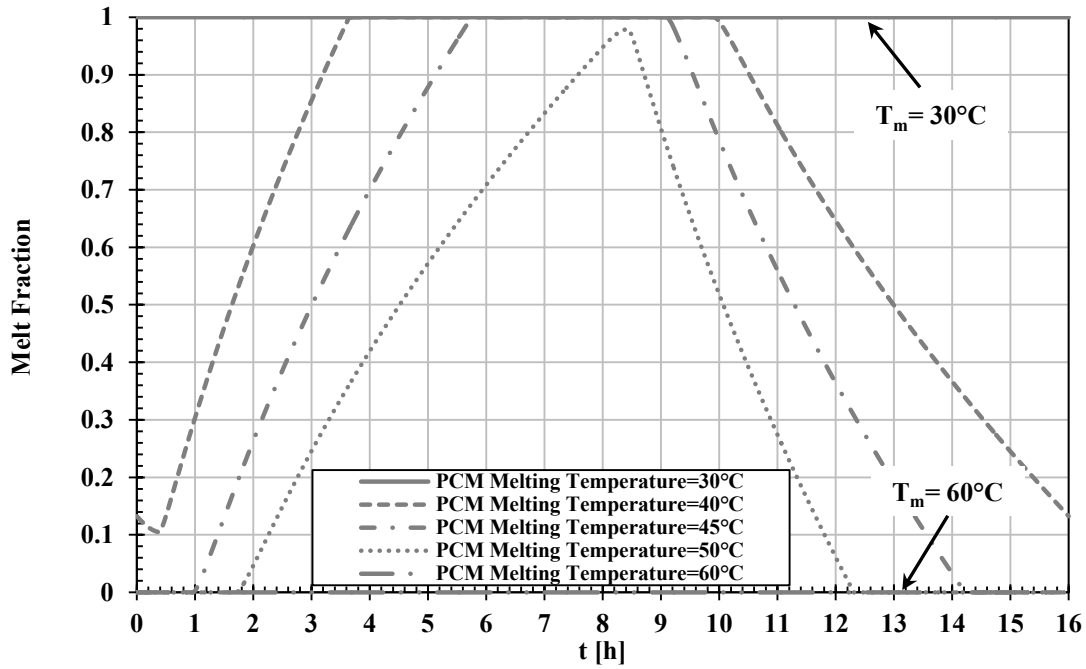

Figure 6.14. The temporal profiles of the PCM melt fraction in the HTES tank with different PCM melting temperatures during the sequential charging/discharging steady state (cyclic) operation.

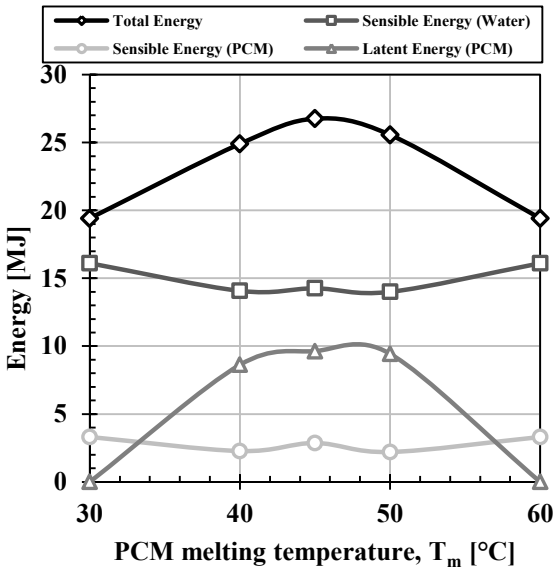

Figure 6.15. Energy accounting [MJ] for the HTES tank versus the PCM melting temperature.

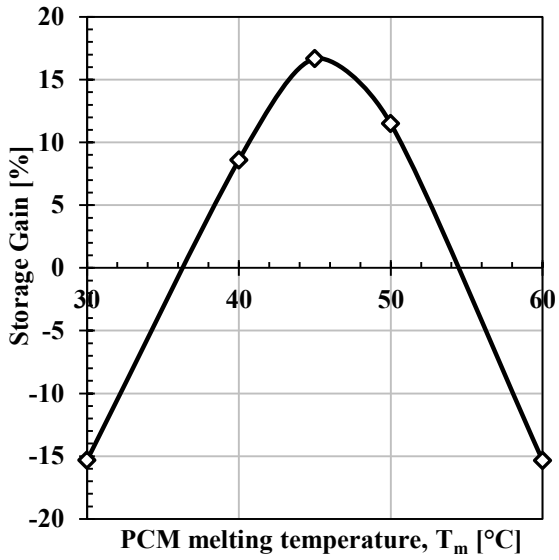

Figure 6.16. Storage gain [%] for the HTES tank versus the PCM melting temperature.

It is concluded that the choice of the melting temperature of the PCM is critical to the performance of the HTES element. An optimum value exists that depends on the operating temperatures of the system (here the average of the inlet temperatures to the coil heat exchangers).

C. Effect of PCM Density (ρ_{PCM})

The density of the PCM is known to be one of the PCM properties that is critical to the design and selection of the latent heat storage systems. High density PCMs allow for more compact storage systems. In addition, PCMs with higher densities are characterized with larger available sensible and latent storage capacities ($\rho_{PCM}c_{PCM}$ and $\rho_{PCM}H_f$). Numerical simulations were performed to study the effect of the PCM density on the dynamic performance and the storage gain of the HTES element. The values tested were chosen to encompass the variability of density of various PCMs available in the market (paraffins, non paraffins and hydrated salts).

Figure 6.17 illustrates that the effect of the PCM density is limited to extending the phase change period during charging and discharging. This observation is also demonstrated in the melt fraction profiles, Figure 6.18. This behavior is primarily attributed to the linear increase of the available latent heat capacity. Figure 6.19 shows that as the density of the PCM increases more energy is stored in the form of latent heat and less is stored in the form of sensible heat. This leads to an increase in the total energy stored/recovered and hence the storage gain, Figure 6.20.

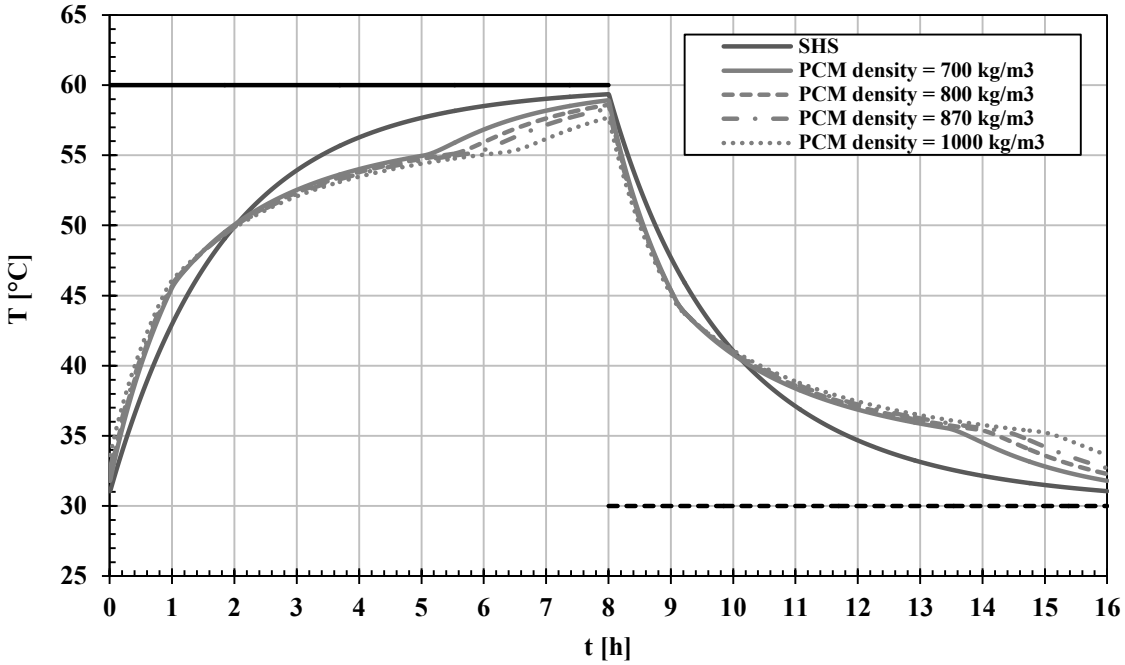

Figure 6.17. The temporal profiles of the water temperature in the SHS and HTES tanks with different PCM densities during the sequential charging/discharging steady state (cyclic) operation.

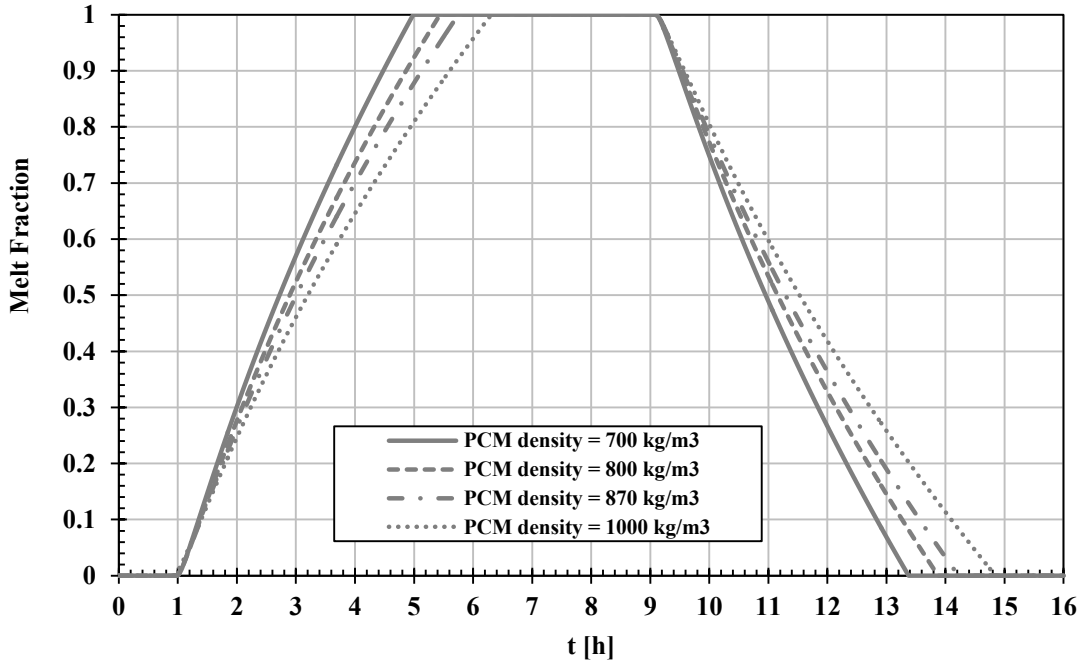

Figure 6.18. The temporal profiles of the PCM melt fraction in the HTES tank with different PCM densities during the sequential charging/discharging steady state (cyclic) operation.

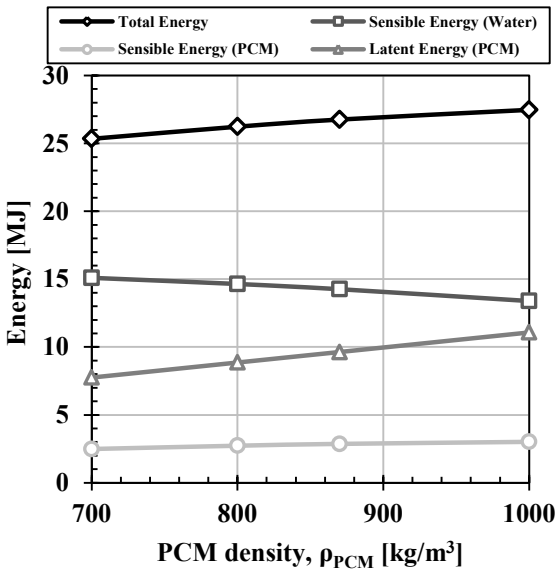

Figure 6.19. Energy accounting [MJ] for the HTES tank versus the PCM density.

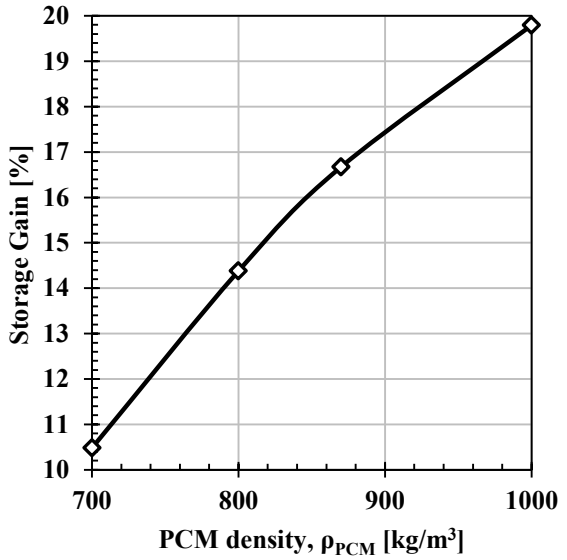

Figure 6.20. Storage gain [%] for the HTES tank versus the PCM density.

D. Effect of PCM Specific Heat Capacity (c_{PCM})

Typical PCMs that suit the low/medium temperature applications are characterized by low specific heat capacity compared to water. Numerical simulations were carried out to explore the effect of the PCM specific heat capacity on the performance of the HTES tank. Four values were chosen to span various PCMs available in the market. Also the limiting case where the specific heat capacity of the PCM is the same as that of water was investigated.

The temperature profiles in Figure 6.21 show that the increase of the PCM specific heat capacity acts to level the water temperature toward the melting temperature of the PCM. This is a result of the decrease of the temperature changes in the storage element with the increase of the PCM specific heat capacity. This acts to prolong the phase change process during the charging and discharging periods as illustrated by Figure 6.22. It is expected that as the specific heat capacity of the PCM approaches that of the water, the rate of temperature change with time before and after the phase change process should be the same as that of the water in the SHS tank. This is observed not to be the case since there exists a thermal resistance between the water and the PCM modules that forces the water temperature in the HTES tank to be higher than in the case with no PCM.

It is seen from Figure 6.23 the total energy slightly increases in the HTES tank with larger PCM specific heat capacity due to the increase of the sensible heat content of the PCM. This leads to a corresponding increase in the storage gain, Figure 6.24. It is noticed as mentioned above that the sensible heat content of the water decreases slightly in reaction to the leveling of the temperature profiles.

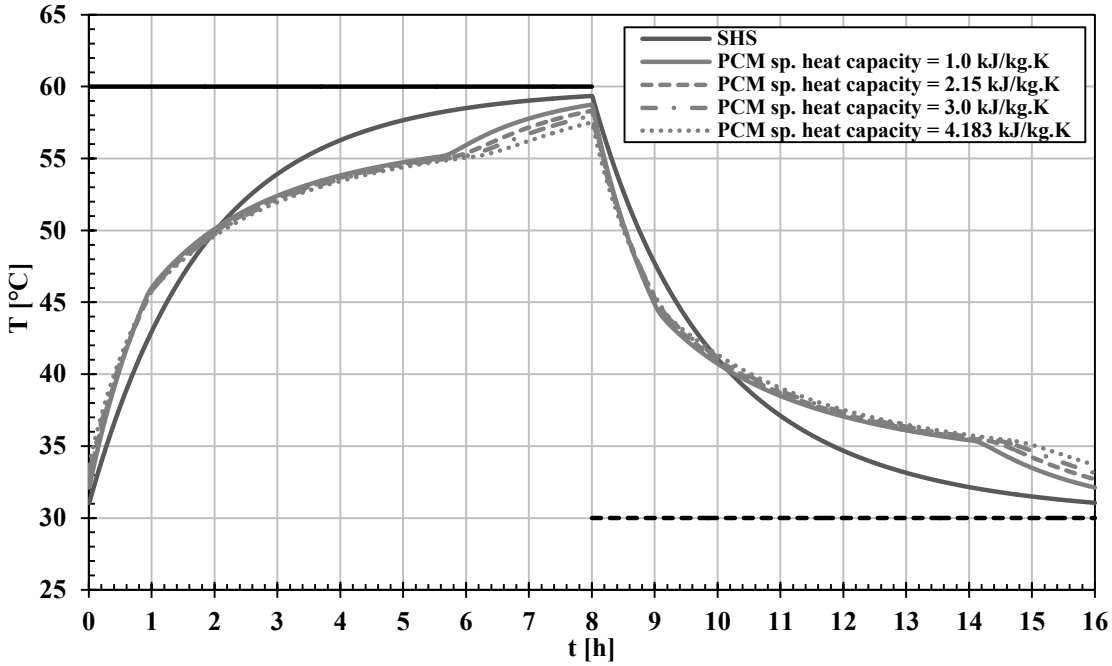

Figure 6.21. The temporal profiles of the water temperature in the SHS and HTES tanks with different PCM specific heat capacities during the sequential charging/discharging steady state (cyclic) operation.

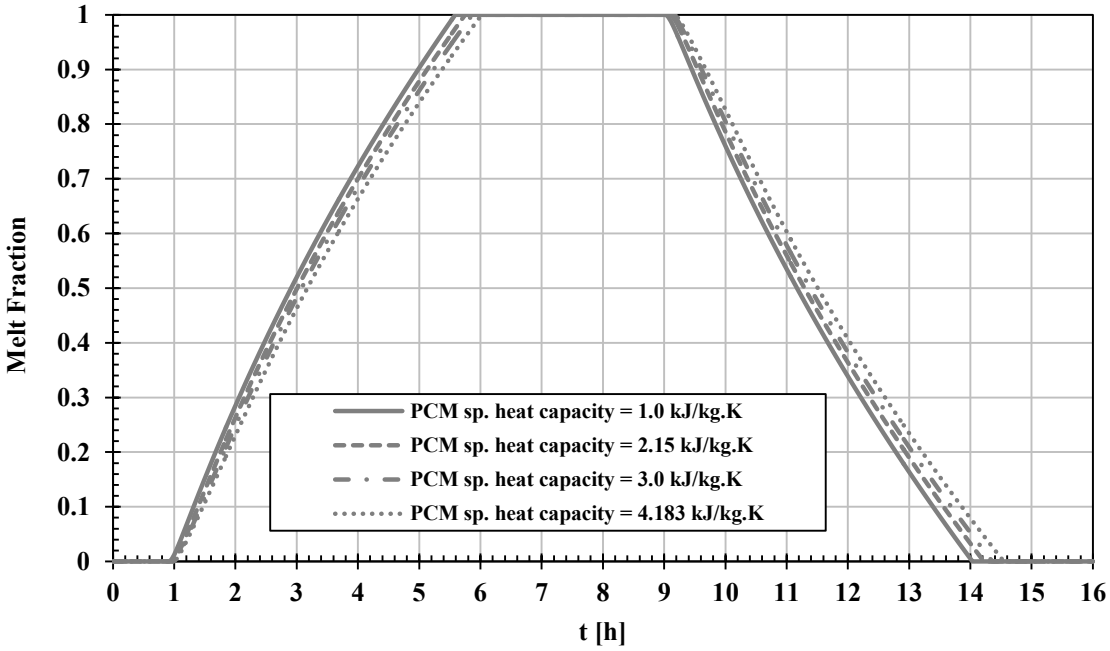

Figure 6.22. The temporal profiles of the PCM melt fraction in the HTES tank with different PCM specific heat capacities during the sequential charging/discharging steady state (cyclic) operation.

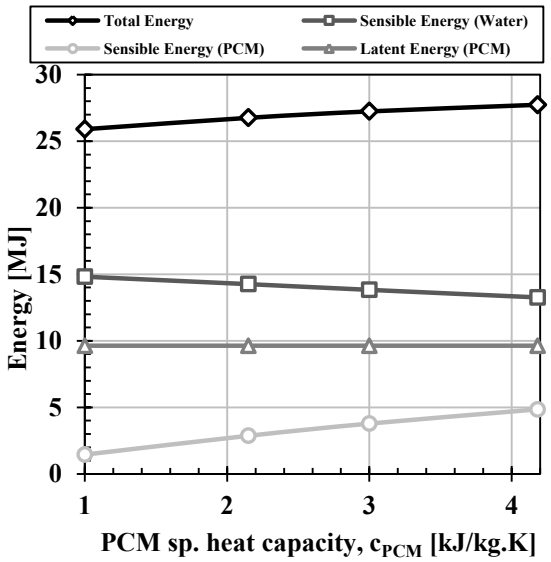

Figure 6.23 Energy accounting [MJ] for the HTES tank versus the PCM specific heat capacity.

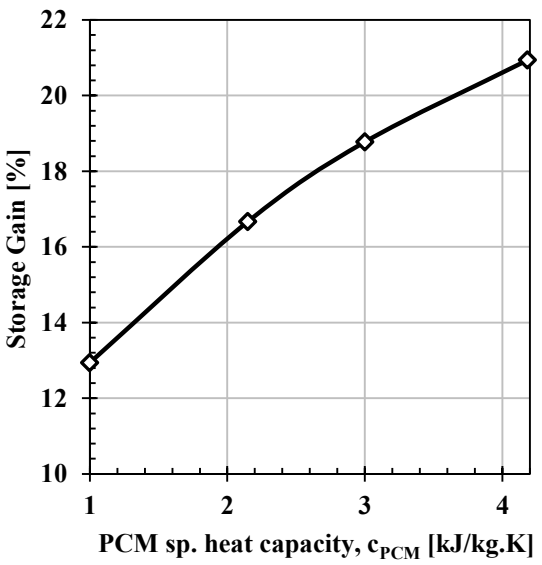

Figure 6.24. Storage gain [%] for the HTES tank versus the PCM specific heat capacity.

E. Effect of PCM Latent Heat of Fusion (H_f)

One of the most crucial properties of the PCM is its latent heat of fusion. It is defined as the amount of energy required to change the phase of one kilogram of the PCM. Different PCMs that are available in market span a broad range of latent heat of fusion [paraffins:~200 kJ/kg, fatty acids:~180 kJ/kg, hydrated salts:~250 kJ/kg and ice for cold storage:~330 kJ/kg] (Abhat 1983).

The effect of increasing the PCM latent heat of fusion on the temperature profiles is similar to that of the PCM specific heat capacity as shown in Figure 6.25. The water temperature in the HTES tank flattens out more towards the melting temperature of the PCM as the latent heat of fusion increases. In this case, there are two reasons behind the prolongation of the phase change process, Figure 6.26; (1) the potential temperature difference between the water and the PCM modules is lower, leading to slower rate of phase change, and (2) larger latent heat of fusion requires larger amounts of energy to melt/solidify

the PCM completely. For the given boundary conditions and charging/discharging time periods, the available energy might not be enough to fully melt/solidify the PCM, see Figure 6.25 when H_f=300 kJ/kg.

It is seen from Figure 6.27 that increasing the latent heat of fusion of the PCM leads to an increase in the latent energy content and a corresponding decrease in the sensible energy content of the HTES tank. This results in larger total energy stored/recovered and hence larger storage gain, illustrated in Figure 6.28.

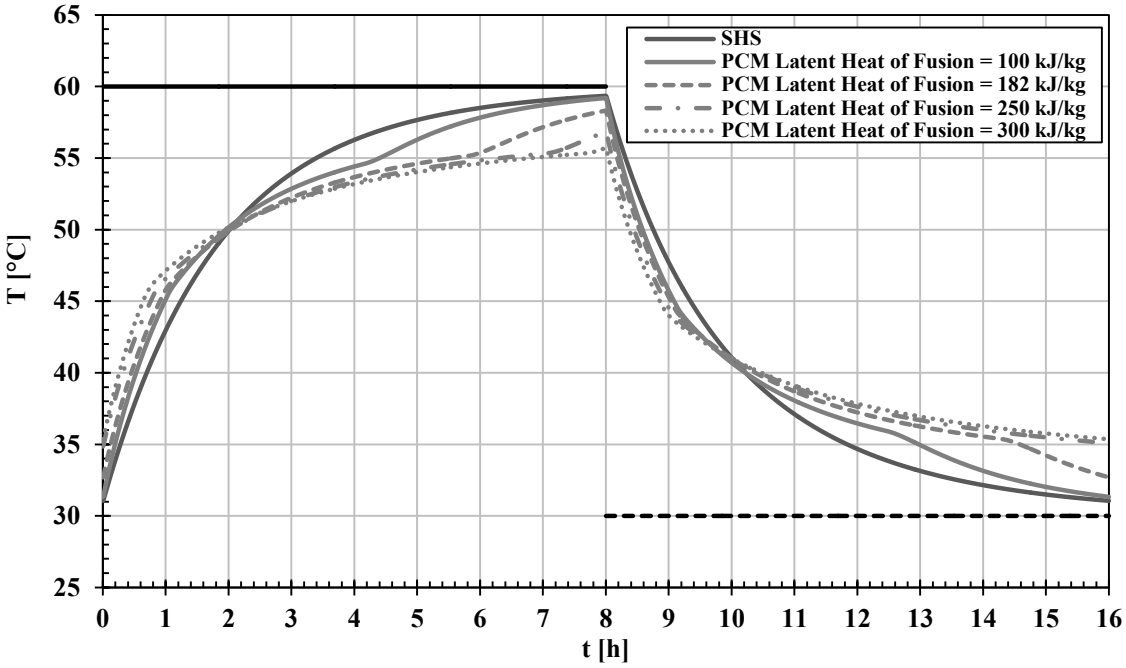

Figure 6.25. The temporal profiles of the water temperature in the SHS and HTES tanks with different PCM latent heat of fusion during the sequential charging/discharging steady state (cyclic) operation.

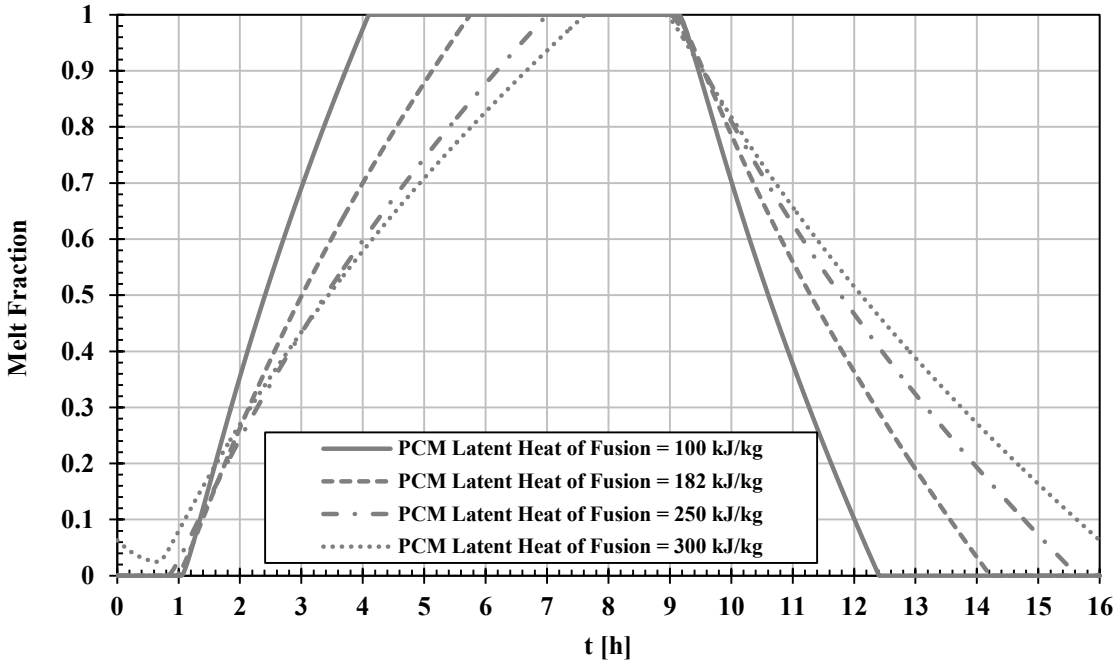

Figure 6.26. The temporal profiles of the PCM melt fraction in the HTES tank with different PCM latent heat of fusion during the sequential charging/discharging steady state (cyclic) operation.

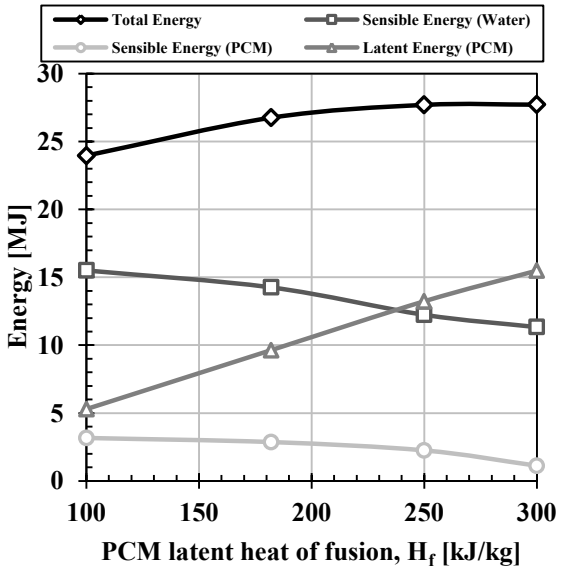

Figure 6.27. Energy accounting [MJ] for the HTES tank versus the PCM latent heat of fusion.

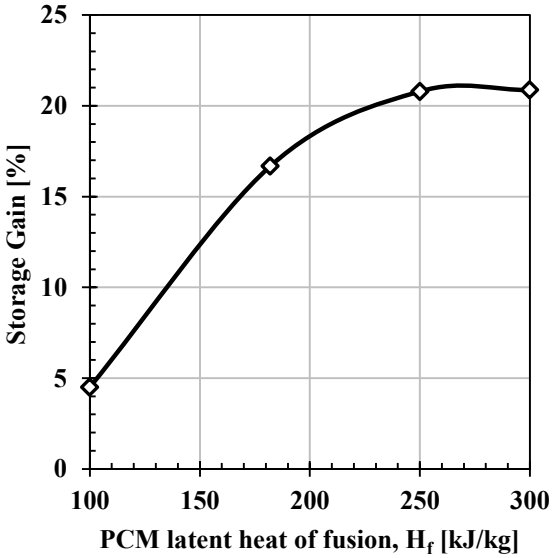

Figure 6.28. Storage gain [%] for the HTES tank versus the PCM latent heat of fusion.

F. Effect of PCM Thermal Conductivity (k_{PCM})

The thermal conductivity of the PCM is a key parameter in the performance of the HTES element since it directly impacts the thermal resistance of the system. PCMs with larger thermal conductivity act to reduce the overall thermal resistance of the storage element to the heat transfer processes during the charging and discharging cycles. Smaller thermal resistance promotes better temperature modulation of the storage element. This, in turn, leads to higher efficiency in storing and recovering the energy.

Figure 6.29 demonstrates the effect of increasing the PCM thermal conductivity on the temperature profiles in the HTES tank. The last case was presented where the PCM was assumed as lumped system (k_{PCM}=large) in order to highlight the limiting case when the PCM acts ideally. It is evident that increasing the PCM thermal conductivity improves the temperature modulation of the HTES tank; i.e. the temperature of the water during melting and solidification approaches the melting temperature of the PCM. The reduction in the thermal resistance of the storage element associated with the increase of the thermal conductivity of the PCM allows for faster phase change process during the charging and discharging periods, also shown in Figure 6.30.

In the limit of high PCM thermal conductivity (PCM treated as lumped system), the water temperature in the HTES tank is seen to maintain a constant value. This is expected since the temperature distribution inside the PCM modules is spatially uniform during the phase change process. This drives the water to seek a steady temperature at which the energy exchange with the heat exchangers is balanced with the heat exchange with the PCM. The closeness of this temperature to the melting temperature of the PCM depends on the thermal resistance between the water and the PCM modules.

The total energy in the HTES tank is expected to increase as the PCM thermal conductivity increases. This is shown in Figure 6.31. The limit of high thermal conductivity is illustrated by the dashed line. It is seen that the total energy asymptotes to a maximum value when $k_{PCM} \geq 1.0$ W/m.K. Beyond this value, the PCM modules are no longer the limiting component of the storage tank, and further increase of the PCM thermal conductivity shall not affect the total energy stored/recovered in/from the HTES tank. Similar trend can be noticed in the storage gain, demonstrated in Figure 6.32.

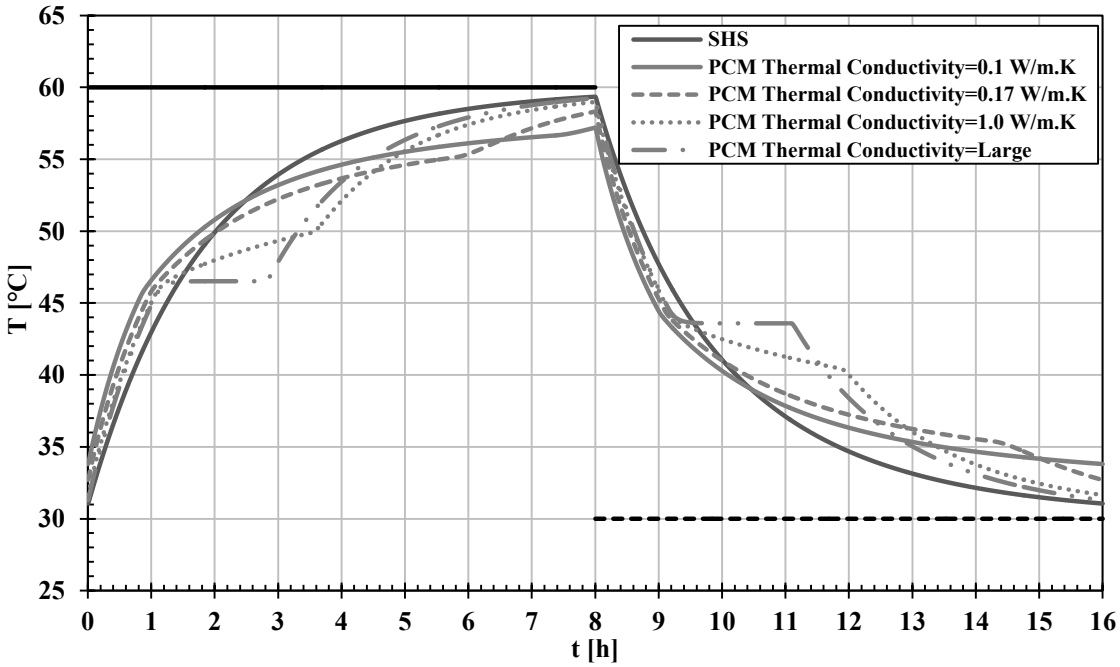

Figure 6.29. The temporal profiles of the water temperature in the SHS and HTES tanks with different PCM thermal conductivities during the sequential charging/discharging steady state (cyclic) operation. The limiting case where the PCM can be treated as lumped system is designated as (k_{PCM}=Large).

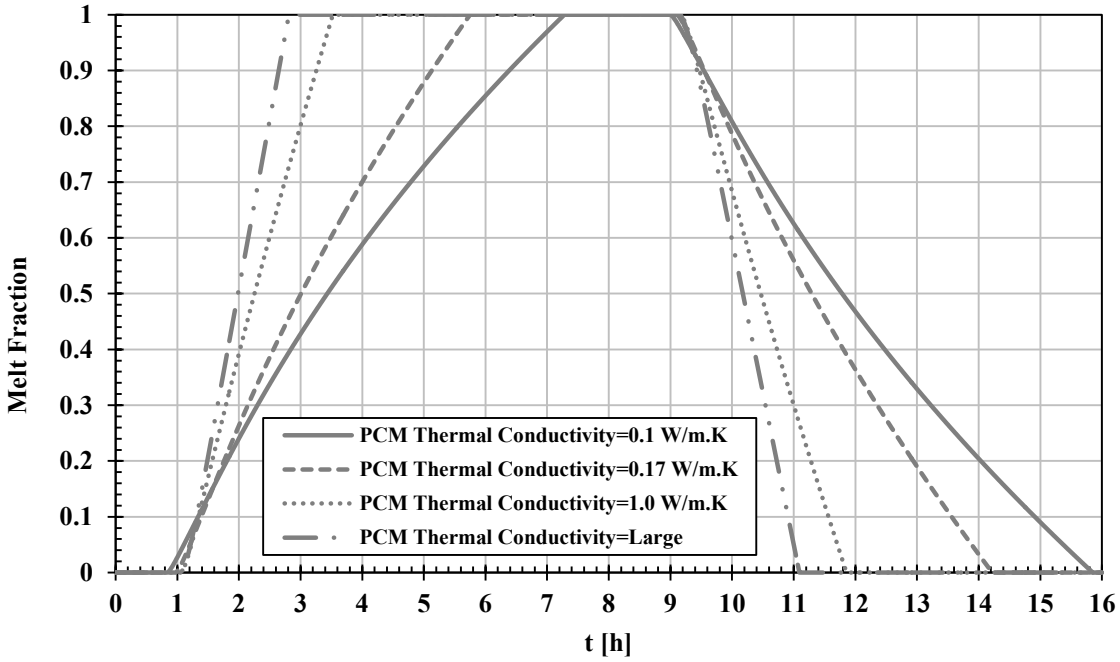

Figure 6.30. The temporal profiles of the PCM melt fraction in the HTES tank with different PCM thermal conductivities during the sequential charging/discharging steady state (cyclic) operation. The limiting case where the PCM can be treated as lumped system is designated as (k_{PCM}=Large).

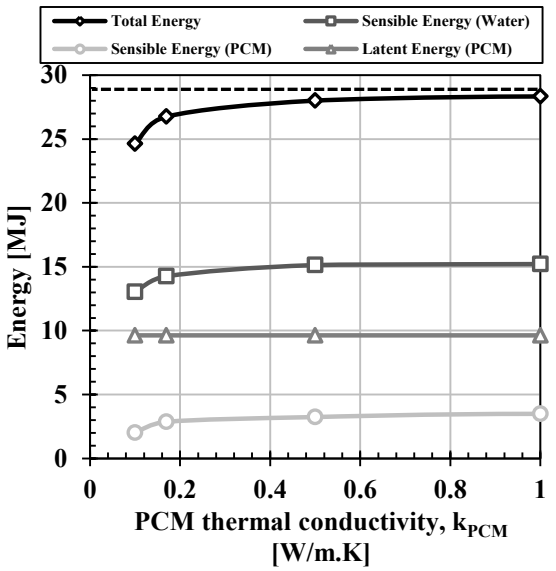

Figure 6.31. Energy accounting [MJ] for the HTES tank versus the PCM thermal conductivity.

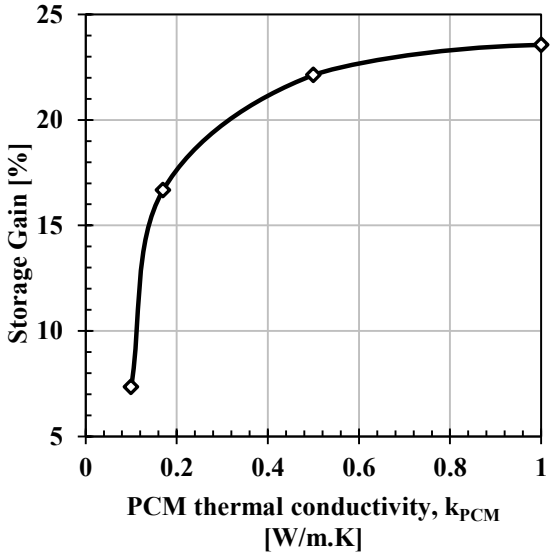

Figure 6.32. Storage gain [%] for the HTES tank versus the PCM thermal conductivity.

G. Effect of PCM Module Thickness (w_{PCM})

The thickness of the PCM modules has a critical influence on the thermal resistance of the HTES element. Thinner modules are characterized by smaller internal thermal resistance since the thermal penetration depth is reduced. Also, for the same total volume of the PCM in the HTES tank, as the module thickness decreases, the number of modules increases and hence, the total surface area of the modules increases. This is illustrated in Table 6.5 which presents PCM module designs with five different thicknesses.

The effect of the PCM module thickness on the water temperature profiles in the HTES tank is shown to be similar to that of the PCM thermal conductivity, Figure 6.33. As the thickness of the modules decreases, the thermal resistance decreases, leading to better temperature modulation of the storage element. Poor design of the PCM modules with larger thickness can increase the thermal resistance of the system to the extent that the PCM undergoes incomplete melting and/or solidification, as shown in Figure 6.34 in the case of w_{PCM} = 60 mm.

Table 6.5. Geometrical constants corresponding to the PCM module thickness.

	PCM Module Thickness (w_{PCM})				
	10 mm	**20 mm**	**30 mm**	**40 mm**	**60 mm**
Number of modules	24	12	8	6	4
Total volume [L]	60.8	60.8	60.8	60.8	60.8
Actual volume fraction (V_{tank}=200 L)	0.31	0.31	0.31	0.31	0.31
Total surface area of PCM module [m^2]	12.17	6.08	4.06	3.04	2.03

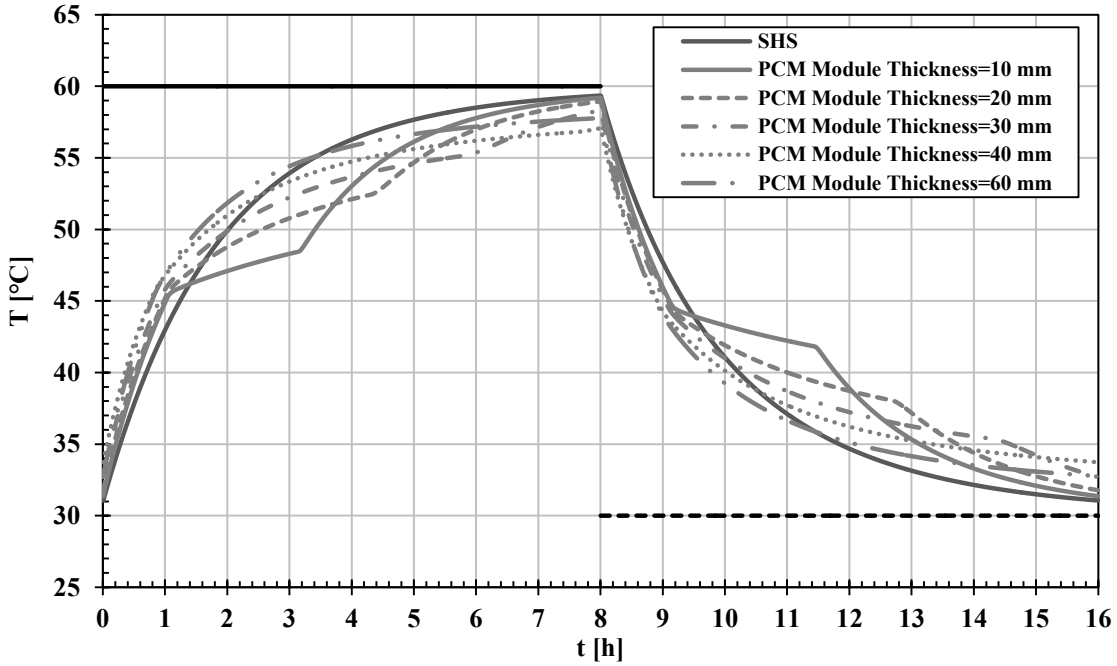

Figure 6.33. The temporal profiles of the water temperature in the SHS and HTES tanks with different PCM module thicknesses during the sequential charging/discharging steady state (cyclic) operation.

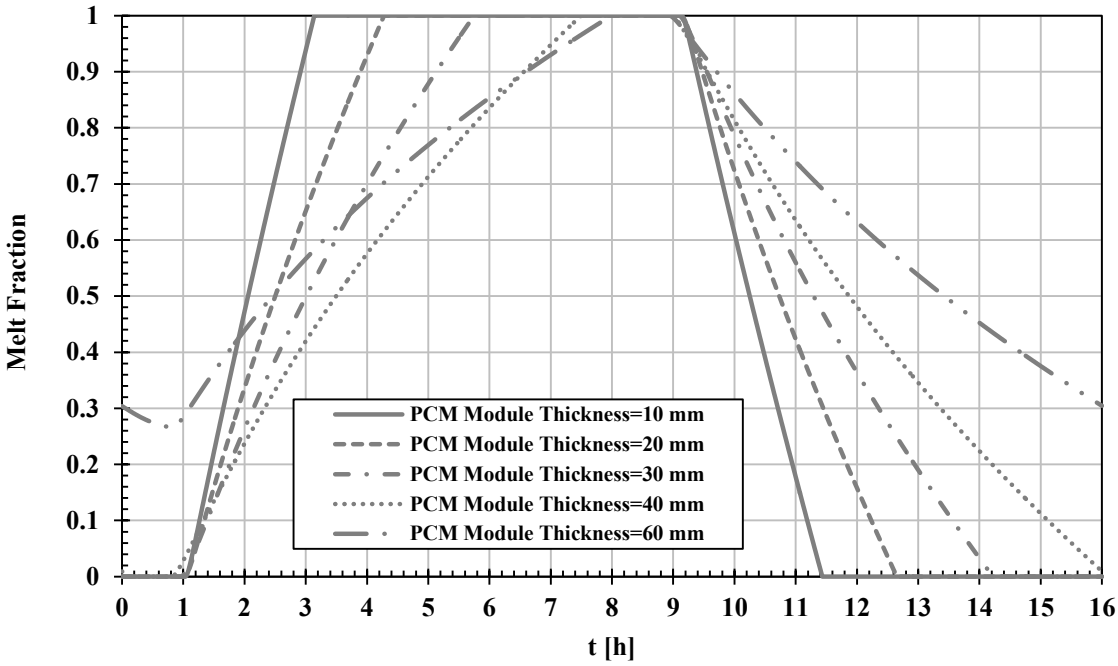

Figure 6.34. The temporal profiles of the PCM melt fraction in the HTES tank with different PCM module thicknesses during the sequential charging/discharging steady state (cyclic) operation.

As a result, in order to maximize the storage gain from the HTES tank, the PCM modules should be designed such that the module thickness is as small as practically possible, Figures 6.35 and 6.36.

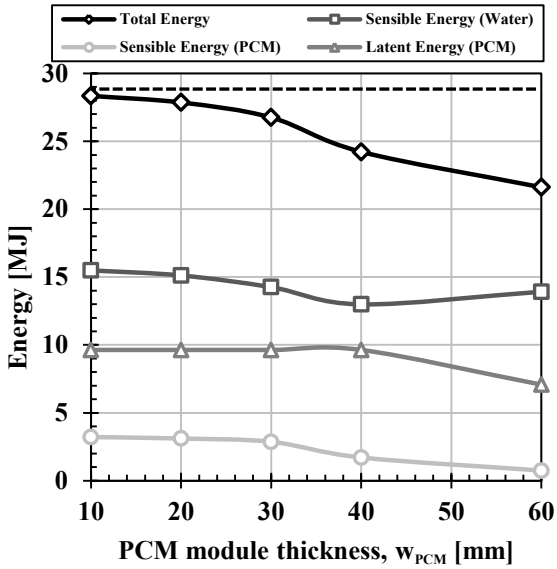

Figure 6.35. Energy accounting [MJ] for the HTES tank versus the PCM module thickness.

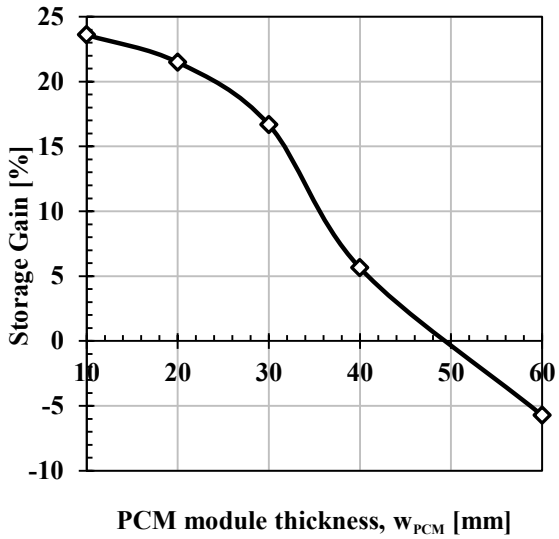

Figure 6.36. Storage gain [%] for the HTES tank versus the PCM module thickness.

H. Effect of Heat Exchanger Coil Length (L_{coil})

The effect of the thermal resistance posed by the indirect heat exchange between the storage element and the bottom and top coil heat exchangers was explored. Increasing the length of the heat exchanger coil increases the surface area of heat transfer and hence, the effectiveness of the heat exchange process. This acts to reduce the thermal resistance between the heat transfer fluids and the water in the storage element. Numerical simulations were carried out to investigate the effect of increasing the coil length on the performance and storage gain from the HTES tank. In order to obtain comparable results, numerical simulations were conducted on the SHS tank with the same coil lengths tested on the HTES tank.

Figures 6.37 and 6.38 show that in both the SHS and the HTES tanks, the larger coil length leads to larger amounts of energy exchange between the heat transfer fluid and the storage medium. This is evident from the considerable increase in the temperature swing of the water in the tank during the same time periods of charging and discharging.

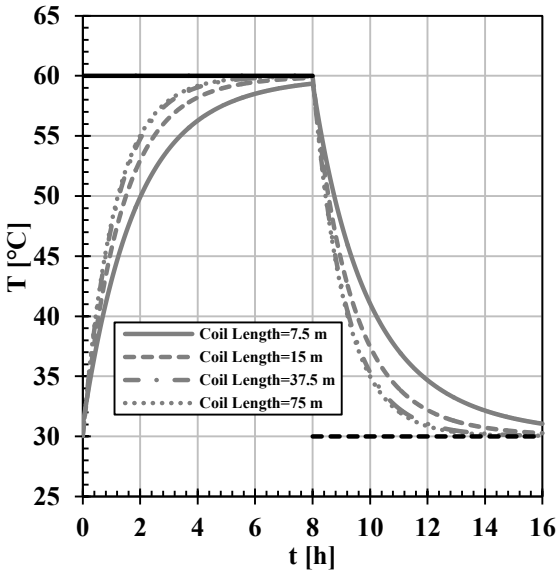

Figure 6.37. The temporal profiles of the water temperature in the SHS tank with different coil lengths of the heat exchangers during the sequential charging/discharging steady state (cyclic) operation.

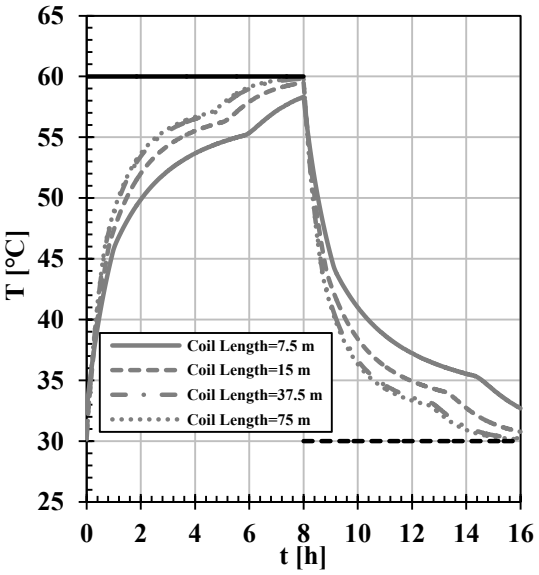

Figure 6.38. The temporal profiles of the water temperature in the HTES tank with different coil lengths of the heat exchangers during the sequential charging/discharging steady state (cyclic) operation.

It is worth noting that the current analysis is assuming isothermal inlet temperatures to the bottom and top heat exchangers during charging and discharging, respectively. As such, the storage tank is said to have reached its maximum capacity when the temperature of the system approaches $T_{in,b}$ after charging and $T_{in,t}$ after discharging. That is why the temperature curves in Figures 6.37 and 6.38 collapse for $L_{coil} \geq 37.5$ m, which is considered the value beyond which the coil effectiveness is close to unity and the performance of the storage element becomes insensitive to further increase in the coil length. A similar trend is

noticed from the temporal profiles of the PCM melt fraction in Figure 6.39. Larger coil surface area leads to higher heat transfer rate which, in turn, promotes for faster melting and solidification processes.

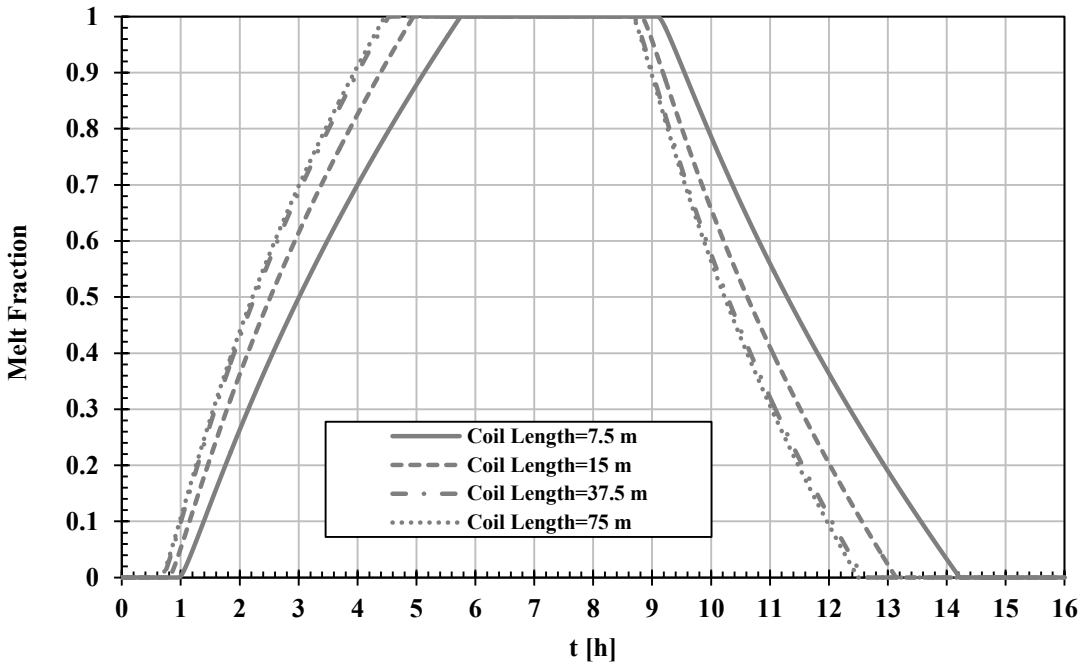

Figure 6.39. The temporal profiles of the PCM melt fraction in the HTES tank with different coil lengths of the heat exchangers during the sequential charging/discharging steady state (cyclic) operation.

Figures 6.40 and 6.41 illustrate the effect of increasing the coil length on the energy accounting and the storage gain of the HTES element. These curves can be used at the design stage to determine the optimum coil length needed to maximize the storage gain of the HTES tank compared to the SHS tank.

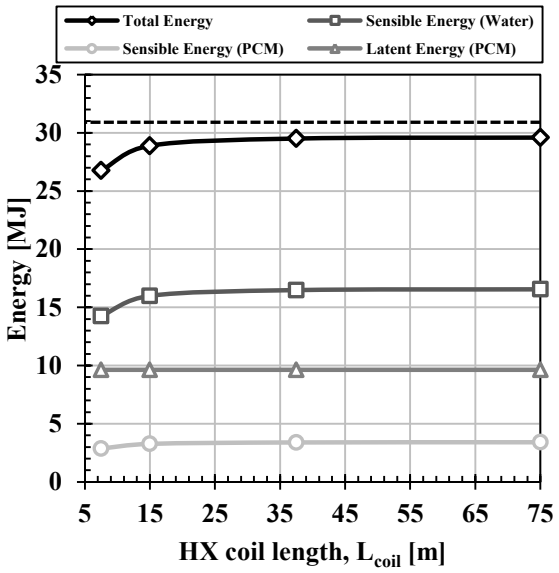

Figure 6.40. Energy accounting [MJ] for the HTES tank versus the coil lengths of the heat exchangers. The dashed line represents the limit when the heat exchanger effectiveness is unity.

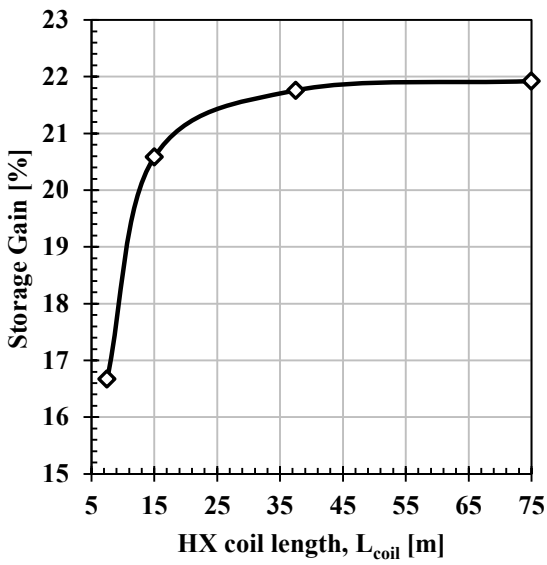

Figure 6.41. Storage gain [%] for the HTES tank versus the coil lengths of the heat exchangers.

In typical applications of thermal energy storage, especially solar thermal domestic hot water (DHW) which is the main focus of this dissertation, the operation scenario deviates greatly from the sequential charging/discharging operation with fixed inlet temperature to the heat exchangers. First, the inlet temperature to the bottom heat exchanger is time variant since it depends on the coupled performance of the solar collector and the return from the storage element. Second, the time intervals when the heat exchangers operate depend on the solar collector control algorithm and the draw pattern of the demand. Last, the effect of the temperature modulation promoted by the existence of PCMs in the HTES tank, on the storage efficiency cannot be shown with fixed inlet temperature to the coil heat exchangers operation. As such, the parametric analysis does not reflect the realistic performance of the HTES, however, it sheds the light on the potential benefits of the PCM in the HTES element. In addition, it illustrates the key design parameters that are critical to the performance of the storage element.

From the parametric analysis, it can be concluded that the parameters can be divided into two groups: (1) the design parameters of the PCM modules: the PCM volume fraction (number of modules), the PCM module thickness and the coil length of the heat exchangers, and (2) selection parameters of the PCM: the melting temperature, density, latent heat of fusion, specific heat capacity and thermal conductivity. The design parameters are easier to control than the selection parameters which are limited to the types of materials available in the market as well as the technological advancement in the area of material properties enhancement.

For a given system with prescribed boundary conditions, the storage gain can be regarded as a representative criterion for comparing the performance of the HTES to the SHS elements. It is concluded that the storage gain from the HTES element can be maximized by

1. Increasing the PCM volume fraction in the tank to the limit where the spacing between the modules does not impede the heat transfer into the PCM (Sarafraz, 2013).
2. Adjusting the PCM melting temperature such that the maximum amount of energy is stored in the form of latent heat. It was shown to be at the average of the operation temperature limits of the storage element.
3. Increasing the heat capacity of the PCM by selecting materials with larger density, specific heat capacity and latent heat of fusion. However, to promote for better temperature modulation it is recommended to focus on maximizing the latent heat capacity of the PCM. This effect will show significant influence on the efficiency of the solar collector in solar thermal applications.

4. Reducing all sources of thermal resistance in the storage element by increasing the coil surface area, selecting PCM with large thermal conductivity and by reducing the thickness of the PCM modules. Also, incorporating various techniques to increase the surface area of the PCM modules such as fins or using micro-encapsulation can lead to significant reduction in the thermal resistance of the storage element and hence, significant increase in storage gain.

The results obtained from the parametric analysis were used to design a HTES tank with the maximum possible storage gain in a sequential charging/discharging operation as before. The boundary conditions were kept fixed. The tank dimensions were kept the same. The PCM module design was adjusted to be 0.5 m in height, 0.51 m in depth and 0.01 m in thickness. The thickness was chosen to be the minimum it can be from the practical point of view. The heat exchangers effectiveness was assumed to be unity, which means that heat transfer rates from the coils are at maximum all the time. The PCM thermal conductivity was assumed to be extremely large that the PCM could be treated as lumped system. The PCM melting temperature was chosen at the optimum for the given operation scenario (i.e., 45°C). The rest of the properties of the PCM were chosen to be as shown in Table 6.2. Three cases were developed to illustrate the means to maximize the storage gain from the HTES element.

Case 1. The maximum PCM volume fraction that can be employed in the HTES tank such that the spacing between modules does not decrease below 10 mm is 0.34. The minimum spacing (s) was chosen to be 10 mm because this was the lower limit of the experimental test matrix discussed in Chapters Four and Five. It is also believed to be the smallest spacing that can be practically applied without intensive interference between the module support rack and the natural convection currents inside the HTES tank.

Table 6.6 shows the critical geometrical constants pertaining to the chosen PCM module design. Table 6.7 demonstrates the energy accounting of the HTES tank as well as the storage gain in Case 1.

Table 6.6. Geometrical constants pertaining to the chosen PCM module design in Case 1.

Number of modules	26
Total volume [L]	66
Actual volume fraction (V_{tank}=200 L)	0.34
Total surface area of PCM module [m^2]	13.7

Table 6.7. Energy accounting and storage gain of the HTES tank in Case 1.

Sensible energy in water [MJ]	**Sensible energy in PCM [MJ]**	**Latent energy in PCM [MJ]**	**Total energy in HTES [MJ]**	**Total energy in SHS [MJ]**	**Storage gain [%]**
16.05	3.69	10.44	30.18	24.29	24.28

Case 2. The tank size and the rectangular design of the PCM modules in Case 1 limited the PCM volume fraction. This posed two issues: (1) the energy stored in the form of sensible heat comprised around 65% of the total energy stored in the HTES, and (2) the surface area of the PCM modules is limited by the number of modules. This will set a minimum to the thermal resistance of the storage element and hence hinders the HTES element from storing more energy. In Case 2, a new design of the PCM modules was proposed using spheres 5 mm in diameter. This design allows for larger packing density in the HTES tank that can go up to 74% of the enclosing volume (Steinhaus, 1999). To account for the containment

volume, the PCM volume fraction was assumed 0.7. Table 6.8 shows the critical geometrical constants pertaining to the chosen PCM module design. Table 6.9 demonstrates the energy accounting of the HTES tank as well as the storage gain in Case 2.

Table 6.8. Geometrical constants pertaining to the chosen PCM module design in Case 2.

Number of modules	2.08×10^{6}
Total volume [L]	136
Actual volume fraction (V_{tank}=200 L)	0.70
Total surface area of PCM module [m^2]	163

Table 6.9. Energy accounting and storage gain of the HTES tank in Case 2.

Sensible energy in water [MJ]	Sensible energy in PCM [MJ]	Latent energy in PCM [MJ]	Total energy in HTES [MJ]	Total energy in SHS [MJ]	Storage gain [%]
7.31	7.62	21.5	36.43	24.29	50.0

The increase of the surface area of the PCM modules leads to considerable reduction of the thermal resistance of the storage element yielding larger amounts of energy stored. Almost two-times increase of the storage gain was obtained. Also, the increase of the PCM volume fraction allows for more energy stored in the form of latent heat than sensible heat. In case 2, only 41% of the total energy stored was stored in the form of sensible heat.

Case 3. It was observed from Case 2 that the amount of energy stored in the form of sensible heat was still significant. This indicated that the storage element is undersized. In Case 3, the PCM module design was maintained the same as in Case 2, but the PCM latent heat of fusion

was chosen to be 800 kJ/kg. Table 6.10 demonstrates the energy accounting of the HTES tank as well as the storage gain in Case 3.

Table 6.10. Energy accounting and storage gain of the HTES tank in Case 3.

Sensible energy in water [MJ]	Sensible energy in PCM [MJ]	Latent energy in PCM [MJ]	Total energy in HTES [MJ]	Total energy in SHS [MJ]	Storage gain [%]
0.17	0.12	89.15	89.42	24.29	268.22

First, it is noticed that more energy was stored in the HTES tank. The HTES stored approximately 3.7 times the energy stored in the SHS tank. Figure 6.42 illustrates the water temperature profiles in the three cases.

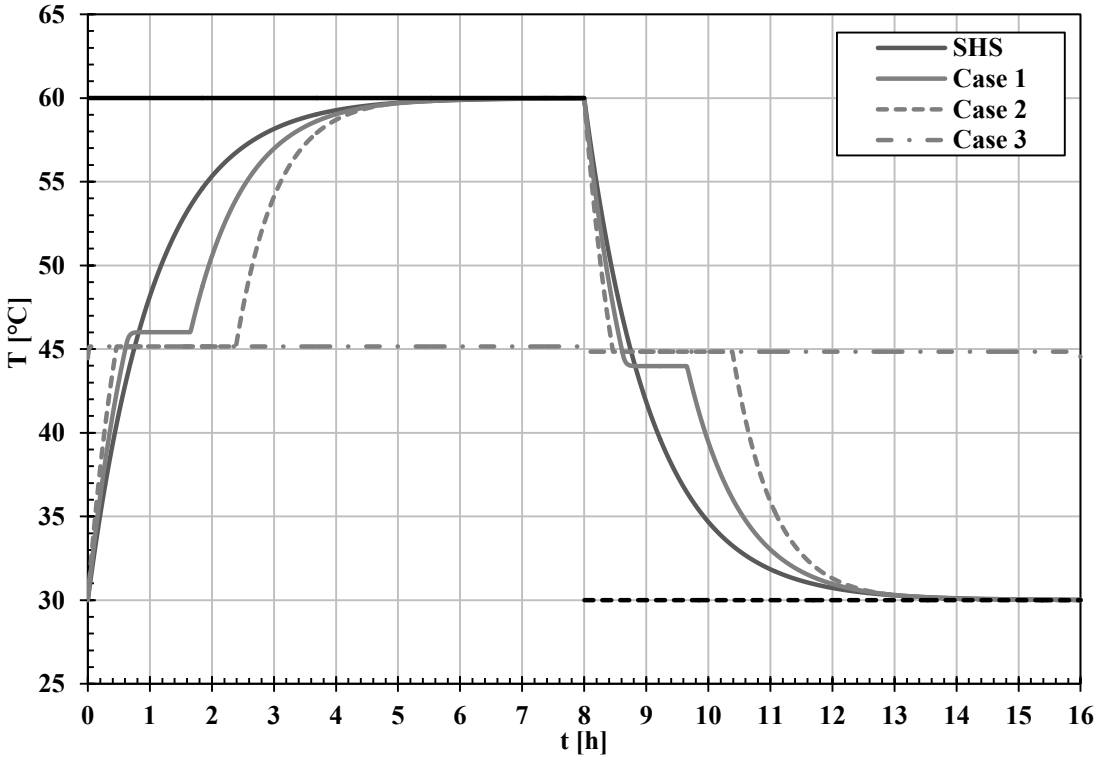

Figure 6.42. The temporal profiles of the water temperature in the SHS and HTES tanks in Case 1, Case 2 and Case 3 during the sequential charging/discharging steady state (cyclic) operation.

It is seen that in Case 3, almost all the energy was stored in the form of latent heat which enhanced the temperature modulation of the HTES tank (i.e., the tank operated continuously at the melting temperature of the PCM). This yielded the highest heat transfer rates from the coil heat exchangers to the storage element, and hence the highest storage gain.

Although it is highly unlikely to find a PCM with such high latent heat of fusion, the case study shows that major advantage of the HTES element is its ability to modulate the temperature of the system around the melting temperature of the PCM. It can be concluded that for a given system with prescribed boundary conditions, the design of the HTES should incorporate:

1. Finding the optimum melting temperature that suits the operation of the system.
2. Reducing the thermal resistances in the storage element in order to maintain the temperature of the system closer to the melting temperature of the PCM.
3. Adjusting the PCM properties that maximize the amount of energy stored in the form of latent heat.

6.2.2. Solar Thermal Domestic Hot Water Application

Although the parametric study revealed many of the characteristics and benefits of the HTES element, the sequential charging/discharging operation scenario does not provide insight into the performance of the HTES for realistic system applications. Consider the solar thermal domestic hot water application which is the main focus of the current study. Figure 6.43 illustrates a typical solar collector loop connected to a SHS tank through the bottom coil heat exchanger. The bottom coil acts as the charging heat exchanger that stores the energy collected from the solar collector into the tank. A pump is used to circulate the heat transfer

fluid between the collector and the storage element. A controller is usually installed and a control algorithm is implemented in order to control the operation time of the pump based on the solar energy availability and the collector inlet temperature. Typically the control algorithm is developed based on the temperature difference between the mean temperature of the solar collector and the return temperature from the storage element (Duffie and Beckmann, 2006). If the temperature difference is sufficiently high, then the pump is engaged. The pump is turned off when the temperature difference falls below a specified value.

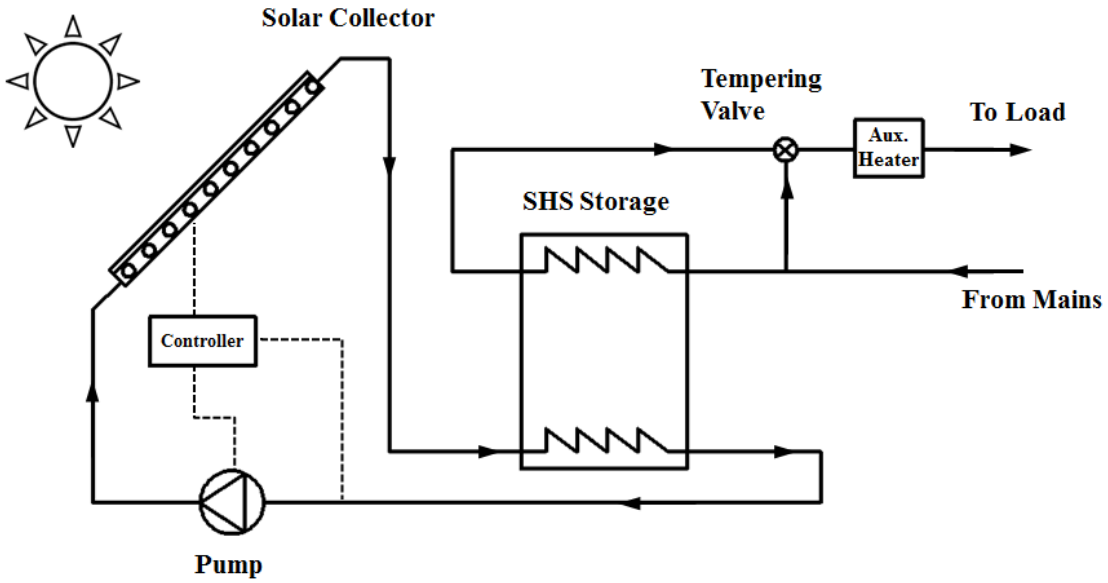

Figure 6.43 Schematic of the solar thermal DHW system with SHS tank.

On the demand side, water typically flows from the mains through the top coil heat exchanger then out to the load. The top coil acts as the discharging heat exchanger that recovers the stored energy and is sent to the load when needed. A thermostatic mixing valve is integrated in the demand loop in order to avoid sending water at a temperature higher than a certain prescribed value (usually 50-60°C). Also, the demand loop is usually equipped with

an auxiliary heating element (typically electric heater or gas burner) in order to maintain the delivered water temperature at a prescribed value.

The key differences between the performance of the storage element in an idealistic operation scenario such as the sequential charging/discharging, and a realistic system such as the solar thermal DHW include:

1. The charging and discharging processes are not always out of phase.
2. The inlet temperature to the bottom heat exchanger (supplied by the collector) is variable with time. The time variability depends on the dynamic behavior at the bottom node of the storage tank as well as the weather conditions (i.e., the solar incidence radiation and the ambient temperature). Thus, the integration of the thermal storage tank with the collector is considered.
3. The demand profile is not always uniform especially in the DHW applications. Typically, the demand profiles are scattered pulses of water draws throughout the day signifying various domestic water usages such as showers and baths.

In this section, the performance of the solar thermal DHW storage system was simulated for both storage elements; the SHS and the HTES. The mathematical model developed in Chapter Three for the storage elements was used in conjunction with solar-thermal performance empirical/analytical equations found in Solar Engineering of Thermal Processes (Duffie and Beckmann, 2013). Although the best representation of the system performance can only be obtained through annual simulations, the computation cost will become too high to justify the feasibility of the results. As such, simulations were carried out for the first day of each season as a representation of the entire year. The performance of such systems in one day is expected to be influenced by their performance in the preceding

days. As such, steady state simulations were conducted where the same day was repeated until the performance of the system reaches a cyclic pattern. This removes the influence of an assumed initial condition for the system.

The weather data, essentially the solar irradiation and the ambient temperature, were extracted from the hourly weather database of TRNSYS 17 software for March 21st, June 21st, September 21st and December 21st in Toronto city in 2012 (Meteonorm software V5.0). Figures 6.44 and 6.45 show the solar irradiation and the ambient temperature profiles for March 21st. The profiles were approximated using sinusoidal functions to be able to interpolate for the input parameters at finer time steps, illustrated by the dashed lines in Figures 6.44 and 6.45. The profiles for the other three days were not shown for brevity. Table 6.11 provides typical values of mains temperature in Toronto (CAN/CSA-F379.1-88, 2004).

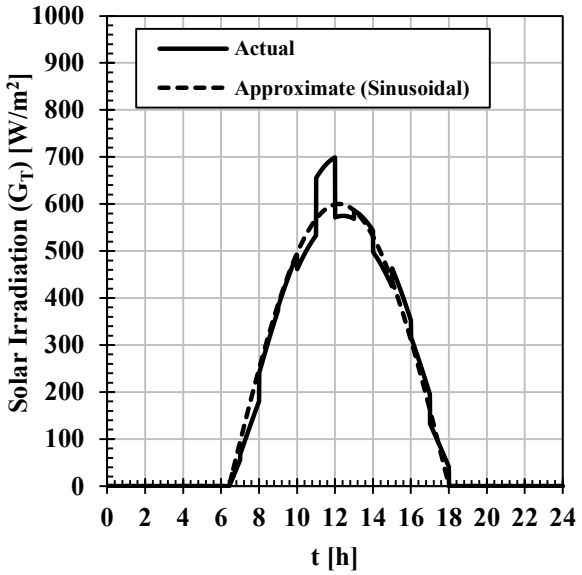

Figure 6.44. Temporal profile of the solar irradiation (G_T) in March 21st in Toronto. Solid line: actual profile from the weather data. Dashed line: approximate profile using a sinusoidal function.

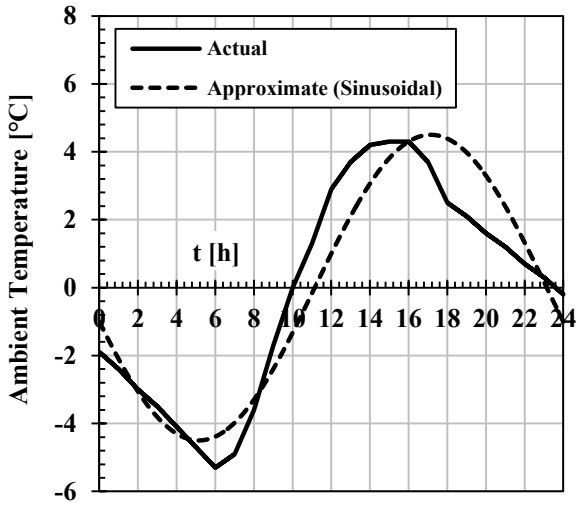

Figure 6.45. Temporal profile of the ambient temperature in March 21st in Toronto. Solid line: actual profile from the weather data. Dashed line: approximate profile using a sinusoidal function.

Table 6.11. The values of the mains water temperature corresponding to these four days (CAN/CSA-F379.1-88, 2004).

Day	**March 21st**	**June 21st**	**September 21st**	**December 21st**
Mains temperature [°C]	8	18	16	8

Two types of load were investigated. First, a theoretical load profile was assumed with uniform draw maintained over certain period of time. Three distinct profiles were studied;

1. In-phase load, where the uniform draw occurs during the same time period when the solar irradiation is greater than zero.
2. Out-of-phase load, where the uniform draw occurs during the time period when the solar irradiation does not exist.
3. Uniform load, where the uniform draw occurs over the whole day.

The draw was taken to be 189 L/day corresponding to the average daily consumption of hot water of a single-family house in Canada (Edwards et al., 2014). Figures 6.46-6.48 illustrate the three different load profiles with respect to the solar irradiation profile in March 21st. The value of the flow rate in each case varies such that the time integral of the flow rate profiles over 24 hours of operation yields 189 litres.

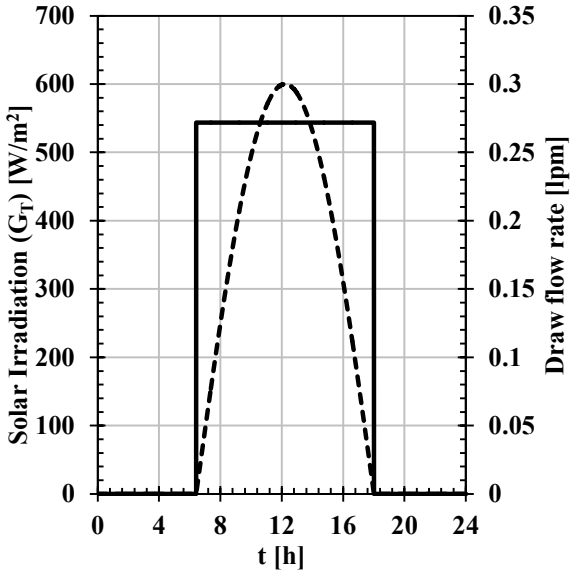

Figure 6.46. Temporal profile of the solar irradiation (G_T) in March 21st in Toronto and draw flow rate in lpm for in-phase load. Solid line: draw flow rate profile (Right Axis). Dashed line: solar irradiation profile (Left Axis).

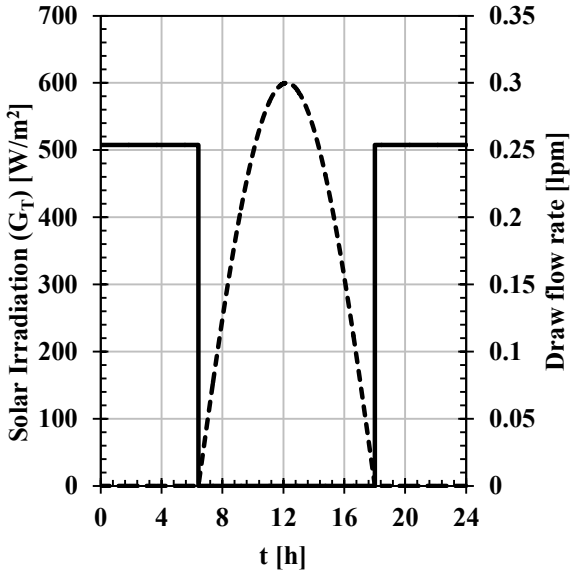

Figure 6.47. Temporal profile of the solar irradiation (G_T) in March 21st in Toronto and draw flow rate in lpm for out-of-phase load. Solid line: draw flow rate profile (Right Axis). Dashed line: solar irradiation profile (Left Axis).

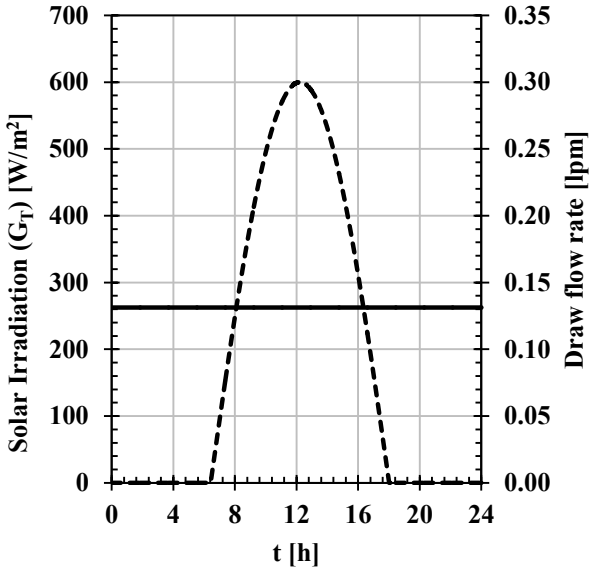

Figure 6.48. Temporal profile of the solar irradiation (G_T) in March 21st in Toronto and draw flow rate in lpm for uniform load. Solid line: draw flow rate profile (Right Axis). Dashed line: solar irradiation profile (Left Axis).

Second, realistic DHW profiles were explored using the statistical study results presented by Edwards et al. (2014) for 73 single-family houses in Québec, Canada. These results were also found to agree with the consumption profiles for DHW in Ontario, Canada (Thomas et al., 2011). These studies divided the DHW consumption into four different patterns; the dominant morning consumption, the dominant evening consumption, the dominant night consumption and the dispersed consumption. Figures 6.49a-d illustrate the different draw patterns.

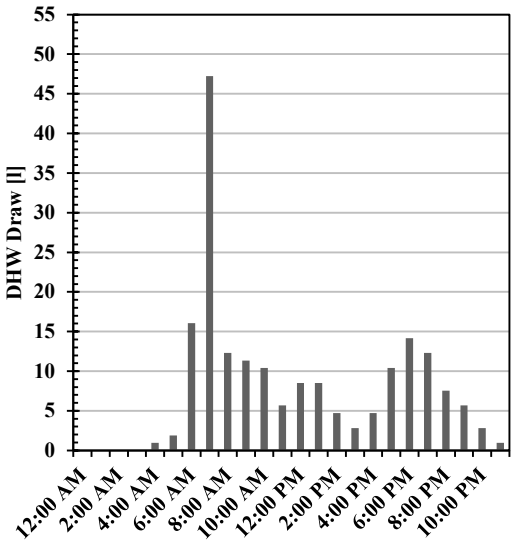

Figure 6.49a. Average daily DHW draws in litres for dominant morning consumers (Edwards et al., 2014)

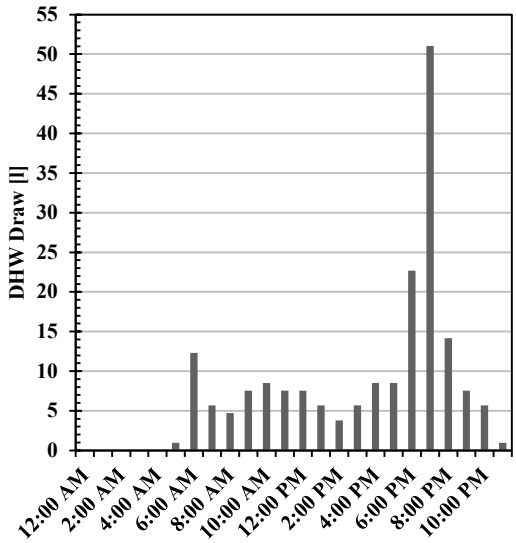

Figure 6.49b. Average daily DHW draws in litres for dominant evening consumers (Edwards et al., 2014)

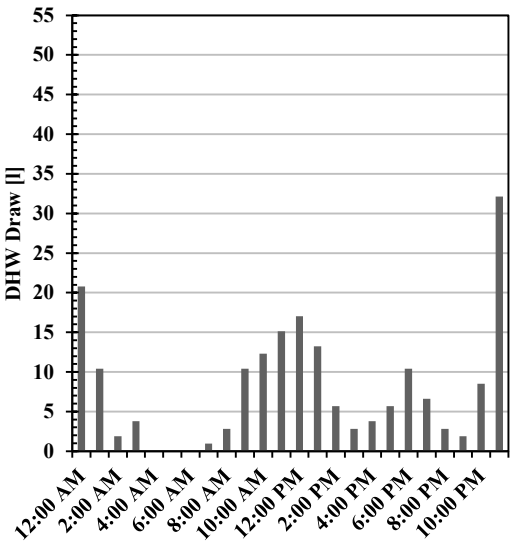

Figure 6.49c. Average daily DHW draws in litres for dominant late night consumers (Edwards et al., 2014)

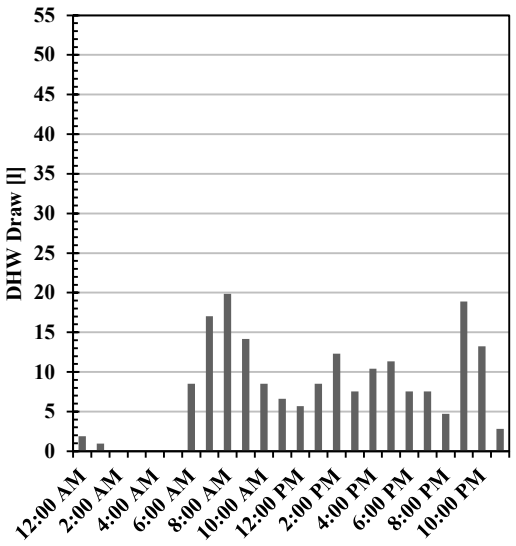

Figure 6.49d. Average daily DHW draws in litres for dispersed consumers (Edwards et al., 2014)

A. Single-tank Sensible Heat Storage (SHS)

Numerical simulations were carried out on a single-tank SHS tank operating in a solar thermal system, shown in Figure 6.43. The four days were simulated individually until the operation of the system reached a steady state. The demand profile was first chosen to be uniform out-of-phase load as illustrated by Figure 6.47. This demand profile was believed to be representative of the case when thermal storage is mostly needed. The main function of the thermal storage component in a given system is to bridge the mismatch between the supply and demand of energy. As such, when the supply and demand exist at the same time, there should be no need for the storage element since the energy can be bypassed directly from the supply side to the demand side.

For single-family residence with an average number of tenants of three, the solar collector area was chosen to be 3 m^2 (~ 1 m^2/person). Typical values were selected for the collector loop parameters as shown in Table 6.12 (Duffie and Beckmann, 2013).

Table 6.12. Design parameters of the solar collector loop.

Parameter	**Value**
Pump flow rate (when powered on) [kg/s]	0.05
Total collector area [m^2]	3
Collector efficiency factor (F')	0.84
Collector $F_R U_L$ [$W/m^2.K$]	4.08
Collector $F_R\tau\alpha$	0.64
Controller ΔT_{ON} [°C]	5
Controller ΔT_{OFF} [°C]	0

The controller ΔT_{ON} and ΔT_{OFF} are calculated as the difference between the mean temperature of the solar collector and the temperature of the bottom node of the storage tank. The value of ΔT_{ON} is typically adjusted to minimize the operation time of the pump when there is not enough energy supplied by the solar collector. This reduces the carryover losses from the warm tank to the colder solar collector during early morning and late afternoon periods. The value of ΔT_{OFF} is typically adjusted relative to ΔT_{ON} in order to avoid the pump cycling. The indoor temperature was assumed to be 20°C in all the simulations for tank losses calculations. The setpoint temperature for the demand was chosen to be 60°C in all the simulations. When the temperature of the water flowing from the top coil heat exchanger of the storage tank to the load is below that setpoint, a controller send a signal to the auxiliary heater to boost the temperature up to the setpoint. When the temperature exceeds the setpoint

value, the controller signals the tempering valve to mix it with the mains water such that the load temperature is regulated at the setpoint.

The storage tank was chosen to have a square cross-section of 0.53 m × 0.53 m and height of 0.72 m, yielding a nominal tank volume of 200 L. The bottom and top heat exchangers were assumed to perform ideally with an effectiveness of unity. The coils were placed in the storage tank such that each of the bottom and top nodes occupies 5% of the tank volume.

The performance of the system was evaluated using the "Solar Fraction". The solar fraction is defined as the ratio between the energy delivered to the load from the storage tank ($E_{delivered}$) and the energy needed by the demand side (E_{load}):

$$Solar\ Fraction = \frac{E_{delivered}}{E_{load}} \tag{6.6}$$

By applying the energy balance on the whole system shown in Figure 6.43 during steady state operation, it can be seen that:

$$E_{delivered} = E_{solar\ incidence} - E_{collector\ losses} - E_{pump} - E_{tank\ losses} \tag{6.7}$$

The terms $E_{solar\ incidence}$, $E_{collector\ losses}$, E_{pump} and $E_{tank\ losses}$ represent the total energy incident on the collector, the thermal losses from the collector to the surrounding, the energy consumed by the pump operation and the thermal losses from the tank. Preliminary calculations showed that the energy consumed by the pump operation is negligible compared to the other terms. Therefore, E_{pump} will be neglected in the subsequent analysis. The solar energy incident on the collector is calculated by:

$$E_{solar\ incidence} = \int_0^{24\ h} F_R\tau\alpha \times G_T \times A_{coll} \times \gamma\ dt \quad (6.8)$$

The multiplier γ takes the value "1" when the pump is running and "0" when the pump is off. The symbol G_T represents the solar irradiation in W/m^2 obtained from the weather database and A_{coll} is the solar collector surface area in m^2.

The collector losses are evaluated using

$$E_{collector\ losses} = \int_0^{24\ h} F_R U_L \times A_{coll} \times (T_{return\ to\ collector} - T_{amb}) \times \gamma\ dt \quad (6.9)$$

The terms $T_{return\ to\ collector}$ and T_{amb} represent the temperature of the heat transfer fluid returning from the bottom heat exchanger of the storage tank to the collector inlet and the ambient temperature surrounding the collector. The former depends on the heat transfer dynamics in the storage element and the latter is an input parameter to the simulations that depends on the weather database, Figure 6.45.

The tank thermal losses are calculated using

$$E_{tank\ losses} = \int_0^{24\ h} (UA)_{tank} \times (T_{average} - T_{surrounding})\ dt \quad (6.10)$$

The terms $T_{average}$ and $T_{surrounding}$ represent the average temperature of water inside the storage tank and the surrounding temperature, respectively. The storage tank is assumed to be located indoors and the surrounding temperature is assumed to be constant at 20°C. The value of the tank loss coefficient U_{tank} was estimated using the experimental results presented in Chapter Five:

$$U_{tank} = 0.58 \times (T_{average} - T_{surrounding})^{0.26} \quad (6.11)$$

When the temperature inside the storage tank is lower than the surrounding temperature, the tank losses are assumed to be equal to zero. The thermal gain is assumed to be negligible.

The energy needed by the load (E_{load}) can be calculated by

$$E_{load} = \int_0^{24\,h} \frac{\rho\, \dot{V}_{load}}{60000} \times c_w \times (T_{setpoint} - T_{mains})\ dt \quad (6.12)$$

The term $\dot{V}_{load}$ represents the DHW demand flow rate in lpm. The $T_{setpoint}$ is the setpoint temperature of the water needed by the load, which is assumed herein to be 60°C. Table 6.13 demonstrates the values of E_{load} corresponding to different days.

Table 6.13. The demand energy corresponding to different days of the year.

Day	**Demand Energy (E_{load}) [MJ]**
March 21st	40.4
June 21st	32.6
September 21st	34.2
December 21st	40.4

Figure 6.50 illustrates the effect of weather data during the operation in different days of the year on the solar fraction of the solar thermal storage system with different storage volumes. It is seen that as the storage volume increases, the solar fraction increases to a maximum, and then it decreases gradually. It is also observed that the effect of operation in

different days of the year act to shift the solar fraction curve vertically. As the solar incidence energy increases, the solar fraction curve shifts upwards as noticed by the curves corresponding to June 21st and September 21st. It is shown that the solar fraction of the system when operating in December 21st is the smallest since the solar irradiation is at minimum during the winter season.

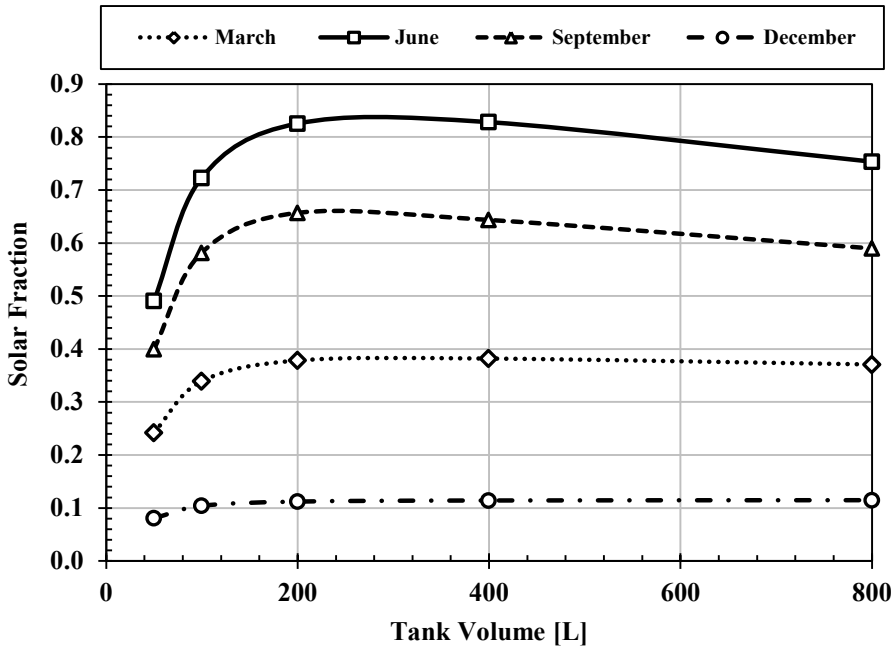

Figure 6.50. Solar fraction versus tank volume for solar thermal DHW system with single-tank SHS operating under out-of-phase load.

Figures 6.51-6.54 demonstrate the effect of weather data in the four different days on the solar incidence energy, collector losses, tank losses and delivered energy in the solar thermal system with different storage volumes. It is observed that as the storage volume increases, the solar incidence energy increases, the collector losses decrease and the tank losses increase.

The increase of the tank losses is attributed to the increase of the surface area of the storage tank. This increase in the thermal losses from the storage tank is the main reason

behind the existence of a local maximum in the delivered energy curves. That is, as the tank volume increases, the net energy collected by the solar collector increases asymptotically, whereas the tank losses increase almost linearly. This results into the occurrence of local maxima in the curves of the delivered energy and the solar fraction.

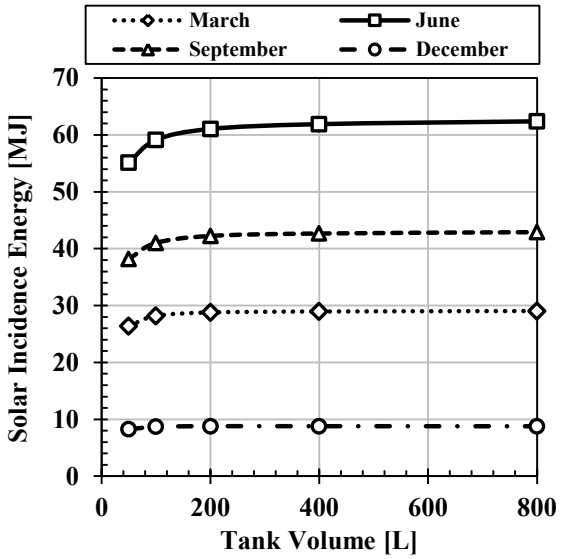

Figure 6.51. Solar incidence energy versus tank volume for solar thermal DHW system with single-tank SHS operating under out-of-phase load.

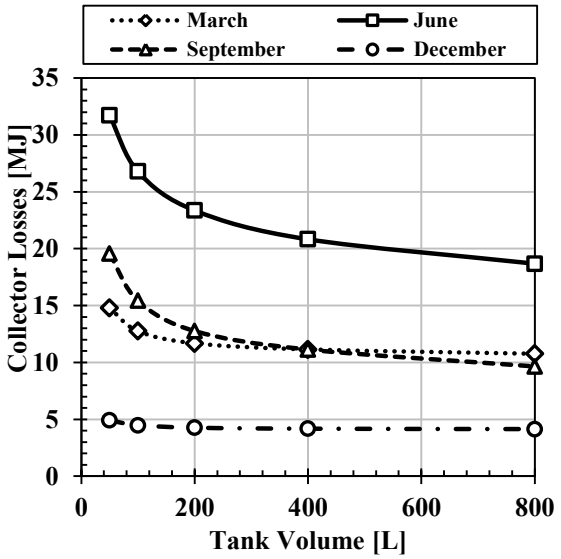

Figure 6.52. Solar collector losses versus tank volume for solar thermal DHW system with single-tank SHS operating under out-of-phase load.

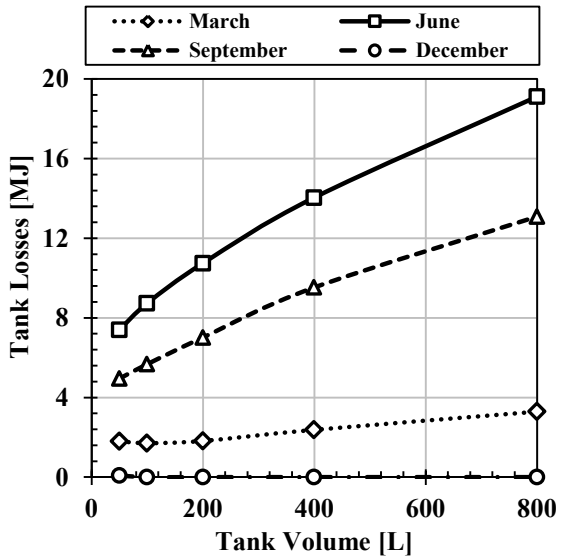

Figure 6.53. Storage tank thermal losses versus tank volume for solar thermal DHW system with single-tank SHS operating under out-of-phase load.

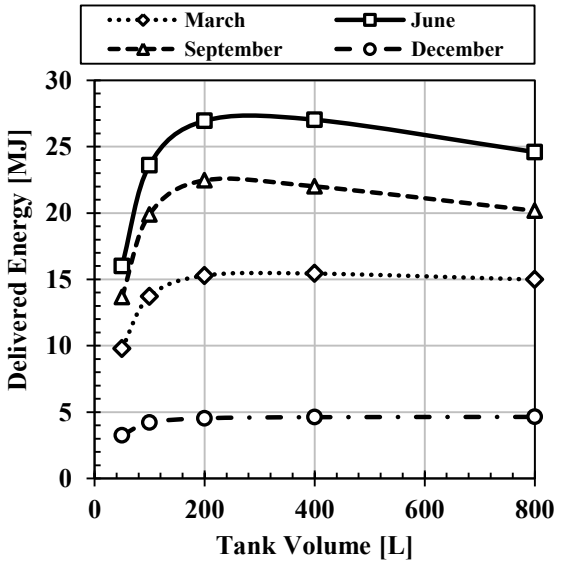

Figure 6.54. Delivered energy versus tank volume for solar thermal DHW system with single-tank SHS operating under out-of-phase load.

In order to evaluate the performance of the solar thermal storage system in a practical context, the maximum available energy that can be collected by the solar collector must be introduced. The solar collector collects the maximum amount of energy when the return temperature to the collector is maintained at the minimum temperature of the system (i.e., the mains temperature). In this condition, the collector losses are at minimum since the mean temperature of the collector is low. Also, the controller is expected to run the pump for longer time periods when the return temperature to the collector is lower. The maximum collectable energy was calculated for the four days and the maximum solar fraction was estimated using

$$Maximum\ Solar\ Fraction = \frac{Maximum\ Collectable\ Energy}{Demand\ Energy\ (E_{load})} \tag{6.13}$$

Table 6.14 presents the values for the maximum collectable energy and the maximum solar fractions for the four days, March 21st, June 21st, September 21st and December 21st. The value of the maximum solar fraction that is larger than one indicates that the available solar energy is larger than the energy required by the load.

Table 6.14. The maximum collectable solar energy corresponding to different days of the year.

Day	**Maximum Collectable Energy [MJ]**	**Maximum solar fraction**
March 21st	27.1	0.67
June 21st	63.5	1.94
September 21st	49.2	1.44
December 21st	6.5	0.16

The reason behind the observed behavior of the solar thermal storage system can be explained by the temporal profiles of the average temperature of the storage tank, the return temperature of the heat transfer fluid to the solar collector, shown in Figures 6.55 and 6.56, respectively. For conciseness, the profiles are presented for March 21st. The profiles for the other days show similar behaviors but with different magnitudes.

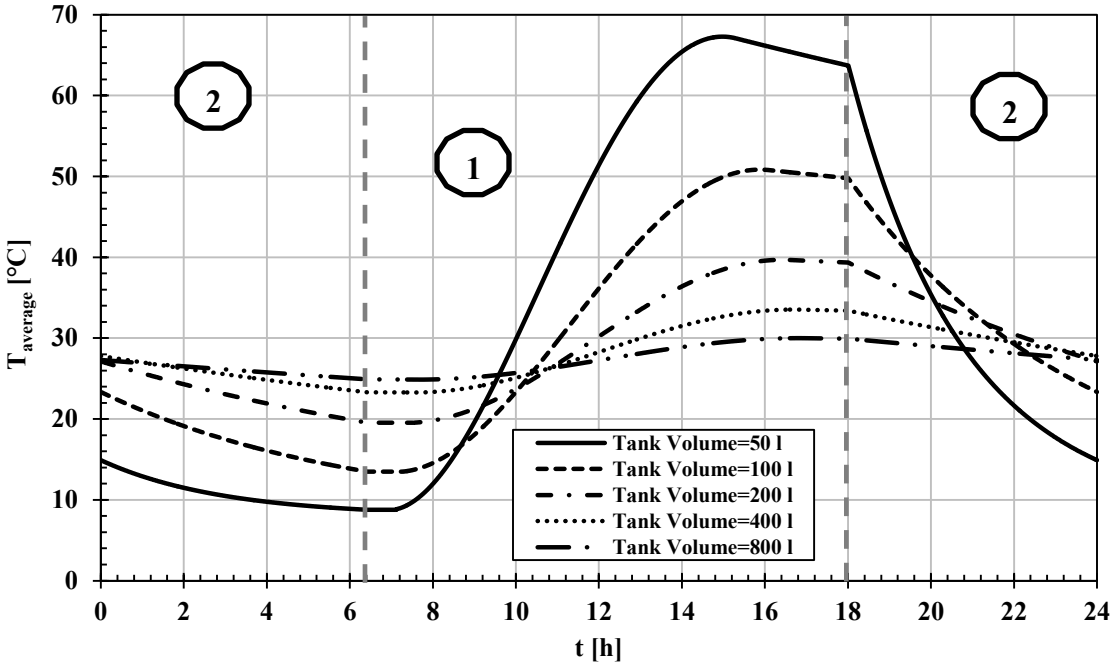

Figure 6.55. Temporal profiles of the average temperature inside the SHS tank with different tank sizes for March 21st weather conditions. Zone 1 indicates the time period in which solar incidence energy exists. Zone 2 indicates the time period in which the solar incidence energy does not exist.

The profile of the average temperature of the storage element illustrates that as the tank volume increases, the temperature swing of the tank decreases. This is primarily attributed to the increase of the heat capacity of the storage element with its volume. The thermal losses from the tank are function of the difference between the average temperature of the storage tank and the surrounding (assumed 20°C). As shown in Figure 6.55, the reason behind the increase of the tank thermal losses with the storage volume cannot be related directly to the average temperature inside the tank. Therefore, it is primarily attributed to the

increase of the surface area of the storage tank. Furthermore, the temperature at the bottom node of the tank directly affects the operation of the pump controller. The lower the temperature inside the tank in the morning, the earlier the pump will operate. However, in the afternoon, the lower the temperature inside the tank, the longer the operation time of the pump, and hence more energy can be collected and stored in the tank.

Figure 6.56 demonstrates the profile of the return temperature from the bottom coil of the storage tank to the solar collector. The profiles are only presented during the operation period of the solar collector pump.

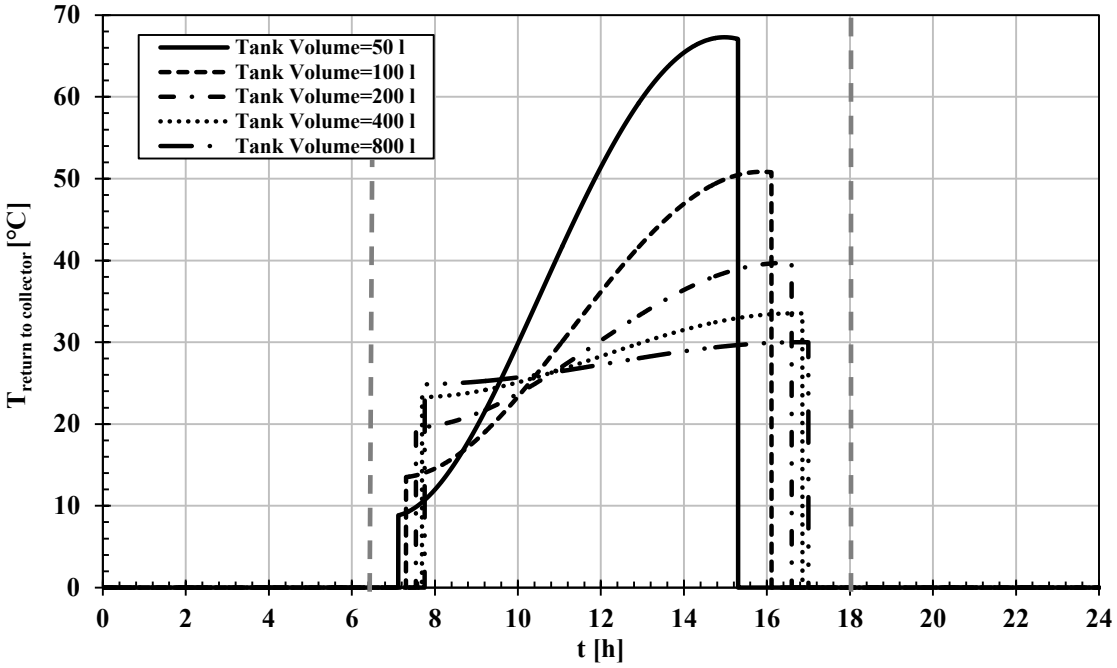

Figure 6.56. Temporal profiles of the return temperature from the bottom coil of the SHS tank to the solar collector for March 21st. The profiles were trimmed to the pump running period.

As previously mentioned, it is seen that the pump operated earlier in the smaller tank because the temperature inside the tank was lower during the early morning. However, the pump operation time is longer in the system with larger tank volume since the temperature inside the tank was lower during the afternoon. This profile also has a great influence on the

performance of the solar thermal storage system. It is worth noting that the thermal losses from the collector are linear function of the difference between the return temperature and the ambient temperature. This means that the higher the return temperature, the larger the collector losses. As a result, the increase of the storage tank volume leads to an asymptotic increase of the net energy collected by the solar collector and a near-linear increase in the thermal losses from the tank.

In order to investigate the annual performance of the solar thermal storage system, annual simulations should be carried out. This comes at a large computation cost especially when intensive parametric studies are involved. As such, the current study proposes an easy way of estimating the annual performance of the solar thermal storage system. Each season of the year will be represented by the steady state performance obtained for the corresponding day. That is, March 21st results will represent the performance during spring, June 21st results will represent the performance during summer, September 21st will represent the performance during fall and December 21st will represent the performance during winter. The average annual solar fraction can then be estimated using

$$Average\ Annual\ Solar\ Fraction = \frac{\sum E_{delivered}}{\sum E_{load}} \tag{6.14}$$

Figure 6.57 illustrates the average annual solar fraction versus the tank volume. It is observed that it performs very close to the performance in March 21st. Also, the importance of this curve lies in the fact that it is the key to the sizing of the storage tank in solar thermal systems. It shows that the best tank size for the given system is 200 litres. Over-sized and under-sized tanks will lead to reduction of the solar fraction of the system.

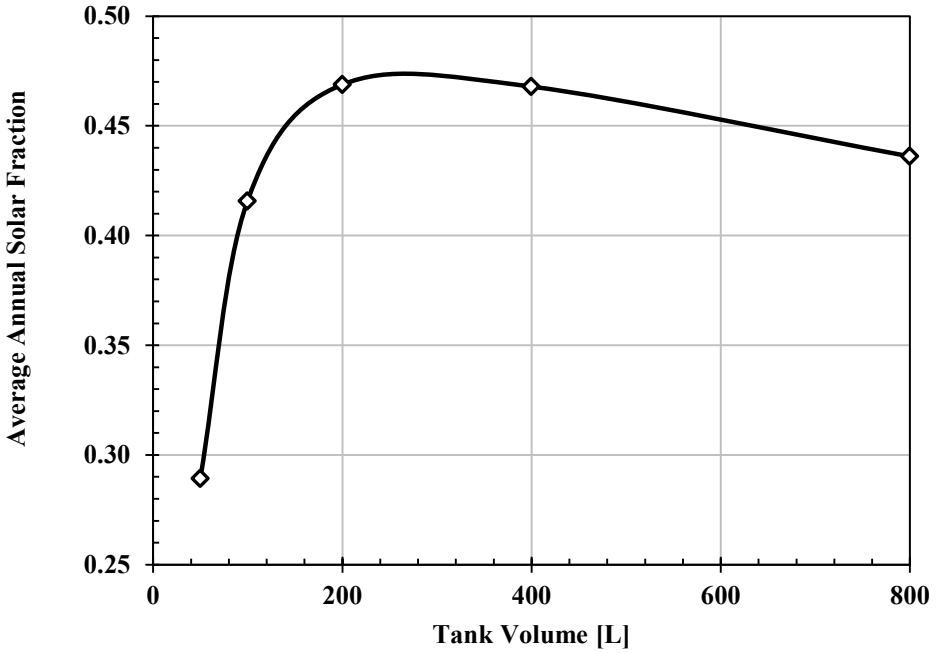

Figure 6.57. Average annual solar fraction versus tank volume for solar thermal DHW system with single-tank SHS operating under out-of-phase load.

The effect of different draw profiles needed to be explored. Numerical simulations were conducted on the solar thermal storage system during steady state operation in March 21st under different demand profiles: in-phase load and uniform load. Figure 6.58 shows the effect of different demand profiles on the solar fraction. It is seen that the solar fraction curves collapse for the larger tank volumes. That is, the solar fraction becomes insensitive to the demand profile as the tank volume increases. At low tank volumes, the solar fraction increases as the load profile becomes in greater alignment with the solar energy availability (i.e., as the load changes from out-of-phase to uniform to in-phase). This is consistent with the role of storage as a mechanism for managing the temporal mismatch between solar energy availability and the household demand for energy. Indeed, in the limit when the solar availability and load are in full alignment, then there is no need for storage and solar fraction

increases as the storage volume decreases and thermal storage acts to penalize system performance as a result of mixing within the tank and heat losses.

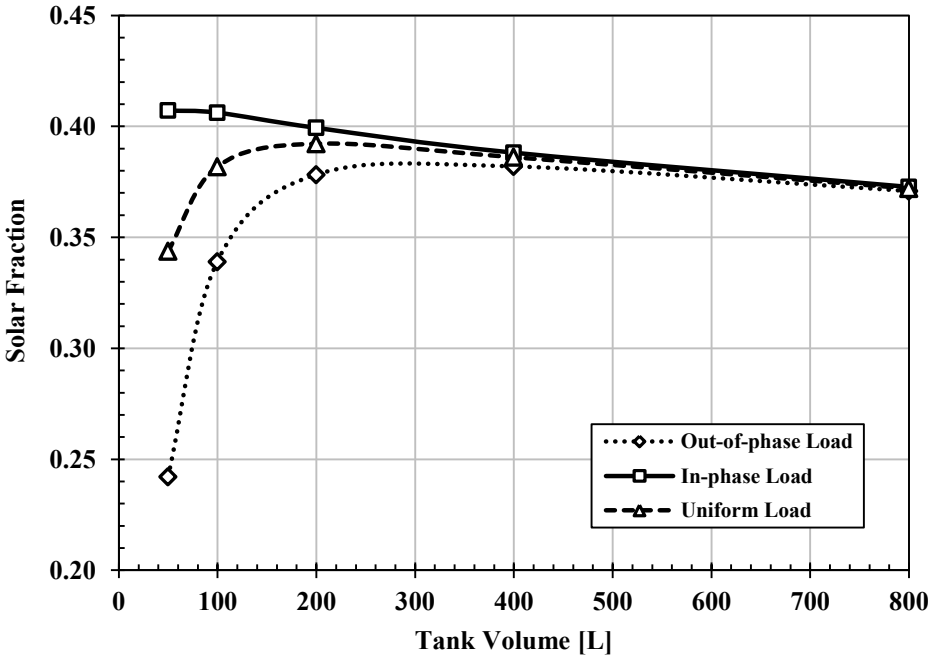

Figure 6.58. Solar fraction versus tank volume for solar thermal DHW system with single-tank SHS operating in March 21st under different demand profiles.

Figures 6.59-6.62 show the effect of the demand profiles on the solar incidence energy, the collector losses, the tank thermal losses and the energy delivered to the load, respectively. The difference in performance between systems operating under different demand profiles can be explained through the average tank temperature and collector return temperature profiles. Figures 6.63a-b and 6.64a-b illustrate these profiles for the tank sizes 100 L and 400 L, respectively.

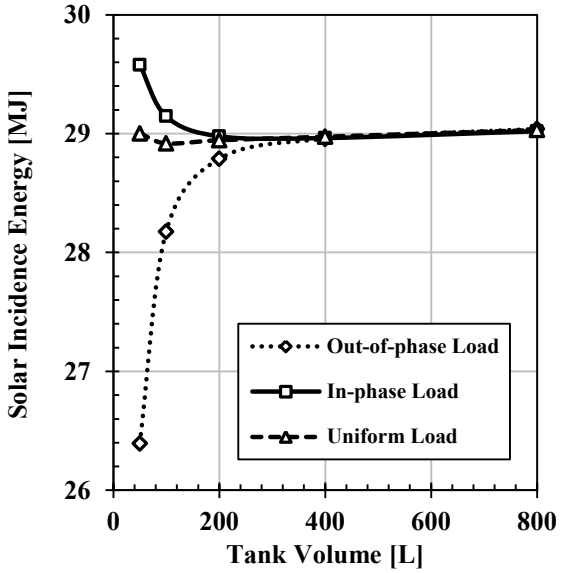

Figure 6.59. Solar incidence energy versus tank volume for solar thermal DHW system with single-tank SHS operating under different demand profiles.

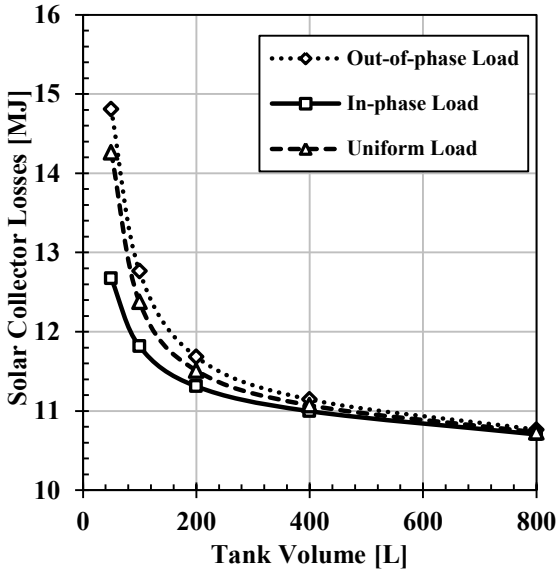

Figure 6.60. Solar collector losses versus tank volume for solar thermal DHW system with single-tank SHS operating under different demand profiles.

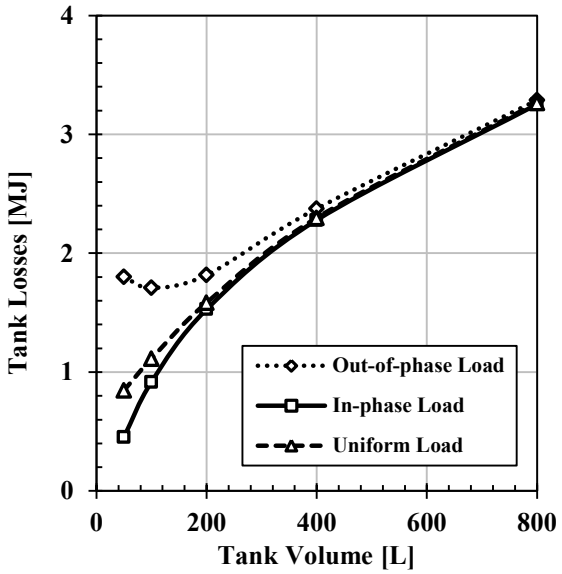

Figure 6.61. Storage tank thermal losses versus tank volume for solar thermal DHW system with single-tank SHS operating under different demand profiles.

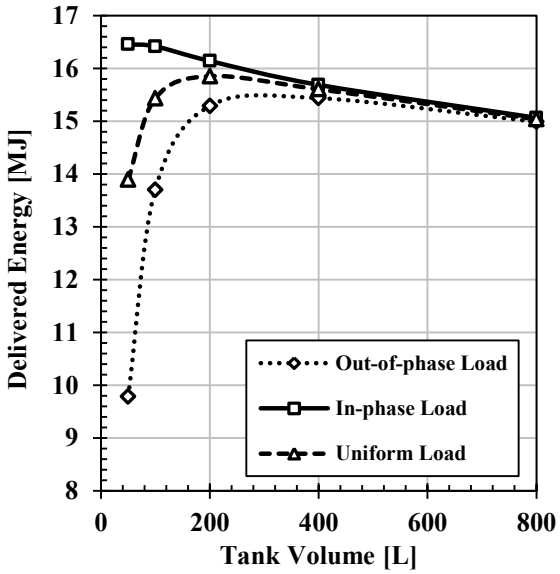

Figure 6.62. Delivered energy versus tank volume for solar thermal DHW system with single-tank SHS operating under different demand profiles.

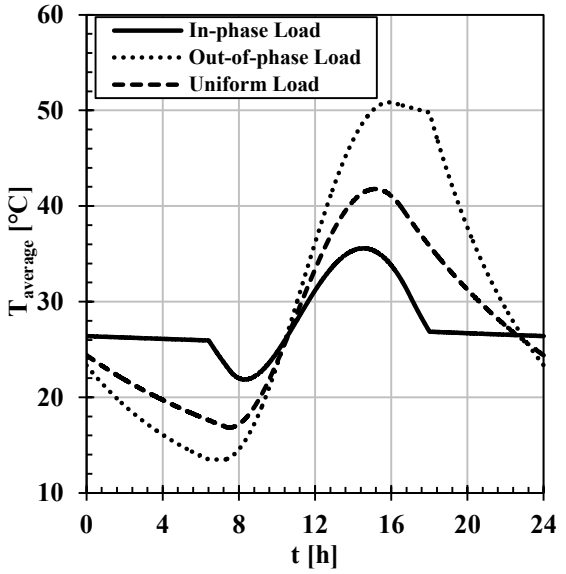

Figure 6.63a. Temporal profiles of the average temperature inside a 100-L SHS tank operating under different demand profiles.

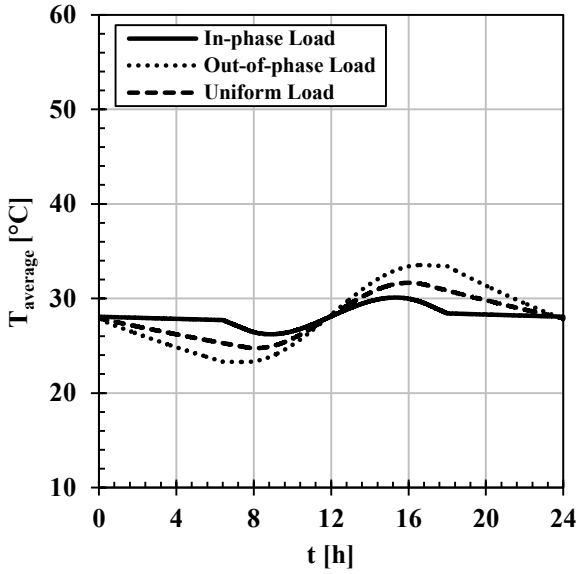

Figure 6.63b. Temporal profiles of the average temperature inside a 400-L SHS tank operating under different demand profiles.

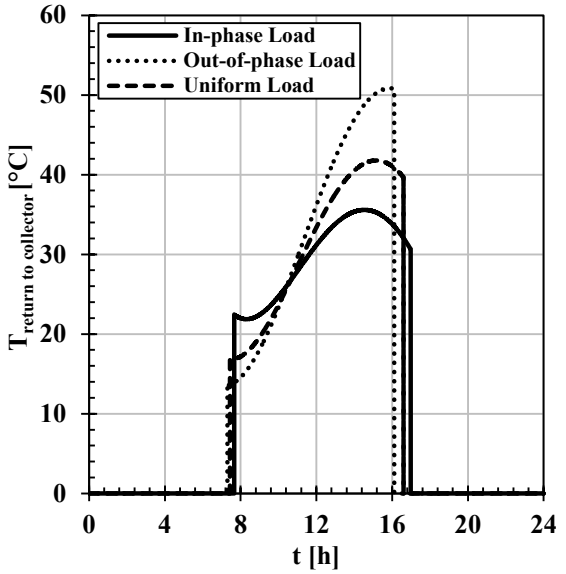

Figure 6.64a. Temporal profiles of the return temperature to the collector from a 100-L SHS tank operating under different demand profiles.

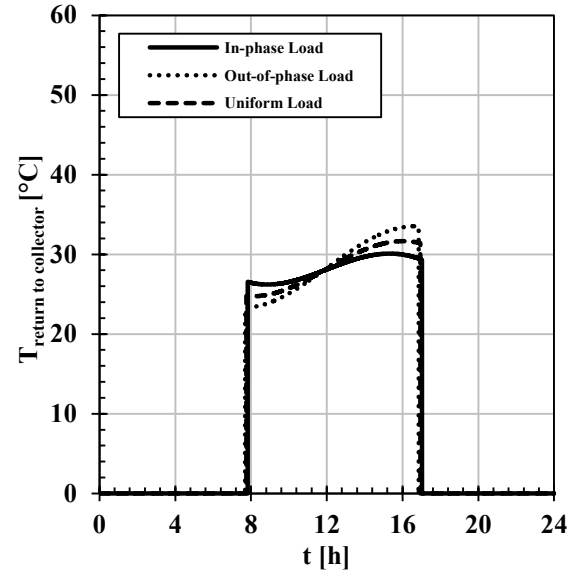

Figure 6.64b. Temporal profiles of the return temperature to the collector from a 400-L SHS tank operating under different demand profiles.

It is seen that the deviation between the performances of the systems with different demand profiles in under-sized tanks is primarily attributed to the temperature swings inside the storage tank. When the demand profile is in-phase with the supply, the temperature levels

inside the tank are low. This leads, first, to longer pump operation time which in turn, helps to increase the collected energy. Second, the thermal losses from the storage tank will be lower due to lower operation temperatures. Third, the return temperature to the solar collector will be lower yielding lower collector losses. In the case of over-sized tank, the temperature swings in the tank are smaller owing to the large heat capacity of the system. As such, the performance of the system becomes insensitive to the type of load.

The performance of the solar thermal storage system under realistic DHW draw patterns was investigated by running numerical simulations using the draw profiles in Figures 6.49a-d. A detailed analysis is demonstrated for the operation of the system in March 21st under dispersed consumption profile (Figure 6.49d). This is meant to show the fundamental differences in the system performance under idealistic and realistic draw patterns. Then, a comparative analysis was undertaken briefly to illustrate the impact of different demand profiles on the performance of the storage system.

Figure 6.65 shows the solar fraction versus the tank volume for the solar thermal storage system operating in March 21st under dispersed consumption profile. It is seen that the solar fraction peaks at a tank size of 200 L. Figure 6.66 demonstrates similar behavior for the energy components of the system as illustrated previously in the cases with idealistic demand profiles. The increase of the thermal losses from the tank in larger tank volumes is the main reason behind the gradual drop of the solar fraction for tank volumes greater than 200 L.

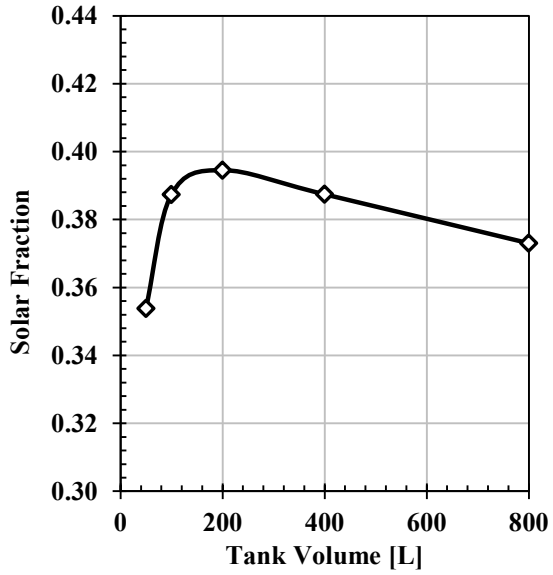

Figure 6.65. Solar fraction versus tank volume for solar thermal DHW system with single-tank SHS operating in March 21st under dispersed consumption profile

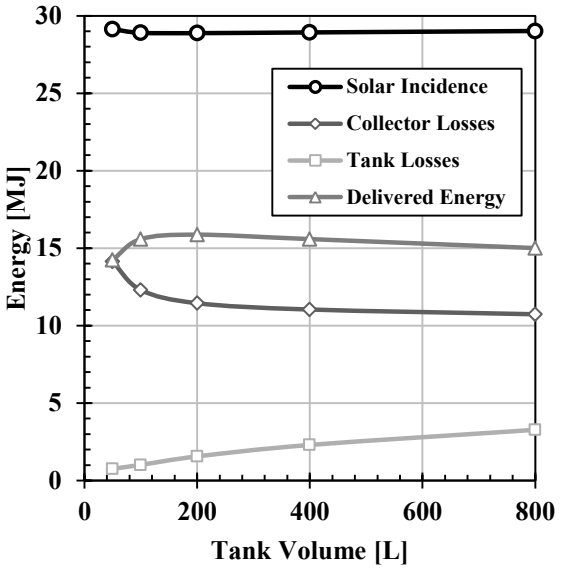

Figure 6.66. Energy components of the solar thermal system versus tank volume for solar thermal DHW system with single-tank SHS operating in March 21st under dispersed consumption profile.

Figures 6.67 and 6.68 demonstrate the temporal profiles of the average tank temperature and the return temperature to the solar collector. The trends are similar to those shown previously in the cases with idealistic demand profiles. However, spiky curves are observed for the smaller storage volumes due to the effect of the discrete hot water draws throughout the day on the energy content of the tank. Each draw causes a significant sudden drop in the tank temperature. These spikes are seen to fade away in larger volumes owing to the larger heat capacity of the larger tanks which acts to damp the abrupt temperature swings of the storage element.

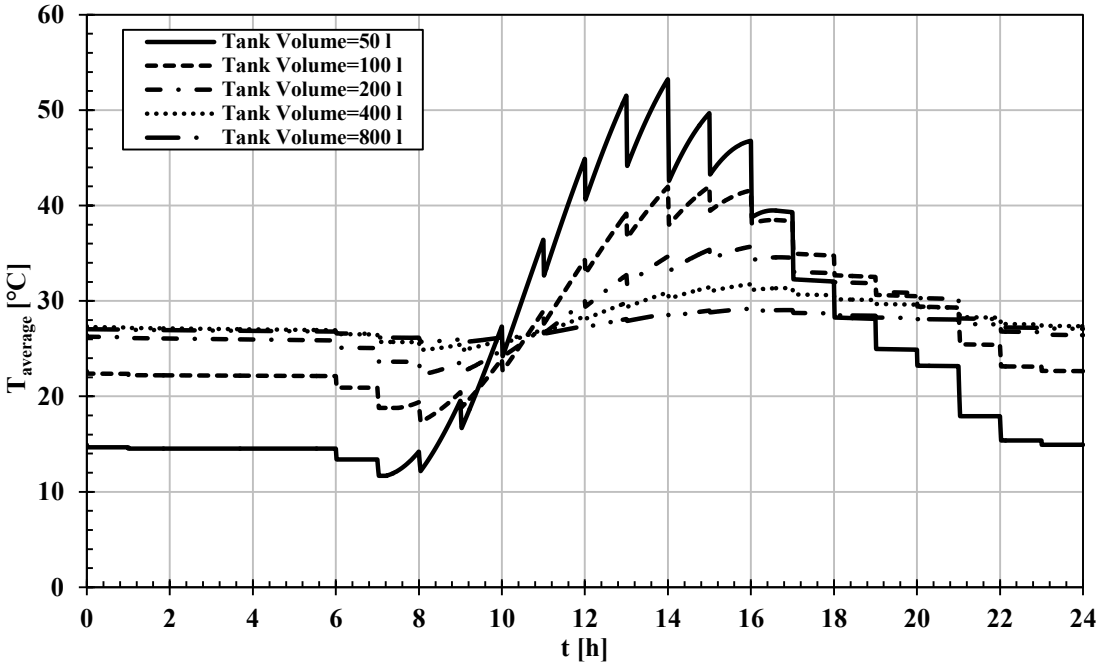

Figure 6.67. Temporal profiles of the average temperature inside the SHS tank with different tank sizes operating in March 21st under dispersed consumption profile.

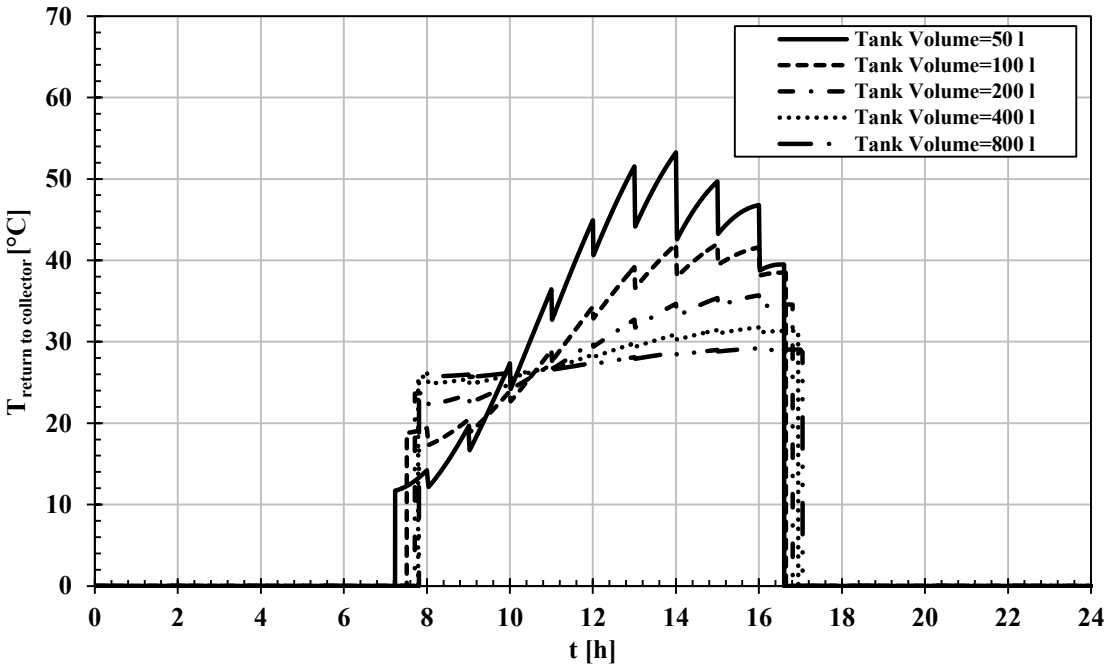

Figure 6.68. Temporal profiles of the return temperature to the collector from SHS tank with different tank sizes operating in March 21st under dispersed consumption profile.

Figure 6.69 compiles the solar fraction profiles versus the tank volume for systems operating under four different draw profiles; dominant morning, dominant evening, late-night and dispersed consumptions. It is observed that the different draw patterns do not show significant impact on the solar fraction. The dashed lines represent the variability limit of ±2% of the mean solar fraction at each tank volume.

Figures 6.70-6.73 demonstrate the effect of different DHW draw patterns on the solar incidence energy, collector losses, tank losses and delivered energy in the solar thermal system with different storage volumes.

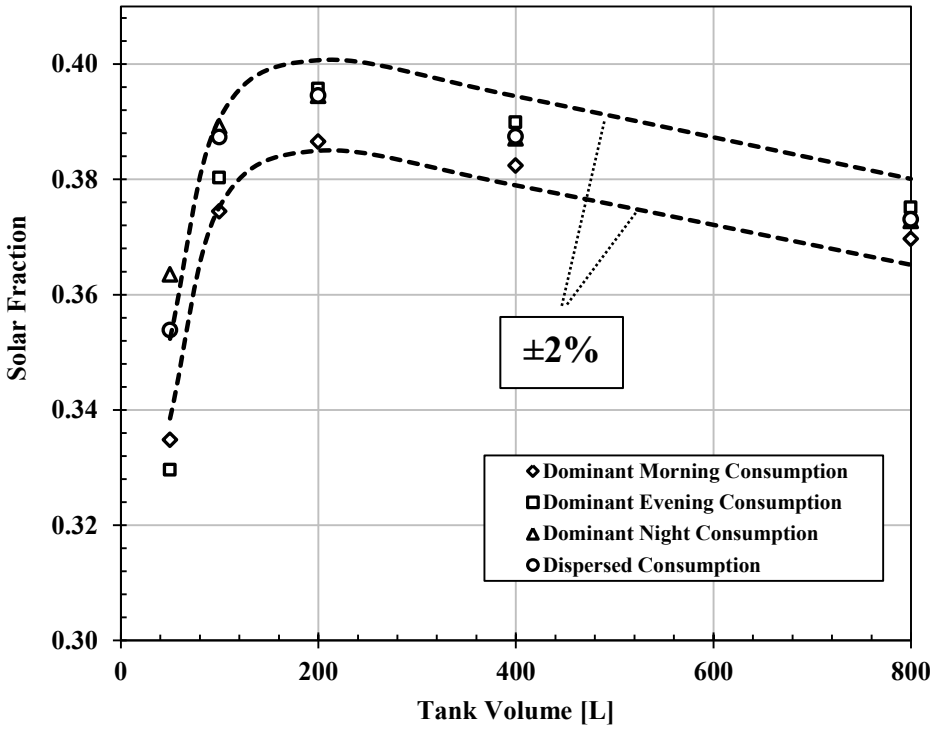

Figure 6.69. Solar fraction versus tank volume for solar thermal DHW system with single-tank SHS operating in March 21st under different DHW draw patterns.

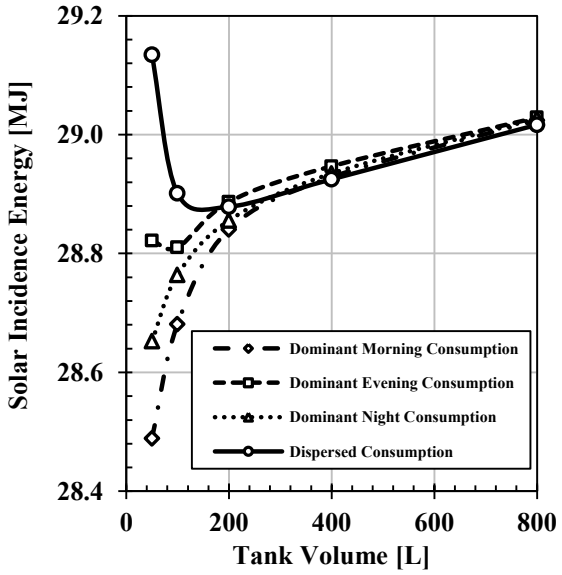

Figure 6.70. Solar incidence energy versus tank volume for solar thermal DHW system with single-tank SHS operating under different DHW draw patterns.

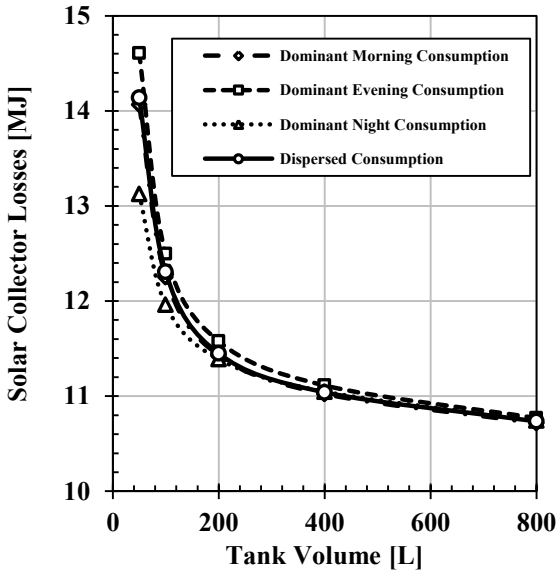

Figure 6.71. Solar collector losses versus tank volume for solar thermal DHW system with single-tank SHS operating under different DHW draw patterns.

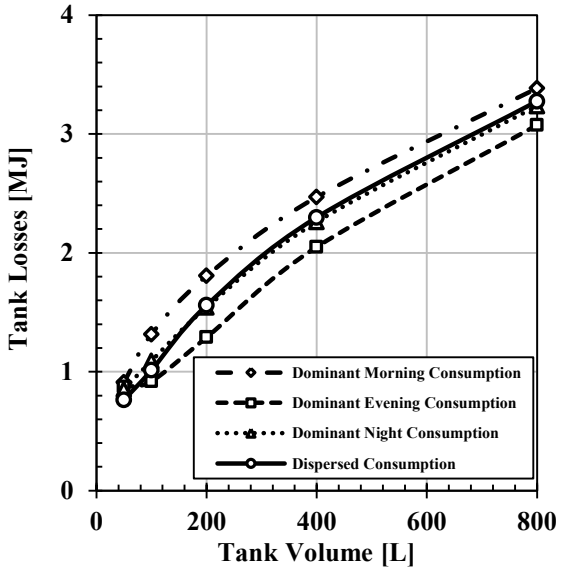

Figure 6.72. Storage tank thermal losses versus tank volume for solar thermal DHW system with single-tank SHS operating under different DHW draw patterns.

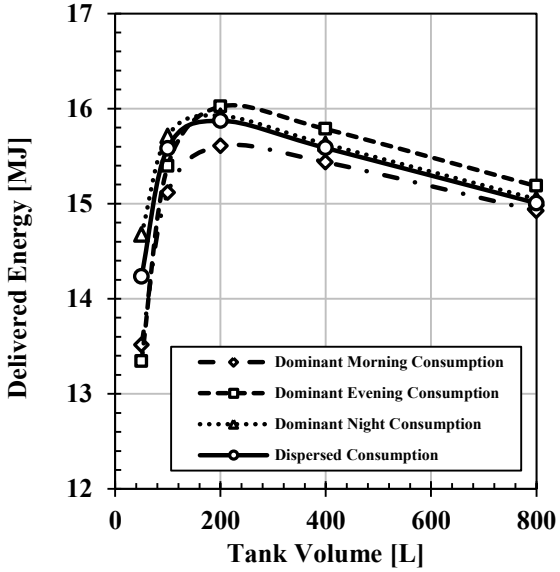

Figure 6.73. Delivered energy versus tank volume for solar thermal DHW system with single-tank SHS operating under different DHW draw patterns.

A. Single-tank Hybrid Thermal Energy Storage (HTES)

In this section, the effect of introducing the HTES tank with PCM on the performance of the solar thermal system is investigated. The benefits of using the HTES over the SHS are highlighted. It was shown in the first section of this chapter that the PCM parameters must be optimized based on the boundary conditions of the system. It was demonstrated that the benefits from the HTES can be maximized by reducing the sources for thermal resistances to heat transfer into and out from the storage element. This can be achieved, first, by enhancing the design of the coil heat exchangers to maximize their effectiveness. Second, the thermal resistance to the heat transfer between the water and the PCM can be minimized by (1) increasing the thermal conductivity of the PCM and/or (2) increasing the surface area of the PCM modules. As such, in this section the heat exchangers will be assumed ideal and the PCM will be assumed as lumped system (large thermal conductivity) to illustrate the potential benefits of the HTES element in real applications.

There are two key design parameters for the PCM that are most critical to the performance of the HTES element and are adjustable, the PCM volume fraction and the PCM melting temperature. The former can be easily adjusted based on the tank size and how much empty space in the tank that can be filled with PCM modules. The latter depends on the range of PCMs available in the market that can suit the operation temperatures in the given system. The rest of the parameters such as the thermophysical properties of the PCM are mostly uncontrollable since they are limited to the type of materials chosen.

It was shown that the average annual performance of the SHS storage system was closer to that of the system in March 21st, as shown in Figures 6.50 and 6.57. As such, the parametric optimization of the HTES system will be conducted using the input weather

profile of March 21st. Then, the performance of the selected design will be tested while operating in different days. The demand profile was chosen to be the out-of-phase load since it represents the case where the storage element is needed the most to bridge the mismatch between the supply and demand.

Numerical simulations were conducted for different HTES tank sizes with ideal bottom and top heat exchangers (effectiveness is equal to unity). Rectangular PCM modules were employed in the HTES tank and were treated as lumped system (negligible internal thermal resistance). In the light of the parametric study performed earlier in this chapter, the HTES tank was filled with PCM modules with a volume fraction of 0.5. This volume fraction was seen to be the maximum with which the tank can be packed while the spacing between the PCM modules is maintained at 10 mm. The melting temperature was chosen to be 30°C for all the simulations. This value was selected based on the average temperature of operation observed in the SHS tank, Figure 6.55. The PCM properties were set in all simulations to the values presented in Table 6.15.

Table 6.15. Thermophysical properties of PCM.

Property	Density (ρ_{PCM}) [kg/m^3]	Specific heat capacity (c_{PCM}) [kJ/kg.K]	Latent heat of fusion (H_f) [kJ/kg]
Value	870	2.15	182

Figure 6.74 illustrates a comparison between the solar fraction of the HTES and the SHS systems with different storage tank sizes. It is shown that HTES system demonstrates similar yet better performance than the SHS system. Looking at the SHS system performance, it is observed that the matched tank size is 200 L (point A in Figure 6.74).

Using the HTES element with the same volume (point B) yields around 5% enhancement of the solar fraction.

It can also be argued that the performance of the matched-size SHS system (point A) can be obtained from the HTES system with half the storage volume (point C). Notice that the 100-L HTES system (point C) outperforms the 100-L SHS system (point D) by approximately 10%. This indicates the ability of the HTES system to reduce the square footage of the storage system by 50%. This sheds the light on the potential benefits of the HTES system compared to the conventional SHS system. It can be concluded that the major advantage of the HTES system stands out in the applications where there are constraints on space available for thermal energy storage. Figures 6.75-6.78 demonstrate the comparison between the energy components of the SHS and the HTES systems.

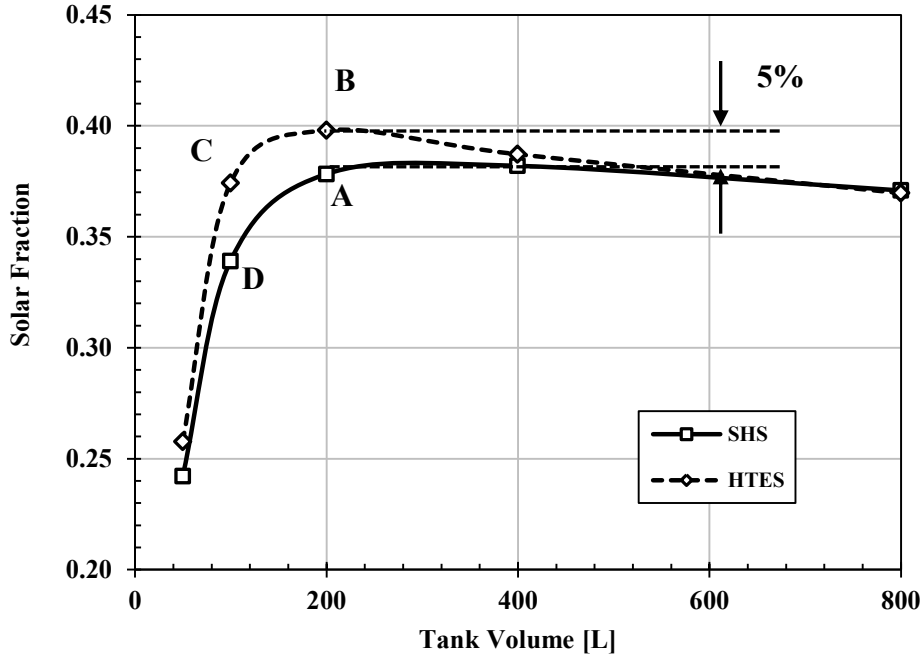

Figure 6.74. Solar fraction versus tank volume for solar thermal DHW system operating in March 21st under out-of-phase load. Comparison between single-tank SHS and single-tank HTES.

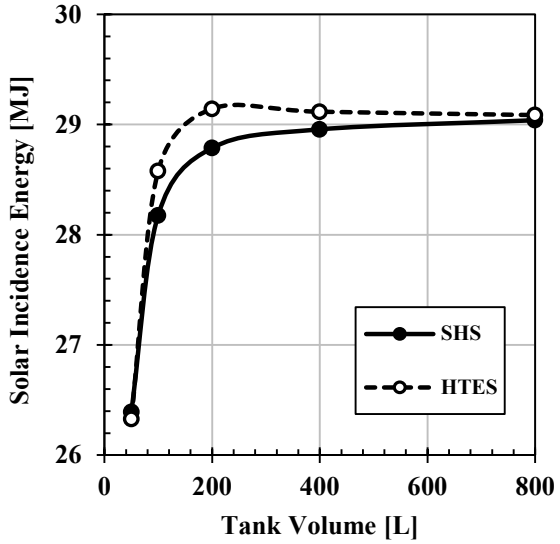

Figure 6.75. Solar incidence energy versus tank volume for solar thermal DHW system with single-tank SHS and HTES operating under out-of-phase load.

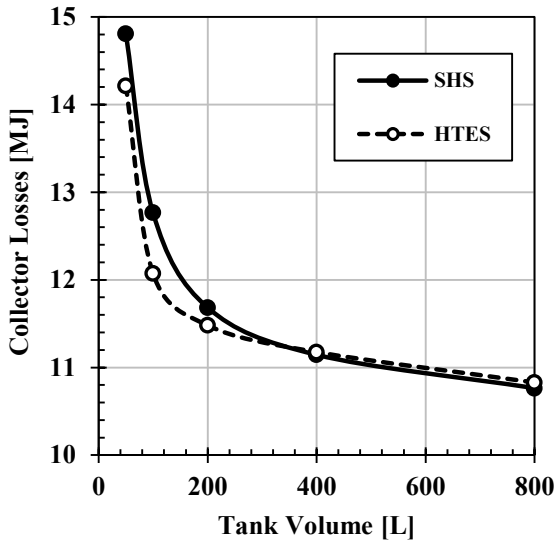

Figure 6.76. Solar collector losses versus tank volume for solar thermal DHW system with single-tank SHS and HTES operating under out-of-phase load.

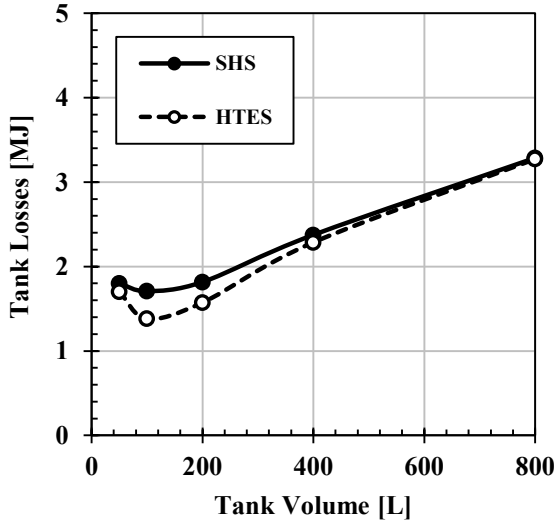

Figure 6.77. Storage tank thermal losses versus tank volume for solar thermal DHW system with single-tank SHS and HTES operating under out-of-phase load.

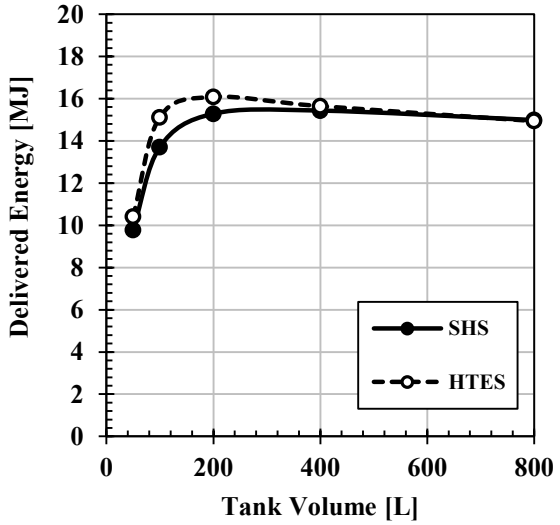

Figure 6.78. Delivered energy versus tank volume for solar thermal DHW system with single-tank SHS and HTES operating under out-of-phase load.

It is seen that the HTES system is typically characterized with larger solar incidence energy, smaller collector losses, and smaller tank losses compared to the SHS system with the same storage volume. This behavior can be explained by looking at the profiles of the average temperature of the tanks and the return temperature to the solar collector. To illustrate the significant differences, the profiles are presented for an under-sized tank (100 L), Figures 6.79 and 6.81, and an over-sized tank (400 L), Figures 6.80 and 6.82. The major advantage of the PCM in the HTES tank appears in modulating the operation temperature of the system around the melting temperature of the PCM. This is more pronounced in under-sized tanks since the large heat capacity of the over-sized SHS tank limits the temperature swing of the system, Figures 6.79 and 6.80. The temperature modulation feature of the PCM in the under-sized tank helps to (1) reduce the thermal losses from the tank, (2) reduce the collector losses since the return temperature to the collector is lower, Figures 6.81 and 6.82, and (3) prolong the operation of the collector loop pump which increases the collected energy.

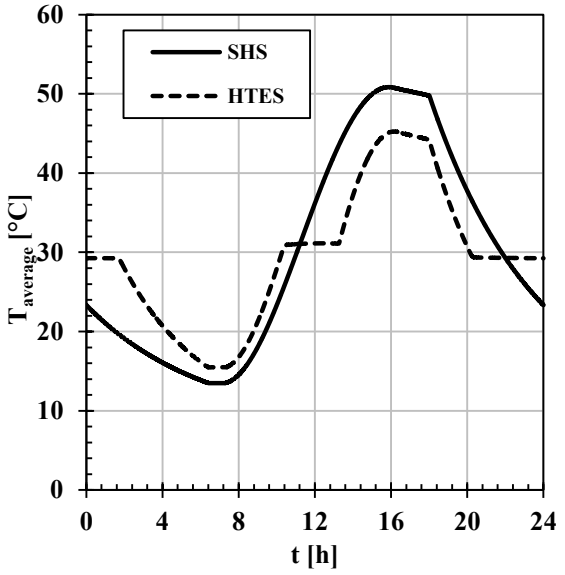

Figure 6.79. Temporal profiles of the average temperature inside a 100-L SHS and HTES tanks operating in March 21st under out-of-phase load.

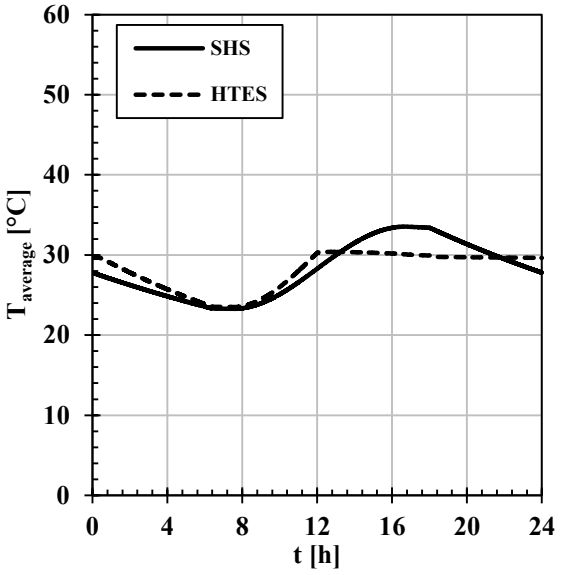

Figure 6.80. Temporal profiles of the average temperature inside a 400-L SHS and HTES tanks operating in March 21st under out-of-phase load.

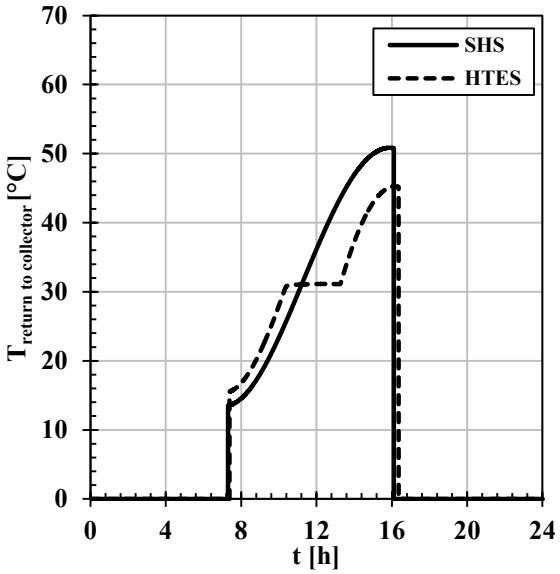

Figure 6.81. Temporal profiles of the return temperature to the collector from a 100-L SHS and HTES tanks operating in March 21st under out-of-phase load.

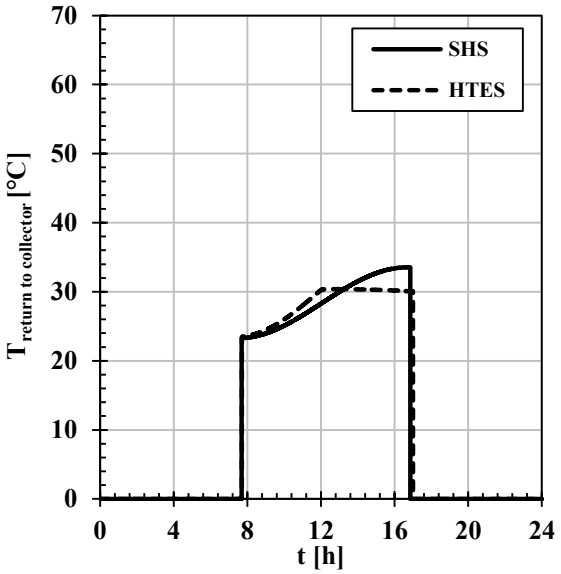

Figure 6.82. Temporal profiles of the return temperature to the collector from a 400-L SHS and HTES tanks operating in March 21st under out-of-phase load.

A parametric study was conducted to optimize the key design parameters of the HTES system, the PCM volume fraction and the melting temperature. The results are presented in Appendix C for two cases where the storage tank is under-sized (100 L) and over-sized (400 L).

It is seen that increasing the PCM volume fraction increases the solar fraction of the HTES system. However, the effect is more pronounced in the case with under-sized tank owing to the better temperature modulation effect of the PCM. Also, the effect of the PCM melting temperature is found to be more pronounced in the under-sized tank. In order to achieve maximum solar fraction, the PCM melting temperature should be chosen to match an optimum value that is a function of the boundary conditions of the system (the supply and demand profiles).

i. Effect of Weather Profile (different days/seasons)

The parametric study provided in Appendix C shows that the best performance of the HTES system in March 21st can be attained when the PCM volume fraction is 0.5 and the melting temperature is 30°C. Numerical simulations were carried out to investigate the performance of the optimized design of the HTES system when operating in different days.

Figures 6.83-6.85 present the solar fraction of the solar thermal system operating with SHS and HTES elements in June 21st, September 21st and December 21st, respectively.

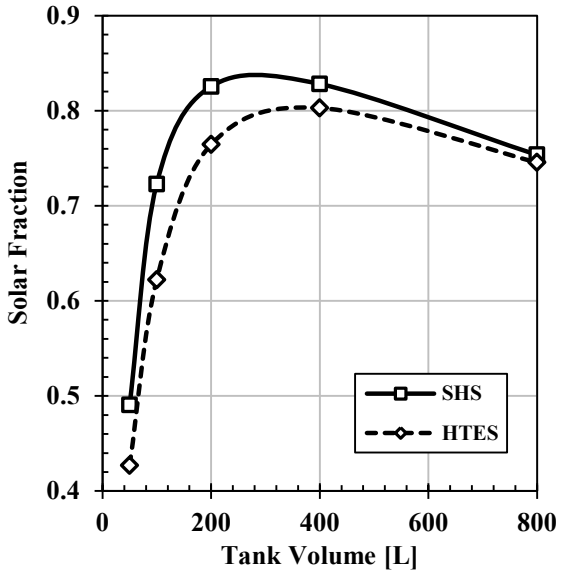

Figure 6.83. Solar fraction versus tank volume for solar thermal DHW system operating in June 21st under out-of-phase load. Comparison between single-tank SHS and single-tank HTES.

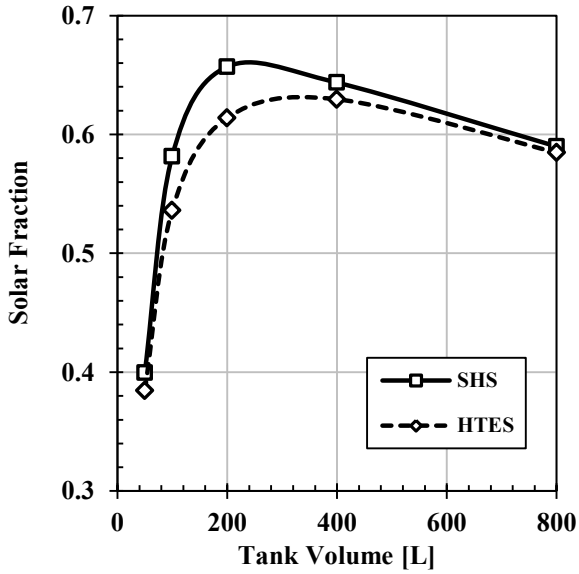

Figure 6.84. Solar fraction versus tank volume for solar thermal DHW system operating in September 21st under out-of-phase load. Comparison between single-tank SHS and single-tank HTES.

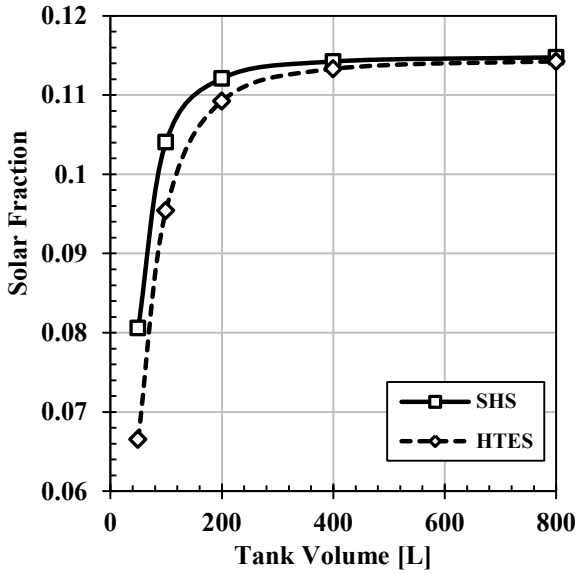

Figure 6.85. Solar fraction versus tank volume for solar thermal DHW system operating in December 21st under out-of-phase load. Comparison between single-tank SHS and single-tank HTES.

It is noticed that the SHS system outperforms the HTES system in all three days. This is primarily attributed to the difference in operation temperature of the system from one day to another. In June, owing to the large availability of solar energy, the average operation temperature of the system was found to be around 80°C. In September, the average operation temperature of the system was found to be around 60°C, whereas in December the average operation temperature of the system was found to be around 17°C due to the limited solar irradiation. This is the reason why in all of these cases, the PCM in the HTES does not undergo phase change, and consequently contributes only to the sensible energy capacity of the system.

This observation motivates the technological advancement in the materials science to invent a phase change material that is capable of altering its melting temperature according to the

operation temperature of the storage system. The theoretical investigation of the potential benefits and feasibility of this concept is recommended for future work.

ii. Effect of Demand Profile

The effect of demand profile on the performance of the solar thermal HTES system was investigated. Figures 6.86 and 6.87 show the solar fraction curves for the in-phase and uniform loads, respectively. As illustrated before, the case where the demand is in phase with the supply does not require a storage element since all the energy can be transferred directly from the supply side to the demand side. The use of the HTES tank did not show significant improvement to the solar fraction of the system, as shown in Figure 6.86. Also, the case of uniform load exhibited an intermediate performance between the case with in-phase load and out-of-phase load. Slight improvement of the solar fraction was noticed by using the HTES element instead of the SHS element, illustrated in Figure 6.87.

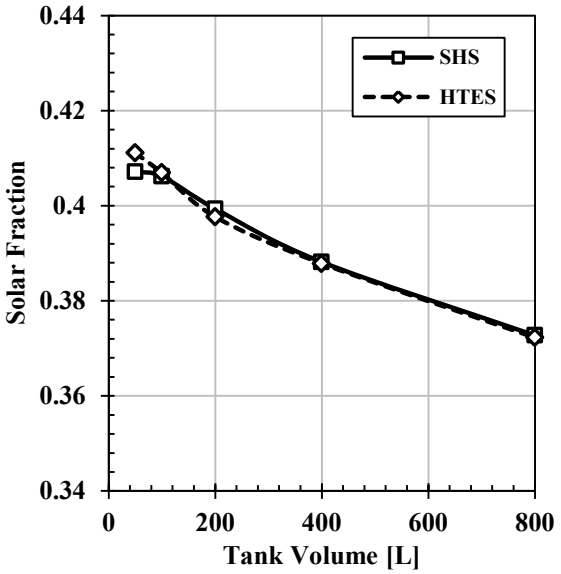

Figure 6.86. Solar fraction versus tank volume for solar thermal DHW system operating in March 21st under in-phase load. Comparison between single-tank SHS and single-tank HTES.

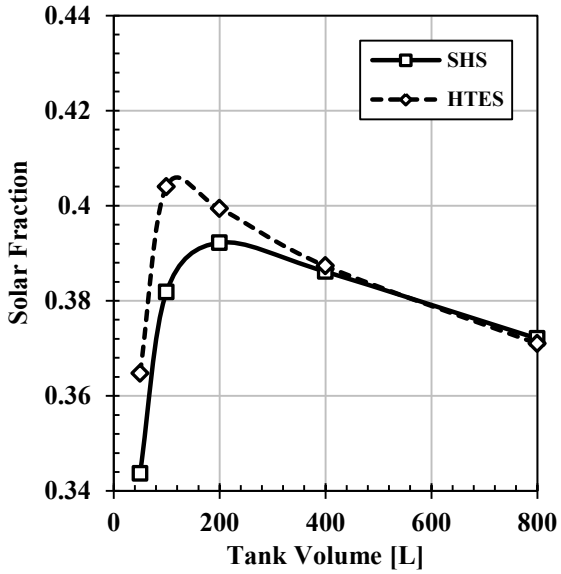

Figure 6.87. Solar fraction versus tank volume for solar thermal DHW system operating in March 21st under uniform load. Comparison between single-tank SHS and single-tank HTES.

Figures 6.88-6.91 illustrate the performance comparison of the solar thermal SHS and HTES systems under realistic DHW draw patterns. It is seen from all the performance curves of different consumption patterns that the SHS system generally outperforms the HTES system. In an attempt to boost the performance of the HTES system, a new design of the PCM modules was explored. Numerical simulations were carried out for the HTES system with PCM encapsulated into 5-mm spheres. Dense packing of spheres can take up to approximately 74% of the packed volume (~26% void fraction). In these simulations, the PCM volume fraction was increased to 0.7. A value of 30% void fraction was dedicated for the coil heat exchangers and the containment material of the PCM. Typically, a spherical capsule of 0.1 mm thickness would occupy less than 10% of the tank volume. Table 6.16 demonstrates the geometric constants associated with the proposed design of the packed bed of PCM spheres.

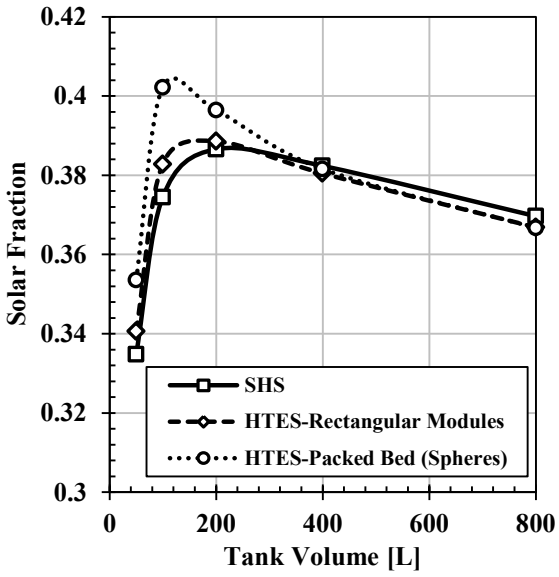

Figure 6.88. Solar fraction versus tank volume for solar thermal DHW system operating in March 21st under dominant morning draw pattern. Comparison between single-tank SHS and single-tank HTES with rectangular PCM modules and spherical packed bed.

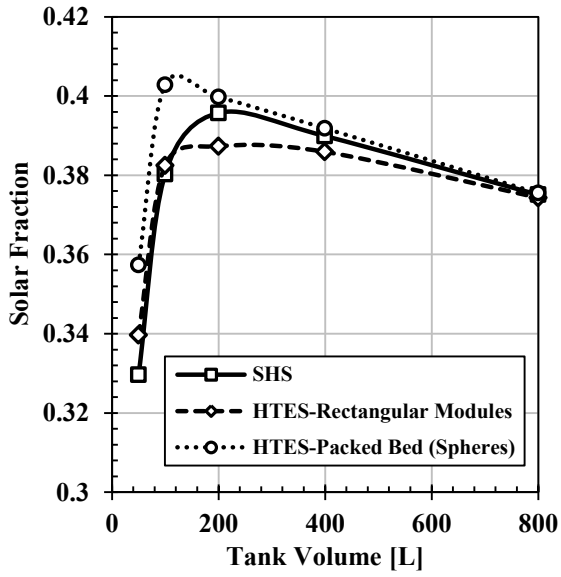

Figure 6.89. Solar fraction versus tank volume for solar thermal DHW system operating in March 21st under dominant evening draw pattern. Comparison between single-tank SHS and single-tank HTES with rectangular PCM modules and spherical packed bed.

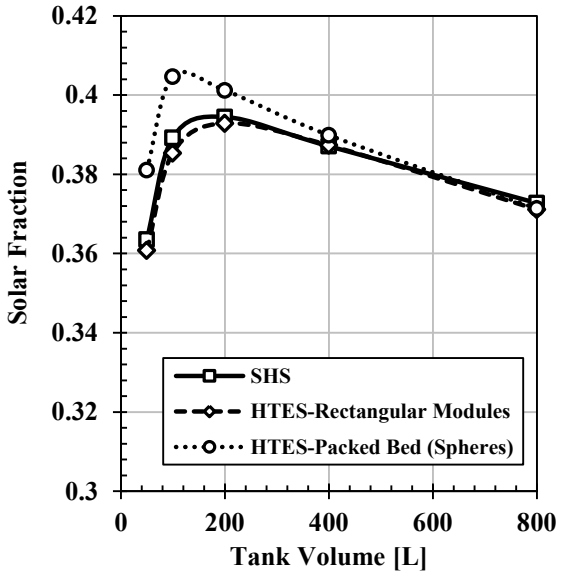

Figure 6.90. Solar fraction versus tank volume for solar thermal DHW system operating in March 21st under dominant late night draw pattern. Comparison between single-tank SHS and single-tank HTES with rectangular PCM modules and spherical packed bed.

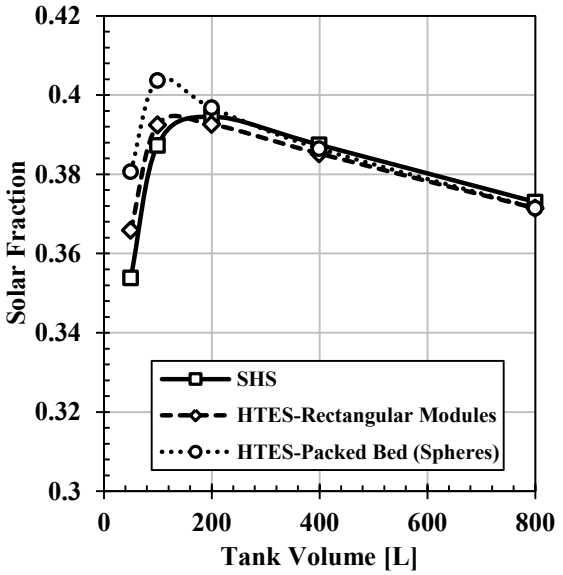

Figure 6.91. Solar fraction versus tank volume for solar thermal DHW system operating in March 21st under dispersed draw pattern. Comparison between single-tank SHS and single-tank HTES with rectangular PCM modules and spherical packed bed.

Table 6.16. Geometrical constants pertaining to the proposed design of the packed bed of PCM spheres.

	Tank Volume [L]				
	50	**100**	**200**	**400**	**800**
Number of modules	0.47×10^6	0.97×10^6	2.05×10^6	4.28×10^6	8.33×10^6
Total volume [L]	30.7	63.7	134	280	545
Actual volume fraction	0.70	0.68	0.69	0.71	0.69
Total surface area of PCM module [m^2]	37.14	76.54	160	336	653

The treatment of the heat transfer between the water and the PCM in the HTES tank was kept unchanged. It is believed that the large increase in the surface area of the PCM modules will outweigh the changes that might encounter the heat transfer coefficient due to the new packing method. As shown in the figures, the new design of the PCM modules is

characterized by more PCM introduced into the HTES tank in addition to a large increase in the surface area of the PCM modules, approximately 20 times the surface area of the rectangular module design. This would result into better temperature modulation of the system and consequently, an enhancement of the solar fraction of the HTES system. It can be concluded that a 200-L SHS tank can be replaced with a 100-L HTES tank employing packed bed of PCM spheres with an enhancement of the solar fraction from 1-3%.

Figures 6.92 and 6.93 show the effect of different designs of the PCM packing on the modulation of the average temperature of the 100-L HTES tank and the return temperature to the collector. These profiles were compared to that of the SHS system while operating in March 21st under a dispersed DHW draw pattern. It is evident that the HTES system with the packed bed of PCM spheres achieves high level of temperature modulation of the system which leads to more solar energy collected and less thermal losses from the system.

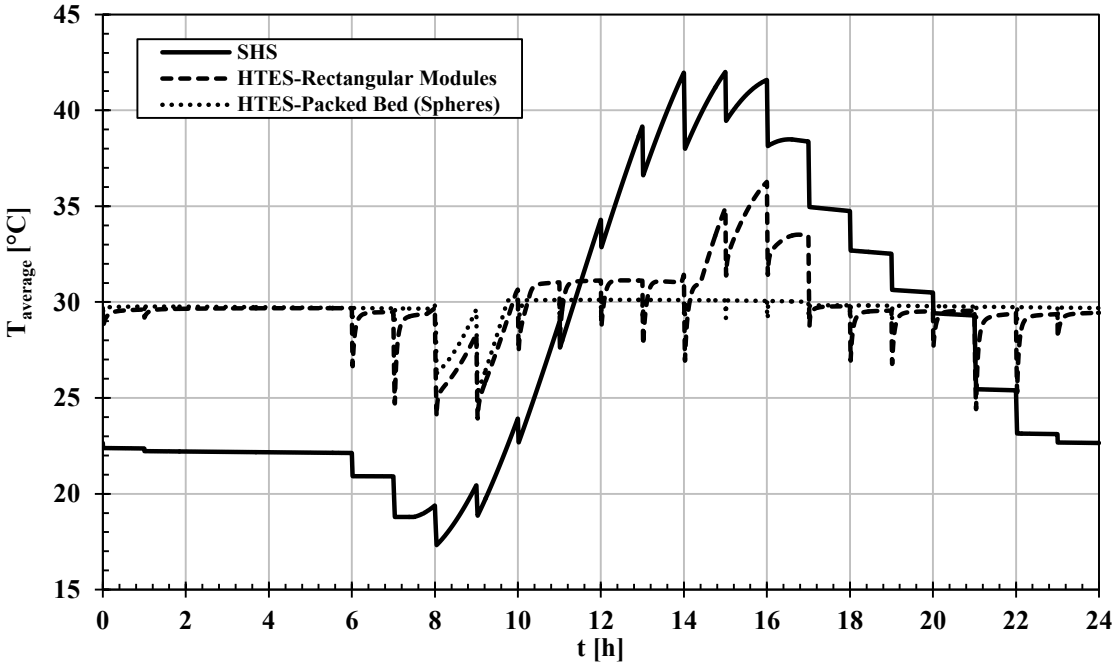

Figure 6.92. Temporal profiles of the average temperature inside a 100-L SHS and HTES tanks with different PCM packing methods operating in March 21st under dispersed draw pattern.

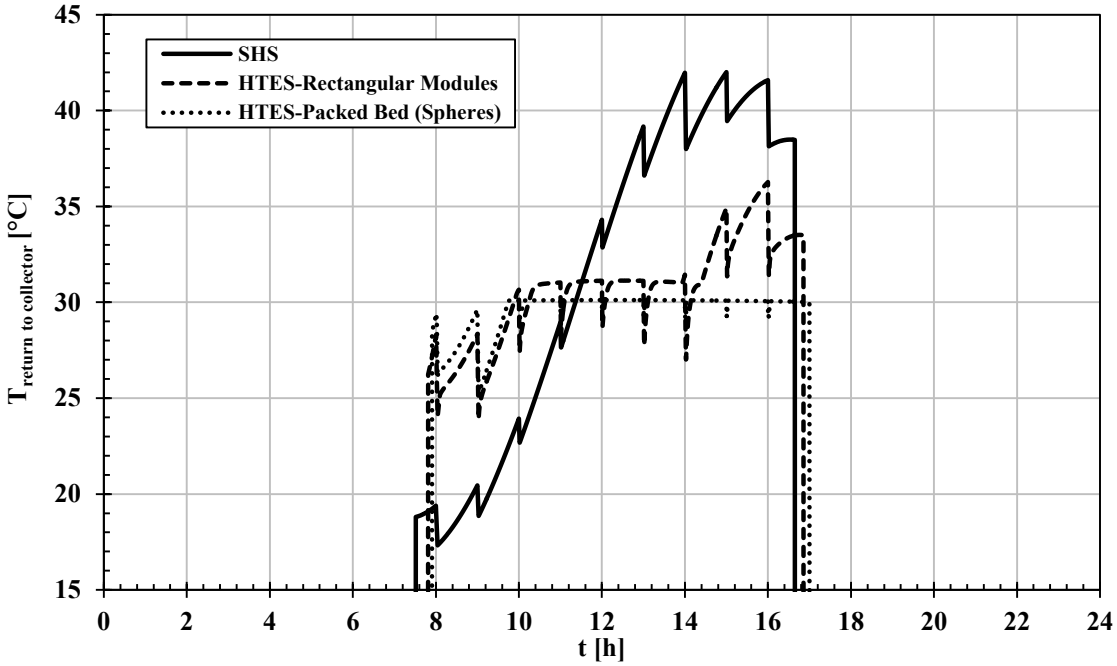

Figure 6.93. Temporal profiles of the return temperature to the collector from a 100-L SHS and HTES tanks with different PCM packing methods operating in March 21st under dispersed draw pattern.

C. Multi-tank (Cascaded) Storage System – SHS versus HTES

In this section the concept of the multi-tank (cascaded) storage system is explored. In medium/large applications such as multi-family residences, motels, restaurants, etc., large water tanks are typically used to satisfy the DHW demands. Despite their good performance, these large tanks require complicated installation procedures and are very difficult to handle and maintain. In addition, they do not offer much flexibility in retrofitting applications since they are difficult to maneuver through doorways. The concept of using a modular multi-tank system that consists of a cascade of serially connected modular tanks can provide a solution to these issues. Moreover, the addition of phase change materials into the tanks may allow for a reduction in the overall size of the thermal storage system. Figure 6.94 illustrates a schematic of a solar thermal DHW system connected to a cascaded HTES with different

PCMs inside each tank. Based on the results from the previous section, each tank in the cascaded storage system was filled 70% by volume with spherically encapsulated PCMs. The diameter of the spheres was 5 mm.

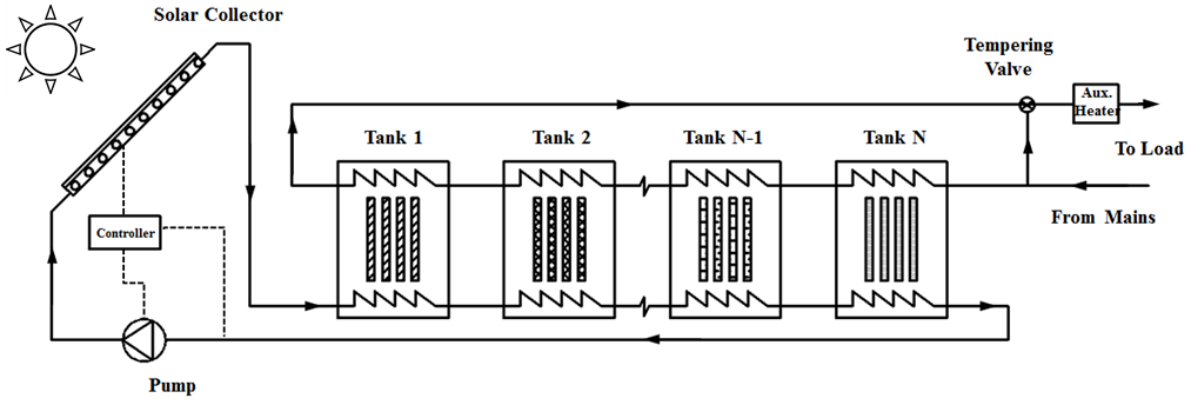

Figure 6.94. Schematic layout of a solar thermal DHW system with multi-tank (cascaded) HTES.

Figure 6.95 shows a HTES tank with a packed bed of spherically encapsulated PCM. In order to suit medium/large DHW applications, the solar collector parameters were sized for an 8-family residence, as provided in Table 6.17.

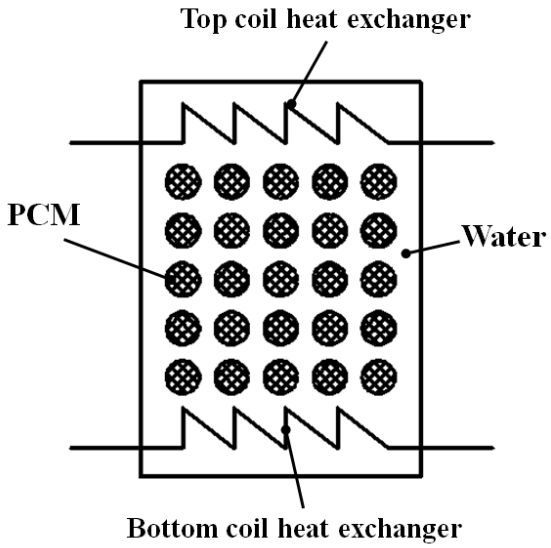

Figure 6.95. Schematic layout of a HTES tank with packed bed of spherically encapsulated PCM.

Table 6.17. Design parameters of the solar collector for 8-family residence solar DHW system.

Parameter	**Value**
Pump flow rate (when powered on) [kg/s]	0.05
Total collector area [m^2]	**24**
Collector efficiency factor (F')	0.84
Collector $F_R U_L$ [$W/m^2.K$]	**3.33**
Collector $F_R\tau\alpha$	**0.52**
Controller ΔT_{ON} [°C]	5
Controller ΔT_{OFF} [°C]	0

A dispersed DHW consumption profile was chosen to suit the daily draw pattern of multi-family residence. The daily consumption was scaled up by eight times. The performance of the 200-L multi-tank HTES system was compared to that of the 200-L multi-tank SHS system. In addition, the performance of the single-tank SHS with the same total volume as that of the multi-tank storage was studied to illustrate the isolated effect of the cascading concept on the sequential stratification of the system. Two sets of numerical simulations were carried out for the multi-tank systems, each with different number of tanks, from 1 to 8 tanks. Another set of numerical simulations was performed on single-tank SHS systems with different tank sizes, 200 L to 1600 L with a step of 200 L. Figure 6.96 illustrates the solar fraction of the large-scale solar thermal DHW system operating in March 21st under dispersed draw pattern.

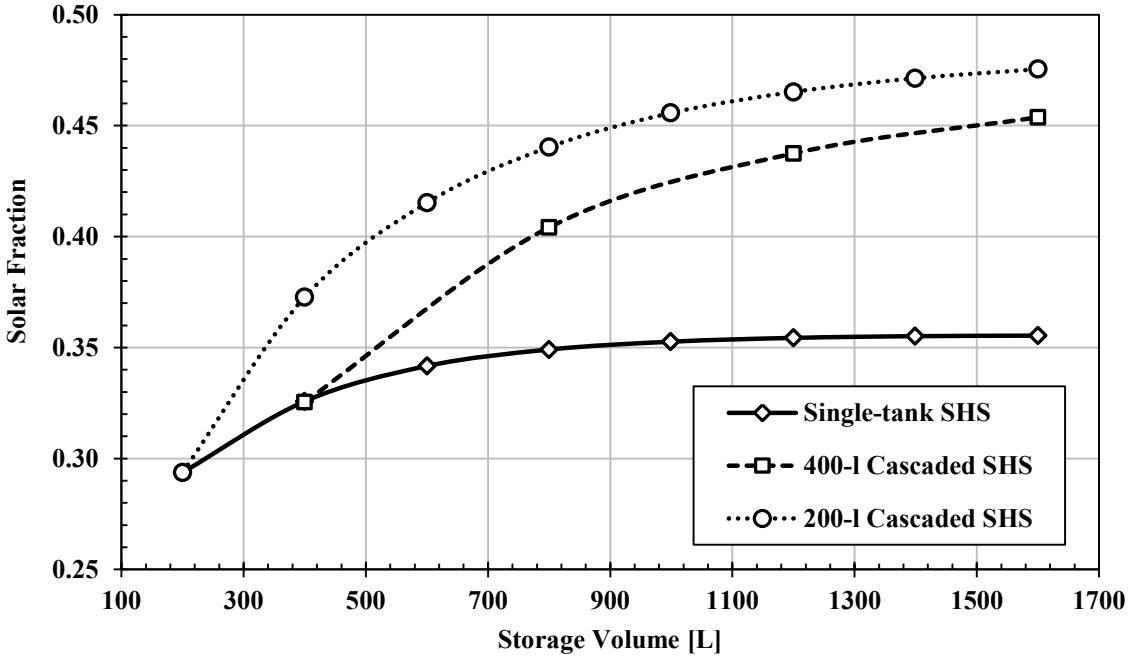

Figure 6.96. Solar Fraction versus total storage volume in litres for solar thermal DHW system operating in March 21st under dispersed draw pattern. Comparison between single-tank SHS and multi-tank SHS with different tank volume.

A comparison is shown between different configurations of SHS elements, (1) single-tank storage, (2) multi-tank storage with tank volume of 400-L each, and (3) multi-tank storage with tank volume of 200-L each. It is seen that the multi-tank storage system significantly outperforms the single tank system. In addition, the multi-tank storage system with smaller tanks performs better than that with larger tank volume for the same total storage volume. For instance, the system with two 200-L tanks achieves around 15% higher solar fraction than the system with one 400-L tank.

Figures 6.97-6.100 show the effect of different configurations of the storage element on the energy components of the solar system; the solar incidence energy, solar collector losses, storage tanks losses and the energy delivered to the load, respectively.

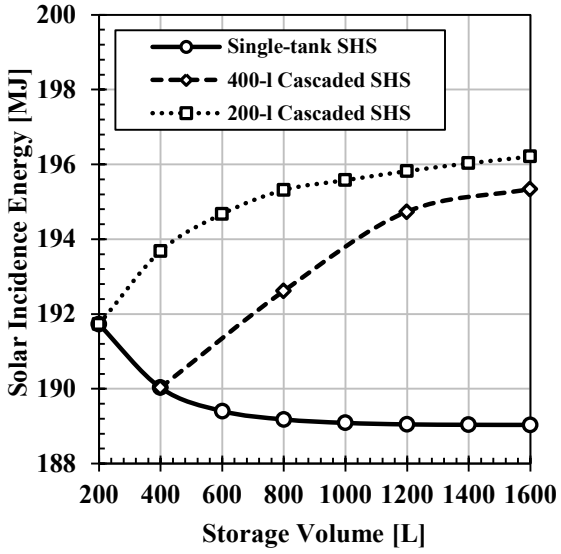

Figure 6.97. Solar incidence energy versus total storage volume in litres for solar thermal DHW system operating in March 21st under dispersed draw pattern. Comparison between single-tank SHS and multi-tank SHS with different tank volume.

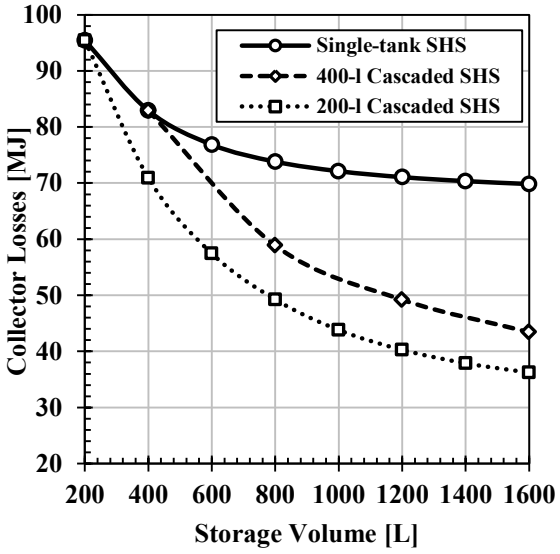

Figure 6.98. Solar collector thermal losses versus total storage volume in litres for solar thermal DHW system operating in March 21st under dispersed draw pattern. Comparison between single-tank SHS and multi-tank SHS with different tank volume.

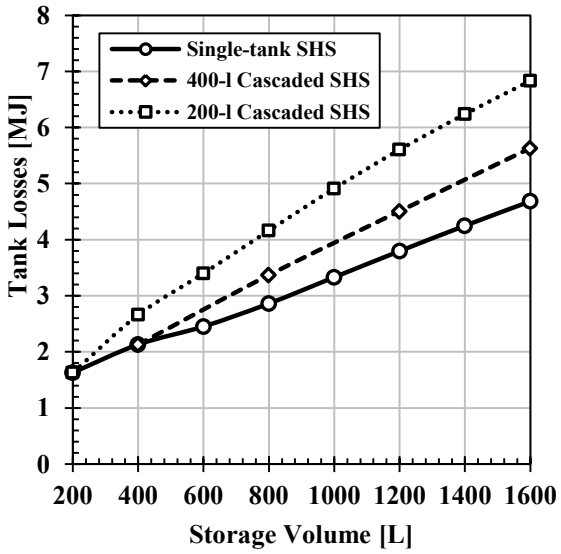

Figure 6.99. Tank thermal losses versus total storage volume in litres for solar thermal DHW system operating in March 21st under dispersed draw pattern. Comparison between single-tank SHS and multi-tank SHS with different tank volume.

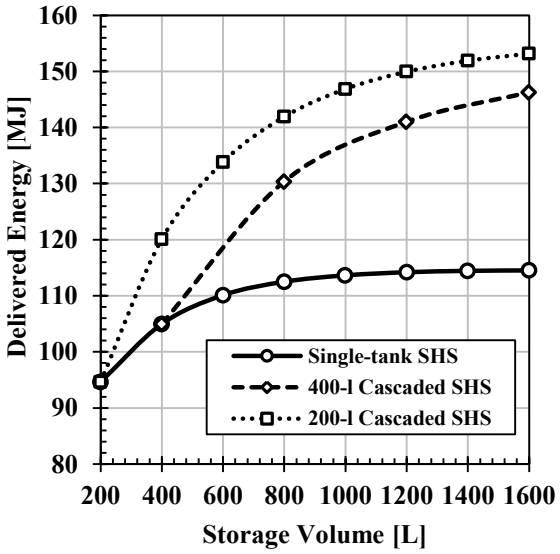

Figure 6.100. Delivered energy versus total storage volume in litres for solar thermal DHW system operating in March 21st under dispersed draw pattern. Comparison between single-tank SHS and multi-tank SHS with different tank volume.

It is observed that the cascaded system with smaller tank volume is characterized with larger solar incidence energy and lower thermal losses from the collector. The former is attributed primarily to prolonged operation of the collector loop pump. The latter is attributed to the lower return temperature to the collector which reduces the losses to ambient air significantly. Figure 6.101 illustrates the temporal profiles of the return temperature to the collector in the solar thermal systems with 1600-L single tank SHS, four 400-L tank cascaded SHS and eight 200-L cascaded SHS.

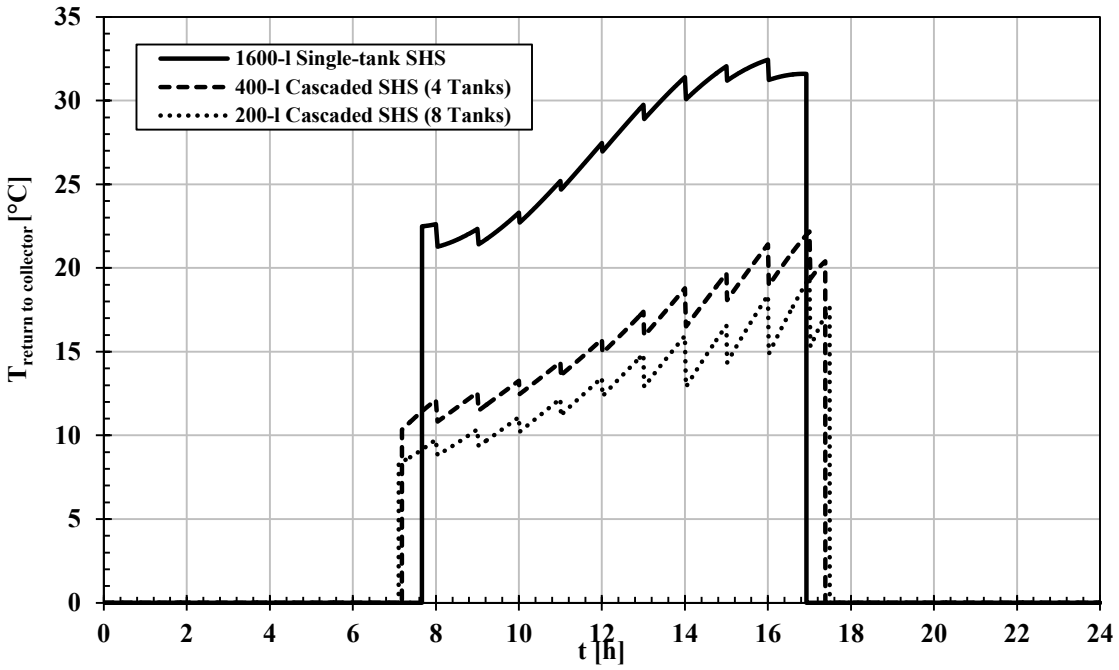

Figure 6.101. Temporal profiles of return temperature to collector for solar thermal DHW system operating in March 21st under dispersed draw pattern. Comparison between 1600-L single-tank SHS and multi-tank SHS with different tank volume, four 400-L tanks and eight 200-L tanks.

The most critical advantage of the multi-tank system is its promotion for sequential stratification. Figures 6.102-6.104 highlight the average temperature profiles in the SHS system with single and cascaded tanks with different tank sizes. It is observed in the multi-tank system that each tank has a distinct temperature profile. The first tank operates at a higher temperature level than the second than the third, etc. This behavior is what is referred

to here as sequential or tank-to-tank stratification. Although each tank performs potentially as a fully mixed tank, the whole storage system performs as one large stratified tank. The larger the number of tanks for a given storage volume, the better sequential stratification can be achieved. In the limit of larger storage volumes (e.g., 1600 L), the large number of small-tank system will have higher thermal losses due to their larger surface area, Figure 6.99. This might lead to a reduction of the solar fraction of the system. In some applications where the storage system is installed indoors, thermal losses from the storage element can offset some the space heating load.

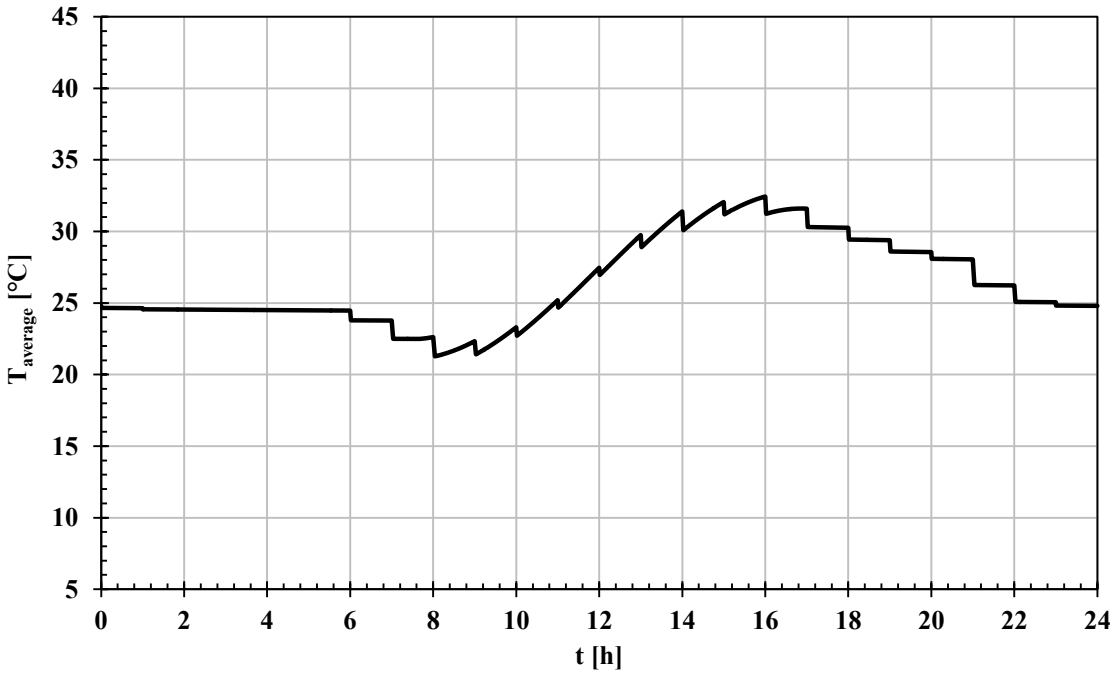

Figure 6.102. Temporal profile of average temperature of single 1600-L tank SHS in a solar thermal DHW system operating in March 21st under dispersed draw pattern.

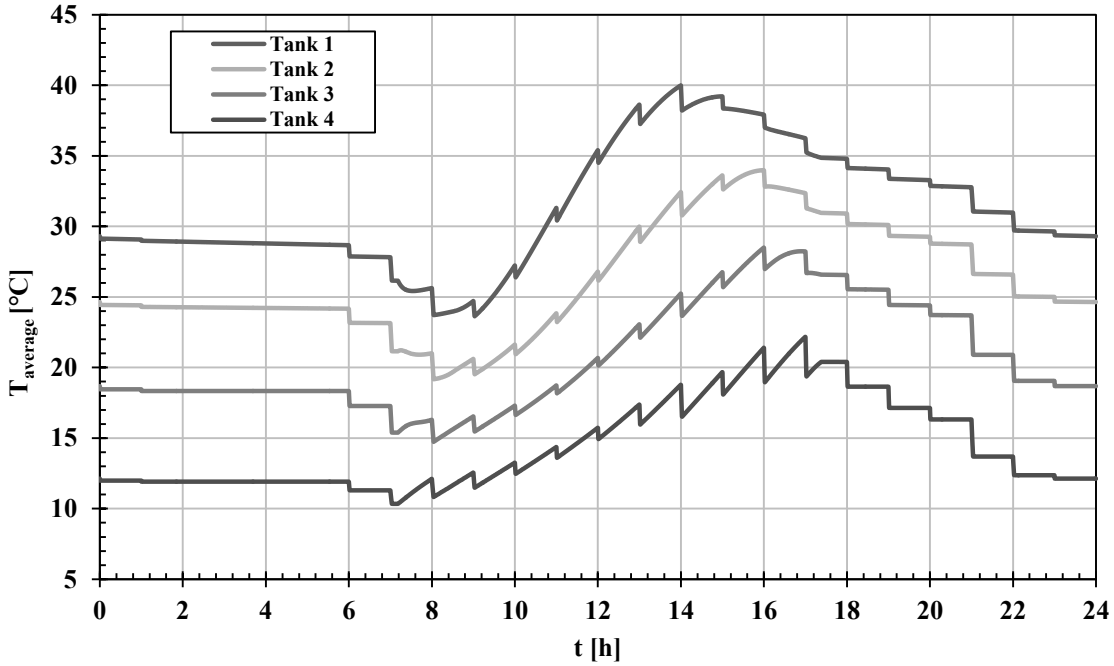

Figure 6.103. Temporal profiles of average temperature of four 400-L SHS tanks in a solar thermal DHW system operating in March 21st under dispersed draw pattern.

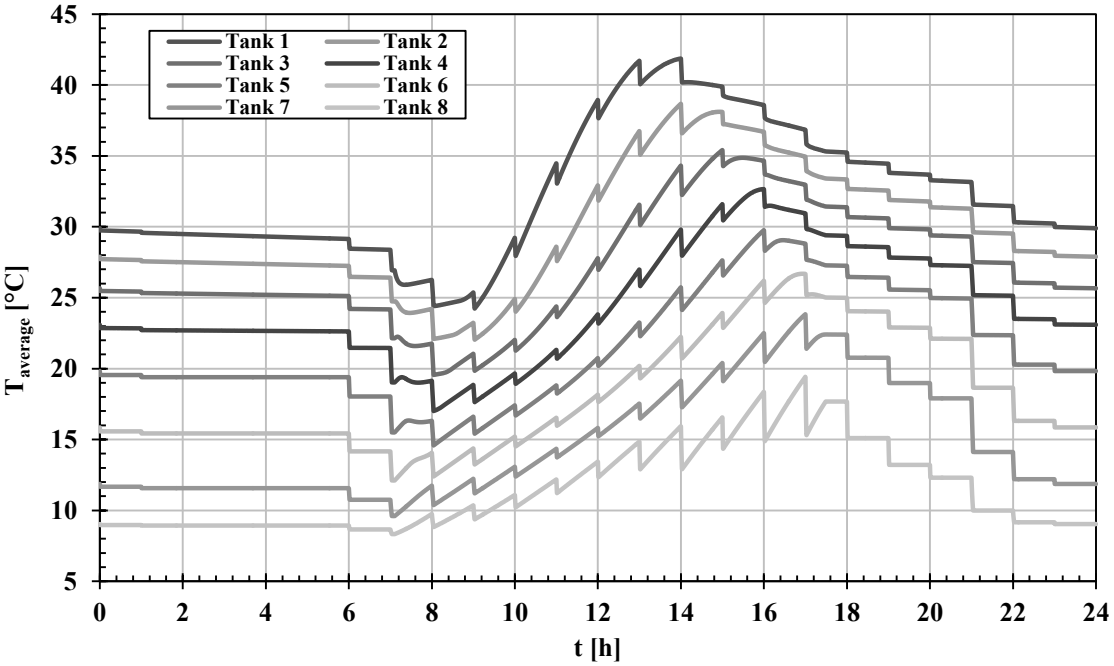

Figure 6.104. Temporal profiles of average temperature of eight 200-L SHS tanks in a solar thermal DHW system operating in March 21st under dispersed draw pattern.

In the light of the results obtained for the 200-L cascaded SHS system, numerical simulations were conducted for the 200-L cascaded HTES with different melting

temperatures in each tank. Numerical simulations were performed with the PCM melting temperatures chosen to coincide with the time weighted average of the operation temperature in the multi-tank SHS system. The values of the PCM melting temperatures are presented in Table 6.18.

Table 6.18. PCM melting temperatures selected for the multi-tank HTES system.

# of tanks	Nominal Storage Volume [L]	PCM melting temperature(s), T_m
1	200	T_{m1}=22°C
2	400	T_{m1}=25°C, T_{m2}=18°C
3	600	T_{m1}=30°C, T_{m2}=24°C, T_{m3}=17°C
4	800	T_{m1}=32°C, T_{m2}=27°C, T_{m3}=21°C, T_{m4}=16°C
5	1000	T_{m1}=33°C, T_{m2}=27°C, T_{m3}=23°C, T_{m4}=19°C, T_{m5}=15°C
6	1200	T_{m1}=33°C, T_{m2}=28°C, T_{m3}=24°C, T_{m4}=21°C, T_{m5}=17°C, T_{m6}=14°C
7	1400	T_{m1}=33°C, T_{m2}=29°C, T_{m3}=26°C, T_{m4}=23°C, T_{m5}=19°C, T_{m6}=16°C, T_{m7}=13°C
8	1600	T_{m1}=33°C, T_{m2}=30°C, T_{m3}=27°C, T_{m4}=24°C, T_{m5}=21°C, T_{m6}=18°C, T_{m7}=15°C, T_{m8}=12°C

Figure 6.105 illustrates a comparison between the performance of the multi-tank SHS and the multi-tank HTES systems. It is seen that the existence of the PCM improves the performance of the storage system by 2-5% for storage volumes less than 1200 litres. It is worth mentioning that the performances of the individual tanks in the multi-tank HTES system are coupled. That is changing the melting temperature in one or more tanks affect the performance of the whole system. This gives rise to the need for an optimization algorithm

that is meant to optimize the selected PCM melting temperatures for maximized system solar fraction. This should be the focus of a future study.

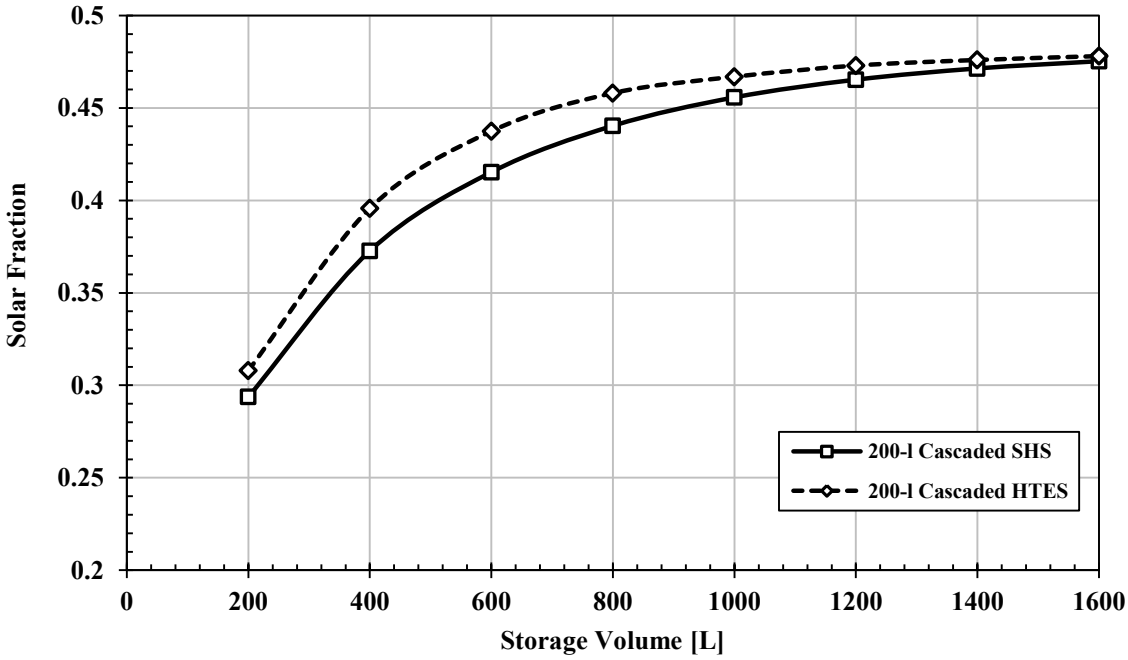

Figure 6.105. Solar Fraction versus total storage volume in litres for solar thermal DHW system operating in March 21st under dispersed draw pattern. Comparison between cascaded 200-L tank SHS and cascaded 200-L HTES with different number of tanks.

In the light of the single-tank performance in solar DHW systems, it was shown that undersized HTES tanks provide better temperature modulation for the system. As such, the previous simulations were repeated for a 75-L cascaded storage system. The same PCM melting temperatures were used as provided in Table 6.19. Figure 6.106 illustrates the comparison between the performance of the 200-L and 75-L cascaded storage systems. It is seen that solar fraction of the 8-tank 200-L cascaded system (~0.47) almost aligns with that of the 8-tank 75-L cascaded HTES system. This indicates the potential reduction of the total storage volume by 62.5%. However, it is shown that the 10-tank 75-L cascaded SHS system performs with a comparable solar fraction. Also, the 8-tank 75-L cascaded SHS system has a solar fraction that is 2% lower than that of the 8-tank 75-L cascaded HTES system. As a

result, a cost analysis is required at this stage to justify the use of the HTES cascaded system over the SHS cascaded system. This analysis is out of the scope of this dissertation.

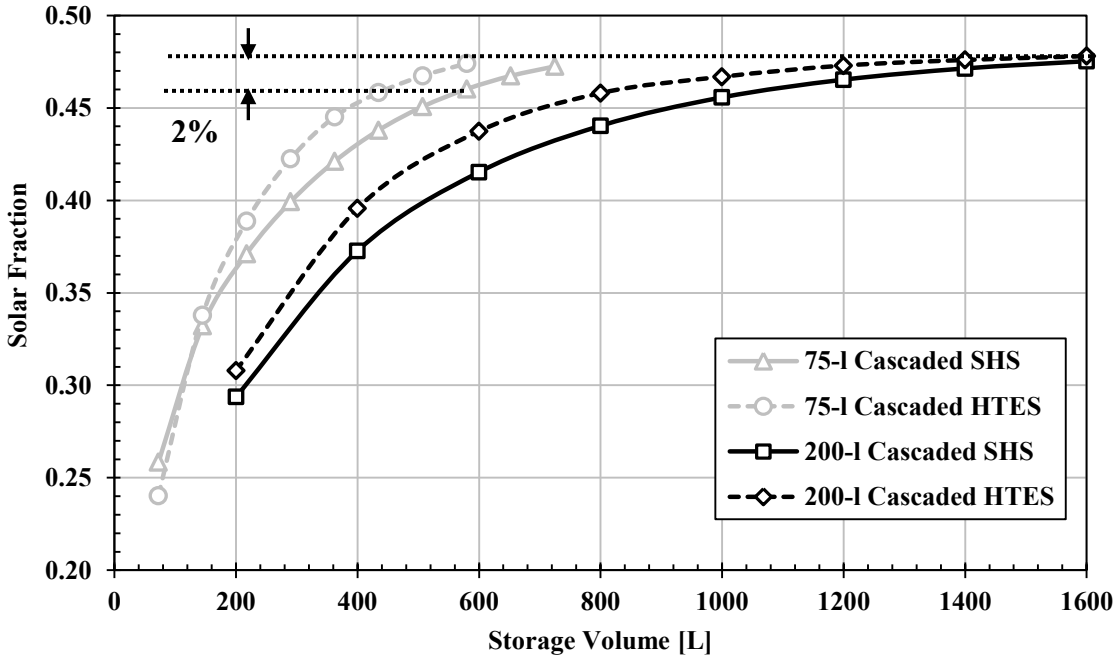

Figure 6.106. Solar Fraction versus total storage volume in litres for solar thermal DHW system operating in March 21st under dispersed draw pattern. Comparison between cascaded 75-L and 200-L cascaded storage (SHS versus HTES) with different number of tanks.

6.3. Summary

The performance of thermal energy storage elements is greatly sensitive to the initial and boundary conditions of operation. As such, the storage elements should be studied in the context of real application under realistic operation conditions. In these applications, the performance of the system is typically independent of the initial condition of the storage element. Also, the boundary conditions are often time variant depending on the supply and demand profiles of the system.

The performance of the single-tank HTES was numerically investigated under sequential charging and discharging operation conditions with isothermal inlet temperatures

to the coil heat exchangers. The PCM promoted temperature modulation effects in the HTES tank which improved the charging and discharging rates compared to the SHS tank. This resulted in higher storage gains in the HTES tank. A parametric analysis was undertaken to explore the effect of the key parameters of the PCM on the performance of the HTES. In addition, it helped to understand the potential benefits of the HTES over the SHS. The parameters were found to split into two groups: (1) the design parameters that are controllable and easy to alter such as: the number of PCM modules and the geometry and dimensions of the PCM modules, and (2) the selection parameters that are uncontrollable due to the limitations on PCMs availability in the market such as: the melting temperature, the density, the specific heat capacity, the latent heat of fusion and the thermal conductivity. The results of the parametric analysis showed that in order to maximize the benefits of the HTES:

1. The PCM volume fraction should be maximized to the limit where the heat transfer inside the storage element is not impeded.
2. The geometry and dimensions of the PCM modules should be designed in a way that allows for larger packing densities. In addition, the design should aim for maximizing the surface area to volume ratio in order to minimize the thermal resistance of the storage element.
3. The PCM melting temperature is considered the most critical parameter in the selection group. Selecting a PCM with a melting temperature outside the operation temperature range will penalize the system due to the poor sensible heat capacity of the PCM compared to water. It was concluded that the PCM melting temperature should be selected to coincide with the average temperature of

operation of the system. This would yield maximum energy exchange with the storage element in the form of latent heat.

4. Among the rest of the selection parameters, the PCM latent heat of fusion has significant impact on the potential storage gains of the HTES. Provided that there is enough available energy for storage, larger latent heat of fusion promotes more energy stored in the form of latent heat. As a result, better temperature modulation could be achieved and hence, better charging and discharging rates.

In the light of the parametric study, the performance of the HTES was compared to that of the SHS in the context of solar thermal DHW application. One day was selected from each season of the year to represent the average available solar energy in that season. The demand profiles for DHW usage were simulated in two different ways: (1) the daily draw was assumed uniform over certain time period during the day depending on whether the demand is uniform, in-phase or out-of-phase with the supply, (2) the daily DHW demand was divided into small discrete draws scattered during the day depending on whether the consumption pattern is dominant morning, dominant evening, dominant night or dispersed.

The performance of the solar thermal storage system is greatly influenced by the season. The solar fraction, which is defined as the ratio of thermal energy delivered to the load from the solar collector to the total demand energy, shifts upwards when the solar incidence radiation increases. It was shown that the solar fraction achieves maximum values in July and minimum values in December.

The performance of the solar thermal storage system under different demand profiles illustrated the role of the storage element in bridging the mismatch between the supply and demand. The storage element is not required when the supply and demand are in phase. In

fact, the storage element acts as a heat exchanger that transfers the heat from the supply side to the demand side. When realistic DHW draw profiles were applied to the system, the different consumption patterns showed slight impact on the solar fraction. However, the HTES was found to outperform the SHS given that the thermal resistance of the system was minimized (i.e., using packed bed of PCM spheres with large surface area to volume ratio).

For medium to large-scale applications, the concept of multi-tank or cascaded storage was shown to promote sequential (tank-to-tank) stratification and hence, the overall efficiency of the system. Higher solar fractions could be obtained by replacing the large fully mixed tank with a series of modular small tanks with the same total volume. The maximum limit of the solar fraction could be attained when the number of tanks approaches infinity. The potential benefits of the HTES originate from the temperature modulation feature of the PCM, especially in undersized tanks. The temperature modulation leads to larger running time of the solar collector pump, lower thermal losses from the solar collector and hence, larger solar fraction. Two challenges, however, arise: (1) the selection of the melting temperatures of PCMs in each individual tank requires an optimization algorithm, and (2) optimizing the PCM melting temperatures for operation in certain day (or season) does not guarantee the best performance in different day (or season). These challenges should be the focus of future studies.

CHAPTER SEVEN

CONCLUSIONS AND RECOMMENDATIONS FOR FUTURE WORK

7.1. Summary and Conclusions

Thermal energy storage (TES) is a key component in many thermal energy systems since it bridges the mismatch between the energy supply and demand. For example in a solar domestic hot water system, the TES component is used to store the excess solar thermal energy during the times when the energy demand is low. Then, the stored energy is recovered and delivered to the demand side when the available solar energy is insufficient. A good design of TES in solar thermal systems helps to reduce the need for auxiliary heating systems that rely primarily on electricity (eg. electric heaters) or fossil fuels (eg. gas burners).

A novel design of a thermal storage tank was introduced by Mather (2000) at the University of Waterloo. The design concept was based on a modular 200-l water tank that is charged and discharged indirectly via two immersed coil heat exchangers situated at the bottom and top of the tank. Generally, the placement of the coil heat exchangers acts to mix the tank fully. However, the thermal diode effect takes place to avoid discharging through the bottom coil heat exchanger or charging through the top coil heat exchanger. In medium/large scale applications, sequential stratification was found to take place in the multi-tank storage, where a number of modular tanks were serially connected through the bottom and top heat exchangers.

The design of the storage tank proposed in this dissertation was inspired by Mather's modular tank. A 200-l square water tank was introduced with rectangular PCM modules. A mathematical model was developed for the single and multi-tank SHS and HTES. The components of the mathematical model were verified against analytical and benchmark solutions. Excellent agreement was observed which indicated the ability of the model to capture the physical behaviors of the storage element accurately. The model was then validated against the experimental results obtained by Mather (2000) for single and multi-tank water storage under various operation scenarios. Good agreement was found between the numerical and experimental results. A test facility was designed and constructed at McMaster University to provide validation for the single-tank HTES element with rectangular PCM modules filled with Lauric acid. The numerical results compared very closely to the experimental results.

Numerical simulations were carried out to investigate the effect of the key design parameters on the performance of the HTES element when the bottom and top heat exchangers were sequentially operated with fixed inlet temperature conditions. This parametric study, though performed under theoretical operation conditions, illustrated the potential benefits of the HTES compared to the SHS. It was concluded that the key PCM parameters must be tuned in a way that maximizes the energy exchange in the form of latent heat. This was achieved primarily by reducing the overall thermal resistance of the storage element through (1) increasing the effectiveness of the heat exchangers, (2) increasing the surface area of the PCM modules, (3) selecting PCMs with high thermal conductivity, and (4) reducing the thickness of the PCM modules. In addition, the melting temperature of the PCM was found to have an optimum value at which the storage gain is maximized. The

melting temperature must be selected such that it is at the average temperature of the storage tank's operation. Any deviation from this value was found to store more energy in the form of sensible heat and hence reduce the storage gain of the HTES element.

The existence of PCM in the storage tank was observed to modulate the operation temperature around the melting temperature of the PCM. This was found to increase the heat transfer rates with the heat exchangers and hence increase the storage gain of the HTES. This important feature was proved to have a critical impact on the performance of the HTES element in solar thermal DHW systems. During the charging process of the storage element, appropriate temperature modulation of the system helps to send fluid with lower temperature to the solar collector. This gives rise to: (1) prolonging the operation of the collector pump, allowing for more solar energy collection, and (2) reducing the thermal losses from the solar collector.

Numerical simulations were carried out for the single-tank HTES in a solar thermal DHW system suitable for single-family demands. The performance of the system was investigated when operating in different days of the year having different solar incidence radiation. Also, different DHW draw profiles were investigated. All the results were presented in terms of the solar fraction as a function of the storage volume. The matched size of the storage element could be defined as the size at which the solar fraction curve started to plateau.

It was concluded that the magnitude and duration of the solar irradiation availability has a profound effect on the solar fraction of the system. It was shown that the solar fraction curve shifts upwards as the solar incidence radiation increases. This is primarily attributed to the elevated temperature level of the system which acted to supply more energy to the

demand side. As a result of this behavior, the SHS element was found to perform better for the majority of the days compared to the HTES element. The PCM parameters could only be tuned to maximize the solar fraction during one-day operation. When the solar irradiation changed, the operation temperature of the system changed, and the PCM would no longer store energy in the latent heat form.

The DHW draw profile was found to have a significant impact on the performance of the solar thermal storage system. It was concluded that the storage element is only critical to the applications where there is a clear mismatch between the supply and demand (i.e., when the supply and demand are out-of-phase). When the supply and demand profiles are in-phase the storage element acts as a heat exchanger that transfers the heat from the solar collector side to the load side. Realistic demand patterns usually consist of discrete hot water draws that are dispersed over the day. Depending on the behavior of the consumer; dominant morning, dominant evening, dominant night or dispersed consumer, the draw pattern might be partly in-phase and partly out-of-phase. However, it was observed that for a given total daily draw, the effect of the different consumers' draw patterns on the solar fraction of the system was negligible.

Sensitivity analysis was then performed to study the effect of the PCM volume fraction and the melting temperature on the solar fraction of an oversized and an undersized system. For the oversized tanks, the effects of the PCM volume fraction and melting temperature were insignificant. Both the SHS and HTES systems performed similarly with no clear benefits of the HTES system. On the other hand, the PCM parameters were found to have a significant effect on the performance of the undersized tank. Increasing the PCM

volume fraction led to higher solar fractions. The PCM melting temperature was found to have an optimum value at which the solar fraction is at maximum.

Last, the concept of multi-tank HTES, with cascaded tanks with different PCMs, was explored. The potential benefits of the proposed system were highlighted compared to the multi-tank SHS when operated in a solar thermal DHW system for multi-family residence demands. The multi-tank system showed high levels of sequential stratification that is favorable to the operation of the solar thermal systems. Introducing PCMs with different melting temperatures inside each tank was found to enhance the solar fraction of the system. This was a result of the temperature modulation promoted by the existence of PCMs in the storage tanks. It was concluded that extensive optimization study is required in order to understand the full benefits of the cascaded HTES system. This would be the scope of a future research project.

7.2. Recommendations for Future Work

This project focused on the study of the performance of a novel design of thermal energy storage element suitable for small-to-large scale solar thermal DHW applications. A simple, yet accurate, simulation tool was successfully developed and experimentally validated to simulate the dynamic performance of the single and multi-tank SHS and HTES systems. The experimental results that were used to validate the model were conducted under idealistic conditions that do not often exist in real applications. More experiments should be performed to investigate the performance of the storage system under realistic operation conditions.

During the lab experiments, the temperature distribution inside the storage tank was monitored by the thermocouple rack that was installed at the centre-line of the tank. The

experimental results showed that the thermocouples' placement did not resolve the temperature gradient in the thermoclines developed during the thermal diode effects. Detailed experiments are recommended in order to provide better understanding of the thermal diode effect and hence, refine the mathematical model for more accurate simulations.

Due to time and resources constraints, simulations were conducted on the performance of the storage systems in four days of the year each representing one season; March 21st (spring), June 21st (summer), September 21st (fall) and December 21st (winter). The annual performance of the solar thermal storage system should be investigated to provide more accurate results about the actual behavior of these systems in realistic applications.

It was concluded that the HTES system exhibited significant reduction of the storage size (50-75%) compared to the SHS system. However, this was based on tuning the PCM parameters during one-day operation. It was shown that using the same HTES system with the tuned parameters in different days yielded poorer performance than the SHS system. As such, it would be of great interest to investigate the ability to synthetize a PCM which is capable of changing its melting temperature with the change of the operation temperature of the system. This should result into maintaining the operation of the PCM in the phase change region where most of the energy exchange is centered on the latent heat. Hence, the HTES system would be constantly tracking its maximum solar fraction.

The numerical results for the multi-tank storage in solar thermal DHW systems were based on the coupling of the mathematical/empirical models for the individual storage tanks and the different components of the solar collector loop. It would be of great benefit to study the performance of the storage system in a realistic solar thermal installation.

In addition, few cases were numerically simulated for the cascaded HTES system with one possible combination of parameters due to shortage of time and resources. It is recommended to undertake an extensive optimization study where the simulation tool is coupled to an efficient optimization algorithm. Hundreds of simulations could be conducted in order to optimize parameters of the PCMs in different individual tanks.

APPENDIX A

COMPONENT MODEL VERIFICATION

In this Appendix, the mathematical models of the coil heat exchanger and the PCM modules were verified against analytical or benchmark solutions. First, the coil heat exchanger model was isolated and tested by considering the heat exchanger submerged in an infinite medium with constant temperature T_∞. A systematic approach was applied to explore the impact of the transient term in the heat exchanger model, the heat exchanger effectiveness and the thermophysical properties.

Second, the PCM model was verified against the well-known benchmark heat transfer problems with phase transformation, Stefan and Neumann problems. The Stefan problem applies to 1-D cases where the wall temperature is constant and the initial temperature of the entire domain coincides with the melting temperature of the PCM. The Neumann problem assumes that the initial temperature of the solution domain is not equal to the melting temperature of the PCM. Both problems have closed-form analytical solutions for the transient temperature and melt front profiles during conduction-dominated melting/solidification inside rectangular PCM modules.

A.1. Coil heat exchanger model

Figure A.1 illustrates the 1-D discretization domain of the coil heat exchanger submerged in an infinite medium with fixed temperature T_∞. The energy equation can be written as

$$M_i c \frac{dT_i}{dt} = \dot{m}c(T_{i-1} - T_i) - UA_{coil}(T_i - T_\infty) \quad \text{(A-1)}$$

The method for calculating UA_{coil} and numerically solving this equation was presented in Chapter Three. Under steady state conditions, the term on the left hand side of Equation (A-1) will vanish. The temperature at the outlet of the heat exchanger can be calculated by

$$T_{out} = T_\infty + (T_{in} - T_\infty)e^{\frac{-UA_{coil}}{\dot{m}c}} \quad \text{(A-2)}$$

Furthermore, the effectiveness of the heat exchanger is at maximum (i.e., $\varepsilon = 1.0$), when $\frac{UA}{\dot{m}c}$ approaches infinity. The outlet temperature accordingly approaches T_∞ and the heat transfer rate from the coil heat exchanger becomes

$$Q_{HX} \rightarrow Q_{HX,max} = \dot{m}c(T_{in} - T_\infty) \quad \text{(A-3)}$$

Consider the case where a coil heat exchanger is submerged in an infinite isothermal medium with a temperature T_∞=20°C. The mass flow rate through the coil is 0.05 kg/s and the inlet temperature is maintained constant at 60°C. Table A-1 presents the geometric parameters of the coil and the thermophysical properties of the internal and external fluids. Transient simulations were carried out for nine different cases (A1-A9) to investigate the sensitivity of the results to the mesh size and time step chosen for the simulations. Cases (A10-A12) were simulated to explore the effect of increasing the length of the coil on the effectiveness of the heat exchanger. The sensitivity of the results to the thermophysical properties of the fluids was investigated through cases (A13-A15).

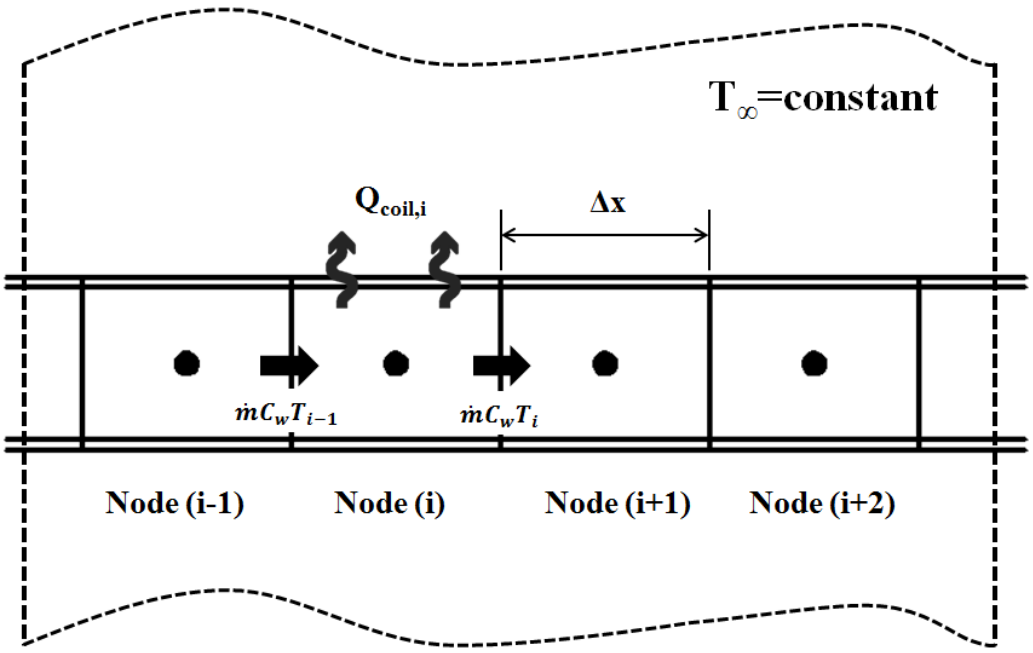

Figure A.1. 1-D discretization domain of the coil heat exchanger model.

Table A.1. The geometric parameters of the coil heat exchanger and the thermophysical properties of the internal and external fluids.

Geometric parameters	d_i=0.0195 m, d_o=0.0222 m, L=7.5 m
Thermophysical properties of the internal fluid, water, assumed constant at T=60°C	ρ=992.2 kg/m^3, c=4183.0J/kg.K, μ=0.467×10^{-3} Pa.s, k=0.641 W/m.K
Thermophysical properties of the external fluid, water, assumed constant at T=60°C	ρ=992.2 kg/m^3, c=4183.0J/kg.K, μ=0.467×10^{-3} Pa.s, k=0.641 W/m.K, β=0.522×10^{-3} K^{-1}

Figures A.2a and A.2b illustrate the effect of the mesh size (N_{coil}) on the outlet temperature and the heat transfer rate of the coil heat exchanger, respectively. Simulations were conducted for the cases A1-A5 where the coil was discretized into 25, 50, 100, 200 and 400 control volumes, respectively. During these simulations, the time step was fixed at 1 s

and the simulations were executed until steady state was attained. The outlet temperature and the heat transfer rate from the coil heat exchanger at steady state were found from the analytical solution to be 32.46°C and 5758 W, respectively.

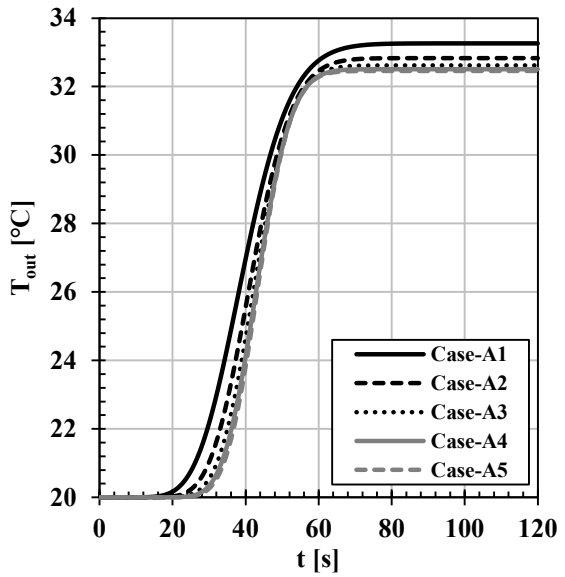

Figure A.2a. The outlet temperature (T_{out}) of the coil heat exchanger versus time (t) for different mesh sizes.

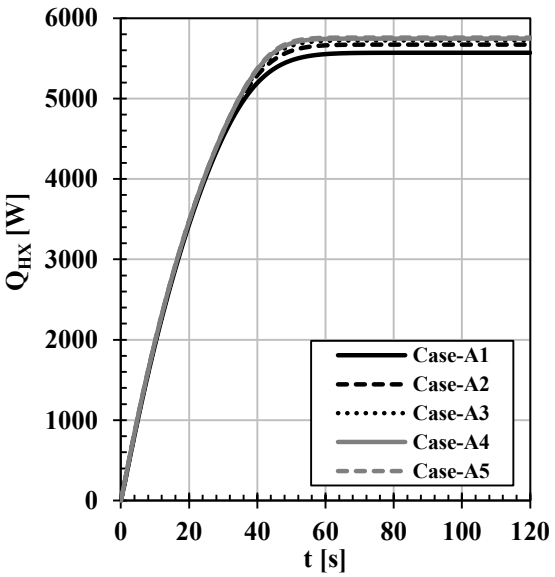

Figure A.2b. The heat transfer rate (Q_{HX}) of the coil heat exchanger versus time (t) for different mesh sizes.

Figures A.2a and A.2b show that the mesh size has a slight effect on the transient variation of the outlet temperature and the heat transfer rate from the coil heat exchanger, especially when $N_{coil} \geq 50$. Figures A.3a and A.3b illustrate the effect of the mesh size on the steady state values of T_{out} and Q_{HX}.

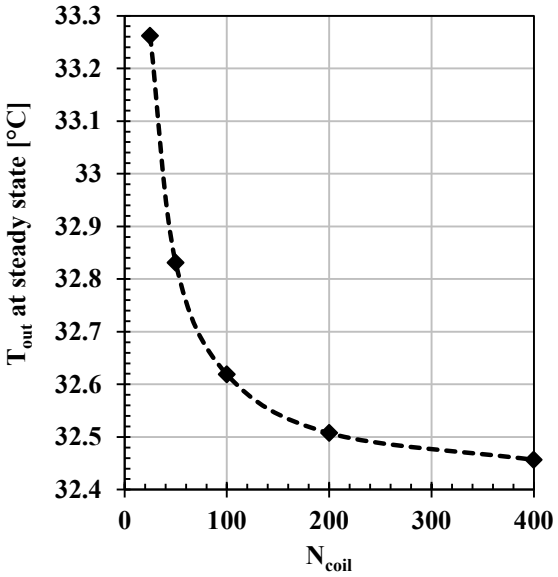

Figure A.3a. The outlet temperature (T_{out}) of the coil heat exchanger at steady state versus the mesh sizes (N_{coil}).

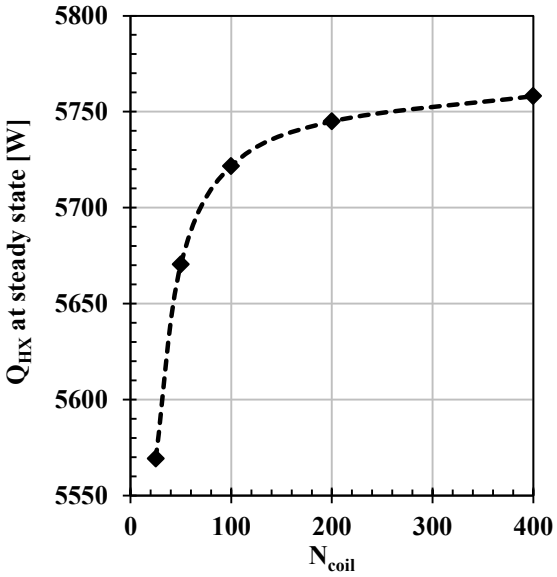

Figure A.3b. The heat transfer rate (Q_{HX}) of the coil heat exchanger at steady state versus mesh sizes (N_{coil}).

Figures A.4a and A.4b show that the time step has a significant effect on the temporal behavior of the outlet temperature and the heat transfer rate from the coil heat exchanger. Cases (A6-A9) were simulated using different time steps Δt=0.1, 2, 4 and 10 s. The mesh size was fixed at N_{coil}=100. Figures A.5a and A.5b illustrate the effect of the time step on the steady state values of T_{out} and Q_{HX}.

The number of control volumes should be chosen to be $N_{coil} \geq 100$, since T_{out} and Q_{HX} were found to deviate by +0.16°C and -0.6% from those obtained with N_{coil}=400. Also, the time step should be set to $\Delta t \leq 4$ s, since the variation of T_{out} and Q_{HX} was found to be unnoticeable. This should maintain the accuracy of the results without sacrificing the speed of the simulations.

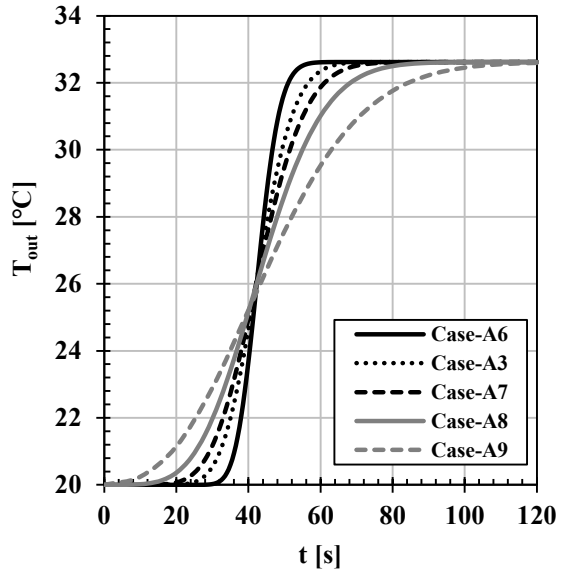

Figure A.4a. The outlet temperature (T_{out}) of the coil heat exchanger versus time (t) for different time steps.

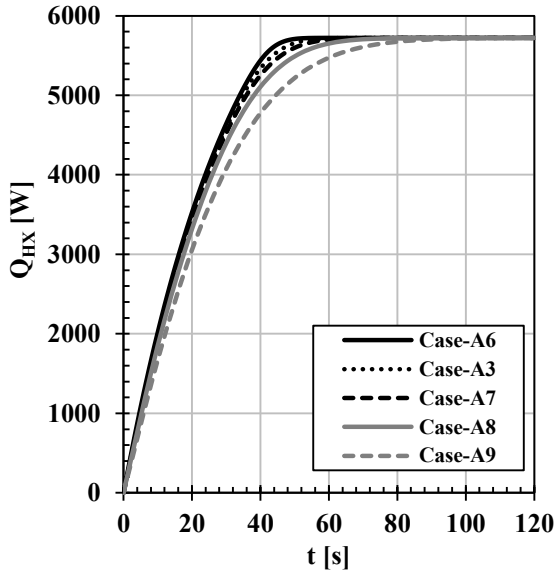

Figure A.4b. The heat transfer rate (Q_{HX}) of the coil heat exchanger versus time (t) for different time steps.

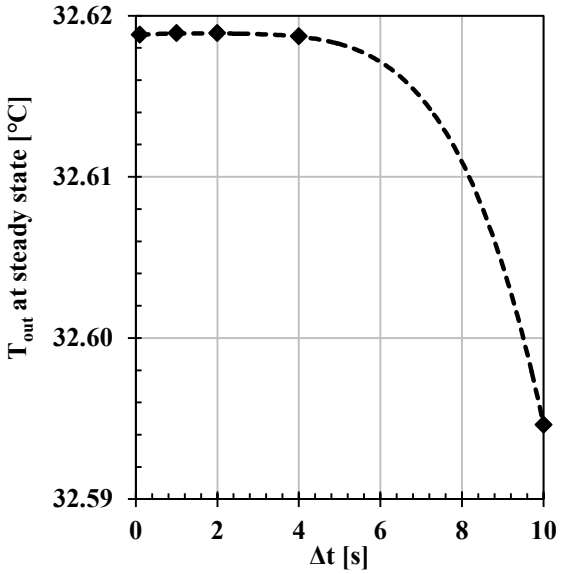

Figure A.5a. The outlet temperature (T_{out}) of the coil heat exchanger at steady state versus the time step (Δt).

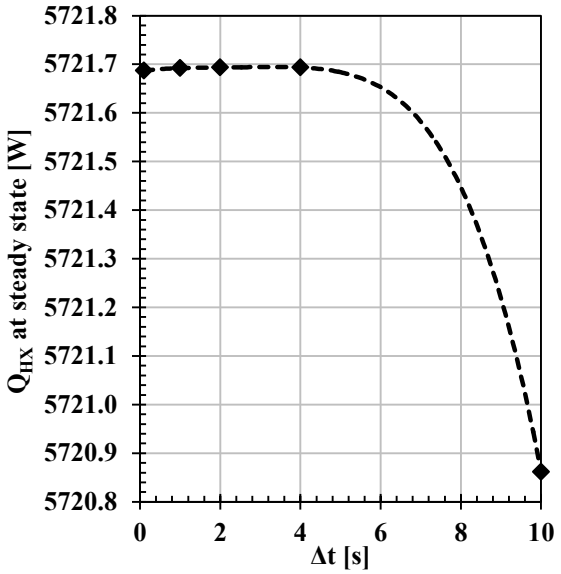

Figure A.5b. The heat transfer rate (Q_{HX}) of the coil heat exchanger at steady state versus the time step (Δt).

The effect of increasing the coil length by 5, 10 and 50 times was investigated in cases (A10-A12), respectively. The mesh size was set to N_{coil}=100 and the time step was fixed at Δt=1 s. As the length of the coil increased the effectiveness of the heat exchanger was found to increase and approach unity, as shown in Figure A.6. Since the effectiveness of

the heat exchanger (ε_{HX}) is defined as the ratio of the heat transfer rate to the maximum heat transfer rate from the heat exchanger

$$\varepsilon_{HX} = \frac{Q_{HX}}{Q_{HX,max}} = \frac{\dot{m}c(T_{in} - T_{out})}{\dot{m}c(T_{in} - T_{\infty})} = \frac{T_{in} - T_{out}}{T_{in} - T_{\infty}} \quad \text{(A-4)}$$

The outlet temperature of the heat exchanger approaches T_{∞}=20°C as the effectiveness approaches unity. Also, Q_{HX} approaches $Q_{HX,max}$ which was calculated to be 8366 W. This was shown in Figures A.7a and A.7b.

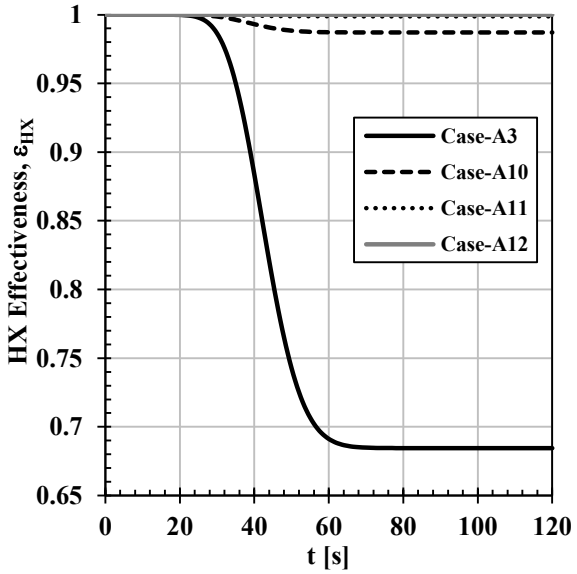

Figure A.6. The heat exchanger effectiveness (ε_{HX}) versus time (t) for different coil lengths. Case-A3: L_{coil}=7.5 m, Case-A10: L_{coil}=37.5 m, Case-A11: L_{coil}=75 m, Case-A12: L_{coil}=375 m.

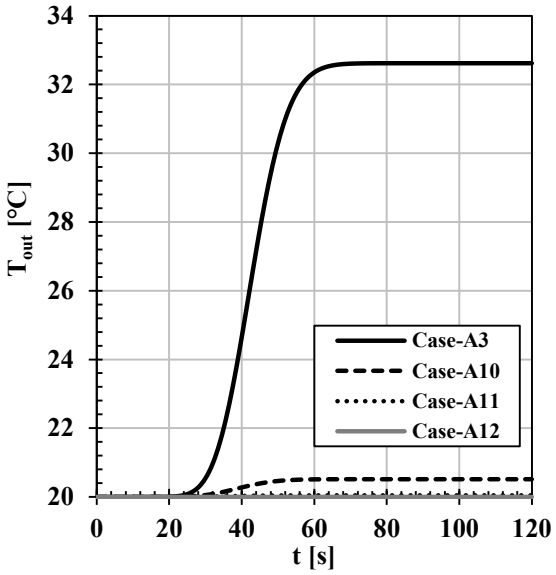

Figure A.7a. The outlet temperture (T_{out}) of the coil heat exchanger versus time (t) for different coil lengths.

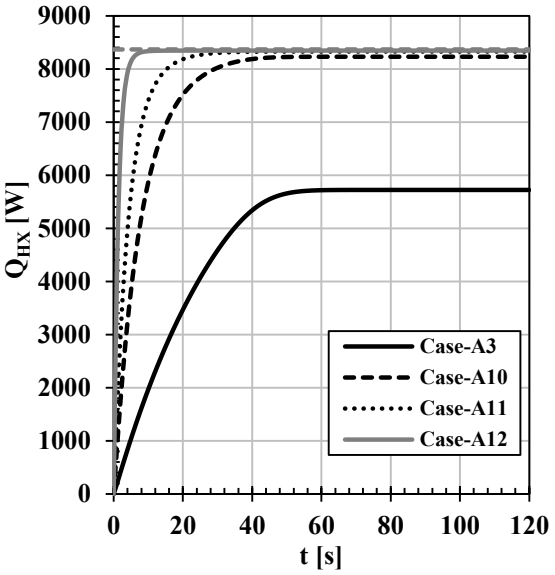

Figure A.7b. The heat transfer rate (Q_{HX}) of the coil heat exchanger versus time (t) for different coil lengths.

The effect of varying the thermophysical properties of the fluids on the inner and the outer sides of the coil heat exchanger was also explored. Cases (A2-A9) were simulated using constant properties on both sides of the coil heat exchanger assumed at 60°C. Cases A13 and A14 were simulated were simulated using constant properties on both sides of the coil heat exchanger assumed at 40°C and 20°C, respectively. Case A15 was simulated using variable properties that were related to the temperature through NBS/NRC steam tables (Haar, 1984). The internal properties were updated every time step at the average temperature between the inlet and outlet temperatures of the coil heat exchanger. The external properties were evaluated every time step at the average temperature between the internal and the external fluids. Figures A.8a and A.8b demonstrate the significant effect of the thermophysical properties of the fluids on the transient performance of the coil heat exchanger. As such, the temperature-dependent properties (Case A15) should be used in the numerical simulations in order to maintain high levels of accuracy in the results.

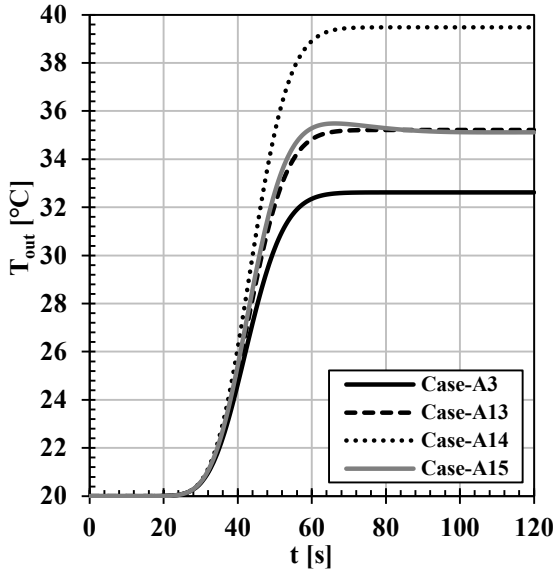

Figure A.8a. The outlet temperature (T_{out}) of the coil heat exchanger versus time (t) for different thermophysical properties.

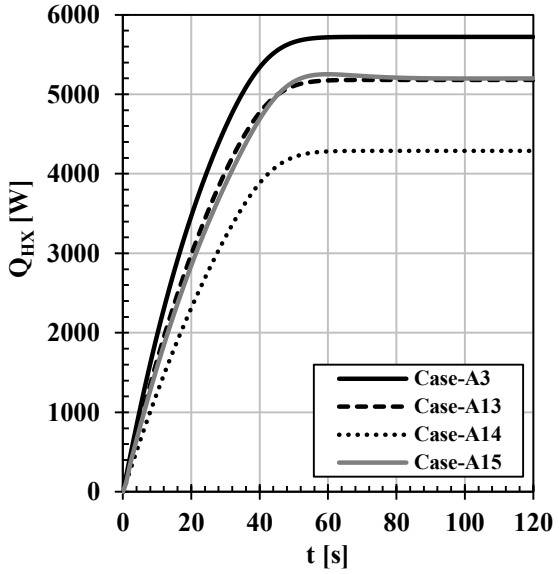

Figure A.8b. The heat transfer rate (Q_{HX}) of the coil heat exchanger versus time (t) for different thermophysical properties.

A.2. PCM model

The mathematical model of the heat transfer through the rectangular PCM module was validated against the Stefan and Neumann benchmark problems (Stefan, 1889). Both problems are governed by conduction-dominated heat transfer through semi-infinite rectangular domains with isothermal boundary condition. Figure A.9 demonstrates the case of a semi-infinite rectangular domain during the melting process when the surface temperature T_0=T(x=0,t) is suddenly raised to a value higher than the melting temperature of the PCM. The melt front interface separates the liquid phase from the solid phase. The only difference between the Stefan and the Neumann problems is in the initial condition. Stefan problem was introduced with an initial temperature equal to the melting temperature of the PCM (i.e., T_{ini}=T_m).

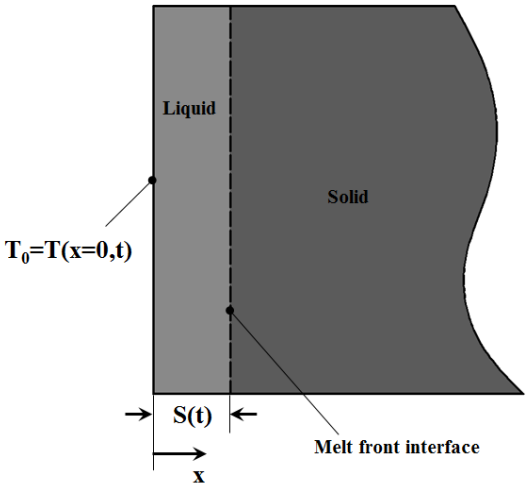

Figure A.9. Schematic for melting process of a semi-infinite rectangular domain with isothermal boundary condition.

As presented in Chapter Three, the governing equation of the melt front motion is given by

$$-k_l \frac{\partial T(S(t),t)}{\partial x} + k_s \frac{\partial T(S(t),t)}{\partial x} = \rho H_f \frac{dS(t)}{dt} \tag{A-5}$$

The melt front motion in the Stefan's problem is only governed by the temperature gradient in the liquid region since the temperature gradient in the solid region is zero. The analytical solution of the Stefan's problem was outlined in Faghri and Zhang (2006)

$$S(t) = 2\lambda\sqrt{\alpha_l t}, \qquad \alpha_l = \frac{k_l}{\rho c_l} \tag{A-6}$$

$$T(x,t) = T_m + (T_0 - T_m)[1 - \frac{\text{erf}(x/2\sqrt{\alpha_l t})}{\text{erf}(\lambda)}] \tag{A-7}$$

$$\lambda e^{\lambda^2}\,\text{erf}(\lambda) = \frac{Ste}{\sqrt{\pi}}, \qquad Ste = \frac{c_l(T_0 - T_m)}{H_f} \tag{A-8}$$

Stefan's problem was first simulated using a 1-D rectangular domain. The length of the domain was chosen to be 60 mm which was found to be long enough to simulate the semi-infinite domain (i.e., the boundary condition does not influence the solution). The PCM was chosen to have a melting temperature, T_m of 40°C and the surface temperature, T_0 was set to 60°C. Table A.2 provides the thermophysical properties assumed for the PCM.

Table A.2. Thermophysical properties of the PCM.

Property	**Value [Unit]**
Density, ρ	870.0 [kg/m^3]
Specific heat capacity of solid and liquid phases, c_s=c_l	2500 [J/kg.K]
Latent heat of fusion, H_f	200 [kJ/kg]
Thermal conductivity of the solid and liquid phases, k_s=k_l	0.15 [W/m.K]

The cell size was set to 0.5 mm and the time step was fixed at 1 s. The simulation was executed for 3600 s. Figure A.10a shows the melt fraction versus time. The melt fraction is defined using the equation

$$Melt\ Fraction(t) = \frac{melt\ front\ position}{length\ of\ the\ domain} = \frac{S(t)}{L_{domain}} \qquad \text{(A-10)}$$

Excellent agreement was found between the analytical and the numerical solutions of the melt fraction. Similar agreement was observed in Figure A.10b for the temperature profiles in the liquid region at different times; 60, 300, 600, 1800 and 3600 s.

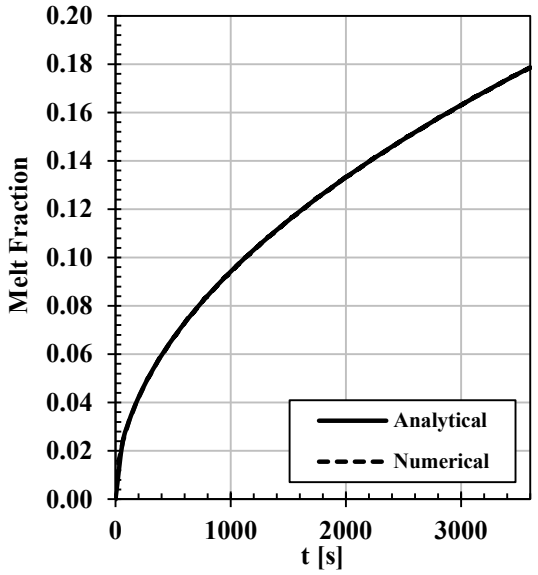

Figure A.10a. Melt fraction of the PCM versus time (t) for the Stefan problem.

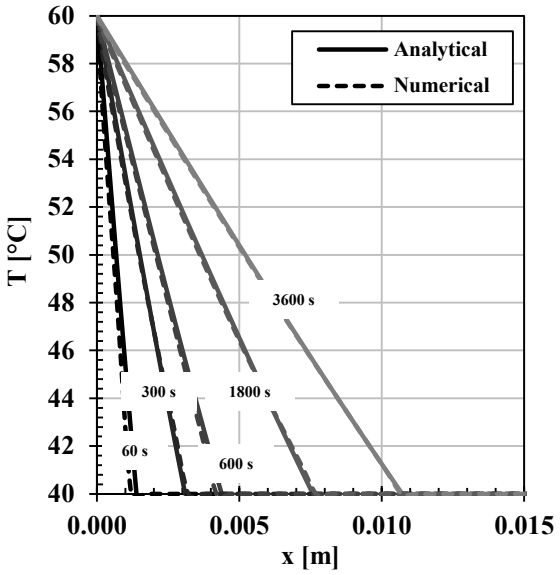

Figure A.10b. Temperature (T) distribution inside the PCM domain versus position (x) at time, t=60, 300, 600, 1800 and 3600 s for the Stefan problem.

For Neumann's problem, the initial temperature was set to be lower than the melting temperature of the PCM (i.e., $T_{ini}<T_m$). As such, the melt front motion in the Neumann's problem is governed by the temperature gradient in both the solid and the liquid regions. The analytical solution of the Neumann's problem was also outlined in Faghri and Zhang (2006),

$$S(t) = 2\lambda\sqrt{\alpha_l t} \tag{A-11}$$

$$\mathrm{T_l(x,t)} = \mathrm{T_m} + (\mathrm{T_0} - \mathrm{T_m})[1 - \frac{\mathrm{erf(x/2\sqrt{\alpha_l t})}}{\mathrm{erf(\lambda)}}] \tag{A-12}$$

$$\mathrm{T_s(x,t)} = \mathrm{T_m} + (\mathrm{T_{ini}} - \mathrm{T_m})[1 - \frac{\mathrm{erfc(x/2\sqrt{\alpha_s t})}}{\mathrm{erfc(\lambda\sqrt{\alpha_l/\alpha_s})}}] \tag{A-13}$$

$$\frac{e^{-\lambda^2}}{\mathrm{erf}(\lambda)} + \frac{k_s/k_l}{\sqrt{\alpha_s/\alpha_l}}\left(\frac{T_{ini} - T_m}{T_0 - T_m}\right)\frac{e^{-\lambda\alpha_l/\alpha_s}}{\mathrm{erfc}(\lambda\sqrt{\alpha_l/\alpha_s})} = \frac{\lambda\sqrt{\pi}}{Ste} \tag{A-14}$$

Figures A.11a and A.11b demonstrate the ability of the PCM model to accurately simulate the physics of 1-D conduction-dominated heat transfer during phase transformation. The cell size was set to 0.5 mm and the time step was fixed at 1 s.

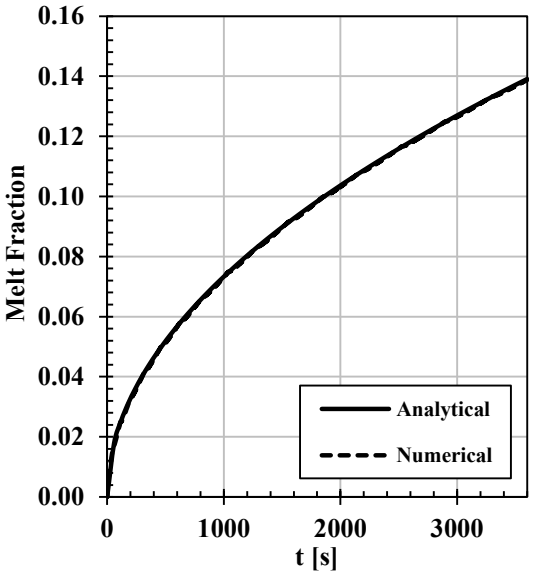

Figure A.11a. Melt fraction of the PCM versus time (t) for the Neumann problem.

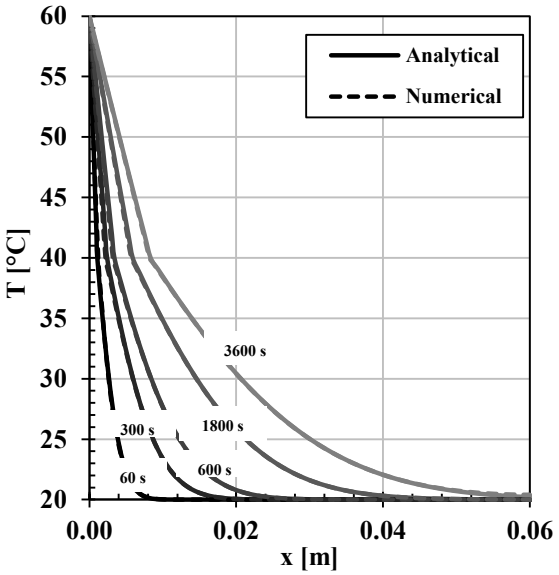

Figure A.11b. Temperature (T) distribution inside the PCM domain versus position (x) at time, t=60, 300, 600, 1800 and 3600 s for the Neumann problem.

The same Neumann's problem was simulated nine different times (Cases B1-B9) to investigate the effect of changing the mesh size, the time step and the Stefan number (Ste) on the accuracy of the PCM model. Table A.3 presents the nine different cases.

The results were compared with the analytical solution based on the temporal distribution of the melt fraction and the spatial distribution of the temperature in the domain at time, t=3600 s. Figures A.12a and A.12b show that the numerical solution is insensitive to the time step chosen for the simulations. However, the numerical solution was found to be influenced by the cell size. Excellent agreement with the analytical solution was found in the cases where $\Delta x \leq 1$ mm, Figures A.13a and A.13b.

Table A.3. Specifications of the nine cases Case B1-B7.

Case	Specifications		
	Cell size (Δx)	**Time step (Δt)**	**Ste**
Case B1	0.5 mm	0.1 s	0.25
Case B2	0.5 mm	1 s	0.25
Case B3	0.5 mm	10 s	0.25
Case B4	0.1 mm	1 s	0.25
Case B5	1 mm	1 s	0.25
Case B6	5 mm	1 s	0.25
Case B7	0.5 mm	1 s	0.025
Case B8	0.5 mm	1 s	2.5
Case B9	0.5 mm	1 s	5

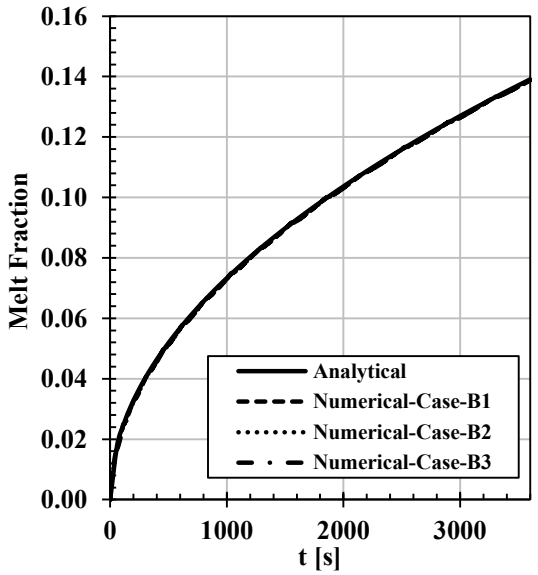

Figure A.12a. Melt fraction of the PCM versus time (t) for the Neumann problem. Effect of the time step (Δt).

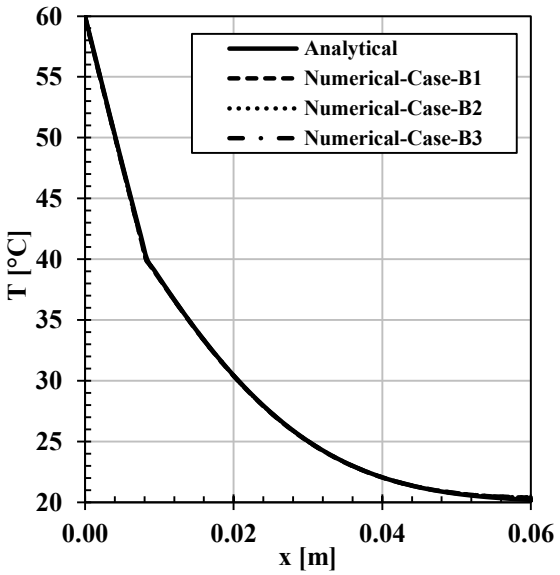

Figure A.12b. Temperature (T) distribution inside the PCM domain versus position (x) at time, t=3600 s for the Neumann problem. Effect of the time step (Δt).

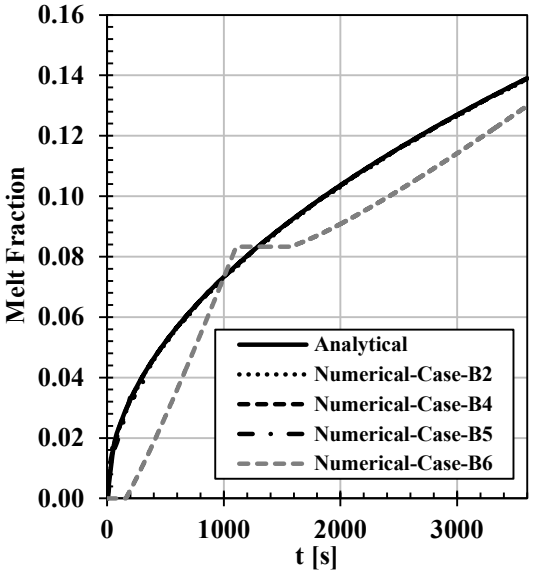

Figure A.13a. Melt fraction of the PCM versus time (t). Effect of the cell size (Δx).

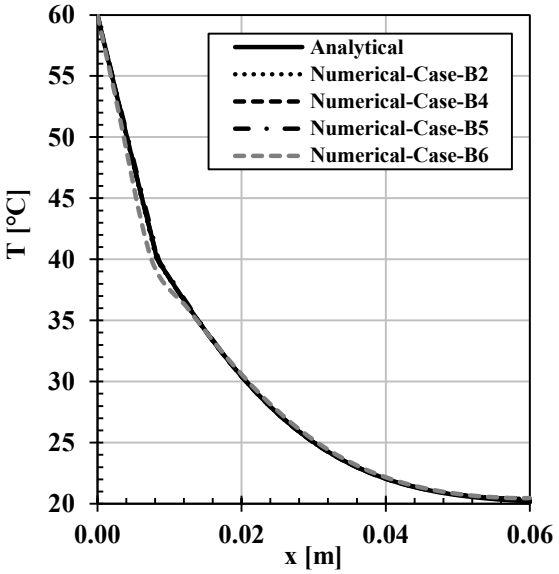

Figure A.13b. Temperature (T) distribution inside the PCM domain versus position (x) at time, t=3600 s. Effect of the cell size (Δx).

The solution of the Neumann's problem is seen to be a function of Stefan number (Ste), Equation (A-14). As such, the sensitivity of the PCM model solution to the Stefan number was explored in cases (B9-B12). The Stefan number ($Ste = \frac{c_l(T_0 - T_m)}{H_f}$) is defined as the ratio of the sensible energy content to the latent energy content of the PCM. That is why the Stefan number is indicative of the speed of the melt front motion in different PCMs. PCMs with low Stefan number are characterized with slow melt fronts, whereas PCMs with high Stefan number have faster melt fronts.

Figure A.14 illustrates that the numerical model is capable of accurately simulating the melt front motion in PCMs with low Stefan number, Ste≤0.25. In order to increase the accuracy of the model in simulating PCMs with higher Stefan number, the cell size has to be reduced accordingly.

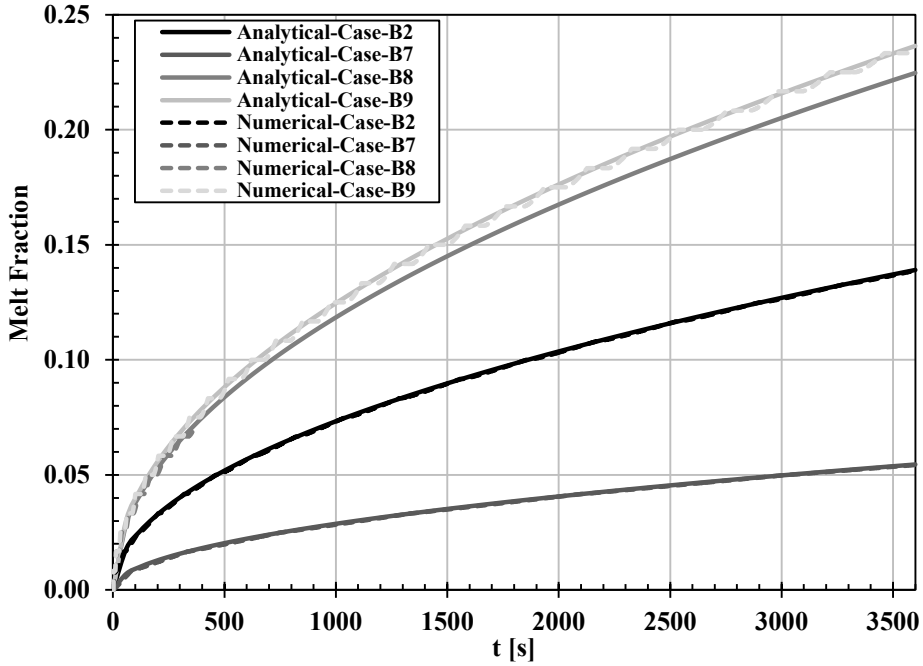

Figure A.14. Melt fraction of the PCM versus time (t) for different Stefan numbers. Case-B2: Ste=0.25, Case-B7: Ste=0.025, Case-B8: Ste=2.5, Case-B9: Ste=5.0.

APPENDIX B

EXPERIMENTAL VALIDATION OF THE MATHEMATICAL MODEL

As discussed in Chapter Four, Experiments (A3-A7) were conducted by Mather (2000) to show different operations of the single and multi-tank SHS. In this Appendix, the results from these experiments were extracted and used to validate the mathematical model for single- and multi-tank SHS.

B.1. Experiment A3

In Experiment A3, the initial temperature of the water inside the tank was 45°C and only the bottom coil heat exchanger was operating with a flow rate of 0.05 kg/s. The inlet temperature was set to 19°C for 1 hour followed by 60°C for 2 hours. Figure B.1 presents the temperature values measured at the outlet of the heat exchanger, the heat exchanger control volume (CV1 in Figure 5.2a) and the average bulk temperature of the tank (the average temperature of CVs 4, 7, 10, 13, 16 and 19 in Figure 5.2a). The dashed line represents the temperature profile of the bottom node from the numerical simulations; Node (b) in Figure 5.2b, while the dotted line depicts the average bulk temperature calculated from the average of the middle and top nodes; Node (bulk) and Node (t). It is seen that the numerical results are in good agreement with the experimental results.

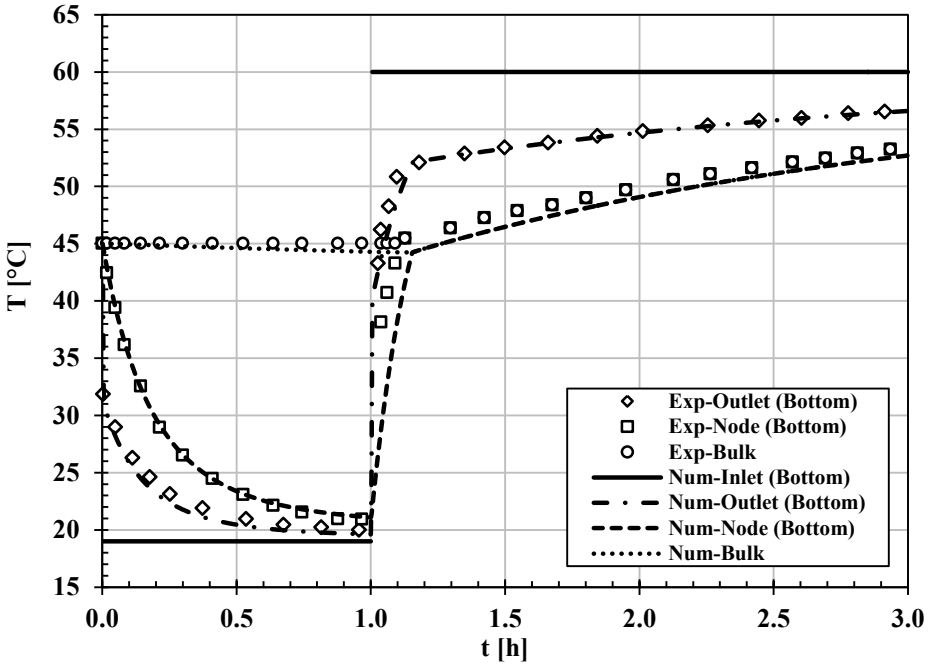

Figure B.1. Temporal profiles of the inlet and outlet temperatures of the bottom coil HX and the temperature of CV1 in Figure 5.2a. The dashed line shows the numerical profile for Node (b) in Figure 5.2b, while the dotted line presents the bulk temperature (the average of the middle and top nodes).

B.2. Experiment A4

A similar experiment was performed for the tank with the top coil heat exchanger operating alone. The initial temperature of the water inside the tank was 25°C. The mass flow rate through the top heat exchanger was fixed at 0.05 kg/s and the inlet temperature was set to 41°C for 1 hour followed by 15°C for 2 hours. The comparison between the experimental and the numerical results are demonstrated in Figure B.2.

It is shown that the numerical model is accurately capturing the physical behaviors that can occur in the SHS tank during different operation scenarios.

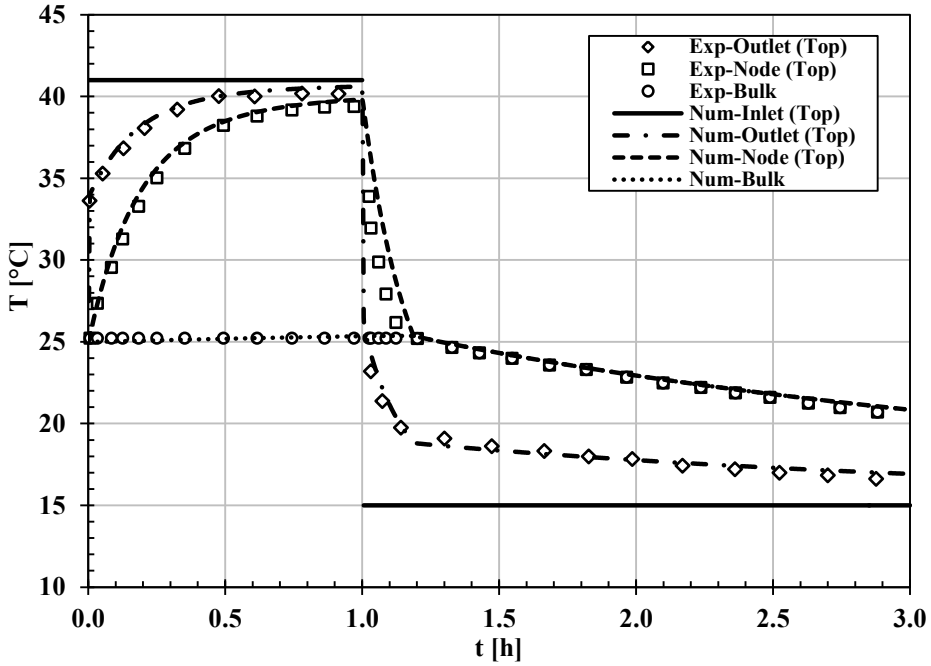

Figure B.2. Temporal profiles of the inlet and outlet temperatures of the top coil HX and the temperature of CV20 in Figure 5.2a. The dashed line shows the numerical profile for Node (t) in Figure 5.2b, while the dotted line presents the bulk temperature (the average of the middle and bottom nodes).

B.3. Experiment A5

In this experiment, the behavior of the single water tank was investigated during simultaneous operation of the bottom and top coil heat exchangers. Table B.1 presents the sequence of the test showing the inlet temperatures to both heat exchangers. Note that the time intervals when there was flow through either of the heat exchangers, the mass flow rate was set to 0.05 kg/s. Figure B.3 shows the comparison between the experimental measurements and the numerical values of the outlet temperatures from the bottom and top heat exchangers as well as the temperature of the bulk region of the tank (the middle node in the numerical model – extends from 60 mm to 702 mm from the bottom of the tank).

Table B.1. Sequence of Experiment A5.

Time interval [h]	T_{in} (bottom)	T_{in} (top)
0-1	60 °C	No flow
1-2	60 °C	30 °C
2-3	No flow	No flow
3-4	60 °C	No flow
4-5	40 °C	No flow
5-6	40 °C	20 °C
6-7	60 °C	20 °C
7-8	No flow	20 °C

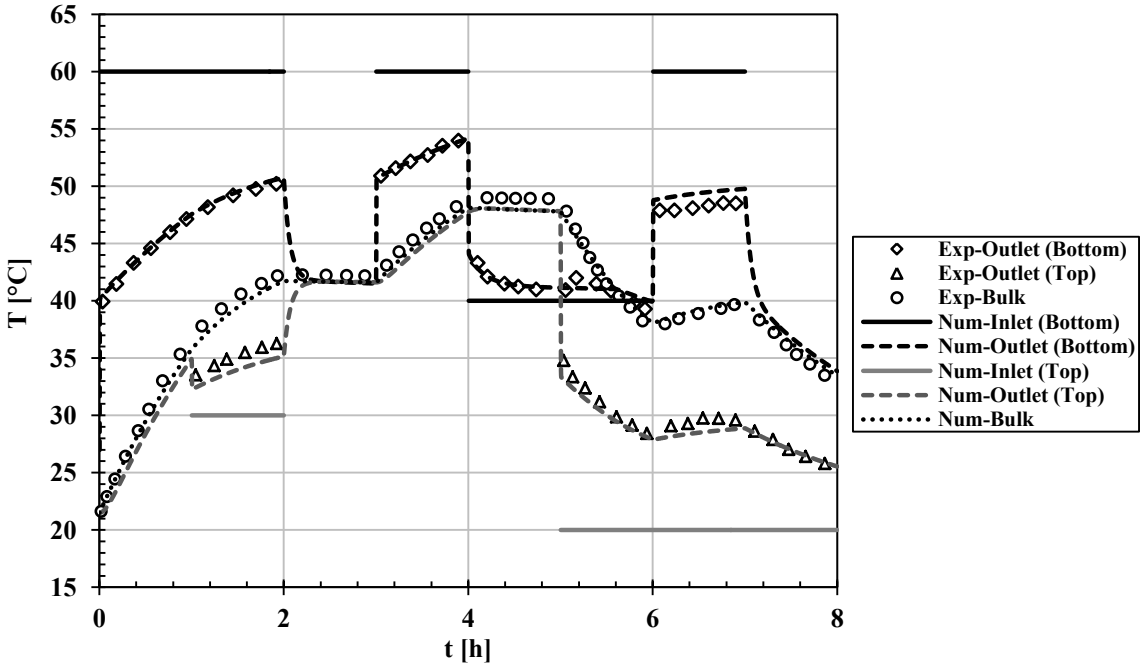

Figure B.3. Temporal profiles of the inlet and outlet temperatures of the bottom and top coil HX and the bulk temperature (average of CVs 4, 7, 10, 13 and 16 in Figure 5.2a). The dotted line presents the temperature of the bulk node in Figure 5.2b.

B.4. Experiment A6

The transient performance of 8-tank storage system was experimentally studied under sequential charging and discharging scenario. The eight tanks were serially connected through the bottom and top coil heat exchangers in a counter-flow configuration, Figure B.4.

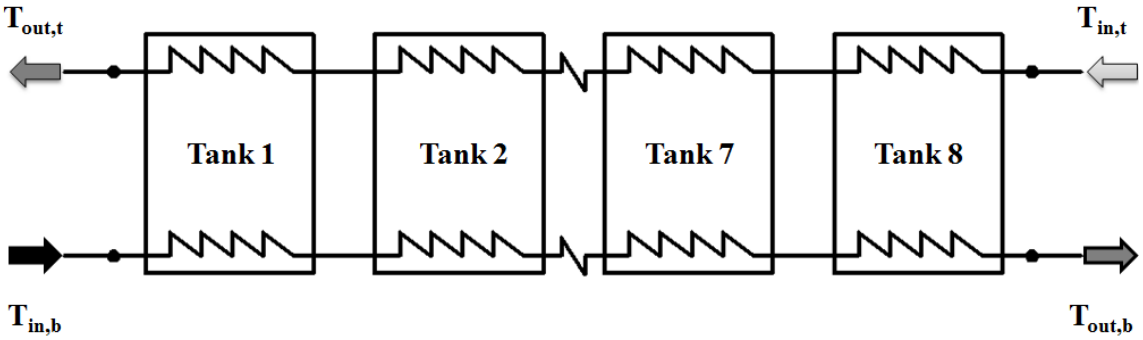

Figure B.4. Schematic of an 8-tank SHS system illustrating the inlet and outlet temperatures of the bottom and top HXs.

The testing procedure is presented in Table B.2 showing the sequence of operation of the bottom and top heat exchangers and the values of inlet temperatures $T_{in,b}$ and $T_{in,t}$.

Table B.2. Sequence of Experiment A6.

Time interval [h]	$T_{in,b}$	$T_{in,t}$	Comments
0-8	60 °C	No flow	Charging with a flow rate of 0.05 kg/s
8-16	No flow	25 °C	Discharging with a flow rate of 0.05 kg/s

The experimental and numerical results are demonstrated in Figure B.5 illustrating the outlet temperatures from the bottom and top heat exchangers of the 8-tank system as well as the average temperature inside tank 1, tank 4 and tank 8. Similar agreement was observed

in the temperatures of the other tanks but the profiles were omitted from the figure for conciseness.

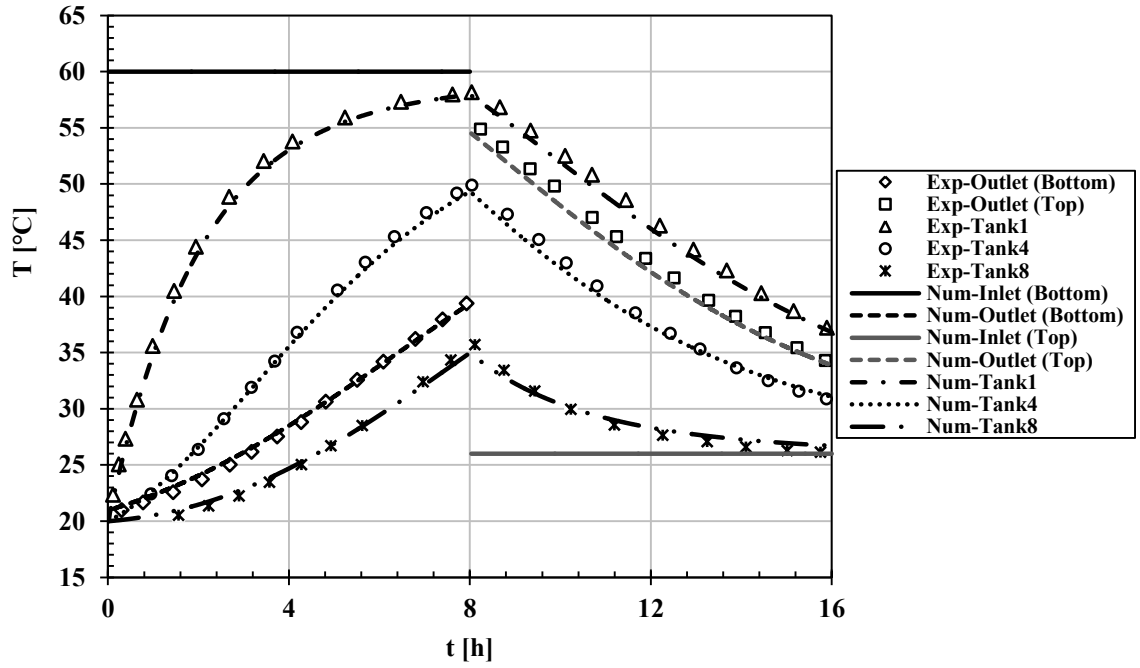

Figure B.5. Temporal profiles of the inlet and outlet temperature of the bottom and top coil HXs and the average bulk temperatures in tanks 1, 4 and 8.

It is shown that the system promotes the sequential or tank-to-tank stratification. The first tank attains the highest temperature level while the last tank attains the lowest temperature level. All the tanks were observed to operate all the time in the fully mixed mode.

B.5. Experiment A7

During realistic operation of storage systems, charging and discharging of the storage tank can occur simultaneously. As such, the last experiment was chosen to validate the numerical model against cases where the multi-tank system operates under simultaneous

operation of both heat exchangers. The 8-tank system in Figure B.4 was subjected to the same testing procedure illustrated in Table B.1.

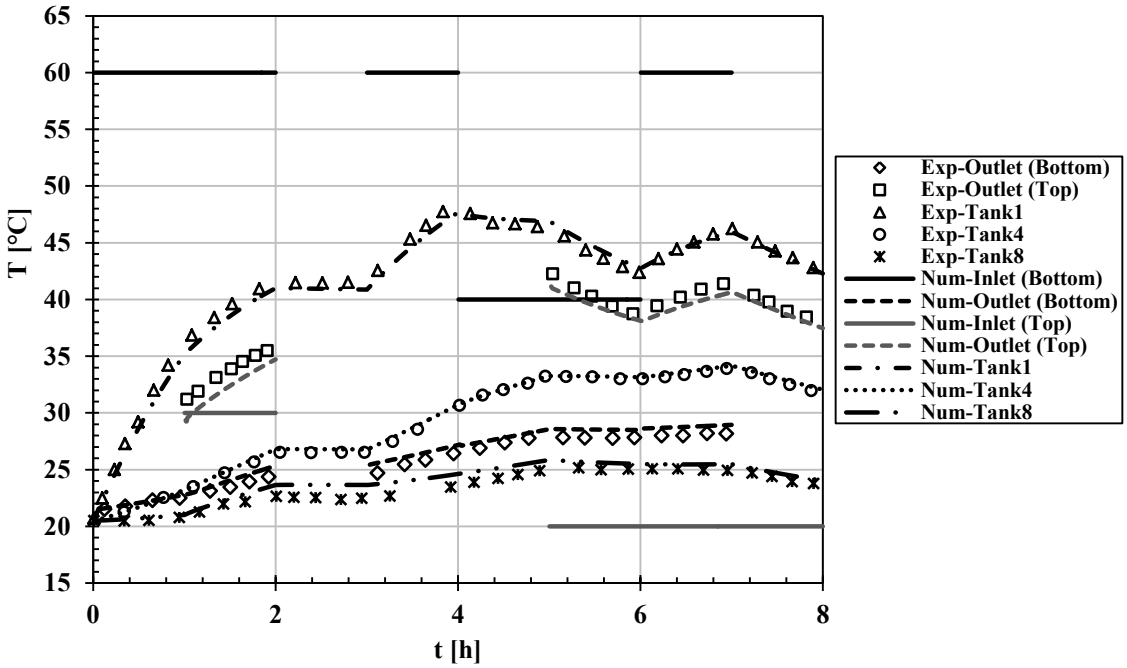

Figure B.6. Temporal profiles of the inlet and outlet temperature of the bottom and top coil HXs and the average bulk temperatures in tanks 1, 4 and 8.

Figure B.6 shows the comparison between the experimental and numerical results illustrating the outlet temperatures from the coil heat exchangers as well as the bulk temperatures of tank 1, tank 4 and tank 8.

APPENDIX C

PARAMETRIC ANALYSIS ON SINGLE-TANK HTES IN SOLAR DHW SYSTEM

A parametric study was conducted to investigate the effect of the key design parameters of the HTES system on the performance of the solar thermal DHW system. The studied parameters are the PCM volume fraction and the melting temperature since they showed critical influence on the potential gains of the HTES system. The design and operation conditions used in the parametric analysis are discussed in details in Section 6.2.2 "B- Single-tank Hybrid Thermal Energy Storage (HTES)". It was shown that the matched size of the SHS tank under the same operation conditions was 200 l. As such, the parametric analysis of the HTES system was carried out on two cases where the storage tank is under-sized (100 l) and over-sized (400 l). This is meant to illustrate the potential benefits of the HTES in reducing the size of the storage element.

Figures C.1 and C.2 illustrate the effect of increasing the PCM volume fraction on the performance of the solar thermal HTES system with tank volumes of 100 l and 400 l, respectively. The PCM melting temperature was set in all the numerical simulations to 30°C. It is seen that increasing the PCM volume fraction increases the solar fraction of the HTES system. However, the effect is more pronounced in the case with under-sized tank. This is primarily attributed to the temperature modulation effect of the PCM. Figures C.3 and C.4 show the temporal profiles of the average water temperature inside the HTES tank. Similar

effects are noticed in the profiles of the return temperature to the collector, Figures C.5 and C.6.

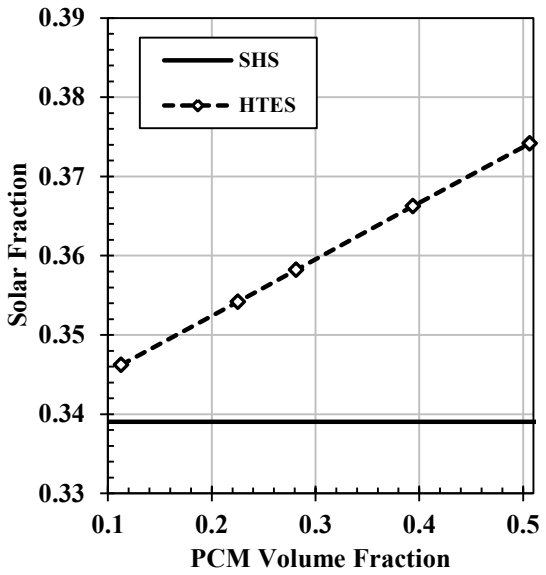

Figure C.1. Solar fraction versus PCM volume fraction for solar thermal DHW system with a 100-l HTES tank operating in March 21st under out-of-phase load. Solid line: Solar fraction for 100-l SHS tank system.

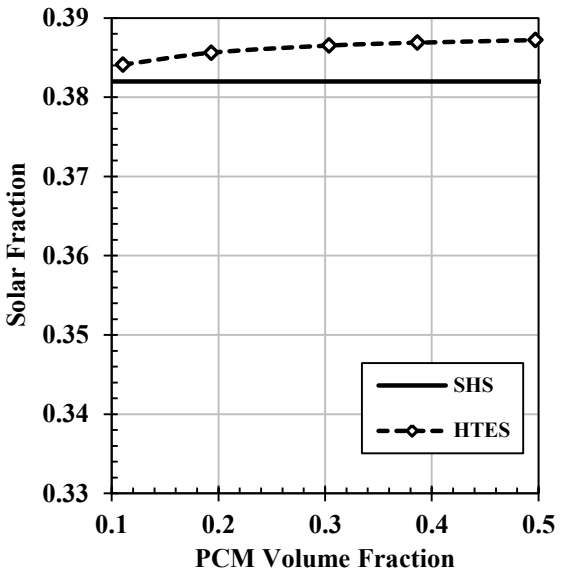

Figure C.2. Solar fraction versus PCM volume fraction for solar thermal DHW system with a 400-l HTES tank operating in March 21st under out-of-phase load. Solid line: Solar fraction for 400-l SHS tank system.

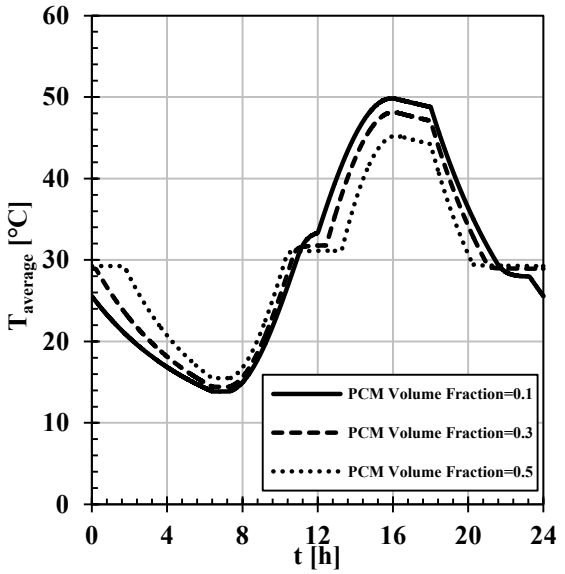

Figure C.3. Temporal profiles of the average temperature inside a 100-l HTES tank with different PCM volume fraction operating in March 21st under out-of-phase load.

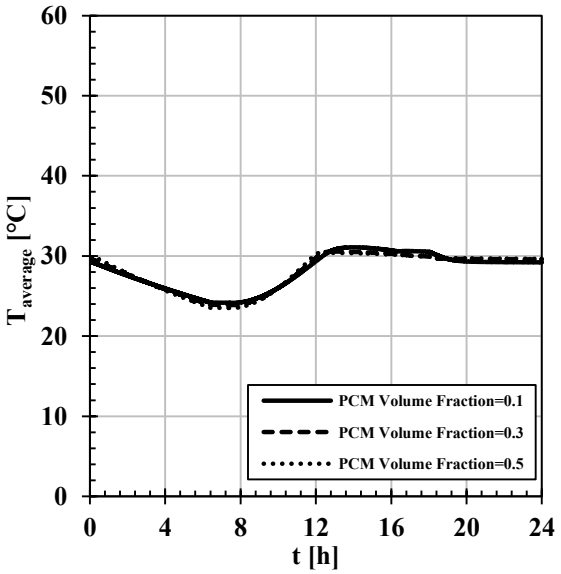

Figure C.4. Temporal profiles of the average temperature inside a 400-l HTES tank with different PCM volume fraction operating in March 21st under out-of-phase load.

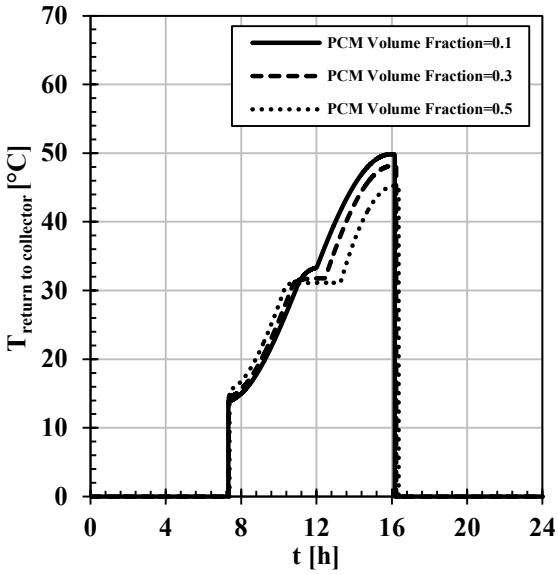

Figure C.5. Temporal profiles of the return temperature to the collector from a 100-l HTES tank with different PCM volume fraction operating in March 21st under out-of-phase load.

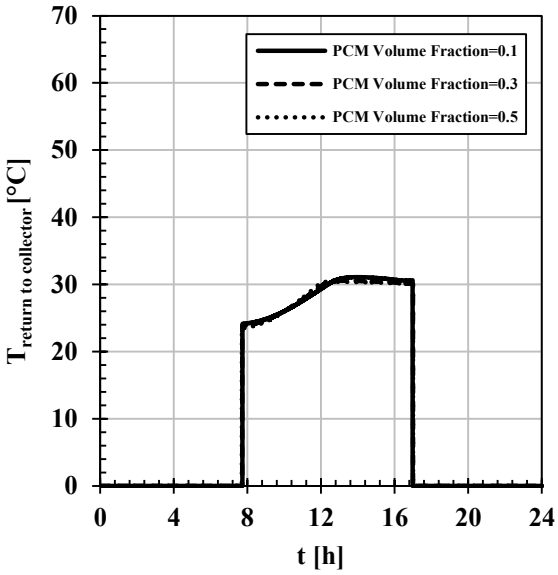

Figure C.6. Temporal profiles of the return temperature to the collector from a 400-l HTES tank with different PCM volume fraction operating in March 21st under out-of-phase load.

The PCM melting temperature is expected to have a critical impact on the performance of the solar thermal HTES system. The PCM melting temperature should be chosen such that most of the energy exchange with the storage element takes place in the form of latent heat. Poor selection of the PCM might lead to lower performance than the SHS system.

Figures C.7 and C.8 illustrate the effect of selecting PCMs with different melting temperatures on the performance of the solar thermal HTES system with tank volumes of 100 l and 400 l, respectively. The PCM volume fraction was set in all the numerical simulations to 0.5. It is seen that the effect of the melting temperature is more pronounced in the under-sized tank. In order to achieve maximum solar fraction, the PCM melting temperature should be chosen to match an optimum value that is a function of the boundary conditions of the system (the supply and demand profiles). Figures C.9-C.12 show the effect of the PCM

melting temperature on the modulation of the operation temperature of the storage element as well as the return temperature to the collector.

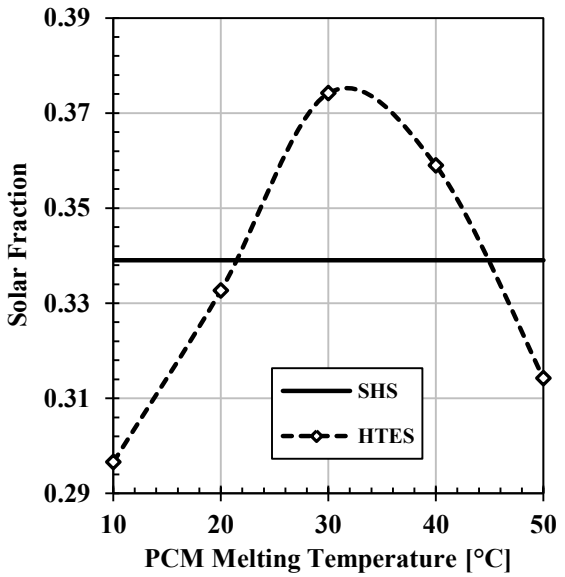

Figure C.7. Solar fraction versus PCM melting temperature for solar thermal DHW system with a 100-l HTES tank operating in March 21st under out-of-phase load. Solid line: Solar fraction for 100-l SHS tank system.

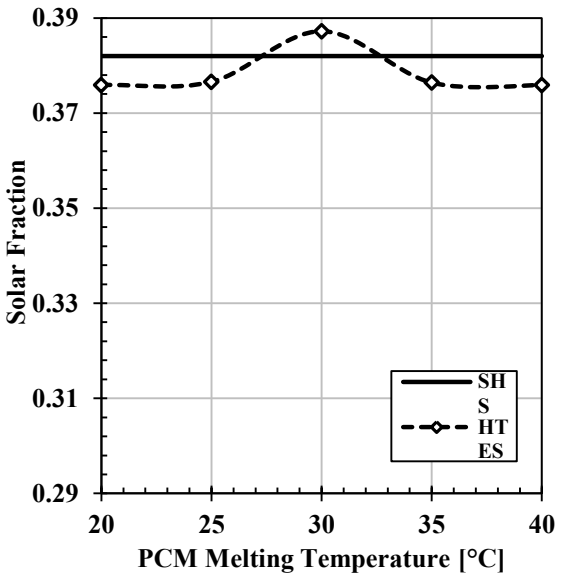

Figure C.8. Solar fraction versus PCM melting temperature for solar thermal DHW system with a 400-l HTES tank operating in March 21st under out-of-phase load. Solid line: Solar fraction for 400-l SHS tank system.

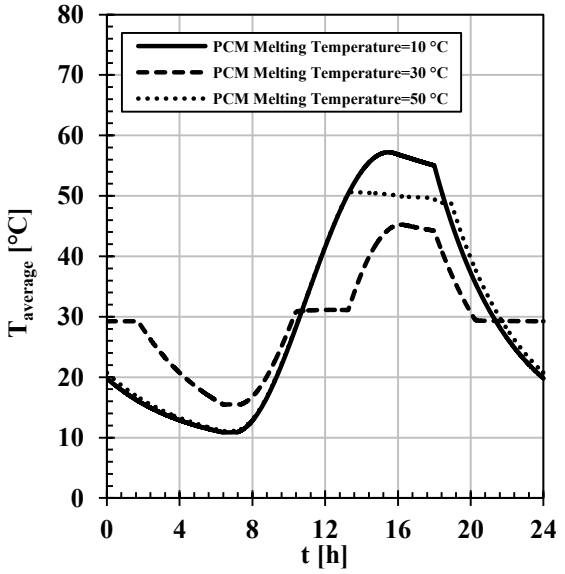

Figure C.9. Temporal profiles of the average temperature inside a 100-l HTES tank with different PCM melting temperature operating in March 21st under out-of-phase load.

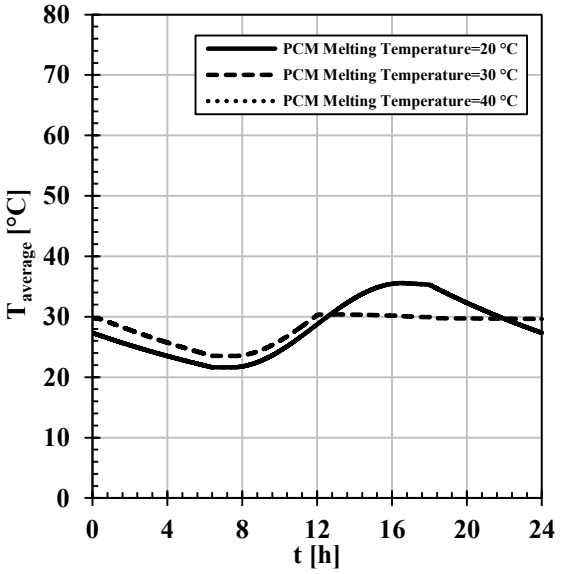

Figure C.10. Temporal profiles of the average temperature inside a 400-l HTES tank with different PCM melting temperature operating in March 21st under out-of-phase load.

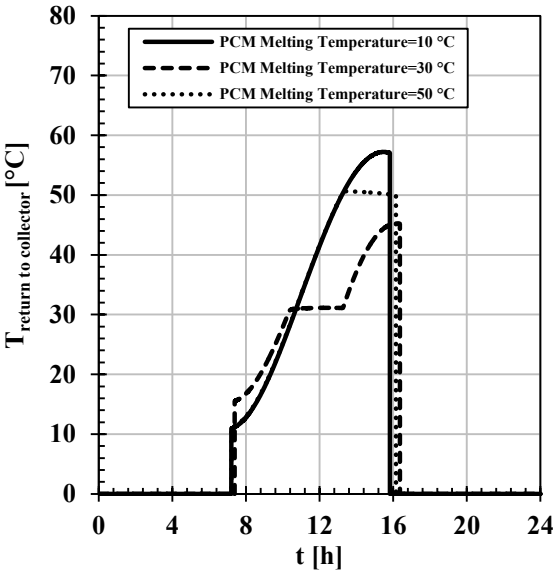

Figure C.11. Temporal profiles of the return temperature to the collector from a 100-l HTES tank with different PCM melting temperature operating in March 21st under out-of-phase load.

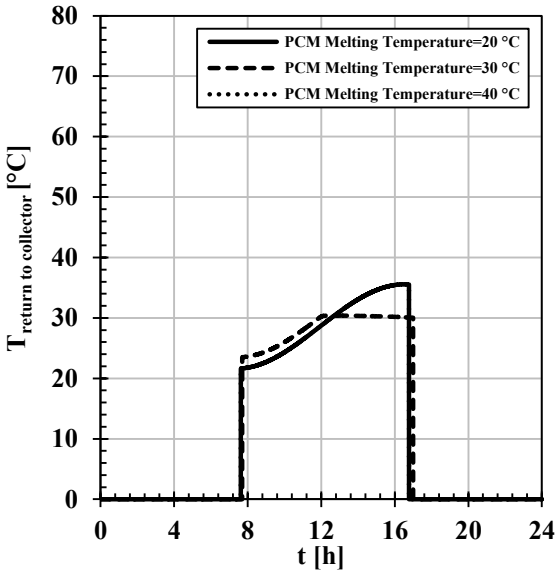

Figure C.12. Temporal profiles of the return temperature to the collector from a 400-l HTES tank with different PCM melting temperature operating in March 21st under out-of-phase load.

APPENDIX D

CALIBRATION OF SENSORS AND UNCERTAINTY ANALYSIS

Prior to experimental testing, all the measurement instruments were calibrated using available reference instruments to increase the accuracy of the measurements. The flow rate of the bottom and top heat exchangers of the storage tank were measured using flow meters. The temperatures at the inlet and outlet of both heat exchangers as well as inside the storage tank were measured using T-type thermocouples. A 1/2-inch Coriolis mass flow meter (Endress+Hauser, Proline Promass 80E - http://www.-endress.com/en/Field-instruments-overview/Flow-measurement-productoverview-/Product-Coriolis-flowmeter-Proline-Promass-80E) was used to calibrate the turbine flow meter (Omega, FTB101 - http://www.omega.ca/pptst_eng/FTB100.html) used for the charging loop flow rate measurement. The base accuracy of the mass/volume flow rate measurement using the Coriolis flow meter is ±0.2% of the reading. A platinum resistance thermometer (PT100 RTD) was used to calibrate all 26 T-type thermocouples used for the temperature measurements. The accuracy of the RTD as reported by the manufacturer was ±0.01°C. Details about the calibration of the measurement instruments are provided below.

D.1. Calibration of the turbine flow meter

The turbine flow meter was installed upstream of the bottom coil (charging) heat exchanger to measure the flow rate at the inlet to the heat exchanger. A signal conditioner

(Omega, FLSC-61 - http://www.omega.ca/pptst_eng/FLSC60.html) was mounted on the turbine flow meter to scale the frequency measurement to 12 Volts-DC output signal that was recorded by the DAQ system. During calibration, both flow meters were connected in series to the Lytron Chiller. Deionized water was used in the chiller and the setpoint temperature was 22°C. The flow rate was adjusted from 0 to 6 lpm with a step of 0.5 lpm. At each setpoint, the data from the turbine flow meter in "Volt" and from the Coriolis flow meter in "litres per minute" was recorded by the DAQ system for 60 s with a sampling rate of 10 S/s.

The results from this calibration are shown in Figure D.1, where the volt signal output from the turbine flow meter is plotted against the volumetric flow rate measurement of the Coriolis flow meter.

A linear regression analysis was applied to the results and the correlation was deduced between the measurements of the calibrated instrument and the reference instruments, as shown in Figure D.1. At each setpoint, the 600 data points were found to be distributed around the mean with a maximum deviation of ±0.04 V and ±0.019 lpm (95% confidence interval or ±2σ). The correlation was applied to the LabVIEW interface of the DAQ system in order to correct the turbine flow rate measurement. Figure D.2 illustrates the corrected flow rate of the turbine flow meter using the correlation (y=0.5315x) against the flow rate measured by the reference flow meter. Figure D.3 shows the deviation of the measurements form the regression correlation. It is seen that deviation lies within ±0.065 lpm (95% confidence interval or ±2σ).

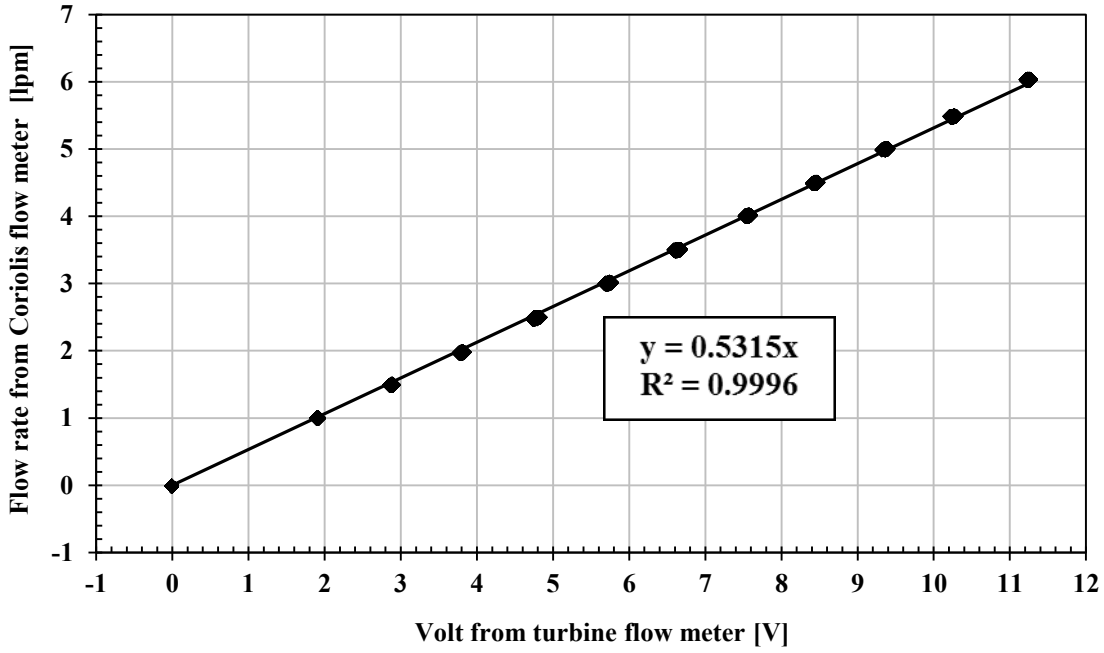

Figure D.1. Voltage signal from the turbine flow meter versus the flow rate measurement from the Coriolis flow meter (before calibration).

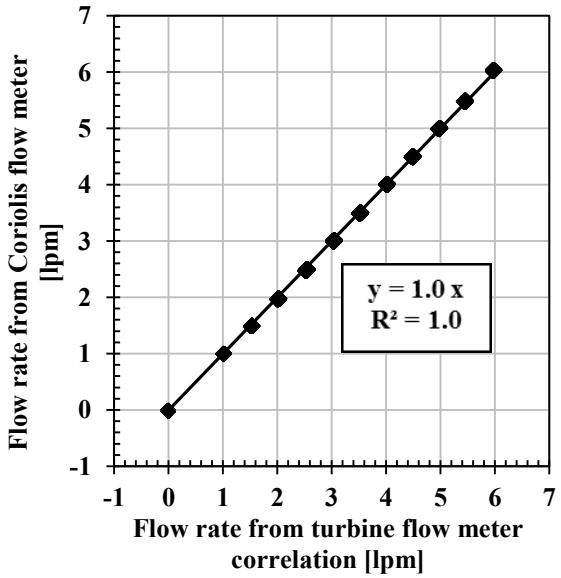

Figure D.2. Corrected flow rate from the turbine flow meter versus the reference flow rate measurement from the Coriolis flow meter (after calibration).

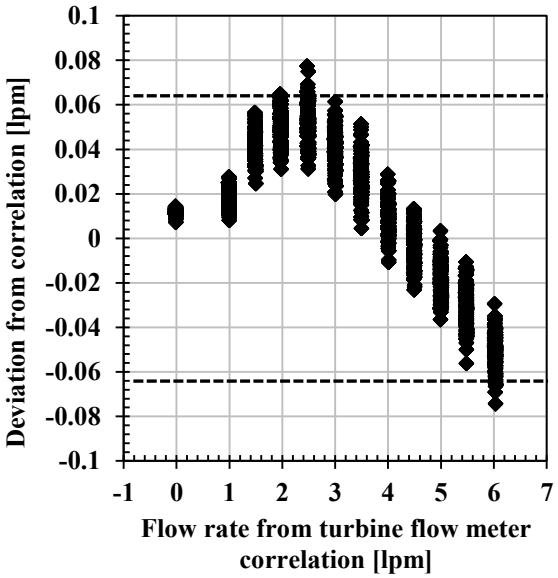

Figure D.3. Deviation (error= Flow rate measured by turbine flow meter – Reference flow rate). The dashed lines show the bounds within which 95% of the data lies (±2σ).

D.2. Calibration of the thermocouples

The 26 T-type thermocouples were calibrated using a reference platinum resistance thermometer (PT100 RTD) in a temperature-controlled thermal bath. The temperature of the thermal bath was set between 10°C and 70°C with a step of 5°C. At each setpoint, the temperatures measured by the RTD and the thermocouples were recorded by the DAQ system at a sampling rate of 2 S/s for 60 seconds. The software cold junction compensation was used to provide a simulated ice-point reference for the thermocouple measurements. Figure D.4 presents a sample of the calibration procedure for two thermocouples at the inlet and outlet of the top coil heat exchanger. The figure shows the temperature measured by the thermocouples plotted against the temperature measured by the reference RTD. The plotted results were taken as the average of the values measured over the 60-second test (the average of 120 data points).

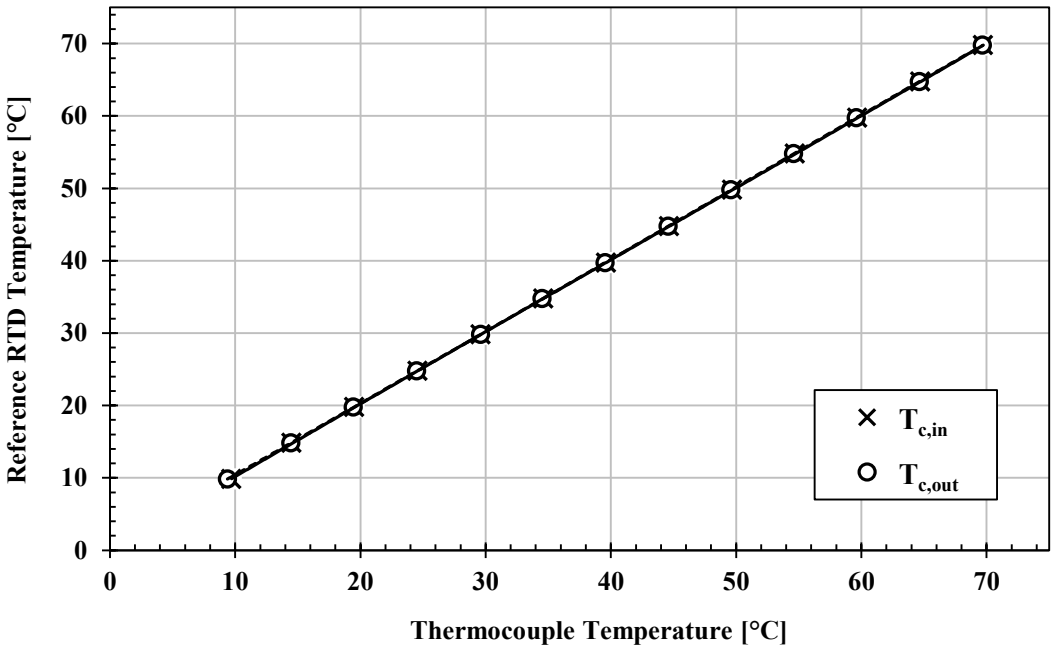

Figure D.4. Measured temperature by thermocouples versus reference temperature measurements by the RTD.

At each setpoint, the maximum deviation of the RTD measurements around their mean was ±0.0062°C, while that of the thermocouples was ±0.071°C. Regression analysis was applied to fit a polynomial to the calibration results. Table D.1 presents the polynomial equations for both thermocouples and the corresponding R^2 values.

Table D.1. The polynomial equations for both thermocouples and the corresponding R^2 values.

	Polynomial Curve Fit	**R^2 Value**
Inlet temperature to the coil ($T_{c,in}$)	$y = 4.6175 \times 10^{-6}x^3 - 5.7015 \times 10^{-4}x^2 + 1.0168x + 7.5674 \times 10^{-2}$	1.0
Outlet temperature to the coil ($T_{c,out}$)	$y = -4.3619 \times 10^{-6}x^3 + 5.9154 \times 10^{-4}x^2 + 0.9716x + 0.6603$	1.0

The polynomial equations for all the thermocouples were entered to the LabVIEW interface of the DAQ system in order to correct the temperature measurements. Figure D.5 shows the corrected thermocouple measurements plotted against the reference RTD measurements. Figure D.6 illustrates the deviation of the thermocouple measurements from the polynomial correlation. It was seen that the maximum deviation observed was ±0.073°C based on 95% confidence interval.

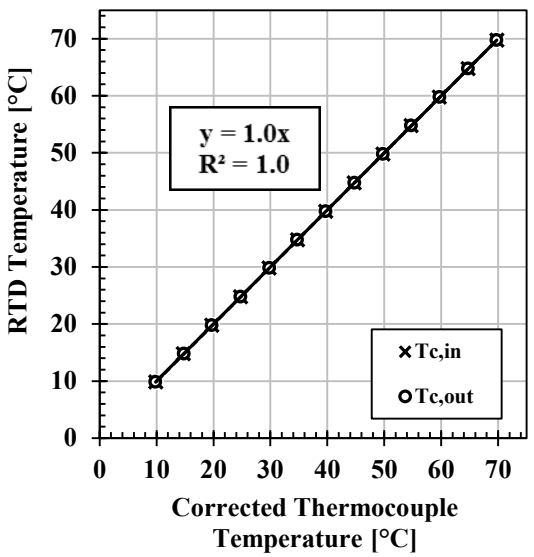

Figure D.5. Corrected measurements of the thermocouples versus reference temperature measurements by the RTD (after calibration).

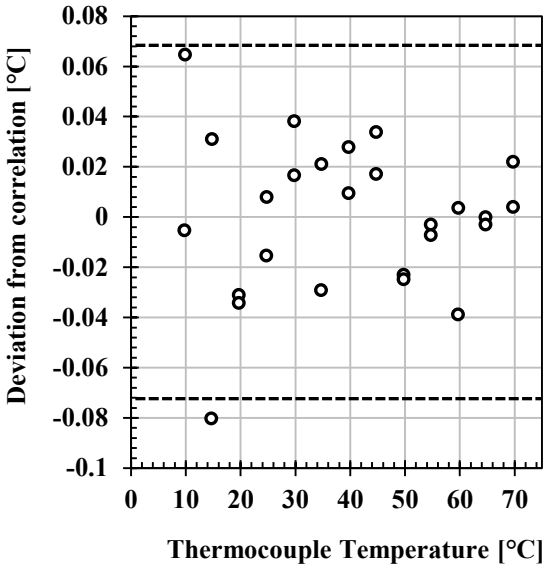

Figure D.6. Deviation of the thermocouple measurements from the polynomial correlation. The dashed lines show the bounds within which 95% of the data lies (±2σ).

D.3. Uncertainty of flow rate measurements

The reference Coriolis flow meter was used to measure the flow rate at the inlet of the top coil heat exchangers. As such, the uncertainty of the top coil flow rate aligned with the accuracy of the reference flow meter, ±0.2% of the reading.

For the turbine flow meter, used for the flow rate measurement at the inlet of the bottom coil heat exchanger, the total uncertainty of the flow rate measurement was estimated by:

$$\delta\dot{V} = \sqrt{\sum_{i=1}^{3}(\delta_i)^2} \tag{D-1}$$

δ_1 : The uncertainty associated with the reference flow meter.

δ_2 : The uncertainty associated with the reproducibility of the measurements.

δ_3 : The uncertainty associated with the regression analysis of the calibration data.

Uncertainty associated with the reference flow meter

The accuracy of the reference Coriolis mass flow meter was taken as provided by the manufacturer (i.e., ±0.2% of the reading). For conservative analysis, the uncertainty was estimated based on the highest limit of the calibration curve (i.e., 6 lpm), to be ±0.012 lpm.

Uncertainty associated with the reproducibility of the measurements

During the calibration of the turbine flow meter, 600 data points were recorded at each setpoint flow rate to evaluate the reproducibility of the measurements. It was shown that the maximum deviation of the measurements from their mean was ±0.04 V for the turbine flow meter and ±0.019 lpm for the Coriolis flow meter. These values were considered an estimate for the reproducibility error of the measurement. The reproducibility error in the voltage signal from the turbine flow rate was converted into an equivalent uncertainty in the flow rate using the linear regression correlation in section D.1. It was estimated to be ±0.021 lpm. As such, the combined effect of the reproducibility errors could be estimated by:

$$\delta_2 = \sqrt{(0.019)^2 + (0.021)^2} = \pm 0.028\ lpm \tag{D-2}$$

Uncertainty associated with the regression analysis of the calibration data

The deviation of the measurements form the regression correlation was shown in Figure D.3 to lie within ±0.065 lpm.

Therefore, the total uncertainty in the turbine flow rate measurement based on 95% confidence interval (±2σ) is given by:

$$\delta\dot{V} = \sqrt{(0.012)^2 + (0.028)^2 + (0.065)^2} = \pm 0.072\ lpm \tag{D-3}$$

D.4. Uncertainty in the temperature measurements

The total uncertainty in the thermocouple measurement was estimated by:

$$\delta T = \sqrt{\sum_{i=1}^{5} (\delta_i)^2} \quad \text{(D-4)}$$

δ_1 : The uncertainty associated with the reference RTD measurement.

δ_2 : The uncertainty associated with the position of the sensor in the thermal bath.

δ_3 : The uncertainty associated with the DAQ system.

δ_4 : The uncertainty associated with the regression analysis of the calibration data.

δ_5 : The uncertainty associated with the reproducibility of the measurement.

Uncertainty associated with the reference RTD measurement

The reference thermometer used for the calibration is a platinum resistance thermometer (PT100 RTD) with reported uncertainty from the manufacture of ±0.01 °C. The gain error of the DAQ card (National Instruments - NI 9219) was reported by the manufacturer to be ±0.1%. For conservative analysis, the uncertainty associated with the gain error of the DAQ card was estimated based on the highest temperature encountered in the experiments (i.e., 60°C), to be ±0.06°C. As a result, δ_1 can be calculated by:

$$\delta_1 = \sqrt{(0.01)^2 + (0.06)^2} = \pm 0.061℃ \quad \text{(D-5)}$$

Uncertainty associated with the position of the sensor in the thermal bath

The uncertainty associated with the assumption of uniform-temperature thermal bath, in which the calibration of the thermocouples was carried out, was determined by measuring the temperature in five different locations in the bath using the thermocouples.

The uncertainty was estimated as the maximum deviation of the measurements from their mean and was found to be ±0.014°C.

Uncertainty associated with the DAQ system

The DAQ card for the thermocouples (National Instruments - NI 9213) was reported to have a typical gain error of ±0.08%, equivalent to ±0.048°C based on the maximum measured temperature (60°C). Also, the accuracy of the built-in cold junction compensation was reported to be ±0.8°C in the temperature range of 0°C to 70°C. As a result, δ_3 can be calculated by:

$$\delta_3 = \sqrt{(0.048)^2 + (0.8)^2} = \pm 0.8℃ \quad \text{(D-6)}$$

Uncertainty associated with the regression analysis of the calibration data

The maximum deviation observed between the calibration data and the calibration polynomial equation was ±0.073°C based on 95% confidence interval, as illustrated in Figure D.6.

Uncertainty associated with the reproducibility of the measurement

The reproducibility uncertainty is estimated as twice the standard deviation for 120 calibration data points at each setpoint temperature. This corresponds to 95% confidence level. The calculated uncertainty was estimated to be ±0.0062°C for the RTD measurements and ±0.071°C for the thermocouple measurements. As a result, δ_5 can be calculated by:

$$\delta_5 = \sqrt{(0.0062)^2 + (0.071)^2} = \pm 0.071℃ \quad \text{(D-7)}$$

Therefore, the total uncertainty in the thermocouple measurement based on 95% confidence interval (±2σ) is given by:

$$\delta T = \sqrt{(0.061)^2 + (0.014)^2 + (0.8)^2 + (0.073)^2 + (0.071)^2} = \pm 0.81℃ \quad \text{(D-8)}$$

D.5. Propagation of measurement uncertainty

A dependent quantity R that is a function of a set of independent variables $(x_1, x_2, \dots, x_N)$ that are measured during the experiments can be modeled as:

$$R = f(x_1, x_2, \dots, x_N) \quad \text{(D-9)}$$

According to Kline and McClintock (1953) and Moffat (1985), the uncertainty of the dependent quantity (ε_R) can be estimated from the individual uncertainties of the independent variable $(\varepsilon_{x1}, \varepsilon_{x2}, \dots, \varepsilon_{xN})$ using the root-sum-square method:

$$\varepsilon_R = \pm \sqrt{\sum_{i=1}^{N} (\frac{\partial R}{\partial x_i} . \varepsilon_{xi})^2} \quad \text{(D-10)}$$

Uncertainty in the heat transfer rate from the coil heat exchangers

The heat transfer rate from the coil heat exchanger into the storage tank is calculated by:

$$Q = \dot{m} c (T_{in} - T_{out}) = \rho c \dot{V} (T_{in} - T_{out}) \quad \text{(D-11)}$$

Where $\dot{m}$ is the mass flow rate of the heat transfer fluid, c is the specific heat capacity of the heat transfer fluid, and T_{in} and T_{out} are the inlet and outlet temperatures of the heat exchanger, respectively.

The uncertainty in the heat transfer rate (ε_Q) can be calculated by:

$$\varepsilon_Q = \pm \sqrt{(\frac{\partial Q}{\partial \dot{m}} . \varepsilon_{\dot{m}})^2 + (\frac{\partial Q}{\partial c} . \varepsilon_c)^2 + (\frac{\partial Q}{\partial T_{in}} . \varepsilon_{T_{in}})^2 + (\frac{\partial Q}{\partial T_{out}} . \varepsilon_{T_{out}})^2} \quad \text{(D-12)}$$

or,

$$\varepsilon_Q = \pm\sqrt{(\frac{\partial Q}{\partial \rho}.\varepsilon_\rho)^2 + (\frac{\partial Q}{\partial c}.\varepsilon_c)^2 + (\frac{\partial Q}{\partial \dot{\forall}}.\varepsilon_{\dot{\forall}})^2 + (\frac{\partial Q}{\partial T_{in}}.\varepsilon_{T_{in}})^2 + (\frac{\partial Q}{\partial T_{out}}.\varepsilon_{T_{out}})^2} \quad \text{(D-13)}$$

As a result, the above equation can be written in terms of relative uncertainties as:

$$\frac{\varepsilon_Q}{Q} = \pm\sqrt{(\frac{\varepsilon_\rho}{\rho})^2 + (\frac{\varepsilon_c}{c})^2 + (\frac{\varepsilon_{\dot{\forall}}}{\dot{\forall}})^2 + 2 * [\frac{\varepsilon_T}{(T_{in} - T_{out})}]^2} \quad \text{(D-14)}$$

The relative uncertainties of the density ($\frac{\varepsilon_\rho}{\rho}$) and the specific heat capacity ($\frac{\varepsilon_c}{c}$) of water were estimated based on tabulated water properties in the temperature range from 15°C to 60°C to be ±0.0098 and ±0.00032, respectively.

During the lab experiments, the flow rate was kept constant and the heat transfer rate from the coils varied with time due to the transient change of the temperature difference (T_{in}-T_{out}). As such, the relative uncertainty of the heat transfer rate ($\frac{\varepsilon_Q}{Q}$) will depend on the value of the heat transfer rate (Q). Two simulations were conducted to estimate the relative uncertainties of the heat transfer rates from coil heat exchangers. The simulation parameters were adjusted to illustrate the uncertainties during the limiting cases of large and small heat transfer rates.

Bottom coil heat exchanger

A numerical simulation was conducted on a SHS tank with similar design parameters as discussed in Section 6.2. The initial temperature was set to 15°C and the inlet temperature to the bottom heat exchanger was fixed at 60°C for 8 hours. The flow rate was adjusted at 3 lpm. Figure D.7. illustrates the heat transfer rate from the bottom heat exchanger and the dashed lines represent the estimated uncertainties based on 95% confidence interval. The relative uncertainty in the heat transfer rate was found to vary

from ±5.1% at the higher limit (5400 W) to ±277.4% at the lower limit (86 W). Despite this, the absolute uncertainty ranges only from 37 W to 281 W. When the heat exchanger operates in the low end of the range, the relative uncertainty becomes high due to the small values of the actual heat transfer rate.

Top coil heat exchanger

Another numerical simulation was conducted on the same SHS tank with the initial temperature at 60°C and the inlet temperature to the top heat exchanger at 15°C. The simulation time was set to 8 hours and the mass flow rate was adjusted at 0.05 kg/s. As expected, the heat transfer rate from the heat exchanger was found to have the same behavior as in Figure D.7. but with a negative sign. However, the calculated uncertainties dropped slightly to ±4.4% at the higher limit and ±277.4% at the lower limit. This slight drop is a result of the higher accuracy of the mass flow meter used in the top heat exchanger loop.

Uncertainty in the energy ratios such as the storage gain

The energy stored or recovered from the storage element could be calculated by integrating the heat transfer rate of the coil heat exchanger over time:

$$E = \int Q_{coil} dt \cong \sum_{i=2}^{N} \frac{\Delta t}{2} (Q_i + Q_{i-1}) \ldots\ldots trapezoidal\ integration \qquad \text{(D-15)}$$

$$E \cong \frac{\Delta t}{2} (Q_i + Q_{i-1}) + \Delta t \sum_{i=2}^{N-1} Q_i \qquad \text{(D-16)}$$

$$\delta_E \cong \Delta t \sqrt{(\frac{\delta_{Q_1}}{2})^2 + \sum_{2}^{N-1}(\delta_{Q_i})^2 + (\frac{\delta_{Q_N}}{2})^2} \quad \text{(D-17)}$$

The uncertainty in the predicted value of energy is calculated using the case presented in Figure D.7. Based on experimental uncertainties:

$$\delta_E \cong \pm 0.15 \text{ MJ}$$

$$Gain \cong \frac{E_{HTES}}{E_{SHS}}$$

$$\delta_{Gain} \cong \pm 0.9\%$$

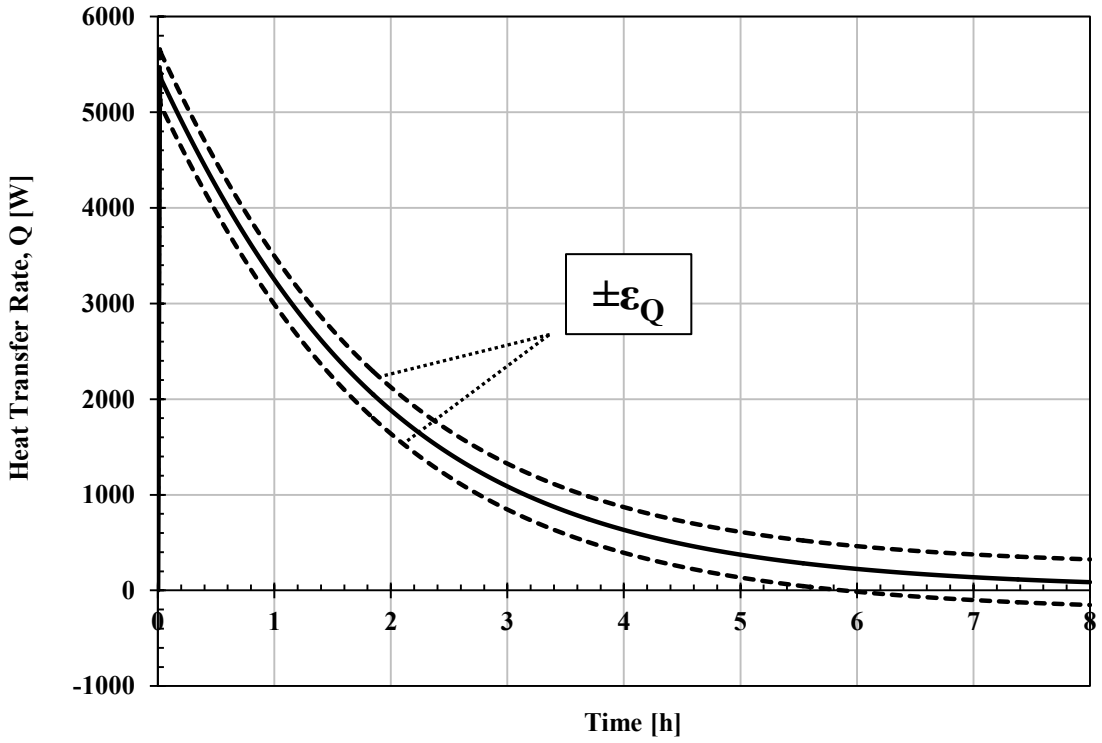

Figure D.7. The heat transfer rate from the bottom heat exchanger versus time. The dashed lines represent the estimated uncertainties based on 95% confidence interval.

REFERENCES

Abhat, A. (1983). Low Temperature Latent Heat Thermal Energy Storage: Heat Storage Materials. **Solar Energy,** 30 (4), 313-332.

Agyenim, F., Hewitt, N., Eames, P., and Smyth, M. (2010). A Review of Materials, Heat Transfer and Phase Change Problem Formulation for Latent Heat Thermal Energy Storage Systems (LHTESS). **Renewable and Sustainable Energy Reviews**, 14 (2), 615-628.

Al-Hinti, I., Al-Ghandoor, A., Maaly, A., Naqeera, I. A., Al-Khateeb, Z., and Al-Sheikh, O. (2010). Experimental Investigation on the Use of Water-Phase Change Material Storage in Conventional Solar Water Heating Systems. **Energy Conversion and Management**, 51 (8), 1735-1740.

Altuntop, N., Arslan, M., Ozceyhan, V., and Kanoglu, M. (2005). Effect of Obstacles on Thermal Stratification in Hot Water Storage Tanks. **Applied Thermal Engineering**, 25 (14), 2285-2298.

Andersen, E., and Furbo, S. (1999). Thermal Destratification in Small Standard Solar Tanks due to Mixing during Tapping. **Proceedings of ISES 1999 Solar World Congress**.

Arata, A.A., de Winter, F. (1991). Design and Performance of Large Solar Water Heating Systems. **Proceedings of ISES 1991 Solar World Congress**, 1306-1312.

Bejan, A. (1982). Entropy Generation through Heat and Fluid Flow. **John Wiley and Sons**, New York.

Bergman, T. L., and Incropera, F. P. (2011). Introduction to Heat Transfer. **John Wiley and Sons**, NewYork.

Bony, J., and Citherlet, S. (2007). Comparison between a New TRNSYS Model and Experimental Data of Phase Change Material in a Solar Combisystem. **Building And Simulation Conference**, Beijing.

Bony, J., and Citherlet, S. (2007-a). Numerical Model and Experimental Validation of Heat Storage with Phase Change Materials. **Energy and Buildings**, 39 (10), 1065-1072.

Buckles, W. E., and Klein, S. A. (1980). Analysis of Solar Domestic Hot Water Heaters. **Solar Energy**, 25 (5), 417-424.

Cabeza, L. F., Ibáñez, M., Sole, C., Roca, J., and Nogués, M. (2006). Experimentation with a Water Tank Including a PCM Module. **Solar Energy Materials and Solar Cells**, 90 (9),

1273-1282.

Canadian Standards Association. (2004). CAN/CSA-F379. 1-88: Solar Domestic Hot Water Systems (Liquid to Liquid Heat Transfer). **Canadian Standards Association**, Mississauga, ON.

Cataford, R. J., and Harrison, S. J. (1990). Factors Affecting Storage Tank Stratification and the Thermal Performance of SDHW Systems. **Solar Energy Society of Canada Inc.**, Halifax, Nova Scotia.

Çengel, Y. A. (1998). Heat Transfer: A Practical Approach. **WBC McGraw-Hill**.

Chinnapandiana, M., Pandiyarajan, V., and Velraj, R. (2011). Experimental Investigation of a Latent Heat Storage System for Diesel Engine Waste Heat Recovery with and without Cascaded Arrangement. **International Conference on Mechanical, Automobile and Robotics Engineering,** 239-243.

Chow, L. C., Zhong, J. K., and Beam, J. E. (1996). Thermal Conductivity Enhancement for Phase Change Storage Media. **International Communications in Heat and Mass Transfer**, 23 (1), 91-100.

Chung, J. D., Cho, S. H., Tae, C. S., and Yoo, H. (2008). The Effect of Diffuser Configuration on Thermal Stratification in a Rectangular Storage Tank. **Renewable Energy**, 33 (10), 2236-2245.

Cianfrini, C., Corcione, M., and Habib, E. (2007). Natural Convection from Multiple Horizontal Cylinders Arranged Side by Side. **HEFAT 2007**.

Crank, J. (1981). How to Deal with Moving Boundaries in Thermal Problems. **Numerical Methods in Heat Transfer**, 50, 177-200.

Cruickshank, C. A., and Harrison, S. J. (2004). Analysis of a Modular Thermal Storage for Solar Heating Systems. **Proceedings of the Joint Conference of the Canadian Solar Buildings Research Network and Solar Energy Society of Canada Inc.(SESCI)**.

Cruickshank, C.A. and Harrison, S.J. (2006). Analysis of a Modular Thermal Storage for Solar Heating Systems. **Proceedings of the Joint Conference of the Canadian Solar Buildings Research Network and Solar Energy Society of Canada Inc. (SESCI)**, Montreal, Quebec.

Cruickshank, C.A. and Harrison, S.J. (2009). Characterization of a Thermosyphon Heat Exchanger for Solar Domestic Hot Water Systems. **Journal of Solar Energy Engineering,** 131 (2).

Cruickshank, C. A., and Harrison, S. J. (2011). Thermal Response of a Series-and Parallel-Connected Solar Energy Storage to Multi-Day Charge Sequences. **Solar Energy**, 85 (1), 180-187.

Cui, H., Hou, X., and Yuan, X. (2003). Energy Analysis of Space Solar Dynamic Heat Receivers. **Solar Energy**, 74 (4), 303-308.

de Gracia, A., Oró, E., Farid, M. M., and Cabeza, L. F. (2011). Thermal Analysis of Including Phase Change Material in a Domestic Hot Water Cylinder. **Applied Thermal Engineering**, 31 (17), 3938-3945.

Dickinson, R. M., Cruickshank, C. A., and Harrison, S. J. (2013). Charge and discharge Strategies for a Multi-Tank Thermal Energy Storage. **Applied Energy**, 109, 366-373.

Douglas, J., and Gallie, T. M. (1955). Variable Time Steps in the Solution of the Heat Flow Equation by a Difference Equation. **Proceedings of the American Mathematical Society**, 6 (5), 787-793.

Duffie, J.A. and Beckman, W.A. (2013). Solar Engineering of Thermal Processes. **John Wiley and Sons York**, NewYork.

Edwards, S., Beausoleil-Morrison, I., and Laperrière, A. (2015). Representative Hot Water Draw Profiles at High Temporal Resolution for Simulating the Performance of Solar Thermal Systems. **Solar Energy**, 111, 43-52.

Energy Fact Book 20015-2016 (2015). **Natural Resources Canada**.

Energy Use Data Handbook - 1990 to 2013 (2016). **Natural Resources Canada**.

Farid, M. M., and Kanzawa, A. (1989). Thermal Performance of a Heat Storage Module Using PCM's with Different Melting Temperatures: Mathematical Modeling. **Journal Of Solar Energy Engineering**, 111 (2), 152-157.

Farid, M. M., Kim, Y., and Kansawa, A. (1990). Thermal Performance of a Heat Storage Module Using PCM's with Different Melting Temperature: Experimental. **Journal of Solar Energy Engineering**, 112 (2), 125-131.

Farid, M. M., Khudhair, A. M., Razack, S. A. K., and Al-Hallaj, S. (2004). A Review on Phase Change Energy Storage: Materials and Applications. **Energy Conversion and Management**, 45 (9), 1597-1615.

Furbo, S., Vejen, N. K., and Shah, L. J. (2005). Thermal Performance of a Large Low Flow Solar Heating System with a Highly Thermally Stratified Tank. **Journal of Solar Energy Engineering**, 127 (1), 15-20.

Ghaddar, N. K. (1994). Stratified Storage Tank Influence on Performance of Solar Water Heating System Tested in Beirut. **Renewable Energy**, 4 (8), 911-925.

Ghajar, A. J., and Zurigat, Y. H. (1991). Numerical Study of the Effect of Inlet Geometry on Stratification in Thermal Energy Storage. **Numerical Heat Transfer**, 19 (1), 65-83.

Gnielinski, V. (1976). New Equation for Heat and Mass Transfer in Turbulent Pipe and Channel Flow. **International Journal of Chemical Engineering**, 16, 359-368.

Gong, Z. X., and Mujumdar, A. S. (1996). Enhancement of Energy Charge-Discharge Rates in Composite Slabs of Different Phase Change Materials. **International Journal of Heat and Mass Transfer**, 39 (4), 725-733.

Griffiths, P. W., and Eames, P. C. (2007). Performance of Chilled Ceiling Panels Using Phase Change Material Slurries as the Heat Transport Medium. **Applied Thermal Engineering**, 27 (10), 1756-1760.

Haar, L. (1984). NBS/NRC Steam Tables**. CRC Press**.

Haillot, D., Franquet, E., Gibout, S., and Bédécarrats, J. P. (2013). Optimization of Solar DHW System Including PCM Media. **Applied Energy**, 109, 470-475.

Han, Z., Zheng, M., Kong, F., Wang, F., Li, Z., and Bai, T. (2008). Numerical Simulation of Solar Assisted Ground-Source Heat Pump Heating System with Latent Heat Energy Storage in Severely Cold Area. **Applied Thermal Engineering**, 28 (11), 1427-1436.

Hasnain, S. M. (1998). Review on Sustainable Thermal Energy Storage Technologies, Part I: Heat Storage Materials and Techniques. **Energy Conversion and Management**, 39 (11), 1127-1138.

Hawlader, M. N. A., Uddin, M. S., and Khin, M. M. (2003). Microencapsulated PCM Thermal-Energy Storage System. **Applied Energy**, 74 (1), 195-202.

Hess, C. F., and Miller, C. W. (1982). An Experimental and Numerical Study on the Effect of the Wall in a Thermocline-Type Cylindrical Enclosure—II Numerical Model. **Solar Energy**, 28 (2), 153-161.

Hollands, K. G. T., and Lightstone, M. F. (1989). A Review of Low-Flow, Stratified-Tank Solar Water Heating Systems. **Solar Energy**, 43 (2), 97-105.

Hollands, K.G.T, Brunger, A.P., Habicher, B. (1991). Active Solar Space-Heating System incorporating 'Low-Flow-Stratified-Tanks' and 'Thin-Fin' Collectors.**17th Annual Conference of the Solar Energy Society of Canada**, 245-249.

Hoogendoorn, C. J., and Bart, G. C. J. (1992). Performance and Modelling of Latent Heat Stores. **Solar Energy**, 48 (1), 53-58.

Ibanez, M., Cabeza, L. F., Sole, C., Roca, J., and Nogues, M. (2006). Modelization of a Water Tank Including a PCM Module. **Applied Thermal Engineering**, 26 (11), 1328-1333.

Jany, P., and Bejan, A. (1988). Scaling Theory of Melting with Natural Convection in an Enclosure. **International Journal of Heat and Mass Transfer**, 31 (6), 1221-1235.

Jegadheeswaran, S., and Pohekar, S. D. (2009). Performance Enhancement in Latent Heat Thermal Storage System: A Review. **Renewable and Sustainable Energy Reviews**, 13 (9), 2225-2244.

Jordan, U., and Vajen, K. (2001). Realistic Domestic Hot-Water Profiles in Different Time Scales. **Report for IEA-SHC Task**, 26.

Kline, S. J., McClintock. F. A. (1953). Describing Uncertainties in Single-Sample Experiments. **Mechanical Engineering**, 75 (1), 3-8.

Kleinbach, E. M., Beckman, W. A., and Klein, S. A. (1993). Performance Study of One-Dimensional Models for Stratified Thermal Storage Tanks. **Solar Energy**, 50 (2), 155-166.

Knudsen, S. (2002). Consumers' Influence on the Thermal Performance of Small SDHW Systems—Theoretical Investigations. **Solar Energy**, 73 (1), 33-42.

Kousksou, T., Bruel, P., Cherreau, G., Leoussoff, V., and El Rhafiki, T. (2011). PCM Storage for Solar DHW: From an Unfulfilled Promise to a Real Benefit. **Solar Energy**, 85 (9), 2033-2040.

Lane, G. A. (1980). Low Temperature Heat Storage with Phase Change Materials. **International Journal of Ambient Energy**, 1 (3), 155-168.

Lavan, Z., and Thompson, J. (1977). Experimental Study of Thermally Stratified Hot Water Storage Tanks. **Solar Energy**, 19 (5), 519-524.

Lutton, E. S. (1967). Thermal Properties and Crystal State. **Fatty Acids**, Part 4, 2584-2641.

Mather, D.W. (2000). Modular Stratified Thermal Energy Storage for Solar Heating Systems. **M.Sc. Thesis**, Department of Mechanical Engineering, University of Waterloo.

Mather, D.W., Hollands, K.G.T. and Wright, J.L. (2002). Single- and Multi-tank Energy Storage for Solar Heating Systems: Fundamentals. **Solar Energy**, 73 (1), 3-13.

Mehling, H., Cabeza, L. F., Hippeli, S., and Hiebler, S. (2002). Improvement of Stratified Hot Water Heat Stores using a PCM-Module. **Proceedings of EuroSun 2002**, University of Bologna, Italy.

Mettawee, E. B. S., and Assassa, G. M. (2007). Thermal Conductivity Enhancement in a Latent Heat Storage System. **Solar Energy**, 81 (7), 839-845.

Mezaki, R., Mochizuki, M., and Ogawa, K. (1999). Engineering Data on Mixing. **Elsevier**.

Michels, H., and Pitz-Paal, R. (2007). Cascaded Latent Heat Storage for Parabolic Trough Solar Power Plants. **Solar Energy**, 81 (6), 829-837.

Moffat, R.J. (1985). Using Uncertainty Analysis in the Planning of an Experiment, **ASME Transactions, Journal of Fluid Engineering**, 107, 173-178.

Morrison, D. J., and Abdel-Khalik, S. I. (1978). Effects of Phase-Change Energy Storage on the Performance of Air-Based and Liquid-Based Solar Heating Systems. **Solar Energy**, 20 (1), 57-67.

Nallusamy, N., Sampath, S., and Velraj, R. (2007). Experimental Investigation on a Combined Sensible and Latent Heat Storage System Integrated with Constant/Varying (Solar) Heat Sources. **Renewable Energy**, 32 (7), 1206-1227.

Naphon, P., and Suwagrai, J. (2007). Effect of Curvature Ratios on the Heat Transfer and Flow Developments in the Horizontal Spirally Coiled Tubes. **International Journal of Heat and Mass Transfer**, 50 (3), 444-451.

NATO Science Committee (1976). Thermal Energy Storage, **NATO Science Committee Conference,** Turnberry, Scotland.

Newton, B. J. (1995). Modeling of Solar Storage Tanks. **MSc. Thesis**, University of Wisconsin, Madison.

Nkwetta, D. N., and Haghighat, F. (2014). Thermal Energy Storage with Phase Change Material—A State-of-The Art Review. **Sustainable Cities and Society**, 10, 87-100.

Orndoff, E., and Trevino, L. A. (2000). Thermal Insulation Performance of Textile Structures for Spacesuit Applications at Martian Pressure and Temperature. **Proceedings of the 2nd International Conference on Safety and Protective Fabrics**, Industrial Fabrics Association, Arlington, VA.

Petrillo, D. W., and Jackson, D. R. (2012). **U.S. Patent No. D665, 280**. Washington, DC: U.S. Patent and Trademark Office.

Ragoonanan, V., Davidson, J. H., Homan, K. O., and Mantell, S. C. (2006). The Benefit of Dividing an Indirect Thermal Storage into Two Compartments: Discharge Experiments. **Solar Energy**, 80 (1), 18-31.

Raithby, G. D., and Hollands, K. G. T. (1975). A General Method of Obtaining Approximate Solutions to Laminar and Turbulent Free Convection Problems. **Advances in Heat Transfer**, 11, 265-315.

Raithby, G. D., and Hollands, K. G. T. (1998). Natural Convection. Handbook of Heat Transfer, 3.

Reddy, M. R., Nallusamy, N., Prasad, A. B., and Reddy, H. K. (2012). Thermal Energy Storage System Using Phase Change Materials: Constant Heat Source. **Thermal Science**, 16 (4), 1097-1104.

Remund, J., Lang, R., and Kunz, S. (2003). Meteonorm V5.0 Software and Handbook on CD-ROM. **Meteotest**, Fabrikstrasse, 14, 3012.

Sarafraz, P. (2013). Thermal Optimization of Flat Plate PCM Capsules in Natural Convection Solar Water Heating Systems. **MSc. Thesis**, McMaster University Hamilton.

Seeniraj, R. V., and Narasimhan, N. L. (2008). Performance Enhancement of a Solar Dynamic LHTS Module having both Fins and Multiple PCMs. **Solar Energy**, 82 (6),

535-542.

Sekulic, D.P. and Krane, R.J. (1992). The Use of Multiple Storage Elements to Improve the Second Law Efficiency of a Thermal Energy Storage System, Part I: Analysis of the Storage Process. **Proceedings of the ECOS 92 on Efficiency, Costs, Optimization and Simulation of Energy Systems, ASME**, New York, 61 – 66.

Shabgard, H., Bergman, T. L., Sharifi, N., and Faghri, A. (2010). High Temperature Latent Heat Thermal Energy Storage Using Heat Pipes**. International Journal of Heat and Mass Transfer**, 53 (15), 2979-2988.

Shabgard, H., Robak, C. W., Bergman, T. L., and Faghri, A. (2012). Heat Transfer and Exergy Analysis of Cascaded Latent Heat Storage with Gravity-Assisted Heat Pipes for Concentrating Solar Power Applications. **Solar Energy**, 86 (3), 816-830.

Shaikh, S., and Lafdi, K. (2006). Effect of Multiple Phase Change Materials (PCMs) Slab Configurations on Thermal Energy Storage. **Energy Conversion and Management**, 47 (15), 2103-2117.

Shah, L. J., and Furbo, S. (2003). Entrance Effects in Solar Storage Tanks. **Solar Energy**, 75 (4), 337-348.

Sharma, A., Tyagi, V. V., Chen, C. R., and Buddhi, D. (2009). Review on Thermal Energy Storage with Phase Change Materials and Applications. **Renewable and Sustainable Energy Reviews**, 13 (2), 318-345.

Sharp, M. K., and Loehrke, R. I. (1979). Stratified Thermal Storage in Residential Solar Energy Applications. **Journal of Energy**, 3 (2), 106-113.

Spur, R., Fiala, D., Nevrala, D., and Probert, D. (2006). Influence of the Domestic Hot-Water Daily Draw-off Profile on the Performance of a Hot-Water Store. **Applied Energy**, 83 (7), 749-773.

Steinhaus, H. (1999). Mathematical Snapshots. **3rd ed. New York: Dover**, 202-203.

Talmatsky, E., and Kribus, A. (2008). PCM Storage for Solar DHW: An Unfulfilled Promise? **Solar Energy**, 82 (10), 861-869.

Taylor, M.J. and Krane, R.J. (1991). Second Law Optimization of a Sensible Heat Thermal Energy Storage System with a Distributed Storage Element – Part 1: Development of the Analytical Model. **Journal of Energy Resources Technology**, 113, 20-26.

Thomas, M., Hayden, A. C. S., Ghiricociu, O., Cane, R. L. D., and Gagnon, R. (2011). A New Study of Hot-Water Use in Canada. **ASHRAE Transactions**, 117 (1).

Tian, Y., and Zhao, C. Y. (2013). A Review of Solar Collectors and Thermal Energy Storage in Solar Thermal Applications. **Applied Energy**, 104, 538-553.

Trelles, J. P., and Dufly, J. J. (2003). Numerical Simulation of Porous Latent Heat Thermal

Energy Storage for Thermoelectric Cooling. **Applied Thermal Engineering**, 23 (13), 1647-1664.

van Koppen, C. W. J., and Thomas, J. S. (1978). Preliminary Performance of The Heating System in the Solar House of the Eindhoven University of Technology. **Eindhoven University of Technology Report no. WPS3-78.11.R291**, The Netherlands.

Velraj, R., Seeniraj, R. V., Hafner, B., Faber, C., and Schwarzer, K. (1997). Experimental Analysis and Numerical Modelling of Inward Solidification on a Finned Vertical Tube for a Latent Heat Storage Unit. **Solar Energy**, 60 (5), 281-290.

Watanabe, T., Kikuchi, H., and Kanzawa, A. (1993). Enhancement of Charging and Discharging Rates in a Latent Heat Storage System by Use of PCM with Different Melting Temperatures. **Heat Recovery Systems and CHP**, 13 (1), 57-66.

Yaws, C. L., and Gabbula, C. (2003). Yaws' Handbook of Thermodynamic and Physical Properties of Chemical Compounds. **Knovel**.

Zalba, B., Marín, J. M., Cabeza, L. F., and Mehling, H. (2003). Review on Thermal Energy Storage with Phase Change: Materials, Heat Transfer Analysis and Applications. **Applied Thermal Engineering**, 23 (3), 251-283.

Zurigat, Y. H., Liche, P. R., and Ghajar, A. J. (1990). Influence of the Inlet Geometry on Stratification in Thermal Energy Storage. **International Journal of Heat and Mass Transfer**, 34, 115-125.